

# Emergent electrodynamics in non-collinear spin textures

## Dissertation

zur Erlangung des  
Doktorgrades der Naturwissenschaften  
(Dr. rer. nat.)

der Naturwissenschaftlichen Fakultät II  
Chemie, Physik und Mathematik  
der Martin-Luther-Universität  
Halle-Wittenberg

vorgelegt von Herrn

**BÖRGE GÖBEL**

geboren am 03.12.1992 in Freiberg



Erstgutachterin: Prof. Dr. Ingrid Mertig  
Zweitgutachter: Prof. Dr. Steffen Trimper  
Drittgutachter: Prof. Dr. Mathias Kläui

Datum der Abgabe: 11.09.2019  
Tag der öffentlichen Verteidigung: 28.01.2020  
Vorsitzender der Promotionskommission: Prof. Dr. Wolf Widdra



## Abstract

This cumulative thesis reports on the investigation of the coupling of electrons and non-collinear spin textures like magnetic skyrmions — small, whirl-like modulations of the collinear ferromagnetic phase. The considered textures typically carry a finite topological charge, which gives rise to the topological Hall effect of electrons and a Hall effect of the spin textures themselves. Using Monte Carlo simulations and micromagnetic spin dynamics simulations, I predict individual biskyrmions (two overlapping skyrmions) in centrosymmetric materials, magnetic bimerons in in-plane magnetized films, and antiferromagnetic skyrmion crystals (the combination of two skyrmions with opposite topological charges). By utilizing the Berry theory and Landauer-Büttiker approaches the topological Hall effect and the magnetoelectric properties of skyrmions are quantified. Furthermore, I predict a purely topologically induced Hall effect of electrons in bimeron crystals, a topological spin Hall effect of electrons in antiferromagnetic skyrmion crystals, and show that magnetic skyrmioniums exhibit a topological Hall signature even though they have a vanishing topological charge. As the perhaps most promising contribution to the utilization of non-collinear spin textures in spintronic applications, a method is established which allows to propel skyrmions parallel to an applied current, 10 times as fast as previously reported.

## Kurzzusammenfassung

In dieser kumulativen Doktorarbeit wird die Wechselwirkung von Elektronen mit nicht-kollinearen Spintexturen, wie zum Beispiel Skyrmionen — kleinen wirbelartigen Anregungen in einer kollinearen ferromagnetischen Phase — untersucht. Die meisten dieser Spintexturen lassen sich durch eine endliche, ganzzahlige topologische Ladung charakterisieren, welche zum Auftreten eines topologischen Hall-Effekts von Elektronen führt und zusätzlich eine transversale Ablenkung der Spintexturen selbst bewirkt. Unter Verwendung von Monte-Carlo-Simulationen und mikromagnetischen Spin-Dynamik-Simulationen wird in dieser Arbeit die Existenz einzelner magnetischer Biskyrmionen (zwei sich überlappende Skyrmionen), sowie periodischer Gitter von Bimeronen (Skyrmionen in Materialien, die in der Ebene magnetisiert sind) und antiferromagnetischer Skyrmionen vorhergesagt. Weiterhin erlauben es die Berry-Theorie und der Landauer-Büttiker-Ansatz, den topologischen Hall-Effekt und den magnetoelektrischen Effekt in nicht-kollinearen Spintexturen zu quantifizieren. Hierdurch werden ein rein topologischer Hall-Effekt für Bimeronen und das topologisch induzierte Äquivalent zum Spin-Hall-Effekt in antiferromagnetischen Skyrmion-Kristallen vorhergesagt und ein topologischer Hall-Effekt eines Skyrmioniums erklärt, der auftritt, obwohl eine solche Spintextur keine topologische Ladung besitzt. Der vielversprechendste Beitrag für eine technologische Anwendung von nicht-kollinearen Spintexturen ist die Simulation und Erklärung einer Methode zur Unterdrückung der transversalen Ablenkung von Skyrmionen, die von elektrischen Strömen bewegt werden. Dadurch könnte das Geschwindigkeitslimit für eine stabile Bewegung von Skyrmionen um eine Größenordnung erhöht werden.



# Contents

<b>1</b>	<b>Introduction</b>	<b>1</b>
<b>2</b>	<b>Magnetic skyrmions</b>	<b>5</b>
2.1	History and theoretical prediction . . . . .	5
2.2	Classification . . . . .	6
2.3	Stabilizing interactions . . . . .	8
2.4	Experimental discovery and steps towards applications . . . . .	16
<b>3</b>	<b>Simulation of magnetic textures</b>	<b>23</b>
3.1	Monte Carlo simulations . . . . .	23
3.2	Spin dynamics simulations . . . . .	26
3.3	Thiele equation . . . . .	30
3.4	Example: Current-driven motion of a magnetic skyrmion . . . . .	33
<b>4</b>	<b>Electronic properties</b>	<b>37</b>
4.1	Berry theory . . . . .	37
4.2	Reciprocal-space Berry curvature and Hall conductivity . . . . .	39
4.3	Spin Hall conductivity, orbital magnetization, and magnetoelectric effect	43
4.4	Tight-binding model . . . . .	47
4.5	Example: Quantum Hall effect . . . . .	49
<b>5</b>	<b>Publications: Magnetic skyrmions</b>	<b>57</b>
5.1	Suppression of the skyrmion Hall effect . . . . .	58
5.2	Topological Hall effect . . . . .	65
5.3	Magnetoelectric effect and orbital magnetization . . . . .	74
<b>6</b>	<b>Publications: Beyond skyrmions</b>	<b>83</b>
6.1	Magnetic biskyrmions in centrosymmetric nanodisks . . . . .	84
6.2	Magnetic bimerons as in-plane analogues of skyrmions . . . . .	95
6.3	Magnetic skyrmioniums in racetrack applications . . . . .	103
6.4	Antiferromagnetic skyrmion crystals and topological spin Hall effect . . .	114
<b>7</b>	<b>Conclusion and perspectives</b>	<b>121</b>
	<b>List of publications</b>	<b>124</b>
	<b>Appendix</b>	<b>126</b>
	<b>References</b>	<b>131</b>





---

## 1 Introduction

**Skyrmion-based racetrack storage devices.** The ever-growing demand of data-storage space and energy-efficient data manipulation has put such an enormous challenge onto the corresponding industry, that Moore's law [1] (the exponential increase of disk space and operation speed) has not been fulfilled over the last years [2]. One idea to drastically increase the storage space is to utilize a magnetic shift device or racetrack storage device [3,4]. Here, the spin degree of freedom of the sample's electrons is used to constitute the carriers of information: The walls between ferromagnetic domains have sizes on the micrometer length scale and can be written, deleted, moved and detected electromagnetically. The racetracks are quasi one-dimensional and the device does not consist of mechanically movable parts allowing to stack individual racetracks to create an innately three-dimensional device with a strongly increased storage density compared to traditional two-dimensional hard disk drives.

Furthermore, one desires to decrease the size of the carriers of information without forfeiting the reliability of the storage devices. For this reason, the idea arose to replace the domain walls in a racetrack device by magnetic skyrmions [5] (Fig. 1). These whirl-like particles are enormously stable at sizes down to a few nanometers [6] and can be driven by currents which are orders of magnitude smaller compared to the driving currents for domain walls [7], therefore constituting an extremely efficient data storage.

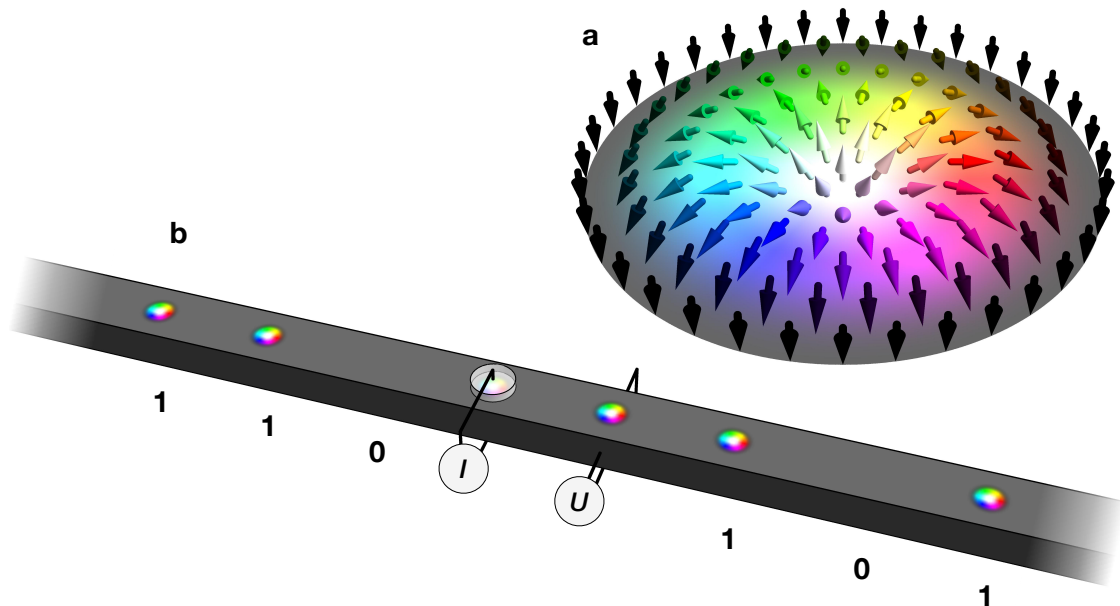


Figure 1: **Skyrmion-based racetrack storage device.** **a** Magnetic skyrmions are non-collinear spin textures constituted by magnetic moments (arrows whose color represents their orientation). **b** They can be written, deleted, moved and read in a narrow ferromagnetic stripe. The information is encoded via bits: the existence of a magnetic skyrmion corresponds to a '1' bit, while a missing skyrmion is interpreted as a '0' bit.

**Magnetic skyrmions.** The field of skyrmionics gained enormous interest in 2009 when magnetic skyrmions were first detected in the non-centrosymmetric material MnSi in the form of a periodic lattice of skyrmion tubes [8]. In the following years, skyrmion crystals and also individual skyrmions [9] have been observed in thin films and at interfaces [10]. The broken space-inversion symmetry in these materials gives rise to the so-called Dzyaloshinskii-Moriya interaction [11,12], which occurs due to spin-orbit coupling, and is the stabilizing mechanism in the vast majority of observed skyrmions and skyrmion lattices. Several examples exist for which the potential carriers of information have been written and deleted in a controlled manner [13] and are detected by their magnetization profile or their characteristic Hall signal [14]. Furthermore, the energy-efficient current-driven motion of skyrmions has been realized [15,16], however with the drawback that they do not move along the applied current direction, i. e., along the racetrack, but also partially towards the edge (Fig. 2). Today, this so called ‘skyrmion Hall effect’ is one of the severest limitations for utilizing skyrmions in racetrack devices: The transverse propulsion of a skyrmion towards the edge of the sample leads to its pinning or even its annihilation. As will be shown in this thesis, the origin for this effect is the non-triviality of the real-space topology of the respective magnetic texture.

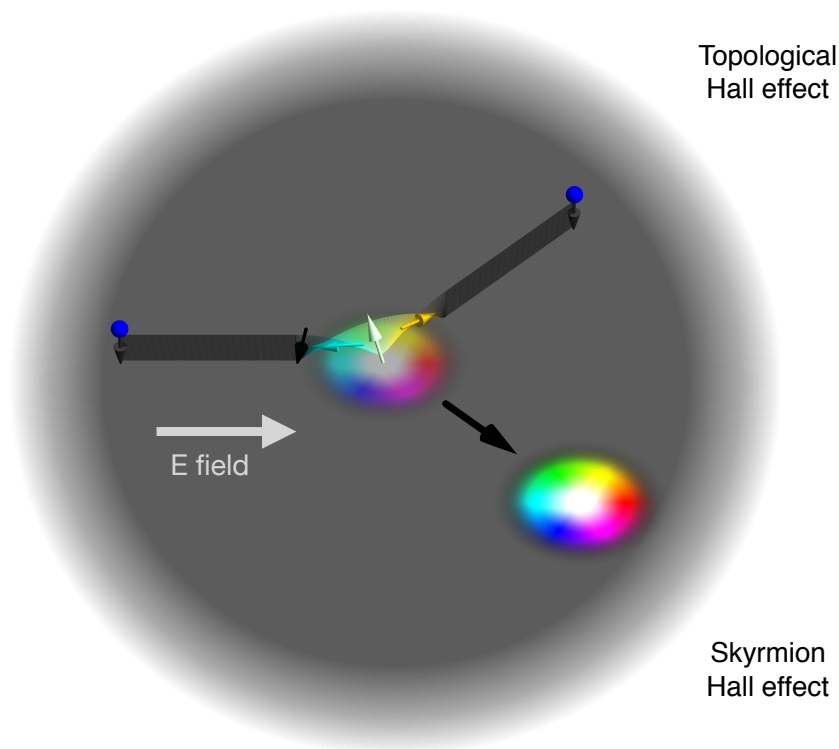


Figure 2: **Emergent electrodynamic effects in skyrmion hosts.** When an electric field is applied in-plane, a current arises, which has a transverse component (topological Hall effect). At the same time, the skyrmion itself is propelled as a consequence of spin torques due to the partial alignment of the current electrons’ spins with the skyrmion texture. This motion occurs at an angle with respect to the current (skyrmion Hall effect). The fundamental origin of both effects lies in the non-trivial real-space topology of the skyrmion.

---

Skyrmions have originally been proposed by Tony Skyrme in 1961 [17, 18] as excitations in a field theory describing interacting pions. Mathematically speaking, skyrmions can be characterized by a topological invariant distinguishing them from the trivial state (e. g. a collinear ferromagnet). This *topological charge* has the integer value of  $+1$  or  $-1$  for skyrmions. Considering a continuous magnetization profile instead of discrete magnetic moments, a skyrmion state can by no means be transformed into a ferromagnetic state. This fingerprint of the non-trivial real-space topology expresses itself in a high stability: While one can speak of a topological protection of skyrmions in a continuous model, magnetic skyrmions in nature (formed by discrete magnetic moments) are not protected strictly speaking but the state can possess such a high energy barrier towards the ferromagnetic groundstate, so that metastable skyrmions can survive at room temperatures for a literal eternity [19].

Furthermore, the topological charge plays a fundamental role in the electrodynamics of electrons interacting with skyrmions (Fig. 2). When an electric field is applied along a film hosting skyrmions, a current emerges which is not parallel to the field: a topological Hall effect is measurable, which is considered the hallmark of non-trivial real-space topology. In a similar way, the skyrmions themselves do also not move along the field direction but are deflected transversally; this is the effect discussed above as skyrmion Hall effect. Several approaches to suppress this effect have been considered, for example replacing the magnetic skyrmion by alternative non-collinear spin textures which have a comparable stability but a vanishing topological charge.

**Goals of this thesis.** Based on this motivation the main goals for this thesis are:

1. Finding ways to suppress the skyrmion Hall effect and to accelerate the current-driven motion of skyrmions in racetrack devices.
2. Gaining a profound understanding of the topological Hall effect that goes beyond relating the measured signal with the skyrmion density.
3. Establishing new hallmarks of topologically non-trivial spin textures for experiments.
4. Predicting and stabilizing alternative non-collinear spin textures, as well as comparing their emergent electrodynamic effects to those of skyrmions.

**Outline of this thesis.** In the following three chapters the foundation is laid for the presented results in the cumulative part of this thesis. First, in Sec. 2 magnetic skyrmions are introduced more thoroughly, including the definition of quantities that allow to characterize different types of skyrmions and related magnetic objects. Different stabilizing mechanisms are presented and relevant experimental findings are reviewed. In Sec. 3. three different methods to describe the real-space properties of non-collinear spin textures are introduced: the Monte Carlo formalism, spin dynamics simulations and an effective description of magnetic quasiparticles by algebraic means called ‘Thiele equation’. The latter two methods are exemplarily demonstrated for the current-driven motion of a skyrmion in a racetrack geometry verifying well established results from the initial proposal of the skyrmion racetrack storage devices in Ref. [5]. Sec. 4 is preparing the results concerning the electronic properties of non-collinear spin textures. The

---

main focus is set on the Berry theory approach which allows to quantify the topological Hall effect in a tight-binding model. Its elegance is demonstrated at the example of the quantum Hall effect, which occurs when a strong magnetic field is applied to a metal. Furthermore, the calculation of related quantities, namely the spin Hall conductivity, orbital magnetization and magnetoelectric polarizability, is explained.

Sec. 5 is the first cumulative part of this thesis. It contains three publications considering magnetic skyrmions. The findings address goals 1, 2 and 3. In publication [BG1] a method to suppress the skyrmion Hall effect is presented, in publication [BG2] unconventional quantization effects and a strong energy dependence of the topological Hall effect of electrons in skyrmion crystals are predicted, and in publication [BG3] a geometrically induced magnetoelectric effect is predicted and established as a new hallmark of skyrmionic phases.

In the second cumulative part (Sec. 6) four publications are presented corresponding to goal 4: the prediction and analysis of alternative magnetic quasiparticles (the four considered textures are depicted in Fig. 3). In publication [BG4] the existence of individual magnetic biskyrmions is predicted in centrosymmetric materials. These objects are the combination of two skyrmions with the same topological charge. In publication [BG5] the magnetic bimeron (a skyrmion in in-plane magnetized samples) is predicted to stabilize under a new type of Dzyaloshinskii-Moriya interaction. In publication [BG6] all constituents of a fully operating racetrack device are simulated, using skyrmioniums (the combination of two skyrmions with a vanishing topological charge in total) as carriers of information. Finally, in publication [BG7] the existence of a periodic lattice of antiferromagnetic skyrmions is predicted. Particularly noteworthy are also the newly established electrodynamic effects: a purely topological Hall effect for bimeron textures, a unique signature in the topological Hall effect for skyrmioniums even though it has a vanishing topological charge, and the prediction of a topologically induced spin Hall effect for antiferromagnetic skyrmions.

The concluding section 7 of this thesis is a summary of the established results and provides an outlook on promising future research projects related to the here presented findings.

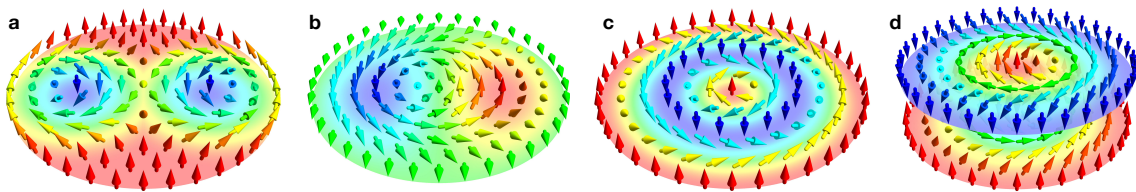


Figure 3: **Considered skyrmion-related quasiparticles in this thesis.** **a** The biskyrmion, **b** the bimeron, **c** the skyrmionium and **d** the antiferromagnetic skyrmion.

---

## 2 Magnetic skyrmions

In this section the magnetic skyrmion is introduced. After a short historic treatise on its theoretical prediction, quantities for the classification of different types of magnetic skyrmions as well as possible stabilizing mechanisms are presented. The quantities become essential later in this thesis for explaining the emergent electrodynamic effects of skyrmions (Sec. 5) and also allow to understand the behavior of more ‘exotic’ spin textures (Sec. 6). The present section closes with a review of the first experimental discoveries of skyrmions, essential advances concerning their racetrack applicability, and the initial observations of the topological Hall effect of electrons in skyrmion crystals.

### 2.1 History and theoretical prediction

The predecessors of magnetic skyrmions are the so called ‘magnetic bubbles’ [20,21]. These objects have been observed already in the 1960’s and have even been commercially used in data storage devices in the 1970’s [22,23]. However, they commonly have sizes on the  $\mu\text{m}$  scale and do not have a strictly enforced topological charge; even topologically trivial bubbles can occur. In order to shrink the inter-bit distance to a few nm and to utilize a topological protection of the bits, magnetic skyrmions are promising candidates to supersede the bubbles and to entirely establish non-volatile magnetic storage devices without mechanically moving parts in our everyday lives [5,24].

Historically, the prediction of skyrmions dates back to the British nuclear physicist Tony Skyrme. In the 1960’s he proposed a theoretical treatment of fundamental particles, such as interacting pions [17,18]. The later called ‘skyrmions’ are the quasiparticle-like topological excitations in the corresponding field theory. Remarkably, these three-dimensional skyrmions are fermions while the pions themselves are bosons. It took until 1989 when a *magnetic* skyrmion was predicted for the first time [25], in the sense that it is formed by magnetic moments [Fig. 4(b)], similar to the case of magnetic bubbles. Here, the skyrmion is treated as a two-dimensional object which may be extended trivially into the third dimension as a skyrmion tube [Fig. 4(c)].

In the initial publication, the existence of periodic arrays of skyrmions was analyzed by means of symmetry predicting several crystallographic classes, which allow for the stabilization of these so called skyrmion crystals [25]. As will be presented in Sec. 2.3 this symmetry consideration traces back to the Dzyaloshinskii-Moriya interaction [11,12] (DMI), a chiral interaction of spins that arises due to spin-orbit coupling and a broken inversion symmetry. A few years later, also the existence of isolated skyrmions was predicted [26]. As an alternative ingredient for the stabilization of such skyrmions, Bogdanov and Rößler considered interfaces, at which the inversion symmetry is broken explicitly. This leads to the emergence of a different type of DMI [27] and the stabilization of a different type of skyrmion crystal, as will be explained in Sec. 2.3.

Experimentally, skyrmion lattices and isolated skyrmions were found roughly 20 years later for the first time [8] confirming the theoretical predictions. In Sec. 2.4 a review of the experimental discovery is presented. Today, skyrmionic objects have been found or predicted in several fields of physics. Besides skyrmions which are formed by magnetic moments, examples comprise skyrmions in quantum Hall systems [28], in Bose-Einstein condensates [29], in liquid crystals [30] or in particle physics [31].

## 2.2 Classification

In this section the geometric quantities ‘polarity’, ‘vorticity’ and ‘helicity’ are introduced, which allow for a characterization of magnetic skyrmions. They dictate the topological charge and the toroidal moment of a skyrmion; both are geometrical quantities that manifest in experimentally accessible observables.

A magnetic skyrmion can be constructed mathematically by a stereographic projection. As shown in Fig. 4, a sphere with a radial magnetic texture is ‘unwrapped’ to a two-dimensional disk. The magnetic texture becomes a whirl-like pattern that is oriented along the  $-z$  direction in the center (originating from the bottom of the sphere) and along the  $+z$  direction at the edge (originating from the top of the sphere) in this case. The reduction of dimension induces a topological charge

$$N_{\text{sk}} = \frac{1}{4\pi} \int \mathbf{m}(\mathbf{r}) \cdot \left( \frac{\partial \mathbf{m}(\mathbf{r})}{\partial x} \times \frac{\partial \mathbf{m}(\mathbf{r})}{\partial y} \right) d^2r. \quad (2.1)$$

Here,  $\mathbf{m}$  is the normalized magnetization density. The topological charge can only have integer values for magnetic excitations in a ferromagnet. It is  $\pm 1$  for magnetic skyrmions, depending on the orientation of the ferromagnetic surrounding.

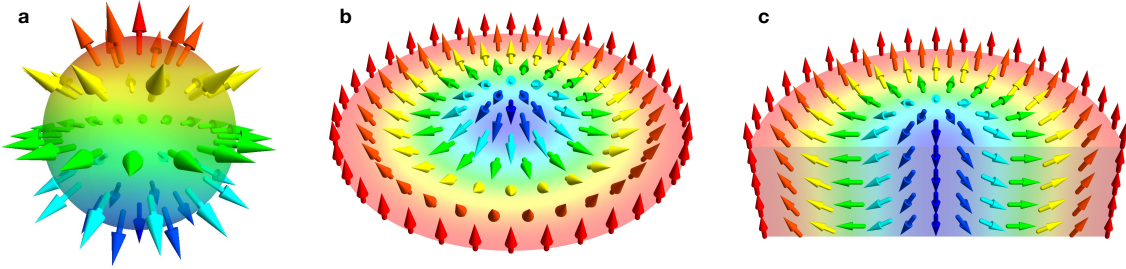


Figure 4: **Stereographic projection.** **a** A three-dimensional sphere with a radial spin texture can be unfolded to construct **b** a magnetic skyrmion with topological charge  $N_{\text{sk}} = -1$  in two dimensions. **c** In real materials this skyrmion is commonly continued trivially along the third dimension as a skyrmion tube.

In a continuous magnetization-density model the topological charge of a magnetic texture cannot change under any continuous transformation. This means in particular that a single skyrmion in a ferromagnetic background cannot be destroyed, since  $N_{\text{sk}}$  would not be conserved in this case. This *topological protection* is less strict in a realistic description of skyrmions as a collective of non-collinear magnetic moments. In this case the skyrmion can be destroyed but it is separated from the ferromagnetic ground state by an energy barrier, which can lead to metastability for more than billions of years [19] under favorable conditions. For this reason, the non-trivial real-space topology is a key element for the utility of skyrmions in spintronics applications of the future.

The integer nature of the topological charge can be understood by expressing the magnetization in spherical coordinates

$$\mathbf{m}(\mathbf{r}) = (\cos \Phi \sin \theta, \sin \Phi \sin \theta, \cos \theta)^T. \quad (2.2)$$

For a skyrmion, the azimuthal angle  $\theta(r)$  of the magnetization only depends on the

length  $r$  of the position vector  $\mathbf{r}$  with respect to the skyrmion's center. The polar angle of the magnetization  $\Phi(\phi)$  only depends on the polar angle  $\phi$  of  $\mathbf{r}$ . The rotational symmetry can be used to transform the expression for the topological charge to [6]

$$N_{\text{Sk}} = \frac{1}{4\pi} \int_0^\infty dr \int_0^{2\pi} d\phi \frac{\partial\Phi(\phi)}{\partial\phi} \frac{\partial\theta(r)}{\partial r} \sin\theta(r) = -\frac{1}{2} \cos\theta(r) \Big|_{r=0}^\infty \cdot \frac{1}{2\pi} \Phi(\phi) \Big|_{\phi=0}^{2\pi}. \quad (2.3)$$

The topological charge can therefore be expressed as a product of polarity  $p$  (first term) and vorticity  $m$  (second term)

$$N_{\text{Sk}} = p \cdot m, \quad p = \pm 1, \quad m = 0, \pm 1, \pm 2, \dots \quad (2.4)$$

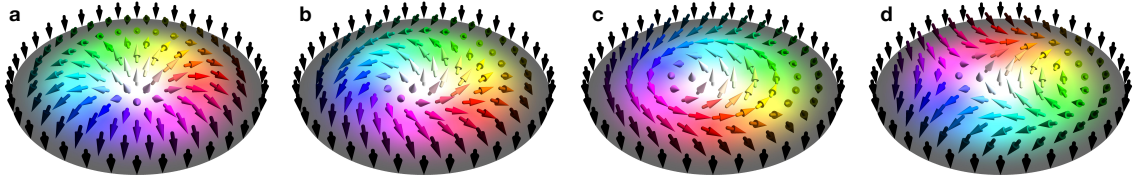


Figure 5: **Different types of skyrmions.** **a** Néel skyrmion with topological charge  $N_{\text{Sk}} = +1$ , polarity  $p = +1$ , vorticity  $m = +1$  and helicity  $\gamma = 0$ . **b** Unspecified skyrmion with  $\gamma = \pi/4$ . **c** Bloch skyrmion with  $\gamma = \pi/2$ . **d** Antiskyrmion with  $N_{\text{Sk}} = -1$ ,  $p = +1$ ,  $m = -1$  and  $\gamma = \pi/2$ . The color encodes the orientation of the magnetic moments.

The polarity indicates whether the central spin of the skyrmion points into positive ( $p = +1$ ) or negative  $z$  direction ( $p = -1$ ). The vorticity quantifies the sense of rotation of the in-plane orientation of the magnetic texture when considering magnetic moments on a circle around the skyrmion's center. The polar angles of magnetization  $\Phi$  and position vector  $\phi$ , as introduced above, are related by

$$\Phi = m\phi + \gamma. \quad (2.5)$$

For a skyrmion the vorticity is  $m = +1$  [Fig. 5(a)], while a vorticity of  $m = -1$  characterizes an antiskyrmion [Fig. 5(d)]. Theoretically, also higher-order (anti-)skyrmions have been predicted [32]. In this case the in-plane magnetization rotates more than once when considering magnetic moments on the aforementioned circle; the vorticity is then  $|m| > 1$ .

Besides the polarity  $p$  and the vorticity  $m$ , the helicity  $\gamma$  is the third geometrical quantity that characterizes a magnetic skyrmion. For  $m = 1$  skyrmions, it can be understood as the offset of the polar angles of the magnetization orientation and the position vector [Eq. (2.5)]. A variation of the helicity is identified with a global rotation of each individual magnetic moment in magnetization space around the net magnetization direction  $z$ . While for an antiskyrmion this is merely equivalent to a rotation in real space around its center, for skyrmions it changes also a physically relevant property: the classical toroidal moment

$$\mathbf{t} = \frac{g\mu_B}{2} \int \mathbf{r} \times \mathbf{m}(\mathbf{r}) d^2r. \quad (2.6)$$

For all antiskyrmions this quantity vanishes regardless of the helicity, due to the broken rotational symmetry. Instead, for skyrmions it is strictly determined by the helicity,

$$\mathbf{t} \propto \sin(\gamma) \mathbf{e}_z. \quad (2.7)$$

This consideration inspired to investigate a skyrmion crystal's magnetoelectric behavior, which is determined by the toroidal moment [33] and leads to the establishment of a new hallmark of skyrmionic phases (presented and explained in publication [BG3] and the corresponding section).

Experimentally, only the cases  $\gamma = 0, \pi$  [a Néel skyrmion in Fig. 5(a)] and  $\gamma = \pi/2, -\pi/2$  [a Bloch skyrmion in Fig. 5(c)] have been observed so far, while intermediate skyrmions are theoretically predicted [Fig. 5(b)]. The type of resulting skyrmion is commonly determined by the type of stabilizing interaction – a relation that is discussed in the following section.

## 2.3 Stabilizing interactions

In the previous section, the topological protection of magnetic skyrmions, formed by a continuous magnetization density, was presented. These objects are stable as long as continuity of the magnetization density is assumed. In nature, magnetic skyrmions are constituted by localized magnetic moments  $\mathbf{s}_i$ , as was implicated by the arrows in all previously shown figures. In that case the local magnetization is discontinuous *per se*, so topological protection is not given. Still, in experiments one observes great stability of magnetic skyrmions even though they are only metastable excitations in the collinear ferromagnetic phase.

In order to understand this stability the different stabilizing interactions of magnetic skyrmions are addressed now. Besides the Heisenberg exchange interaction, which favors a collinear alignment of magnetic moments, there are other interactions that energetically favor spin canting. In nature this non-collinearity is often enforced by the Dzyaloshinskii-Moriya interaction (DMI) [11, 12]. It is the stabilizing mechanism in the vast majority of currently identified skyrmion hosts. Still, there exist other stabilizing mechanisms [6], namely frustrated exchange interactions and the dipole-dipole interaction, which will also be presented in the following.

### Heisenberg interaction, Zeeman interaction and anisotropies

Phenomenologically, the existence of a comparably strong interaction, which favors a parallel alignment of neighbored magnetic moments, is necessary to explain the existence of ferromagnetism. This fundamental interaction is called 'Heisenberg interaction' or 'exchange interaction' and has the representation

$$H = -J \mathbf{s}_1 \cdot \mathbf{s}_2, \quad J > 0 \quad (2.8)$$



in spin space. This phenomenological term can be straightforwardly derived from symmetry considerations of the wave functions of two interacting electrons, as will be presented in the following, similar to Refs. [34,35].

The starting point is the quantum mechanical Hamiltonian

$$H = \frac{p_1^2}{2m} + \frac{p_2^2}{2m} + V(\mathbf{r}_1, \mathbf{r}_2). \quad (2.9)$$

Here,  $m$  is the electron mass,  $p_i$  the momentum operator and  $V$  the interaction potential depending on the electrons' positions  $\mathbf{r}_i$ . Since this Hamiltonian is independent of the spin, the antisymmetric wavefunction can be separated into a spatial wavefunction  $|r\rangle^\pm$  and a spin-dependent wavefunction  $|s\rangle^\pm$ ,

$$|\psi\rangle = |r\rangle^\mp |s\rangle^\pm. \quad (2.10)$$

One of the two wavefunctions needs to be symmetric (+), while the other one has to be antisymmetric (-). This means, that for the total spin of the two electrons  $S = 1$  (symmetric triplet state  $|1\rangle \equiv |s\rangle^+$ ) the spatial wavefunction has to be antisymmetric, and for  $S = 0$  (antisymmetric singlet state  $|0\rangle \equiv |s\rangle^-$ ) the spatial wavefunction is symmetric. The corresponding eigenenergies  $E^\pm$  differ in general and can effectively be related with the total spin expectation value due to the above symmetry argumentation. Therefore, an effective Hamiltonian  $\tilde{H}$  has to exist which returns the same eigenenergies  $E^\pm$  but is spin and not space dependent:

$$\tilde{H} |0\rangle = E^+ |0\rangle, \quad (2.11)$$

$$\tilde{H} |1\rangle = E^- |1\rangle. \quad (2.12)$$

The aim is now to find an expression for the effective spin-dependent Hamiltonian  $\tilde{H}$ . For this reason, a spin-dependent term is needed that returns different results for  $S = 0$  and  $S = 1$ . One uses  $S = s_1 + s_2$  to arrive at two expressions for  $S^2$

$$\hbar^2 S(S+1) \quad \text{and} \quad \frac{3}{2}\hbar^2 + 2\mathbf{s}_1 \cdot \mathbf{s}_2. \quad (2.13)$$

Due to their equivalence one finds

$$\mathbf{s}_1 \cdot \mathbf{s}_2 = \begin{cases} -\frac{3}{4}\hbar^2 & \text{if } S = 0 \\ \frac{1}{4}\hbar^2 & \text{if } S = 1 \end{cases} \quad (2.14)$$

to return different results for the two values of  $S$ , allowing to explicitly construct the effective spin-dependent Hamiltonian

$$\tilde{H} = H_0 - \frac{1}{\hbar^2} (E^+ - E^-) \mathbf{s}_1 \cdot \mathbf{s}_2. \quad (2.15)$$

Here  $H_0 = (E^+ + 3E^-)/4$  is a constant that can be dropped.

This Hamiltonian can be generalized allowing to describe more than two spins and is also applicable in the classical limit. The exchange interaction in the Heisenberg model reads

$$H_{\text{exchange}} = -\frac{1}{2} \sum_{i,j} J_{ij} \mathbf{s}_i \cdot \mathbf{s}_j. \quad (2.16)$$

Here, the sum runs over all magnetic moments and  $J_{ij}$  is the exchange constant that is determined experimentally or can in principle be calculated from  $J_{ij} = (E_{ij}^+ - E_{ij}^-)/\hbar$ . The factor 1/2 accounts for double counting each interaction.

Often, for simplicity, only nearest-neighbor exchange is considered with a uniform exchange constant  $J$ . In this case, the exchange interaction can be generalized for a continuous magnetization density [ $\mathbf{m}(\mathbf{r})$  is the normalized unitless density] as

$$H_{\text{exchange}} = \int \sum_{ij} \tilde{J} \left( \frac{\partial m_i}{\partial x_j} \right)^2 d^3r. \quad (2.17)$$

In this expression  $\tilde{J}$  is the exchange stiffness in units of energy per meter. This expression becomes useful when large, continuous magnetic textures are considered like in micromagnetic simulations.

Coming back to the consideration from the beginning of this section, a uniformly positive exchange constant will lead to a parallel alignment of all moments, explaining the existence of ferromagnets. For a uniformly negative exchange constant the ground state of magnetic moments on a square lattice is a collinear antiferromagnet. Each spin is oriented anti-parallel with respect to its four neighbors giving a checkerboard-type magnetic order. However, on a hexagonal lattice each atom has six nearest neighbors. They would all be anti-parallel to the reference moment but pairs of these neighbors are nearest neighbors themselves, so they should also align antiferromagnetically. The resulting texture is a compromise of these interactions. It is a non-collinear state that originates purely from geometrical frustration.

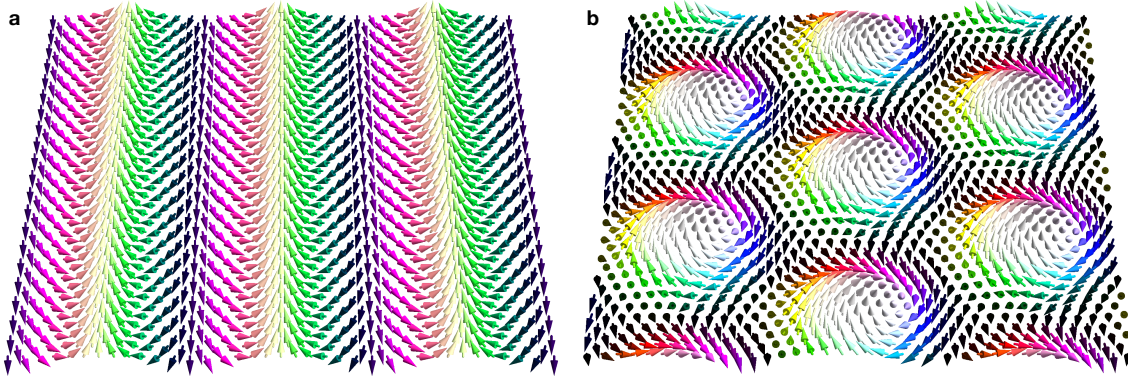


Figure 6: **Spin spiral and skyrmion crystal.** **a** Spin spiral with order vector  $\mathbf{q}$  along  $e_x$ . **b** Skyrmion crystal generated as the superposition of the spin spiral from panel a with 2 other spin spirals rotated by  $\pm 120^\circ$ , respectively.

If one introduces additional frustration by a ferromagnetic interaction between nearest neighbors  $J_1 > 0$  and an antiferromagnetic interaction between second-nearest neighbors  $J_2 < 0$ , this non-collinearity becomes even more preferable. The ground state is a helical phase; a spin spiral without net magnetization [Fig. 6(a)]. Considering a finite

temperature, the stable orientation can even be a skyrmion lattice [Fig. 6(b)], as has been shown in Ref. [36]. A necessary ingredient is the application of an external magnetic field  $\mathbf{B}$  along the direction of the net magnetization of skyrmions, which is out-of-plane. This field makes the skyrmion energetically favorable over the helical phase, which has no net magnetization. The magnetic field is introduced in the Hamiltonian via a Zeeman interaction which has the same type of mathematical expression as the exchange (here  $\mu$  is the magnitude of the magnetic moment),

$$H_{\text{Zeeman}} = - \sum_i \mu \mathbf{s}_i \cdot \mathbf{B}. \quad (2.18)$$

Including also an easy-axis anisotropy along the direction  $\mathbf{n} = \mathbf{e}_z$ ,

$$H_{\text{anisotropy}} = - \frac{K}{2} \sum_i (\mathbf{s}_i \cdot \mathbf{n})^2, \quad (2.19)$$

favors moments pointing out-of-plane, as is typically the case in thin films. This leads to a further stabilization of magnetic skyrmions. As was shown in Ref. [37] skyrmions can be stabilized even at zero temperature when an easy-axis anisotropy is present.

As a closing comment, it is worth mentioning that skyrmions, which are stabilized by frustrated exchange interactions have a non-fixed helicity. A common rotation of all magnetic moments around any axis in magnetization space leaves the system's energy invariant. This is why the experimentally unobserved skyrmion type with a helicity between that of Bloch and Néel skyrmions [Fig. 5(b)] has been predicted theoretically in frustrated magnets. Due to the strong spin canting, skyrmions, which are stabilized by frustrated exchange, have diameters of only a few nanometers which may be a reason why they remain unobserved in experiments up to now.

The aforementioned invariance of the Heisenberg exchange interaction with respect to collective rotations of the magnetic moments in magnetization space was an inspiration to consider also rotations around an in-plane axis. This led to the prediction of individual bimerons (in-plane skyrmions as introduced in Sec. 6) and bimeron crystals (presented in publication [BG5] and the corresponding section).

### Dzyaloshinskii-Moriya interaction

Even though the possibility of observing a non-collinear spin texture is already given by frustrated exchange interactions, most of the observed magnetic skyrmions exist at sizes of several tens or even hundreds of nanometers, suggesting the existence of another interaction. Furthermore, the observed skyrmions have a fixed helicity. This brings about the necessity of a chiral character of this interaction. The responsible interaction is the antisymmetric exchange, also called Dzyaloshinskii-Moriya interaction [11, 12] (DMI)

$$H_{\text{DMI}} = \frac{1}{2} \sum_{ij} \mathbf{D}_{ij} \cdot (\mathbf{s}_i \times \mathbf{s}_j), \quad (2.20)$$

which occurs due to spin-orbit coupling and a broken inversion symmetry. It can be derived as a correction to the exchange interaction in second order perturbation theory [38]. The type of broken inversion symmetry determines the orientation of the Dzyaloshinskii-Moriya vectors  $D_{ji} = -D_{ij}$ . As the name tells, the antisymmetric exchange allows for a generalization of the exchange in the sense that the exchange constant is actually a  $3 \times 3$  matrix. The antisymmetric part is then the DMI while the conventional exchange constant enters the diagonal.

For a single pair of magnetic moments the DMI energetically favors the configuration, for which the moments and the DMI vector are pairwise perpendicular to each other. However, since the conventional exchange interaction (favoring a parallel alignment for  $J > 0$ ) is also present, the magnetic moments will orient at an angle  $< 90^\circ$  which is determined by the ratio  $D/J$  for a system with uniform DMI strength and exchange interactions. Since the DMI is a correction to the exchange, this ratio is commonly small, resulting in a spiral configuration of magnetic moments in the ground state. The period of this magnetic texture ranges from a few to a hundred nanometers.

A prominent example of a material with DMI is MnSi, a non-centrosymmetric B20 compound with broken inversion symmetry. The ground state is a helical phase with a period of  $19 \text{ nm} = 41.66 a$  (lattice constant  $a$ ) [8]. In this material, skyrmions have been detected for the first time at a finite temperature and under the presence of an applied magnetic field.

At the present state of research, almost all skyrmions that have been detected in experiments are indeed stabilized by the DMI. The specific type of helical phase or magnetic skyrmion depends on the type of inversion symmetry breaking and the orientation of the DMI vectors, which are determined by the Moriya rules [12].

### Moriya rules

The symmetry rules of Moriya allow to deduce the orientation of the Dzyaloshinskii-Moriya vectors from symmetry arguments. The midpoint of a bond  $r$  between two magnetic atoms is analyzed with respect to inversion symmetry, mirror symmetry (mirror planes with normal  $n$ ) and rotational symmetry (at least two-fold rotational symmetry with axis along  $a$ ). The rules read [12]:

1. If the midpoint is a center of inversion, then  $D = 0$ .
2. If the midpoint is on a mirror plane with  $n \parallel r$ , then  $D \perp r, n$ .
3. If the midpoint is on a mirror plane with  $n \perp r$ , then  $D \parallel n$ .
4. If a two-fold rotation axis with  $a \perp r$  exists, then  $D \perp a$ .
5. If a two or more-fold rotation axis with  $a \parallel r$  exists, then  $D \parallel r$ .

### Consequences for magnetic skyrmions

In this section the three types of DMI which stabilize experimentally observed skyrmion hosts are presented: interfacial DMI, bulk DMI, and anisotropic DMI.

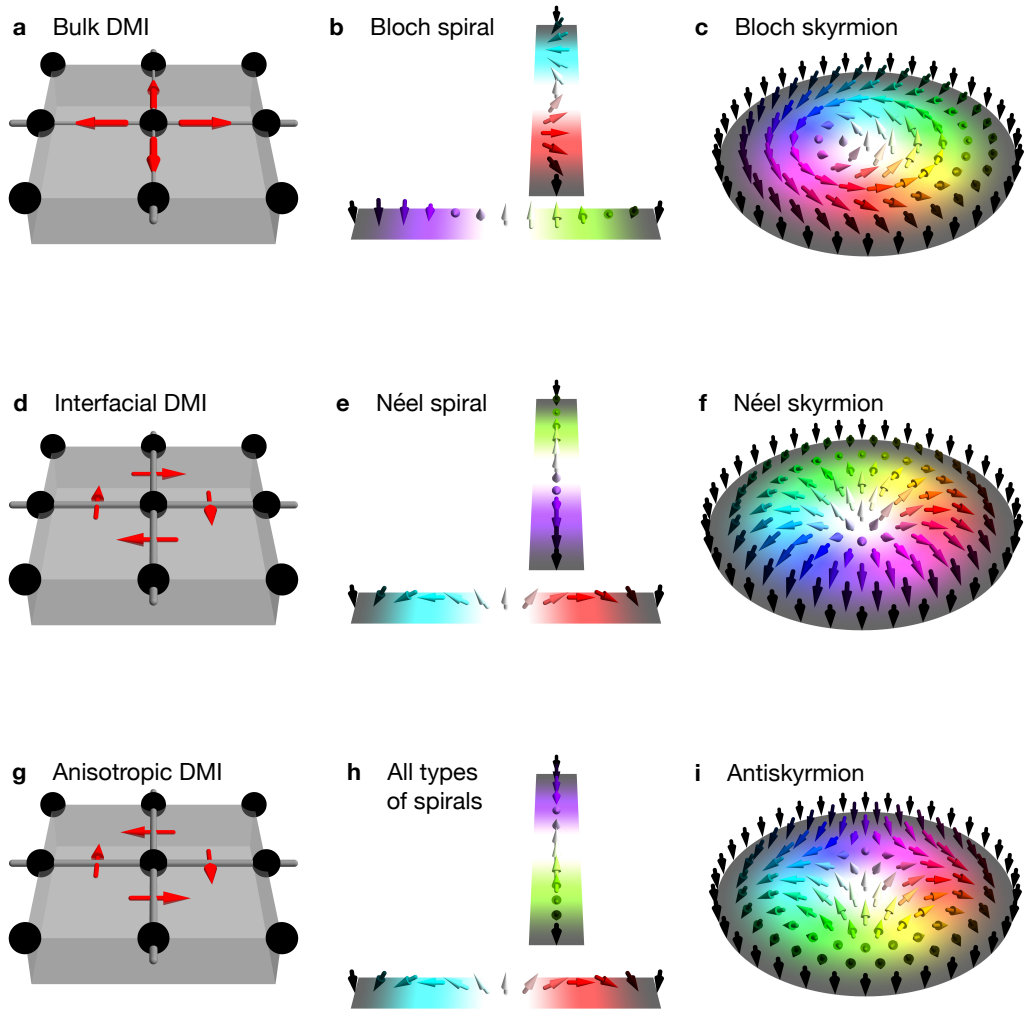


Figure 7: **Typical Dzyaloshinskii-Moriya interactions and resulting spin textures.** The top row represents a non-centrosymmetric B20 material like MnSi with a bulk DMI. **b** A Bloch spiral along different directions and **c** Bloch skyrmions can be stabilized. The middle row corresponds to an interface like Co/Pt with **d** interfacial DMI. In these systems **e** Néel spirals and **f** Néel skyrmions are (meta)stable states. The bottom row corresponds to layered systems like the Heusler material  $\text{Mn}_{1.4}\text{Pt}_{0.9}\text{Pd}_{0.1}\text{Sn}$  resulting in **g** an anisotropic interfacial DMI. In this system, **h** all different types of spirals are stabilized along different directions. The skyrmionic solution is **i** the antiskyrmion. In panels a, d, and g the black spheres are magnetic atoms and the red arrows represent the DMI vectors along the corresponding bonds. In all other panels the arrows represent magnetic moments where the color encodes their orientation.

**Interfacial DMI.** Most convenient to understand is the interfacial DMI. Here, the inversion symmetry is explicitly broken by an interface. Instead of a continued arrangement of magnetic atoms, different atoms appear at the different sides. The orientation of the DM vectors can be determined in the following way: Looking at a bond of two magnetic atoms (1,2) with a third atom (0) that has the same distance to atoms 1 and

2, i. e., it is located in the mirror plane with  $\mathbf{n} \parallel \mathbf{r}$  but also in the mirror plane with  $\mathbf{n} \propto (\mathbf{r}_1 - \mathbf{r}_0) \times (\mathbf{r}_2 - \mathbf{r}_0) \perp \mathbf{r}$ , there is no inversion or rotational symmetry, and Moriya rules number 2 and 3 tell

$$\mathbf{D} \propto (\mathbf{r}_1 - \mathbf{r}_0) \times (\mathbf{r}_2 - \mathbf{r}_0). \quad (2.21)$$

This expression is also known as ‘Levy-Fert rule’ [39]. The emerging DMI vector points perpendicular to the bond and lies in the interfacial plane. For a square lattice the  $C_4$  symmetry allows to deduce the other DM vectors from a symmetry analysis as seen in Fig. 7(d), i. e., the magnitude and sign of the DMI  $D$  is equal for all bonds.

In the continuous limit, this DMI reads [40]

$$H_{\text{interface}} = \int \tilde{D} \left( m_x \frac{\partial m_z}{\partial x} - m_z \frac{\partial m_x}{\partial x} + m_y \frac{\partial m_z}{\partial y} - m_z \frac{\partial m_y}{\partial y} \right) d^3r. \quad (2.22)$$

The DMI constant  $\tilde{D}$  has a dimension of energy/length<sup>2</sup>. This type of interaction stabilizes Néel spirals, for which the magnetic moments rotate so that they are oriented partially along the spiral direction [Fig. 7(e)]. As a metastable solution Néel skyrmions [Fig. 7(f)] are stabilized, as observed for example at Fe/Ir(111) interfaces [10].

This arising type of skyrmion can for example be comprehended by considering a magnetic moment that points out-of-plane along the  $+z$  direction (like in the center of the skyrmion) and by thinking about the orientation of a magnetic moment corresponding to a bond along the  $x$  direction. The arising DM vector  $\mathbf{D} = -D\mathbf{e}_y$  gives a bond energy of  $H_{\text{DMI}} = -Dm_1^z m_2^x$ . For this reason, the second spin is tilted in  $x$  direction since this reduces the energy. This leads to the stabilization of a Néel skyrmion: The spin next to the center spin of the skyrmion is tilted away from the center as in Fig. 7(f).

**Bulk DMI.** In non-centrosymmetric materials like the B20 phase of MnSi, in which skyrmion crystals have been observed first [8], the DMI is named ‘bulk DMI’. The rather complicated three-dimensional structure of this material breaks the inversion symmetry intrinsically. If the structure is projected onto a square lattice (as in micromagnetic simulations), the effective DMI vectors point along the bonds [Fig. 7a]. Considering a continuous magnetization density, the energy is expressed as

$$H_{\text{bulk}} = \int \tilde{D} \left( m_y \frac{\partial m_z}{\partial x} - m_z \frac{\partial m_y}{\partial x} + m_z \frac{\partial m_x}{\partial y} - m_x \frac{\partial m_z}{\partial y} + m_x \frac{\partial m_y}{\partial z} - m_y \frac{\partial m_x}{\partial z} \right) d^3r. \quad (2.23)$$

The first four terms correspond to the DMI vectors depicted in Fig. 7(a). The other terms correspond to the bonds along the out-of-plane direction. For this setup the arising spin spirals are of Bloch type [Fig. 7(b)], where the magnetic moments rotate so that they have a component perpendicular to the spiral direction. The Bloch skyrmion [Fig. 7(c)] is characterized by a helicity of  $+\pi/2$  or  $-\pi/2$ .

**Anisotropic DMI.** Recently, also antiskyrmions have been observed experimentally [41] in the Heusler material  $\text{Mn}_{1.4}\text{Pt}_{0.9}\text{Pd}_{0.1}\text{Sn}$ . There, the magnetic Mn atoms form layers with Pt layers in between. For bonds between the Mn atoms along the  $x$  direction the Pt atoms are located in the layer above and for bonds along the  $y$  direction the atoms are located below the bond, giving rise to the so called ‘anisotropic DMI’ [Fig. 7(g)].

In principle, this interaction is allowed when the  $C_{4v}$  or  $C_{3v}$  symmetries of square and hexagonal lattices are broken [42], e.g. by deformation. It reads in the continuous formulation

$$H_{\text{anisotropic}} = \int \tilde{D} \left( m_x \frac{\partial m_z}{\partial x} - m_z \frac{\partial m_x}{\partial x} - m_y \frac{\partial m_z}{\partial y} + m_z \frac{\partial m_y}{\partial y} \right) d^3r. \quad (2.24)$$

For different ordering vectors of the spin spirals, different types of spin spirals are stabilized [Fig. 7(h)]: Along the  $x$  direction one finds a Néel spiral and along the  $y$  direction a Néel spiral with opposite sense of winding. At an angle of  $45^\circ$  the spiral is of Bloch type and even intermediate states exist at other angles. The anisotropic DMI leads to the stabilization of antiskyrmions as a metastable solution or as stable crystals when a magnetic field is applied [Fig. 7(i)]. This antiskyrmion is characterized by a negative vorticity  $m = -1$  and allows to recognize the different types of spin spirals from Fig. 7(h).

In principle, other types of DMI can occur if the inversion symmetry is broken in another way. For example, in publication [BG5] we discuss a type of DMI which allows to stabilize a new quasiparticle: the magnetic bimeron (it is introduced in Sec. 6). In order to perform simulations, this type of DMI and also the anisotropic DMI were implemented in the computer code mumax3 [43,44].

### Dipole-dipole interaction

The third major mechanism, which allows for the stabilization of magnetic skyrmions, is the dipole-dipole interaction [6]. This interaction accounts for the attractive and repulsive interactions of the negative and positive poles of two magnetic dipoles. The interaction between the magnetic moments  $\mathbf{s}_i$  and  $\mathbf{s}_j$  at distance  $r_{ij}$  is angular dependent,

$$H_{\text{dd},ij} = -\frac{\mu_0}{4\pi} \left( 3 \frac{(\mathbf{s}_i \cdot \mathbf{r}_{ij})(\mathbf{s}_j \cdot \mathbf{r}_{ij})}{r_{ij}^5} - \frac{\mathbf{s}_i \cdot \mathbf{s}_j}{r_{ij}^3} \right). \quad (2.25)$$

The dipole-dipole interaction is a long-range interaction and stabilizes skyrmionic bubbles and other non-collinear spin textures of larger sizes ( $\approx 100 \text{ nm} - 1 \mu\text{m}$ ) compared to the skyrmions stabilized by frustrated exchange interactions or by DMI [6]. Even though the dipole-dipole interaction is commonly weaker than the exchange interaction, for long distances it becomes the dominating interaction. This behavior is essential for the stabilization of non-collinear spin textures and short-range approximations are not able to explain metastability [45,46].

Since every magnetic moment interacts with every other magnetic moment, the computation of this term is very demanding in computer codes. Still, one can utilize a short-range approximation, considering nearest neighbors only and dropping the second term

$$H_{\text{dd,approx}} \propto - \sum_{\langle i,j \rangle} (\mathbf{s}_i \cdot \mathbf{r}_{ij})(\mathbf{s}_j \cdot \mathbf{r}_{ij}), \quad (2.26)$$

to determine which type of skyrmion type is favored energetically. One has to keep

in mind that by this approximation alone none of the considered skyrmions would be stable. In publication [BG4] we have shown that Bloch skyrmions are favored over Néel skyrmions by this interaction. Still, the dipole-dipole interaction is achiral in the sense that Bloch skyrmions with helicities of  $\pm\pi/2$  are energetically equivalent.

In some publications, skyrmions stabilized by the dipole-dipole interaction are called ‘bubbles’ and are strictly distinguished from skyrmions stabilized by the DMI. The only geometrical difference is however their  $m_z$  profile: While skyrmions in the close sense exhibit a continuously changing profile from e. g.  $-z$  to  $+z$  back to  $-z$ , bubble skyrmions have a wide area in their center where the out-of-plane magnetization is constant. The non-collinearity is condensed into a very narrow domain wall between the inner part and the surrounding. Since both objects are topologically equivalent, they will both be addressed by the term ‘skyrmion’ in the following.

## 2.4 Experimental discovery and steps towards applications

Now that a general understanding of the properties of magnetic skyrmions and possible stabilizing mechanisms has been imparted, this section is attributed to the experimental discovery of magnetic skyrmions. Many of the introduced concepts will be addressed again. First, a brief historic overview on the discovery of different types of skyrmions is given. Thereafter, more recent findings are presented that have motivated many of the publications which will be presented in the cumulative part of this thesis.

### Detection of magnetic skyrmions

After the prediction of magnetic skyrmions in 1989 [25], Mühlbauer *et al.* [8] were the first to observe skyrmions experimentally in 2009 [‘A-phase’ in Fig. 8(a)]. The authors of that publication performed neutron scattering experiments of a MnSi sample with an applied magnetic field. For small temperatures and moderate fields two symmetric intensity maxima in the intensity of this reciprocal-space-measurement technique indicated a periodicity of the magnetic texture in real space along the corresponding crystallographic direction. The magnetic texture is in a helical phase [Fig. 8(a)], i. e., a spin spiral. In the ‘A-phase’, for higher temperatures, three energetically degenerate spin spirals (occurring at a mutual angle of  $120^\circ$ ) are superposed giving six intensity maxima in reciprocal space [Fig. 8(b)]. Such a superposition is equivalent to a periodic lattice of skyrmions (as was presented in Fig. 6) that is continued as a lattice of tubes along the magnetic field direction.

One year later, these findings have been confirmed by Lorentz transmission electron microscopy (TEM) images of a similar sample [9] (cf. Fig. 9). In this real-space representation of the magnetic texture it becomes apparent that the skyrmions are of Bloch type with a helicity of  $\gamma = \pi/2$ . They are stabilized by the bulk DMI as introduced in Sec. 2.3. After the observation of skyrmion crystals in MnSi more skyrmion hosts in the family of non-centrosymmetric B20 materials have been identified.

Another year later, in 2011, a second class of skyrmions was observed experimentally [10]. A periodic lattice of Néel skyrmions was identified at the interface of Fe and Ir(111). Here, the heavy Ir atoms induce an interfacial DMI as explained in Sec. 2.3. Compared to a Bloch skyrmion all magnetic moments are rotated around the perpendicular direction giving the Néel skyrmion a helicity of  $\gamma = 0$ .



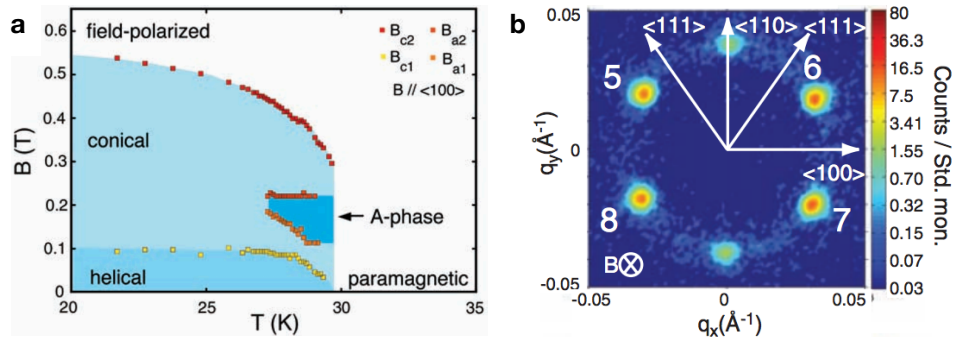


Figure 8: **First observation of magnetic skyrmions.** **a** Measured phase diagram of MnSi. The ‘A-phase’ denotes the skyrmion crystal phase. **b** Neutron scattering image with six intensity maxima in reciprocal space corresponding to the wave vectors of the superimposed spin spirals which form a skyrmion crystal. Both panels: From (S. Mühlbauer *et al.* Skyrmion Lattice in a Chiral Magnet. *Science* **323**, 915 (2009) Ref. [8]). Reprinted with permission from AAAS.

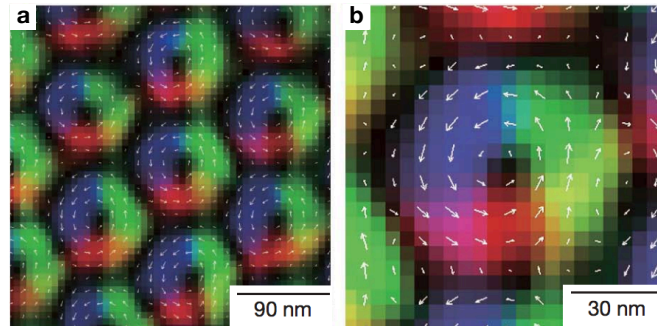


Figure 9: **First real-space observation of a magnetic skyrmion crystal.** **a** Reconstructed image from an over- and underfocussed Lorentz transmission electron microscopy measurement of the skyrmion crystal phase in MnSi. The arrows and colors represent the in-plane orientation of the magnetic moments. **b** Magnified representation of a single skyrmion from panel a. Adapted by the permission from Springer Nature Terms and Conditions for RightsLink Permissions Springer Nature Customer Service Centre GmbH: Macmillan Publishers Limited Nature Real-space observation of a two-dimensional skyrmion crystal, X. Z. Yu *et al.* 2010; Ref. [9].

Such interfaces of magnetic and heavy metal materials have been proven to be promising for the control of the resulting skyrmion texture. Generating two distinct interfaces with opposite signs of the DMI constants in a ‘sandwich’ structure, like Ir/Co/Pt, enhances the effective strength of the DMI [47], which is even controllable by varying the layers’ thicknesses. Consequently, the stability of skyrmions is drastically increased, which allowed for the detection of skyrmions even at room temperature in such multi-layer systems [47–50].

In 2017 also antiskyrmion crystals were observed [41]. These textures require an anisotropic DMI (cf. Sec. 2.3), which is for example induced by the non-symmetric layer stacking in the Heusler material  $\text{Mn}_{1.4}\text{Pt}_{0.9}\text{Pd}_{0.1}\text{Sn}$ . Antiskyrmions have a vorticity of  $m = -1$ . For this reason, the rotational symmetry is broken. This brings about new

possibilities for spintronics applications. Furthermore, in thicker samples, where the dipole-dipole interaction becomes considerable as well, skyrmions and antiskyrmions can both be present in such a material, as was shown for the first time in our experimental collaboration in publication [BG13].

Today, these three types of (anti-) skyrmion crystals have been observed in a manifold of materials. Furthermore, it is worth mentioning that skyrmions have not only been found in ferromagnetic materials but also in ferrimagnets [51], multiferroics [52] and ferroelectric materials [53].

Even though skyrmion tubes with a varying helicity along the tube direction have been observed recently [54], skyrmion tubes with a fixed helicity, different to that of Bloch and Néel-type skyrmions, remain unobserved. Furthermore, skyrmions in in-plane magnetized materials lack observation, which motivated the prediction of magnetic bimerons in publication [BG5].

### Steps towards applications

In the following, relevant findings for spintronics applications of skyrmions in ferromagnets are presented. On that account many predictions exist: skyrmions may be utilized for logic computing [55], in transistors [56], as microwave devices [57] or magnonic devices [58]. In this thesis, the racetrack storage device is in the center of interest. As explained in the introduction, it is one of the most promising applications of magnetic skyrmions [3,5]. Here, the existence of a skyrmion at certain positions encodes '1' bits, while a missing skyrmion corresponds to a '0' bit. As will be presented in the following, the four essential processes 'writing', 'deleting', 'moving', and 'reading' of these bits have been realized experimentally.

### Writing and deleting skyrmions in thin films

To utilize skyrmions in spintronic devices, these quasiparticles have to appear individually and not as periodic lattices. This happens naturally, when the stabilizing magnetic field is increased and a skyrmion lattice transforms into the field-polarized phase. However, methods for a controlled generation and deletion are inevitable. As one example, the controlled writing and destructing of skyrmions by spin-polarized currents from a scanning tunneling microscopy (STM) tip has been shown for a PdFe/Ir sample [13] (Fig. 10). In this particular case the externally applied magnetic field is chosen such that the skyrmion and the ferromagnetic states are energetically equivalent and the temperature has been decreased to 4.2 K so that thermal switching is extremely improbable. The injected spins are oriented out-of-plane and switch a 'bit' at an average rate on the Hz scale. By increasing or decreasing the field, either the ferromagnetic or the skyrmionic state becomes more favorable, respectively, allowing for a deterministic switching of bits.

Over the following years several alternative writing mechanisms have been realized or predicted. Besides the presented generation due to spin torques [5,13,59], skyrmions can be generated by locally applied magnetic fields [60,61], by electric fields [62], laser pulses [63], electron pulses [64] or by defects and at boundaries [65–67]. An overview of generating mechanisms is given in several review articles on magnetic skyrmions [6,68,69].

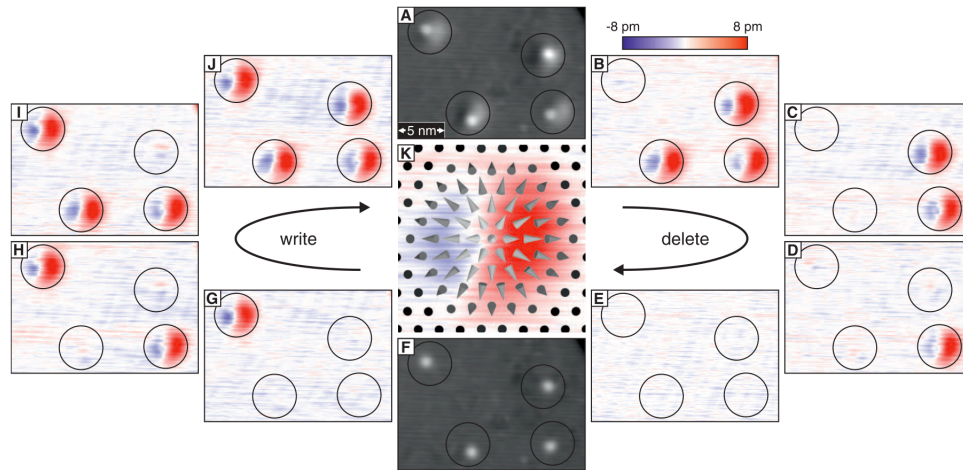


Figure 10: **Writing and deleting of magnetic skyrmions.** Left (G-J): Writing process of four magnetic skyrmions by local spin-polarized currents from a scanning tunneling microscope tip polarized out-of plane. The images have been detected by an in-plane polarized scanning tunneling microscope tip. The color represents the signal difference to the reference state in panel F (red: positive, blue: negative). Right (B-E): Deleting process. Here, the switching process is reversible, occurring at an average rate on the Hz scale. It can be made deterministic favoring the writing (the deleting) process by decreasing (increasing) the magnetic field. Panels A and F show the raw measurements before and after the writing process. Panel K shows the spin texture: a Néel skyrmion. From (N. Romming *et al.* Writing and Deleting Single Magnetic Skyrmions. *Science* **341**, 636 (2013) Ref. [13]). Reprinted with permission from AAAS.

### Current-driven motion of magnetic skyrmions

In this thesis the focus is set mainly on the emergent electrodynamic effects of skyrmions. One of those is the current-driven motion of skyrmions whose mathematical background will be discussed in more detail in the section on simulation techniques (Sec. 3.2). The propulsion of skyrmions can be realized typically by two scenarios:

The easiest way is to apply an electric current directly along the magnetic racetrack where the resulting spin-polarized current interacts with the magnetic moments that form the skyrmion. As a consequence of the spin-transfer torque, a skyrmion is moved along the track or a skyrmion crystal moves as a whole, which was first observed in bulk MnSi [7,70]. The skyrmion velocity was found to be proportional to the current density except for very low currents, for which the skyrmions are pinned. The critical current density, where the skyrmions start moving, was determined to be around  $10^6$  A/cm<sup>2</sup> which is much smaller than that for domain walls, in great favor of technological applications.

The second method is to consider a multilayer system consisting of the actual ferromagnetic racetrack layer interfaced with a heavy metal material. Here, the charge current generates a pure spin current via the spin Hall effect which is injected into the ferromagnetic layer. Due to the possibility of large angles between a skyrmion's magnetic moments and the injected spins, larger spin torques are generated and a skyrmion

moves faster. In Ref. [15] this motion has been realized. However, as is observable in Fig. 11, the skyrmion does not move in the middle of the track but is pushed towards the edge. The reason for the transverse component of this motion is the skyrmion Hall effect originating in the topological charge of the skyrmion (for a derivation and detailed explanation see Sec. 3.4). One of the main goals of this thesis is to suppress this effect. It has been achieved by changing the racetrack materials (publication [BG1]) or by considering alternative quasiparticles (publications [BG6] and [BG7]).

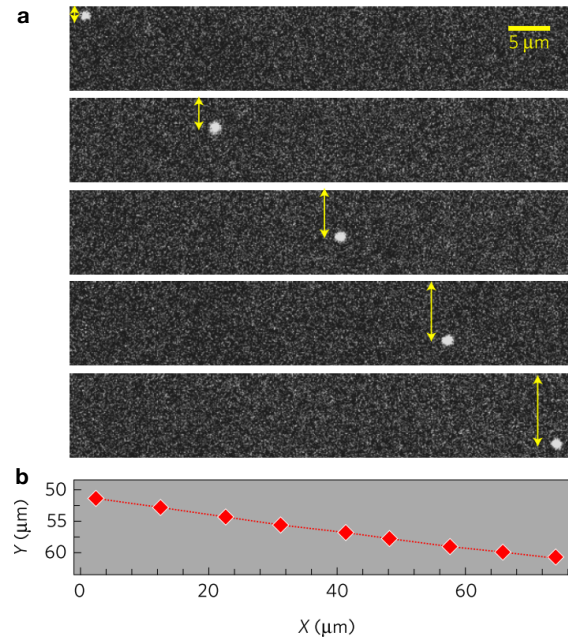


Figure 11: **Current-pulse-driven skyrmion motion.** **a** Magneto-optic Kerr effect measurements show a single skyrmion in a Ta/CoFeB/TaO<sub>x</sub> racetrack. Due to a rather small DMI ( $D \leq 0.5 \text{ mJ/m}^2$ ), the skyrmion has a large diameter of approximately  $1 \mu\text{m}$ . The current pulse is applied for  $50 \mu\text{s}$  between each panel with a magnitude of  $j_x = 2.8 \text{ MA/cm}^2$ . Panel **b** summarizes the trajectory. Adapted by the permission from Springer Nature Terms and Conditions for RightsLink Permissions Springer Nature Customer Service Centre GmbH: Macmillan Publishers Limited, part of Springer Nature Nature Physics Direct observation of the skyrmion Hall effect, W. Jiang *et al.* 2016; Ref. [15].

### Topological Hall effect and detection of skyrmions

The last required constituent for constructing a racetrack storage device is reading the magnetic skyrmions. This can in principle be achieved by real-space imaging similar to Fig. 9. It is however impracticable for production-line applications. A more elegant method is an electrical detection. Here, one aims at utilizing the unique Hall signal of the magnetic skyrmion.

Differently to most spin textures, like spin spirals, a skyrmion phase does not only exhibit a conventional Hall effect (proportional to the external field  $B_z$ ; cf. the detailed discussion in the later section 4.5) and an anomalous Hall effect (proportional to the net magnetization  $M_z$ ) but also an additional contribution which arises due to the topological charge density of the skyrmion. It is therefore labeled ‘topological Hall effect’ (a

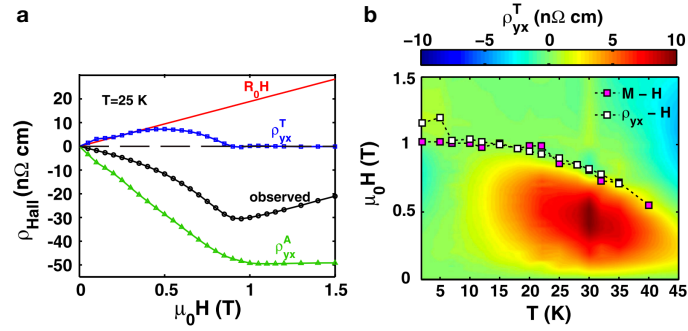


Figure 12: **Hall effects in MnSi.** **a** Hall resistivity of a 50 nm thick MnSi film at a fixed temperature of  $T = 25$  K. The measured signal (black) is separated into three contributions: the conventional Hall effect (red), the anomalous Hall effect (green) and the topological Hall effect (blue). **b** Topological contribution in the phase diagram. The signal is non-zero mainly in the skyrmion crystal phase. The dashed line indicates the phase boundary to the field-polarized phase. Both panels: Reprinted (figure) with permission from (Y. Li *et al.* Physical Review Letters **110**, 117202 (2013); Ref. [71]; Robust Formation of Skyrmions and Topological Hall Effect Anomaly in Epitaxial Thin Films of MnSi. Copyright (2013) by the American Physical Society.

more detailed explanation will be given in the publication section 5.2). Experimentally, the topological Hall effect was first observed in 2012 for the skyrmion crystal phase of MnSi by Schulz *et al.* [70] as a drop in the Hall signal when scanning the temperature. In later publications, the magnetic-field dependence was analyzed [71]. The signal can be decomposed into the three aforementioned contributions

$$\rho_{xy} = R_0^{\text{HE}} B_z + R_0^{\text{AHE}} M_z + R_0^{\text{THE}} \langle n_{\text{Sk}} \rangle \quad (2.27)$$

as can be seen in Fig. 12(a). The topological contribution occurs only for fields below 1 T which is where the skyrmion crystal phase is stabilized in this case. Note, that the mapping of the signal over field and temperature in Fig. 12(b) looks very similar to the phase diagram which was determined by neutron scattering [Fig. 8(a)]. Only the critical field is larger here, since only a 50 nm thick film is considered. For a 10 nm thick film the critical field increases even further [71].

Since the topological Hall effect is unique for topologically non-trivial spin textures, its existence allows in principle for an unambiguous detection of skyrmions in racetrack devices (skyrmions are well distinguished for example from domain walls). The utilization of the Hall effect for a local measurement was realized in 2018 by Maccariello *et al.* [14]. The authors considered a multilayer racetrack and measured the voltage change between two thin leads attached to the track [Fig. 13(a)]. In parallel, they compared their results with real-space images. As a result they found a linear relation of the Hall signal and the number of skyrmions between the leads [Fig. 13(b)]. However, as the authors point out, the main contribution to the voltage arises from the anomalous Hall effect due to the locally reduced net magnetization. The estimated topological contribution to the signal is two orders of magnitude smaller. This means that in the considered sample with skyrmions of 100 nm size the signal cannot be distinguished from that of domain walls.

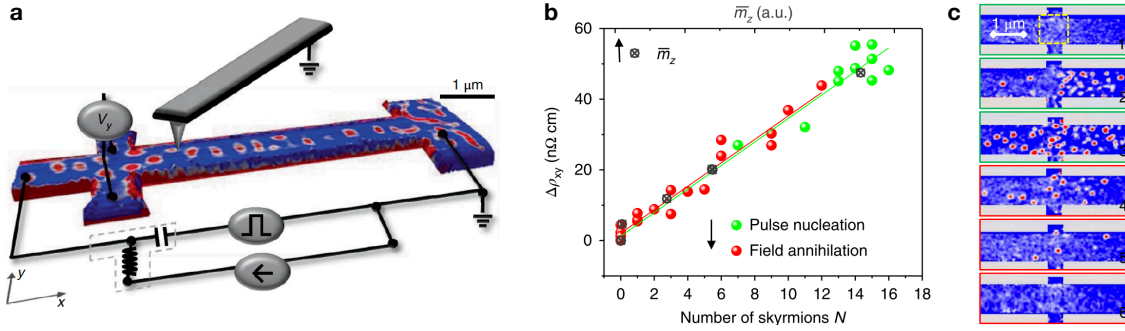


Figure 13: **Electrical detection of magnetic skyrmions.** **a** Multilayer racetrack with measured out-of-plane magnetization (red and blue) by local probe magnetic force microscopy. The combination with a Hall measurement allows to relate the Hall resistivity response with the local skyrmion density. **b** Transverse resistivity for multiple configurations (examples shown in **c**). The increase in resistivity compared to the ferromagnetic state is proportional to the number of skyrmions between the leads. Green data points have been measured at constant magnetic fields during the nucleation of skyrmions by current pulses; for the red points the field has been increased so that the number of skyrmions is reduced. Adapted by the permission from Springer Nature Terms and Conditions for RightsLink Permissions Springer Nature Customer Service Centre GmbH: Macmillan Publishers Limited, part of Springer Nature Nature Nanotechnology Electrical detection of single magnetic skyrmions in metallic multilayers at room temperature, D. Maccariello *et al.* 2018; Ref. [14].

Luckily, for the actual realization of a skyrmion racetrack device, much smaller skyrmions are the optimal candidates for the carriers of information. Since the anomalous Hall effect scales with the skyrmions' area but the topological Hall effect does not, a drastical increase of the importance of the topological Hall effect is expected for the practicable case. Note for example, how in MnSi the topological Hall effect has a similar magnitude compared to the anomalous Hall effect at low fields [Fig. 12(a)]. The work of Maccariello *et al.* [14] proves that an electrical local detection of skyrmions is in principle possible. For an actual application, smaller skyrmions need to be considered and the racetrack has to be fabricated much narrower.

A detailed discussion of the topological Hall effect is presented in the publication section 5.2. This effect is an essential part of this PhD thesis: it is considered for skyrmions in publication [BG2], [BG8] and [BG9], and for other quasiparticles in publications [BG5] (for the bimeron), publication [BG6] (for the skyrmionium), and publication [BG7] (for the antiferromagnetic skyrmion).

---

### 3 Simulation of magnetic textures

In the previous section magnetic skyrmions have been introduced as one of the most prominent examples of non-collinear spin textures. For a continuous magnetization density their stability is a manifestation of non-trivial real-space topology. However, since this density is condensed near magnetic atoms, a skyrmion can be viewed to be formed by discrete magnetic moments. Then, a stabilizing mechanism like the DMI is inevitable.

In this section the foundation is laid for the simulation and the quantitative description of the aforementioned stabilization of magnetic textures, as well as for the simulation of their current-driven motion. First, in Sec. 3.1 the Monte Carlo method is explained. It allows to determine the stable ground state of a cluster of magnetic moments. Thereafter, in Sec. 3.2 the Landau-Lifshitz-Gilbert equation is introduced. This equation allows to simulate the temporal propagation of a spin cluster or a magnetization density even when externally perturbed. It can be utilized to simulate the current-driven motion of non-collinear spin textures. An elegant way to effectively describe this process by means of an algebraic equation of motion is the Thiele equation, presented in Sec. 3.3. The latter two concepts are exemplarily demonstrated for the current-driven motion of a Néel skyrmion in a racetrack geometry in Sec. 3.4.

#### 3.1 Monte Carlo simulations

An efficient way to determine the ground state of a spin system, i. e., the spin texture with the lowest energy, is to conduct Monte Carlo simulations [72]. A cluster of magnetic moments is initialized in a random configuration and is then relaxed in the following way for zero temperature: A randomly selected magnetic moment is reoriented along a randomly determined direction. Thereafter, the total energies before and after this reorientation are compared. If the reorientation lowers the total energy of the system, the altered moment is accepted. If the reorientation increases the total energy, the initial state is restored. Repeating this step gradually decreases or conserves the energy of the spin system.

However, this procedure convergences towards a local energy minimum which might not be the global ground state. This can be avoided by considering a finite temperature. The so called ‘Metropolis algorithm’ [73] allows for the acceptance of a reorientation by chance, even if the total energy of the spin cluster is increased by a reorientation of a magnetic moment. The new configuration is accepted with the probability

$$p = \max\{\exp(-\Delta E/k_B T), 1\}. \quad (3.1)$$

In case the energy decreases  $\Delta E < 0$  by the reorientation, the probability is 1. For  $\Delta E > 0$  the probability is given by an Arrhenius law ( $T > 0$  temperature,  $k_B$  Boltzmann constant). Since the total energy of the system depends only on the reoriented spin and the spins which are directly interacting with it (typically nearest neighbors),  $\Delta E$  can be calculated using only a few spins instead of the whole cluster.

The convergence speed of the Monte Carlo method can be increased by including several modifications which are more sophisticated than the Metropolis algorithm [72]. Examples are ‘parallel tempering’, ‘importance sampling’ and ‘over-relaxation’. The

efficiency of these additions depends strongly on the considered system. In publication [BG7] for example, the system has been heated periodically for only a few Metropolis steps each time. This way, local energy minima could be overcome while the temperature, which is highly relevant for the magnetic texture, remained low in the long term.

For the Monte Carlo simulations in publications [BG5] and [BG7] an in-house Fortran90 code (mainly created by Alexander Mook and adapted by me to the needs of the considered systems) has been used. Test simulations have been presented in his PhD thesis [74] and also in my master thesis [75]. One of these tests is reviewed in the following.

### Stabilization of a skyrmion crystal

Besides being a verification for the used code, the following considerations demonstrate the technical details that need to be accounted for, before starting a simulation. At the same time, the stabilization of skyrmions from frustrated exchange interactions is exemplarily shown.

Utilizing the Monte Carlo method, a typical phase diagram of a skyrmion host can be simulated; cf. Fig. 14. Here, frustrated exchange interactions are considered on a hexagonal lattice with an external magnetic field  $\mathbf{B}$  oriented along the out-of-plane direction, as introduced in Sec. 2.3. The frustration is induced by opposite signs for the exchange interactions of nearest neighbors  $J_1$  and third-nearest neighbors  $J_3 = -3J_1$ . Fig. 14 is adapted from my master thesis [75] where the used Monte Carlo code has been tested by reproducing Fig. 1 of Ref. [36]. In that publication a skyrmion crystal has also been realized for the case of  $J_2 \neq 0$  and  $J_3 = 0$ .

**Stabilized magnetic textures.** In Fig. 14 the phase boundaries (gray lines) are taken from Ref. [36], while the color indicates the number of skyrmions determined from the stabilized spin texture at the given parameters. For vanishing magnetic field and temperature, the ground state is in a helical phase ('single  $q$ '); a spin spiral which is characterized by a single ordering vector  $\mathbf{q}$ , like in Fig. 6(a). For high fields the system transitions to the field-polarized phase, while it transitions to the paramagnetic phase upon increasing the temperature. Near this phase boundary the skyrmion crystal phase ('triple  $q$ ') is stabilized, like in Fig. 6(b). Here, the topological charge has a finite value. In Ref. [36] also a 'double- $q$  phase' and a 'Z phase' have been characterized. In the Z phase thermal fluctuations are so large that skyrmions and antiskyrmions appear in the same spin cluster. This behavior is unique for the frustrated exchange mechanism. Since the exchange interaction energy is invariant under variation of the skyrmions' helicity  $\gamma$  and also their vorticity  $m = \pm 1$  (characterizing skyrmions and antiskyrmions, respectively), simulations for the same parameters will result in different types of skyrmion crystals even in the triple- $q$  phase.

**Cluster size.** The 'multi- $q$ ' labeling originates in the mathematical construction of the magnetic phases. A skyrmion crystal is for example constructed by the superposition of three spin spirals, therefore the alternative name 'triple- $q$  state'. Hence, the skyrmion size can be calculated from the spiral pitch  $\lambda = 2\pi/q = \pi a / \arccos[\frac{1}{4}(1 + \sqrt{1 - 2J_1/J_3})]$ , which is determined by the exchange constants [36]. The cluster size of  $72 \times 72$  and the



exchange constants have been chosen such that a finite number of skyrmions fits the lattice commensurately. This consideration is highly important before performing simulations, and has been accounted for also in the publications [BG5] and [BG7]. The aim is to simulate a perfectly periodic bulk skyrmion crystal. However, due to computational limitations, only finite spin clusters can be simulated. Choosing a non-fitting cluster size would lead to a deformation of the skyrmions due to the boundary conditions, altering the energetic profile of the skyrmion host — an effect which would not be present in an experimental quasi-infinite system. It should therefore be avoided in the simulation as well.

Here,  $3N^2/(4\lambda^2) = 364$  skyrmions fit the spin cluster geometrically. This number is however underestimated by the numerical calculation; the maximum value in Fig. 14 is  $\approx 280$ . However, it would be achieved if the skyrmion phase would extend down to zero temperature. The finite temperatures lead to thermally distorted skyrmions, so that the numerical calculation of the skyrmion number gives a smaller result than what is expected from geometry.

The agreement of the presented simulations with those of Ref. [36] suggests the correctness of the used computer code and sets the foundation of publication [BG11], where the transport properties of magnons in exactly these skyrmion crystals has been simulated. Furthermore, the Monte Carlo code has been used to simulate the skyrmion, bimeron and antiskyrmion crystals in publication [BG5], as well as the antiferromagnetic skyrmion crystals in Fig. [BG7].

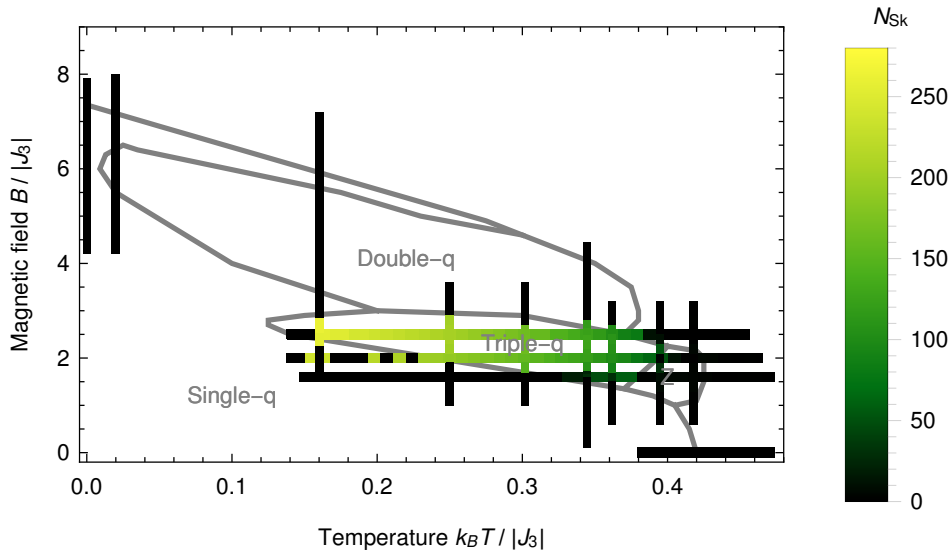


Figure 14: **Phase diagram of a frustrated skyrmion host.** Adapted from Ref. [75] reproducing Fig. 1 of Ref. [36]. The skyrmion number (colored bar) is non-zero mainly in the skyrmion-crystal phase (“triple- $q$ ”). The calculations were carried out for a cluster of size  $72 \times 72$  with exchange parameters  $J_1/J_3 = -1/3$ .

### 3.2 Spin dynamics simulations

In this section the Landau-Lifshitz Gilbert (LLG) equation is derived. It is the equation of motion of magnetic moments and allows to compute their temporal propagation instead of merely finding the configuration of lowest energy (as is done in Monte Carlo simulations). In the following, the precessional term is derived (which was introduced by Landau and Lifshitz [76]), the damping term is introduced (as predicted by Gilbert [77]) and spin torques are explained (originally introduced by Slonczewski [78]).

#### Precession

In linear response, the angle between a classical magnetic moment  $\mathbf{M}$  (here not normalized) and its corresponding effective magnetic field

$$\mathbf{B}_{\text{eff}} = -\frac{\partial H}{\partial \mathbf{M}'} \quad (3.2)$$

is fixed if the energy in the system

$$E = -\mathbf{M} \cdot \mathbf{B}_{\text{eff}} \quad (3.3)$$

is conserved. The effective magnetic field covers all interactions of the magnetic moment with external fields and also other magnetic moments that enter the lattice Hamiltonian  $H$ .

The magnetic moment precesses around  $\mathbf{B}_{\text{eff}}$  with a constant frequency. This can be derived from the equation of motion of the quantum mechanical spin operator  $\mathbf{s}$  [74]

$$\dot{\mathbf{s}} = -\frac{i}{\hbar} [\mathbf{s}, H]. \quad (3.4)$$

Since the aim is to describe classical magnetic moments  $\mathbf{M} = -\gamma \mathbf{s}$  (only the spin contribution is considered here), the Hamiltonian is expanded to first order in the spin [79]

$$[s_i, H] = [s_i, \sum_{j=x,y,z} \frac{\partial H}{\partial s_j} s_j + O(\mathbf{s}^2)] \quad (3.5)$$

$$= i\hbar \sum_j \epsilon_{ijk} \frac{\partial H}{\partial s_j} s_k + O(\mathbf{s}^2) \quad (3.6)$$

$$= i\hbar \left( \frac{\partial H}{\partial \mathbf{s}} \times \mathbf{s} \right) \cdot \mathbf{e}_i + O(\mathbf{s}^2). \quad (3.7)$$

Exchanging the quantum mechanical operators with the corresponding expectation values (Ehrenfest theorem) and dropping the higher order terms (classical limit) gives

$$\frac{\partial \mathbf{M}}{\partial t} = -\gamma \mathbf{M} \times \mathbf{B}_{\text{eff}} \quad (3.8)$$

with  $\gamma = g\mu_B/\hbar$ . As expected, this equation leads to a precession of the magnetic moment around its effective magnetic field (cf. cone in Fig. 15).

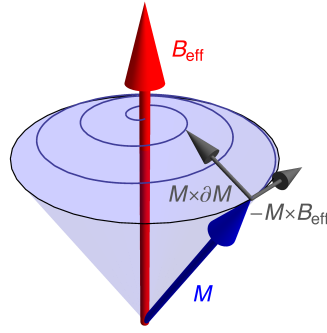


Figure 15: **Damped precession of a magnetic moment.** The magnetic moment  $M$  precesses around its effective magnetic field  $B_{\text{eff}}$ . Due to the Gilbert damping the system converges to a parallel alignment of both quantities.

### Damping

In Ref. [77] a phenomenological damping term was added to Eq. (3.8) which accounts for energy dissipation (mainly due to excitations of phonons and conduction electrons [77, 79]). When the system is fully relaxed, each magnetic moment points along its respective effective magnetic field. For this reason, the damping term has to point perpendicular to the precessional term towards the effective magnetic field. Consequently, the damping term was introduced as

$$\frac{\alpha}{M_s} \mathbf{M} \times \frac{\partial \mathbf{M}}{\partial t}. \quad (3.9)$$

Here,  $M_s$  is the saturation magnetization and  $\alpha$  is the dimensionless Gilbert damping parameter. The corresponding term alters the precessional trajectory to a damped precession, where the orientation of a magnetic moment converges towards a parallel alignment with its effective magnetic field (cf. Fig. 15). In total, this yields the Landau-Lifshitz-Gilbert equation

$$\frac{\partial \mathbf{M}}{\partial t} = -\gamma \mathbf{M} \times \mathbf{B}_{\text{eff}} + \frac{\alpha}{M_s} \mathbf{M} \times \frac{\partial \mathbf{M}}{\partial t}. \quad (3.10)$$

The effective magnetic field  $B_{\text{eff}}$  determines the quantitative behavior of the propagation of a magnetic moment's orientation. It allows to also include external perturbations like spin torques.

### Spin torque

In the following, the interaction of magnetic moments with electron spins is introduced. This allows to describe the current-driven motion of non-collinear spin textures via spin torques. The corresponding term in the LLG equation is derived for the most simple case, as in Ref. [80]: the ferromagnetic layer of interest (magnetization along  $M_1$ ) is interfaced with a second ferromagnetic layer which is assumed to have a constant magnetization along  $M_2$  for all times. Both layers shall have non-parallel magnetizations  $M_1 \nparallel M_2$ . When a current is applied perpendicularly to the layers, the conduction elec-

trons coming from the second ferromagnet have a spin  $s \parallel M_2$ . When they are injected into the first ferromagnetic layer, they generate a spin accumulation  $s_{\text{acc}}$  interacting with  $M_1$  via the exchange interaction

$$H_{\text{ex}} = -\bar{J}s_{\text{acc}} \cdot M_1. \quad (3.11)$$

For this reason, an additional term to the effective magnetic field arises, which is  $\bar{J}s_{\text{acc}}$ . However, only the component  $s_{\text{acc}}^\perp$ , which is perpendicular to  $M_1$ , has an effect. Therefore, the LLG equation describing the magnetic moments of layer one reads

$$\frac{\partial M_1}{\partial t} = -\gamma M_1 \times (B_{\text{eff}}^0 + \bar{J}s_{\text{acc}}^\perp) + \frac{\alpha}{M_s} M_1 \times \frac{\partial M_1}{\partial t}. \quad (3.12)$$

It has to be noted that  $s_{\text{acc}}^\perp$  is in general not parallel to  $s$  (the injected spin polarization parallel to  $M_2$ ) but is per definition perpendicular to  $M_1$ . For this reason, it can be formally expressed as [80]

$$\bar{J}s_{\text{acc}}^\perp = As \times M_1 + B(s \times M_1) \times M_1. \quad (3.13)$$

Inserting this equation into Eq. (3.12) gives

$$\frac{\partial M_1}{\partial t} = -\gamma M_1 \times (B_{\text{eff}}^0 + Bs) - \gamma AM_1 \times (s \times M_1) + \frac{\alpha}{M_s} M_1 \times \frac{\partial M_1}{\partial t}. \quad (3.14)$$

After relabeling  $M_1$ , the effective magnetic field  $B_{\text{eff}}^0$  (excluding the term due to the injected spins  $H_{\text{ex}}$ ) and the prefactors of the torque terms, the LLG equation reads

$$\frac{\partial M}{\partial t} = -\gamma M \times B_{\text{eff}} + \frac{\alpha}{M_s} M \times \frac{\partial M}{\partial t} + \tau_{\text{FL}} M \times s + \tau_{\text{IP}} M \times (s \times M). \quad (3.15)$$

The first torque term is called ‘field-like’ (FL) or ‘out-of-plane’ torque. It is commonly small [81] compared to the second torque term, called ‘in-plane’ (IP) torque, and has no qualitative influence on the motion of non-collinear spin textures, as will be shown in the next section. Therefore, it is neglected for the rest of this thesis.

**Spin-orbit torque.** Besides the possibility to inject spins from the perpendicular direction via a second ferromagnetic layer, the ferromagnet of interest can also be interfaced with a heavy metal (HM) layer [5] [Fig. 16(a)]. A charge current mainly flows in the HM and the spin Hall effect (SHE) [82–84] generates a pure spin current along the perpendicular direction. Spins  $s$  are injected like in the case explained above. Again, the spins generate a torque that affects the magnetization of the FM layer. Since it arises due to the spin-orbit interaction, the torque is also labeled ‘spin-orbit torque’ (SOT).

In this scenario the magnitude of the in-plane torque can be determined by a sophisticated analysis of the conduction electrons in the ferromagnetic layer. This allows to write the version of the LLG equation that is considered for the rest of this paper

$$\frac{\partial M}{\partial t} = -\gamma M \times B_{\text{eff}} + \frac{\alpha}{M_s} M \times \frac{\partial M}{\partial t} + \frac{\epsilon\beta}{M_s} M \times (s \times M), \quad (3.16)$$

with the spin-orbit-torque constant [81]

$$\epsilon\beta = \frac{\gamma_e \hbar j \Theta_{\text{SH}}}{2eM_s d_z}. \quad (3.17)$$

Here,  $\gamma_e = \gamma/\mu_0 = 1.760 \times 10^{11} \text{ T}^{-1}\text{s}^{-1}$  is the gyromagnetic ratio of an electron,  $\Theta_{\text{SH}}$  is the spin Hall angle,  $d_z$  is the thickness of the ferromagnetic layer,  $j$  is the current density, and  $M_s$  is the saturation magnetization.

In the publications [BG1],[BG4],[BG5],[BG6] this equation has been solved using a modified version of the GPU-accelerated micromagnetic software package Mumax3 [43, 44] (based on nvidia's language 'cuda' and google's language 'go').

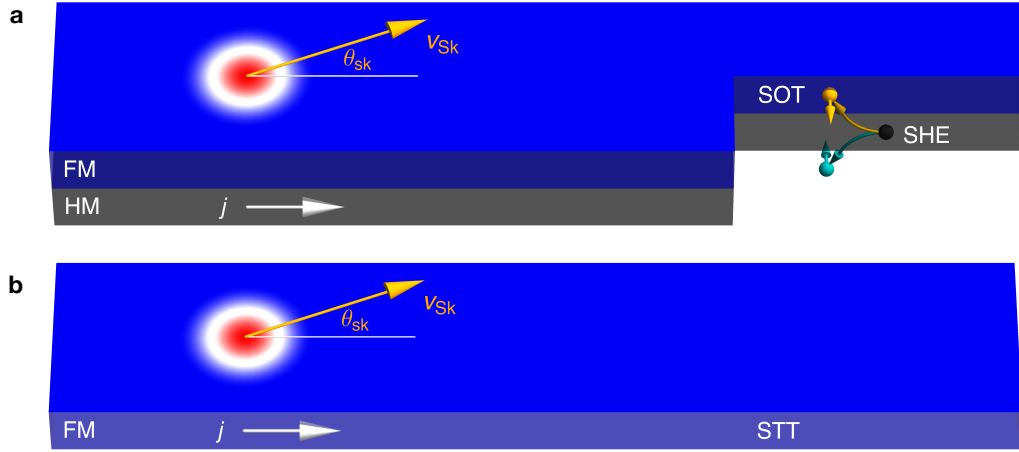


Figure 16: **Racetrack geometries.** **a** Spin-orbit-torque scenario of perpendicular spin injection: A charge current (density  $j$ ) along the heavy metal (HM) layer is translated into a spin current by the spin Hall effect (SHE). This current is oriented along the perpendicular direction with spins polarized perpendicular to both currents. These spins (yellow) are injected into the ferromagnetic (FM) racetrack layer. **b** Spin-transfer-torque scenario where a current is applied directly along the FM layer. There, the current becomes spin polarized and generates a torque wherever the magnetization density is not uniform. Both setups allow to move a magnetic skyrmion (circular object; the color represents the out-of-plane magnetization density) but at an angle  $\theta_{\text{sk}}$  with respect to  $j$ . This figure is partially adapted from publication [BG1].

**Spin-transfer torque.** Another possibility that allows for the current-driven motion of non-collinear spin textures is the 'spin-transfer torque'. Here the electron current flows in a single magnetic layer, where the electron spin partially aligns with the texture. Instead of a fixed spin orientation  $s$  (like in the SOT scenario), the 'injected' electron spin is determined by the magnetic texture itself [85]

$$s - M \propto (j \cdot \nabla)M. \quad (3.18)$$

The orientation of  $s$  can differ from  $M$  when the latter is non-collinear ( $M$  is meant here as a continuous magnetization density but the derivative can be discretized to cover also

localized magnetic moments). The effect is enhanced if the current density  $j$  is increased. The LLG equation is then derived by analogy with the SOT case.

Since the misalignment of spins with respect to the texture is given by the local change of the texture, only torques smaller than in the SOT scenario can be achieved. For this reason, in the following considerations, only the SOT scenario is discussed since it allows to drive magnetic quasiparticles at much lower driving-current densities compared to the STT scenario [5].

### 3.3 Thiele equation

In order to understand the results of spin dynamics simulations better, it is desirable to find an algebraic, effective description for the motion of non-collinear spin textures. For this reason, in the following, the ‘Thiele equation’ [86] is derived and generalized. The essence of the Thiele equation is to consider spin textures that do not change drastically while moving. The ansatz of a steady motion leads to the relation

$$\frac{\partial M_i}{\partial t} = -v_j \frac{\partial M_i}{\partial x_j}, \quad (3.19)$$

where  $x$  is the center coordinate of the magnetic quasiparticle and  $v$  is its velocity. Using this approximation, all non-collinearities of the spin texture can be condensed in tensors, which include the spatial derivative of the magnetic texture  $\partial M_i / \partial x_j$ . These terms have to be calculated only once and then an algebraic equation is solved to determine the trajectory of the quasiparticle instead of having to propagate the LLG equation time step by time step. The derivation of the Thiele equation follows the original publication [86].

The ansatz for the Thiele equation assumes that the total force in the system vanishes. The force density

$$f_i = -\mu_0 B_k^{\text{eff}} \frac{\partial M_k}{\partial x_i} \quad (3.20)$$

will be separated into several terms that compensate each other. To determine these forces the LLG equation (3.16) with the SOT term is multiplied by  $\mathbf{M} \times (\cdot)$  from the left side

$$\mathbf{M} \times \frac{\partial \mathbf{M}}{\partial t} = -\gamma \mathbf{M} \times (\mathbf{M} \times \mathbf{B}_{\text{eff}}) + \frac{\alpha}{M_s} \mathbf{M} \times \left( \mathbf{M} \times \frac{\partial \mathbf{M}}{\partial t} \right) - \frac{\epsilon \beta}{M_s} \mathbf{M} \times [\mathbf{M} \times (\mathbf{s} \times \mathbf{M})]. \quad (3.21)$$

Utilizing the relations  $\frac{\partial \mathbf{M}}{\partial x_i} \perp \mathbf{M} \perp \frac{\partial \mathbf{M}}{\partial t}$ , which follow from  $|\mathbf{M}| = \text{const.}$ , and  $\mathbf{a} \times (\mathbf{a} \times \mathbf{b}) = -a^2 \mathbf{b}$  for perpendicular vectors, this simplifies to

$$\mathbf{M} \times \frac{\partial \mathbf{M}}{\partial t} = \gamma M_s^2 \mathbf{B}_{\text{eff}} - \alpha M_s \frac{\partial \mathbf{M}}{\partial t} + \epsilon \beta M_s (\mathbf{s} \times \mathbf{M}). \quad (3.22)$$

The term  $\mathbf{M}(-\gamma \mathbf{M} \cdot \mathbf{B}_{\text{eff}}) \propto \mathbf{M}$  has been dropped since the resulting force vanishes. The

equation can be solved for the effective field

$$\mathbf{B}^{\text{eff}} = \frac{1}{\gamma M_s^2} \mathbf{M} \times \frac{\partial \mathbf{M}}{\partial t} + \frac{\alpha}{\gamma M_s} \frac{\partial \mathbf{M}}{\partial t} - \frac{\epsilon \beta}{\gamma M_s} (\mathbf{s} \times \mathbf{M}). \quad (3.23)$$

The three terms are labeled ‘gyroscopic’, ‘dissipative’ and ‘spin-torque’ terms, respectively. The vector product is expressed via the Levi-Civita symbol  $\underline{\epsilon}$  (note Einstein’s sum convention)

$$B_k^{\text{eff}} = \frac{1}{\gamma M_s^2} \epsilon_{kln} M_l \frac{\partial M_n}{\partial t} + \frac{\alpha}{\gamma M_s} \frac{\partial M_k}{\partial t} - \frac{\epsilon \beta}{\gamma M_s} \epsilon_{kln} s_l M_n, \quad (3.24)$$

and the time derivative is substituted by the spatial derivative [Eq. (3.19)]

$$B_k^{\text{eff}} = -\frac{1}{\gamma M_s^2} \epsilon_{kln} M_l v_j \frac{\partial M_n}{\partial x_j} - \frac{\alpha}{\gamma M_s} v_j \frac{\partial M_k}{\partial x_j} + \frac{\epsilon \beta}{\gamma M_s} \epsilon_{kln} s_l M_n. \quad (3.25)$$

The three force density contributions are therefore [Eq. (3.20)]

$$f_i^{\text{gyro}} = \frac{\mu_0}{\gamma M_s^2} \epsilon_{kln} M_l \frac{\partial M_n}{\partial x_j} \frac{\partial M_k}{\partial x_i} v_j, \quad (3.26)$$

$$f_i^{\text{diss}} = \frac{\mu_0 \alpha}{\gamma M_s} \frac{\partial M_k}{\partial x_j} \frac{\partial M_k}{\partial x_i} v_j, \quad (3.27)$$

$$f_i^{\text{torque}} = \frac{\mu_0 \epsilon \beta}{\gamma M_s} \epsilon_{kln} s_l M_n \frac{\partial M_k}{\partial x_i}. \quad (3.28)$$

A gyroscopic tensor can be defined as

$$\tilde{g}_{ij} = \frac{1}{d_z M_s^3} \epsilon_{kln} M_l \frac{\partial M_n}{\partial x_j} \frac{\partial M_k}{\partial x_i} = -\frac{1}{d_z M_s^3} \mathbf{M} \cdot \left( \frac{\partial \mathbf{M}}{\partial x_i} \times \frac{\partial \mathbf{M}}{\partial x_j} \right), \quad (3.29)$$

which relates the force density and the velocity

$$\mathbf{f}^{\text{gyro}} = \frac{M_s d_z \mu_0}{\gamma} \underline{\tilde{g}} \mathbf{v}. \quad (3.30)$$

Since the gyroscopic tensor is antisymmetric, it can be expressed as a vector  $\mathbf{g}$  allowing to rewrite the gyroscopic force density,

$$\mathbf{g} = (\tilde{g}_{yz}, \tilde{g}_{zx}, \tilde{g}_{xy})^T, \quad \mathbf{f}^{\text{gyro}} = -\frac{M_s d_z \mu_0}{\gamma} \mathbf{g} \times \mathbf{v}. \quad (3.31)$$

For the dissipative term a dissipative tensor  $\underline{d}$  is defined, which relates the force and the velocity as well,

$$d_{ij} = \frac{1}{d_z M_s^2} \left( \frac{\partial \mathbf{M}}{\partial x_i} \cdot \frac{\partial \mathbf{M}}{\partial x_j} \right), \quad \mathbf{f}^{\text{diss}} = \frac{M_s d_z \mu_0}{\gamma} \underline{d} \mathbf{v}. \quad (3.32)$$

On the contrary, the torque tensor  $\underline{i}$  relates the force with the injected spin orientation,

$$i_{ij} = \frac{1}{d_z M_s^2} \left( \frac{\partial \mathbf{M}}{\partial x_i} \times \mathbf{M} \right)_j, \quad \mathbf{f}^{\text{torque}} = \frac{\epsilon \beta M_s d_z \mu_0}{j \gamma} j \underline{i} \mathbf{s}. \quad (3.33)$$

To arrive at the forces that compensate each other in the Thiele equation,

$$\mathbf{F}^{\text{gyro}} + \mathbf{F}^{\text{diss}} + \mathbf{F}^{\text{torque}} + \mathbf{F}^{\text{ext}} = 0, \quad (3.34)$$

the force densities have to be integrated over the extent that is considered to be a quasi-particle (QP). Additionally to the gyroscopic, dissipative and torque terms, an extrinsic force  $\mathbf{F} = -\nabla U(\mathbf{r})$  is considered. The interaction potential  $U(\mathbf{r})$  accounts for the interaction of a magnetic quasiparticle with other non-collinearities or the sample's edge. In total, the Thiele equation reads

$$b \mathbf{G} \times \mathbf{v} - b \underline{D} \alpha \mathbf{v} - B j \underline{i} \mathbf{s} = \nabla U(\mathbf{r}) \quad (3.35)$$

with the gyroscopic vector, the dissipative tensor and the torque tensor

$$\mathbf{G} = \int_{\text{QP}} \mathbf{g} \, d\mathbf{r}, \quad \underline{D} = \int_{\text{QP}} \underline{d} \, d\mathbf{r}, \quad \underline{I} = \int_{\text{QP}} \underline{i} \, d\mathbf{r}, \quad (3.36)$$

respectively, and with the constants

$$b = \frac{M_s d_z}{\gamma_e}, \quad B = \frac{\epsilon \beta M_s d_z}{j \gamma_e} = \frac{\hbar}{2e} \Theta_{\text{SH}}. \quad (3.37)$$

For a thin film in the  $xy$ -plane the gyroscopic vector only has a  $z$  component

$$\mathbf{G} = -\frac{1}{d_z M_s^3} \int_{\text{QP}} \mathbf{M} \cdot \left( \frac{\partial \mathbf{M}}{\partial x} \times \frac{\partial \mathbf{M}}{\partial y} \right) d\mathbf{r} \, \mathbf{e}_z, \quad (3.38)$$

which is proportional to the topological charge

$$\mathbf{G} = -4\pi N_{\text{Sk}} \mathbf{e}_z. \quad (3.39)$$

The dissipative tensor reads

$$D_{ij} = \frac{1}{d_z M_s^2} \int_{\text{QP}} \left( \frac{\partial \mathbf{M}}{\partial x_i} \cdot \frac{\partial \mathbf{M}}{\partial x_j} \right) d\mathbf{r} \quad (3.40)$$

resulting in

$$D_{ij} = \int_{\text{QP}} \left( \frac{\partial \mathbf{m}}{\partial x_i} \cdot \frac{\partial \mathbf{m}}{\partial x_j} \right) d^2 r \quad (3.41)$$



for a two-dimensional array of normalized magnetic moments. The torque tensor becomes

$$I_{ij} = \frac{1}{d_z M_s^2} \int_{\text{QP}} \left( \frac{\partial \mathbf{M}}{\partial x_i} \times \mathbf{M} \right)_j d\mathbf{r} \quad (3.42)$$

which can be simplified in a two-dimensional system to

$$I_{ij} = \int_{\text{QP}} \left( \frac{\partial \mathbf{m}}{\partial x_i} \times \mathbf{m} \right)_j d\mathbf{r}. \quad (3.43)$$

*Comment on the out-of-plane torque term.* In the derivation of the LLG equation with SOT term [Eq. (3.16)] it was stated that the out-of-plane torque term does not drive non-collinear spin textures and merely alters their shape (therefore it only affects their motion indirectly on a quantitative level). This can be understood by analogy with the above consideration of the in-plane torque term: The out-of-plane torque term leads to two contributions to the effective magnetic field. The first term is oriented along the magnetic moment and the second one is parallel to  $\mathbf{s}$  for all lattice sites. Therefore, even though the out-of-plane term may affect the size and shape of a non-collinear magnetic object, it does not generate a finite effective force in the Thiele equation.

### 3.4 Example: Current-driven motion of a magnetic skyrmion

Starting from the LLG equation — an analytically unsolvable system of differential equations describing the propagation of every magnetic moment — the Thiele equation — an analytically solvable system of algebraic equations describing the velocity of a magnetic quasiparticle — has been derived. In this section the derived theory will be demonstrated at the example of the current-driven motion of a magnetic Néel skyrmion in a thin Co film on Pt, as initially presented in Ref. [5]. This system is the foundation of publication [BG1]. In a similar fashion the motion of a bimeron and a skyrmionium have been explained in publications [BG5] and [BG6].

In the following, the results of micromagnetic simulations [explicitly propagating the LLG equation with SOT term in Eq. (3.16)] are overlaid with the results of analytical considerations [solving the Thiele equation (3.35)]. The system of Co/Pt is described by the parameters listed in Tab. 1 (taken from Ref. [5]). Since the system is an interface of magnetic atoms and heavy metal atoms [cf. Fig. 16(a)], an interfacial DMI arises, which stabilizes Néel skyrmions as explained in Sec. 2.3.

For a Néel skyrmion characterized by  $N_{\text{Sk}} = -1$  and  $\gamma = 0$  the tensors  $\underline{D}$  and  $\underline{I}$  have the following shapes:

$$D_{xx} = D_{yy}, \quad D_{ij} = 0 \quad \text{else}, \quad (3.44)$$

$$I_{xy} = -I_{yx}, \quad I_{ij} = 0 \quad \text{else}. \quad (3.45)$$

Even in a confined sample, where the rotational symmetry of the skyrmion is broken, the above equations are good approximations. For a Néel skyrmion in a racetrack [periodic

Saturation magnetization	0.58 MA/m
Exchange stiffness	15 pJ/m
DMI constant	3 mJ/m <sup>2</sup>
Uniaxial anisotropy ( $z$ )	0.8 MJ/m <sup>3</sup>
Gilbert damping	0.3
Spin Hall angle	0.4

Table 1: **Micromagnetic parameters of a Co/Pt interface.** The parameters have been taken from Ref. [5]. For several of these parameters different values have been presented elsewhere, e. g. for the DMI in Ref. [87] or for the spin Hall angle in Ref. [88]. Using altered values will not qualitatively change the skyrmion's behavior as long as it can still be meta-stabilized.

boundary conditions along  $x$ , therefore  $U(\mathbf{r}) = U(y)$ ] the Thiele equation reads

$$-4\pi N_{\text{Sk}} b \begin{pmatrix} -v_y \\ v_x \\ 0 \end{pmatrix} = bD_{xx}\alpha \begin{pmatrix} v_x \\ v_y \\ 0 \end{pmatrix} + BI_{xy} \begin{pmatrix} s_y \\ -s_x \\ 0 \end{pmatrix} j + \begin{pmatrix} 0 \\ \partial_y U(y) \\ 0 \end{pmatrix}. \quad (3.46)$$

For injected spins along  $-y$  ( $s_x = 0$  and  $s_y = -1$ ) and for skyrmions far from the edge [ $\partial_y U(y) = 0$ ] the equation simplifies to

$$-4\pi N_{\text{Sk}} b \begin{pmatrix} -v_y \\ v_x \\ 0 \end{pmatrix} = bD_{xx}\alpha \begin{pmatrix} v_x \\ v_y \\ 0 \end{pmatrix} - BI_{xy} \begin{pmatrix} j \\ 0 \\ 0 \end{pmatrix}. \quad (3.47)$$

The  $y$  component of this equation gives the relation for the skyrmion Hall angle

$$\tan \theta_{\text{sk}} = \frac{v_y}{v_x} = -\frac{4\pi N_{\text{Sk}}}{D_{xx}\alpha}. \quad (3.48)$$

The  $x$  component yields the skyrmion velocity characterizing the motion along the track

$$v_x = \frac{BI_{xy}}{bD_{xx}\alpha} j - \tan \theta_{\text{sk}} v_y. \quad (3.49)$$

The skyrmion moves at the skyrmion Hall angle towards the confinement of the race-track. While approaching the edge, the potential  $U$  and also the corresponding force on the skyrmion  $-\partial_y U$  increase until either the transverse motion is compensated [stable motion as in Fig. 17(a)] or until the maximum repulsion force is overcome [edge annihilation as in Fig. 17(b)]. For small enough current densities the motion in  $y$  direction is suppressed if

$$4\pi b v_x = \partial_y U(y)|_{y=y_{\text{comp}}}. \quad (3.50)$$

The skyrmion will then move along the confinement at a steady velocity [first term in Eq. (3.49)]. If the extremum of the force due to the confinement potential  $F_0 = -\partial_x U(x)|_{\text{extremum}}$  is overcome, the skyrmion annihilates at the edge of the racetrack.

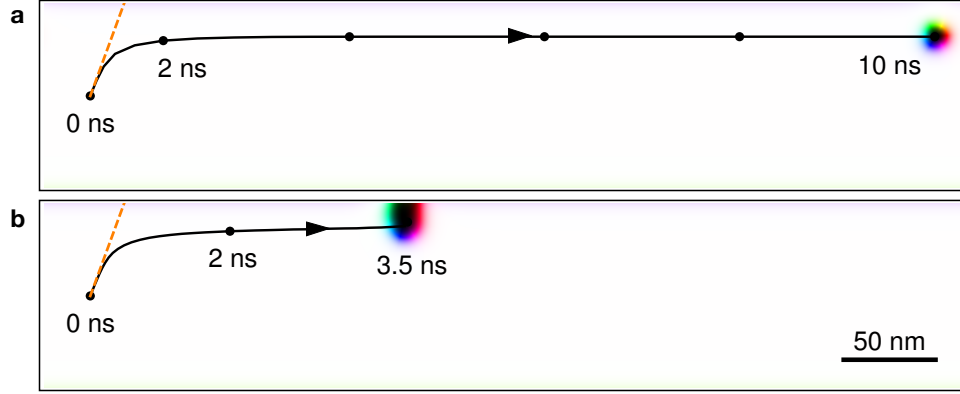


Figure 17: **Current-driven motion of a racetrack skyrmion.** The stabilized Néel skyrmion ( $N_{\text{Sk}} = -1$  and helicity  $\gamma = 0$ ) is driven by the spin-orbit torque in a  $500 \text{ nm} \times 100 \text{ nm}$  Co/Pt racetrack with periodic boundary conditions along the track. A charge current is applied along the  $x$  direction in the HM layer where the spin Hall effects leads to a generation of a spin current that is injected from the perpendicular direction into the simulated FM layer with spins pointing along the  $-y$  direction. Black indicates the skyrmion's trajectory and orange is the expected trajectory from the Thiele equation without considering the skyrmion-edge interaction. In the beginning, the skyrmion moves along this line at an angle of approximately  $70^\circ$  with respect to the charge current direction. **a** The effective current density is  $\Theta_{\text{SH}}j_x = 2.0 \frac{\text{MA}}{\text{cm}^2}$  and the skyrmion creeps along the edge after about 2 ns due to the repulsive skyrmion-edge interaction. **b** The effective current density is increased to  $\Theta_{\text{SH}}j_x = 3.0 \frac{\text{MA}}{\text{cm}^2}$  where the skyrmion annihilates after approximately 3.5 ns. The magnetic texture is visualized as in the previous figures.

The highest possible velocity is therefore

$$v_c = \pm |F_0| \frac{1}{4\pi b} = \pm |F_0| \frac{\gamma e}{4\pi M_s d_z} \quad (3.51)$$

at a critical current density of

$$j_c = \pm |F_0| \frac{1}{4\pi} \frac{D_{xx}\alpha}{BI_{xy}} = \pm |F_0| \frac{D_{xx}\alpha}{4\pi I_{xy}} \frac{2e}{\hbar\Theta_{\text{SH}}}. \quad (3.52)$$

Fig. 17 shows that this behavior is in good agreement with the micromagnetic simulations. The stabilized Néel skyrmion is described by  $N_{\text{Sk}} = -1$ ,  $D_{xx} = 15$  and  $I_{xy} = 60 \text{ nm}$ . This gives a skyrmion Hall angle of  $\theta_{\text{sk}} = 70^\circ$ .

To determine the critical current density and the highest possible velocity,  $U(y)$  has to be determined. The numerically computed value of the critical force is around  $|F_0| = 8 \text{ meV/nm}$ , similar to the case presented in the supplementary material of publication [BG1]. This results in

$$v_c = 62 \frac{\text{m}}{\text{s}}, \quad j_c \Theta_{\text{SH}} = 2.3 \frac{\text{MA}}{\text{cm}^2}. \quad (3.53)$$

In agreement with this consideration, the current density  $j_{\Theta_{\text{SH}}} = 2.0 \text{ MA/cm}^2 < j_c^{\Theta_{\text{SH}}}$  results in a steady motion of the skyrmion along the confinement at a velocity of  $v_x = 53 \text{ m/s}$  [Fig. 17(a)]. In Fig. 17(b) the current density was increased to  $j_{\Theta_{\text{SH}}} = 3.0 \text{ MA/cm}^2$ , which is larger than the critical value. The skyrmion annihilates at the edge after a few ns.

Following from these consideration, the maximum propulsion velocity of a skyrmion driven by SOT is limited by the skyrmion Hall effect. A critical velocity of around  $50 \text{ m/s}$  at a bit spacing of around  $50 \text{ nm}$  gives a maximal operation rate of  $1 \text{ Gbit/s}$ , which is not sufficient for future demands in data accessibility. In reality, the skyrmion Hall effect is even more detrimental: skyrmions will not creep along defect-decorated edges. A skyrmion will annihilate instead and the information in the device is lost. For this reason, a suppression of the skyrmion Hall is essential and several solutions are presented in the cumulative sections of this thesis, namely the utilization of low-symmetric heavy metals in publication [BG1] or the utilization of alternative magnetic quasiparticles with a vanishing topological charge in publications [BG6] and [BG7].

---

## 4 Electronic properties

In the previous section the foundation was set for simulating the current-driven motion of non-collinear spin textures. As was shown at the example of a Néel skyrmion, spin textures with a non-trivial real-space topology will not move parallel to an applied current; a transverse force occurs.

In this section the behavior of the electrons that form the current is analyzed. Upon traversing a non-collinear spin texture, the conduction electrons' spin reorients partially along the spatially-dependent magnetic texture. Therefore, the topological properties of the texture are adapted by the current electrons and manifest themselves as a phase factor in their wave function. In the following, the Berry theory is used to derive the force on the electrons corresponding to such a phase factor and to quantify the corresponding Hall conductivity.

This section is structured as follows. First, the definitions of the Berry phase and the Berry curvature are motivated in Sec. 4.1. These quantities allow to calculate the Hall conductivity of electrons in periodic bulk crystals, as will be presented in Sec. 4.2. In Sec. 4.3 the spin Hall conductivity, the orbital magnetization and the magnetoelectric polarizability are introduced. These quantities are related to the Berry theory in a wider sense and have been calculated in publications [BG3] and [BG9] for skyrmions and in [BG7] for antiferromagnetic skyrmions. To model the electronic properties the tight-binding formalism is used in all cases. It is explained in Sec. 4.4 and demonstrated to be compatible with the Berry theory approach in Sec. 4.5. There, the quantum Hall effect is exemplarily quantified. This sets the foundation for the calculation and discussion of the topological Hall effect of electrons in topologically non-trivial spin textures in publications [BG2], [BG5], [BG8] and [BG9].

### 4.1 Berry theory

In the following, the Berry phase, the Berry connection and the Berry curvature are derived, following Berry's original publication [89]. Besides application of this concept in condensed-matter physics, the Berry theory can be utilized to describe other phenomena like the rotation of the plane of oscillation of Foucault's pendulum in classical mechanics [90]. In quantum mechanical systems, the Berry phase is a phase factor by which a wave function differs before and after traversing a closed loop in parameter space. In this thesis the parameter space is the reciprocal space. As will be shown in Sec. 4.2, the Berry curvature then allows to calculate the transverse conductivity of electrons under application of an external field or in the presence of a skyrmion crystal.

To derive the Berry curvature one considers a Hamiltonian  $H(\mathbf{R})$  that depends on a set of parameters  $\mathbf{R}(t)$ , which are time-dependent. At every point of time  $t$  the stationary Schrödinger equation

$$H(\mathbf{R}(t)) |n(\mathbf{R}(t))\rangle = E_n |n(\mathbf{R}(t))\rangle \quad (4.1)$$

is fulfilled. Here,  $|n(\mathbf{R}(t))\rangle$  is the  $n$ -th eigenstate with eigenenergy  $E_n$ . The time propagation of the wave function  $|\psi(t, \mathbf{R}(t))\rangle$  follows the time-dependent Schrödinger equation

tion

$$H(\mathbf{R}(t)) |\psi(t)\rangle = i\hbar \frac{\partial}{\partial t} |\psi(t)\rangle. \quad (4.2)$$

If the parameters  $\mathbf{R}(t)$  are varied adiabatically along a path in parameter space, a state  $|n(\mathbf{R}(t))\rangle$  cannot change its quantum number  $n$  as long as the eigenenergies are non-degenerate. The wave function then reads

$$|\psi(t, \mathbf{R}(t))\rangle = \exp \left\{ -\frac{i}{\hbar} \int_0^t dt' E_n(\mathbf{R}(t')) \right\} \exp[i\gamma_n(t)] |n(\mathbf{R}(t))\rangle. \quad (4.3)$$

The first exponential function accounts for the time propagation and contains the dynamic phase factor. Additionally, the wave function can accumulate a second phase factor  $\gamma_n(t)$ , which is a geometric phase, later called ‘Berry phase’. To determine this formally introduced phase, the time-dependent Schrödinger equation is solved. One finds

$$\frac{\partial}{\partial t} |\psi(t, \mathbf{R}(t))\rangle = \left( \dot{\mathbf{R}}(t) \nabla_{\mathbf{R}} |n\rangle + i\dot{\gamma}_n(t) |n\rangle - \frac{i}{\hbar} E_n |n\rangle \right) \quad (4.4)$$

$$\times \exp \left\{ -\frac{i}{\hbar} \int_0^t dt' E_n(\mathbf{R}(t')) \right\} \exp[i\gamma_n(t)]. \quad (4.5)$$

Inserting this into the Schrödinger equation (4.2) gives

$$\dot{\gamma}_n(t) |n\rangle = i\dot{\mathbf{R}}(t) \nabla_{\mathbf{R}} |n\rangle \quad (4.6)$$

and after multiplication with  $\langle n|$  from the left

$$\dot{\gamma}_n(t) = i\dot{\mathbf{R}}(t) \langle n | \nabla_{\mathbf{R}} |n\rangle. \quad (4.7)$$

The above equation can be integrated along a closed path in the parameter space to arrive at an expression for the Berry phase

$$\gamma_n = \oint i \langle n | \nabla_{\mathbf{R}} |n\rangle \cdot d\mathbf{R}. \quad (4.8)$$

The integrand of this equation

$$\mathbf{A}_n(\mathbf{R}) = i \langle n | \nabla_{\mathbf{R}} |n\rangle \quad (4.9)$$

is called ‘Berry connection’. It can be identified as a geometric vector potential which is not gauge invariant. The corresponding ‘field’, the Berry curvature

$$\mathbf{\Omega}_n(\mathbf{R}) = i \langle \nabla_{\mathbf{R}} n | \times | \nabla_{\mathbf{R}} n \rangle, \quad (4.10)$$

is the curl of the Berry connection. It is gauge-invariant just like a real magnetic field in conventional electrodynamics.

Alternatively, the Berry curvature can be expressed in terms of eigenstates and eigenenergies. For a three-dimensional order parameter, the above expression is expanded

$$\Omega_n(\mathbf{R}) = i \sum_m \langle \nabla_{\mathbf{R}} n(\mathbf{R}) | m(\mathbf{R}) \rangle \times \langle m(\mathbf{R}) | \nabla_{\mathbf{R}} n(\mathbf{R}) \rangle \quad (4.11)$$

$$= -i \sum_m \langle n(\mathbf{R}) | \nabla_{\mathbf{R}} | m(\mathbf{R}) \rangle \times \langle m(\mathbf{R}) | \nabla_{\mathbf{R}} | n(\mathbf{R}) \rangle. \quad (4.12)$$

Using

$$\langle m(\mathbf{R}) | \nabla_{\mathbf{R}} | n(\mathbf{R}) \rangle = \frac{\langle m(\mathbf{R}) | \nabla_{\mathbf{R}} H | n(\mathbf{R}) \rangle}{E_n(\mathbf{R}) - E_m(\mathbf{R})} \quad (4.13)$$

for  $n \neq m$ , the result is [89]

$$\Omega_n(\mathbf{R}) = i \sum_{m \neq n} \frac{\langle n(\mathbf{R}) | \nabla_{\mathbf{R}} H | m(\mathbf{R}) \rangle \times \langle m(\mathbf{R}) | \nabla_{\mathbf{R}} H | n(\mathbf{R}) \rangle}{[E_n(\mathbf{R}) - E_m(\mathbf{R})]^2}. \quad (4.14)$$

The advantage of this formula is that it is calculated directly from the eigenstates and eigenenergies. The gradient is now applied to the Hamiltonian which in many cases allows for an analytical calculation. This saves computation time when numerically calculating the Berry curvature.

## 4.2 Reciprocal-space Berry curvature and Hall conductivity

### Berry curvature in periodic crystals

In the context of solid-state physics, the Berry curvature is defined in reciprocal space, which accounts for the translational symmetry of a crystalline material. Bloch's theorem [91] tells that the wave function  $\psi_n(\mathbf{k}, \mathbf{r})$  can be expressed as a product

$$\psi_n(\mathbf{k}, \mathbf{r}) = \exp(i\mathbf{k} \cdot \mathbf{r}) u_n(\mathbf{k}, \mathbf{r}), \quad (4.15)$$

where  $u_n(\mathbf{k}, \mathbf{r})$  has the same real-space periodicity as the lattice. To define the Berry curvature with respect to this lattice-periodic part of the wave function, the stationary Schrödinger equation is rewritten as [92, 93]

$$e^{-i\mathbf{k} \cdot \mathbf{r}} H e^{i\mathbf{k} \cdot \mathbf{r}} u_{n,\mathbf{k}}(\mathbf{r}) = E_{n,\mathbf{k}} u_{n,\mathbf{k}}(\mathbf{r}). \quad (4.16)$$

The left side defines a new Hamiltonian

$$\tilde{H}(\mathbf{k}) = e^{-i\mathbf{k} \cdot \mathbf{r}} H e^{i\mathbf{k} \cdot \mathbf{r}} \quad (4.17)$$

that acts on  $u_{n,\mathbf{k}}(\mathbf{r})$ . Note, that the wave vector  $\mathbf{k}$  has deliberately been written as a parameter (from now on  $\mathbf{R} \equiv \mathbf{k}$ ) which is adiabatically changing, in order to determine the Berry phase, connection and curvature.  $\tilde{H}$  is the lattice-periodic Hamiltonian that is later considered in the tight-binding model. The Berry curvature is now defined as [92]

$$\Omega_n(\mathbf{k}) = i \langle \nabla_{\mathbf{k}} u_n | \times | \nabla_{\mathbf{k}} u_n \rangle. \quad (4.18)$$

Like the band dispersion  $E_n(\mathbf{k})$ , the Berry curvature is periodic in reciprocal space and has to be calculated only in the first Brillouin zone. However, it is not solely determined by  $E_n(\mathbf{k})$  but information on the lattice-periodic part of the eigenfunctions  $|u_n\rangle$  is required.

The reason why the Berry curvature accounts for the topological properties of an electron system becomes apparent from the fact that the integral over the Brillouin zone, called ‘Chern number’

$$C_n = \frac{1}{2\pi} \int_{\text{BZ}} \Omega_n^z(\mathbf{k}) d^2k, \quad (4.19)$$

can only have integer values [94] (here written for a two-dimensional system).

The precise role of the Berry curvature and the Chern number for electronic transport will be derived in the following. For now, we settle with the fact that they account for the topological properties of the system and lead to the emergence of priorly unexpected observables. As one example, Thouless *et al.* [94] used the concept of topology to explain why a quantized Hall effect appears for large magnetic fields (will be discussed in detail in Sec. 4.5). For this work he has been awarded the Nobel prize in 2016 together with Haldane and Kosterlitz for their “theoretical discoveries of topological phase transitions and topological phases of matter” (Nobel Foundation). Their works set the foundation for the understanding and discovery of topological materials (like topological insulators [95]), which have been in the eminent focus of research ever since.

### Emergence of a Berry curvature

In order for the Berry curvature or Chern numbers to be non-zero, one can analyze two important symmetries of electronic systems. The Berry curvature is antisymmetric under time-reversal symmetry [75]

$$\Omega_n(\mathbf{k}) = -\Omega_n(-\mathbf{k}) \quad (\text{time-reversal symmetry}) \quad (4.20)$$

and symmetric under inversion symmetry

$$\Omega_n(\mathbf{k}) = \Omega_n(-\mathbf{k}) \quad (\text{inversion symmetry}). \quad (4.21)$$

For this reason, the Berry curvature vanishes if both symmetries are present. Furthermore, physical observables (like the Hall conductivity) are always determined by an integral over an energy contour or energy range. As long as the time-reversal symmetry is conserved, even in the case of broken inversion symmetry,  $E_n(\mathbf{k}) = -E_n(\mathbf{k})$  leads to the cancellation of the Berry curvature contributions from  $\mathbf{k}_0$  and  $-\mathbf{k}_0$ . This means, to have an actual effect, the time-reversal symmetry has to be broken, e. g. by the application of a magnetic field or by accounting for a magnetic texture. Reversely, it is inevitable to account for the Berry curvature-induced effects when describing the electronic behavior of magnetic systems, including skyrmion crystals and other non-collinear spin textures.



### Hall conductivity

In the following, the precise relation between the reciprocal-space Berry curvature and the Hall conductivity is established.

When an electric field  $\mathbf{E}$  is applied to a metal, electrons move because of their charge  $q = -e$ . This leads to the emergence of an electric current density  $\mathbf{j}$ . In the most simple case, the electric field and the current density are parallel but this is not strictly enforced by Ohm's law

$$\mathbf{j} = \underline{\sigma}\mathbf{E}, \quad \mathbf{E} = \underline{\rho}\mathbf{j}. \quad (4.22)$$

Here,  $\underline{\sigma}$  and  $\underline{\rho}$  are inverse tensors: the conductivity and the resistivity, respectively. In the case of broken time-reversal symmetry, e. g. when a magnetic field is applied or a magnetic texture is present, transverse transport-tensor elements can appear.

In 1934 Bloch, Peierls, Jones and Zener derived the semiclassical equations of motion of a Bloch electron wave packet in electromagnetic fields [91, 96, 97]. In 1999 a crucial missing term, the so called 'anomalous velocity', was found, modifying the equations of motion to [98]

$$\dot{\mathbf{r}} = \mathbf{v}_n(\mathbf{k}) - \dot{\mathbf{k}} \times \boldsymbol{\Omega}_n(\mathbf{k}), \quad (4.23)$$

$$\hbar\dot{\mathbf{k}} = q\mathbf{E} + q\dot{\mathbf{r}} \times \mathbf{B}. \quad (4.24)$$

Here,  $\mathbf{v}_n = \hbar^{-1} \frac{\partial E_n(\mathbf{k})}{\partial \mathbf{k}}$  is the group velocity and, by analogy,  $-\dot{\mathbf{k}} \times \boldsymbol{\Omega}_n(\mathbf{k})$  is the anomalous velocity. The second equation accounts for the Lorentz force: the wave vector  $\mathbf{k}$  changes under application of an electric field  $\mathbf{E}$  and magnetic field  $\mathbf{B}$ . Due to the similarity of the two equations, the Berry curvature  $\boldsymbol{\Omega}_n(\mathbf{k})$  can be considered a 'reciprocal magnetic field'. This implies a transverse deflection of electrons even in the absence of a magnetic field: In this case  $\dot{\mathbf{k}} \parallel \mathbf{E}$  point along the Hall bar. In a two-dimensional system the Berry curvature is always oriented perpendicular to the plane, therefore inducing an anomalous velocity pointing along the transverse direction. This formally explains why the anomalous Hall effect and the topological Hall effect can occur without the application of a magnetic field.

The precise relation of the conductivity and Berry curvature can for example be derived utilizing the Boltzmann equation, as is presented in Appendix A. The result of this derivation for a two-dimensional system is

$$\sigma_{xx} = -e^2 \frac{1}{2\pi} \sum_n \int_{\text{BZ}} v_{n,x}(\mathbf{k})^2 \tau_n(\mathbf{k}) \left. \frac{\partial f}{\partial E} \right|_{E=E_n(\mathbf{k})} d^2k, \quad (4.25)$$

$$\sigma_{xy} = -\frac{e^2}{h} \frac{1}{2\pi} \sum_n \int_{\text{BZ}} \Omega_n^z(\mathbf{k}) f(E_n(\mathbf{k}) - E_F) d^2k. \quad (4.26)$$

Here,  $f$  is the equilibrium Fermi-distribution function, and  $\tau_n(\mathbf{k})$  is the relaxation time, which arises due to extrinsic effects. For this reason, only the transverse element is purely intrinsic. Using Eq. (4.14) it can be rewritten as

$$\sigma_{xy}(E_F) = -\frac{e^2}{h} \frac{1}{2\pi} 2 \operatorname{Im} \sum_{m \neq n} \int \frac{\langle n | \partial_{k_x} H | m \rangle \langle m | \partial_{k_y} H | n \rangle}{(E_n - E_m)^2} f(E_n(\mathbf{k}) - E_F) d^2k. \quad (4.27)$$

For  $T = 0$  the transverse conductivity is only affected by states below the Fermi energy  $E_F$

$$\sigma_{xy}(E_F) = -\frac{e^2}{h} \frac{1}{2\pi} \sum_n \int_{E_n(\mathbf{k}) \leq E_F} \Omega_n^z(\mathbf{k}) d^2k. \quad (4.28)$$

If the Fermi energy is situated in a band gap, the Hall conductivity is given by the sum over the Chern numbers  $C_n$  of all occupied (occ) bands

$$\sigma_{xy} = -\frac{e^2}{h} \sum_n^{\text{occ}} C_n, \quad C_n = \frac{1}{2\pi} \int_{\text{BZ}} \Omega_n^z(\mathbf{k}) d^2k. \quad (4.29)$$

Since  $C_n$  can only have integer values, non-trivial Chern numbers lead to quantized transport. As shown by Hatsugai [99,100], the origin is the occurrence of topologically protected edge states, which make the system conducting at the edges (and generate a non-zero  $\sigma_{xy}$ ), while the bulk remains insulating. The quantitative difference of left- ( $w_n^l$ ) and right-propagating ( $w_n^r$ ) edge states in the gap above band  $n$  is given by the winding number  $w_n$

$$w_n^l - w_n^r = w_n \equiv \sum_{m \leq n} C_m. \quad (4.30)$$

This relation allows to deduce boundary properties purely from bulk information and is therefore called ‘bulk-boundary correspondence’. A material which exhibits these edge states is labeled ‘Chern insulator’.

## Conclusion

Summarizing this section, a mathematical description for the Hall conductivity was established [Eq. (4.27)] and the implications for Chern insulators have been discussed. The presented method utilizes the Berry curvature that accounts for the topological properties in a periodic system. It allows to describe conventional crystalline matter under application of an external magnetic field (as will be discussed in Sec. 4.5), and in the presence of periodic magnetic textures (as in the case of skyrmion crystals in publications [BG2], [BG8] and [BG9], bimeron crystals in publication [BG5], and antiferromagnetic skyrmion crystals in publication [BG7]).

To quantify an emerging current for non-periodic magnetic textures (e.g. an individual skyrmion in a racetrack device), other methods have to be considered, that are not directly related to a Berry phase or curvature. In publication [BG6] the Landauer-Büttiker approach will be used to calculate the topological Hall effect of individual skyrmioniums in a racetrack device. The method is introduced in the corresponding section 6.3 and is further explained in Appendix B.

### 4.3 Spin Hall conductivity, orbital magnetization, and magnetoelectric effect

In the previous sections the mathematical foundation for the simulation of the current-driven motion of non-collinear spin textures (goals 1 and 4 from the introduction) and for the quantification of the topological Hall effect of electrons in these textures (goals 2 and 4) has been established. This section introduces three more observables which allow to substantiate new hallmarks of the skyrmion crystal phase (goal 3) and other non-collinear spin textures (goal 4). All of the here introduced quantities ‘spin conductivity’, ‘magnetoelectric polarizability’, and ‘orbital magnetization’ can be considered wide topics by themselves. I limit the following discussion to the essential ideas and present how I have implemented the computation of these quantities in a computer code.

Similar to the derivation of the charge conductivity, one can derive expressions for other observables in Kubo theory. Relevant for this thesis are the spin conductivity (as considered for a skyrmion crystal in publication [BG9] and for an antiferromagnetic skyrmion crystal in publication [BG7]) and the magnetoelectric polarizability (as discussed for different types of skyrmion crystals in publication [BG3]). Both quantities are not determined by the reciprocal-space Berry curvature, but a spin Berry curvature and a mixed Berry curvature (defined in magnetization and in reciprocal space), respectively. Furthermore, the orbital magnetization is introduced (as calculated in publication [BG3] for skyrmion and antiskyrmion crystals). It is partially related to the reciprocal-space Berry curvature but cannot be formulated by analogy with the three observables mentioned above.

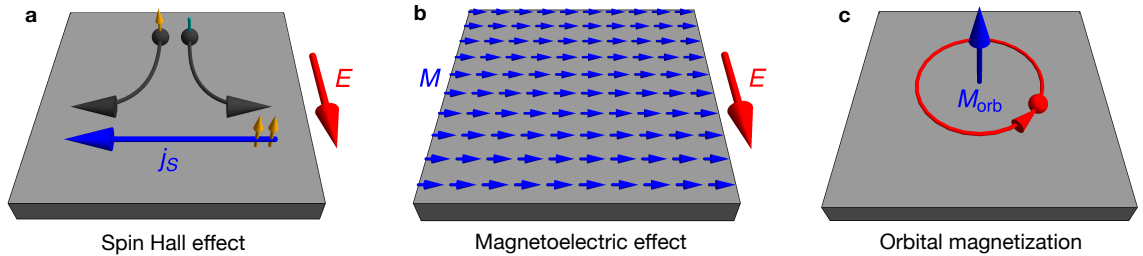


Figure 18: **Alternative hallmarks of skyrmionic phases.** **a** The transverse spin conductivity quantifies the spin Hall effect where two spin-polarized charge currents compensate each other with respect to the charge (gray) but add up in spin (yellow and green). A pure spin current (blue) emerges along the transverse direction. **b** The magnetoelectric polarizability quantifies the magnetoelectric effect. As one consequence it leads to the emergence of a magnetization (blue) if an electric field (red) is applied. Here, a transverse magnetoelectric effect is depicted as occurring in spin textures with a finite toroidal moment. **c** The orbital magnetization arises due to the circulation of electrons (red). An orbital contribution to the magnetization (blue) arises additionally to the spin moment of the material. It is oriented perpendicularly to the circulation plane.

### Spin conductivity

The intrinsic part of the spin conductivity can be defined straightforwardly [101] by analogy with the charge conductivity [Eq. (4.27)]

$$\sigma_{\alpha\beta}^{\gamma}(E) = -2 \operatorname{Im} \frac{e}{2} \frac{1}{(2\pi)^2} \sum_{m \neq n} \int \frac{\langle n | \partial_{k_{\alpha}} H | m \rangle \langle m | \frac{1}{2} \{ \partial_{k_{\beta}} H, \sigma_{\gamma} \} | n \rangle}{(E_n - E_m)^2} f(E_n(\mathbf{k}) - E) d^2k, \quad (4.31)$$

where  $\sigma_{\gamma}$  is the generalized  $\gamma$  Pauli matrix and  $\{ \cdot, \cdot \}$  is the anti-commutator. Here, one velocity operator has been exchanged with the spin-current operator and the quantum of spin conductivity in two dimensions is not  $e^2/h$  but  $(e^2/h)(\hbar/2e) = e/4\pi$ .

In some sense, the integrand can be considered a ‘spin Berry curvature’ but in this case it is a  $3 \times 3 \times 3$  tensor that cannot be reduced to a three component vector as was the case for the reciprocal-space Berry curvature. The reason is that the  $\sigma_{\alpha\beta}^{\gamma}$  element is not necessarily the sign reversed of the  $\sigma_{\beta\alpha}^{\gamma}$  element. Also, longitudinal elements  $\sigma_{\alpha\alpha}^{\gamma}$  are well defined, which implies that an intrinsic contribution to the longitudinal spin conductivity exists.

The transverse element  $\sigma_{xy}^{\gamma}$  characterizes the spin Hall effect [82–84]. As an example, in non-magnetic materials with spin-orbit coupling, spins of opposite orientations are deflected into opposite directions leading to the cancellation of the charge current and the emergence of a pure spin current [Fig. 18(a)]. Such a spin Hall effect can have multiple origins (side jump, skew scattering and intrinsic geometrical reasons [102]). As will be shown, non-collinear spin textures can lead to the emergence of a pure spin Hall effect as well.

In the cumulative part of this thesis (Sec. 5.2 and 6.4) a local spin conductivity is used to calculate the spin Hall effect of electrons in non-collinear spin textures. Here, instead of the  $\gamma$  axis for the spin (commonly  $z$  is considered), the local magnetic moment’s orientation is used at each lattice site.

### Magnetoelectric polarizability

The magnetoelectric polarizability (in two dimensions)

$$\alpha_{ij}(E_F) = g\mu_b \frac{e}{2\pi} \sum_{n \text{ occ}} \int D_n^{(ij)}(\mathbf{k}) d^2k \quad (4.32)$$

quantifies the magnetoelectric effect

$$\alpha_{ij} = \frac{\partial P_i}{\partial B_j} = \frac{\partial M_j}{\partial E_i}. \quad (4.33)$$

As was first described in 1888 [103], the effect implies that a magnetic field induces a polarization and, as Onsager reciprocal effect, that an electric field induces a magnetization

[Fig. 18(b)]. The integrand

$$D_n^{(ij)}(\mathbf{k}) = -2 \operatorname{Im} \sum_{l \neq n} \frac{\langle n | \partial_{k_i} H | l \rangle \langle l | \sigma_j | m \rangle}{(E_n - E_l)^2} \quad (4.34)$$

can be labeled a ‘mixed Berry curvature’, since it is defined in reciprocal and real space (note that the magnetic field is defined in real space and that  $\partial_B H \propto \sigma$ ).

The derivation of Eq. (4.32) is based on the so called ‘modern formulation’ of the polarization [104, 105]. This polarization changes by [106]

$$\Delta P_i = e \sum_n \int_{\text{occ}} \frac{1}{(2\pi)^d} \operatorname{Im} \langle \partial_{k_i} u | \partial_{B_j} u \rangle \, dk \, dB_j \quad (4.35)$$

upon variation of the  $j$  component of  $\mathbf{B}$ . A formal motivation for the emergence of this effect can be established by expanding the free energy with respect to the electric and magnetic fields  $\mathbf{E}$  and  $\mathbf{B}$  [107]

$$F(\mathbf{E}, \mathbf{B}) = F_0 - P_i^S E_i - M_i^S B_i - \frac{1}{2} \epsilon_0 \epsilon_{ij} E_i E_j - \frac{1}{2} \mu_0 \mu_{ij} B_i B_j - \alpha_{ij} E_i B_j - \dots \quad (4.36)$$

Differentiation gives

$$P_i(\mathbf{E}, \mathbf{B}) = -\frac{\partial F}{\partial E_i} = P_i^S + \epsilon_0 \epsilon_{ij} E_j + \alpha_{ij} B_j, \quad (4.37)$$

$$M_i(\mathbf{E}, \mathbf{B}) = -\frac{\partial F}{\partial B_i} = M_i^S + \mu_0 \mu_{ij} H_j + \alpha_{ji} E_j. \quad (4.38)$$

Up to quadratic order the polarization  $\mathbf{P}$  (magnetization  $\mathbf{M}$ ) is determined by the spontaneous polarization  $\mathbf{P}^S$  (spontaneous magnetization  $\mathbf{M}^S$ ), the electric susceptibility  $\underline{\epsilon}$  (magnetic susceptibility  $\underline{\mu}$ ) and the magnetoelectric polarizability  $\underline{\alpha}$ . The latter quantifies the aforementioned magnetoelectric effect.

The linear magnetoelectric effect can only arise if the spatial inversion symmetry and the time-reversal symmetry are simultaneously broken [33]. Therefore, it can occur for inversion symmetric lattices in case the magnetic texture breaks this particular symmetry. Possible textures are characterized by the pseudoscalar  $a$ , the toroidal moment  $\mathbf{t}$  and the quadrupole magnetic moment  $q$  [33]

$$a = \frac{g\mu_B}{3} \sum_n \mathbf{r}_n \cdot \mathbf{s}_n, \quad (4.39)$$

$$\mathbf{t} = \frac{g\mu_B}{2} \sum_n \mathbf{r}_n \times \mathbf{s}_n, \quad (4.40)$$

$$q_{ij} = \frac{g\mu_B}{2} \sum_n \left( r_{ni} s_{nj} + r_{nj} s_{ni} - \frac{2}{3} \delta_{ij} \mathbf{r}_n \cdot \mathbf{s}_n \right). \quad (4.41)$$

These quantities allow to express the term of the free energy that corresponds to the magnetoelectric effect as [108]

$$F_{\text{me}} = -a(\mathbf{E} \cdot \mathbf{B}) - \mathbf{t} \cdot (\mathbf{E} \times \mathbf{B}) - q_{ij}(E_i B_j + E_j B_i). \quad (4.42)$$

By symmetry this means that

$$\mathbf{P} = -\mathbf{t} \times \mathbf{B}, \quad \mathbf{M} = \mathbf{t} \times \mathbf{E}. \quad (4.43)$$

In other words, the transverse tensor element of the magnetoelectric polarizability is proportional to the toroidal moment of the magnetic texture. This moment changes its sign under time reversal and under space inversion and is defined in the above given manner where the sum runs over all basis atoms;  $\mathbf{r}_i$  is defined with respect to the inversion center of the lattice.

As was explained in Sec. 2.2, the toroidal moment of a skyrmion is proportional to the sine of its helicity. This was one motivation for publication [BG3] in which the magnetoelectric effect was investigated for different types of skyrmion crystals and new hallmarks of the skyrmion crystal phase were established.

### Orbital magnetization

A quantity that cannot be related purely to a Berry curvature is the orbital magnetization [109]

$$\begin{aligned} M_z(E_F) &= \frac{1}{(2\pi)^2} \int_{\text{occ}} m_n^{(z)}(\mathbf{k}) \, d^2k \\ &+ \frac{e}{\hbar} \frac{1}{(2\pi)^2} \int_{\text{occ}} \frac{\Omega_n^{(xy)}(\mathbf{k}) - \Omega_n^{(yx)}(\mathbf{k})}{2} [E_F - E_n(\mathbf{k})] \, d^2k. \end{aligned} \quad (4.44)$$

The measured magnetization is not purely given by the spin moments but also has an orbital component, even though small in most materials. When a wave packet rotates, it generates a magnetic moment which is measured as a magnetization component perpendicular to the circulation plane [Fig. 18(c)]. The first term of this orbital magnetization contains the orbital magnetic moment [110, 111]

$$\mathbf{m}_n(\mathbf{k}) = -\frac{e}{2\hbar} \text{Im} \sum_{l \neq n} \frac{\langle n | \nabla_{\mathbf{k}} H | l \rangle \times \langle l | \nabla_{\mathbf{k}} H | n \rangle}{E_n(\mathbf{k}) - E_l(\mathbf{k})}, \quad (4.45)$$

capturing the intrinsic contributions of the Bloch electrons. The second term is determined by the Berry curvature of all occupied bands; it accounts for the change of the phase-space volume, as presented in Ref. [109].

The orbital magnetization fulfills the relation

$$\frac{\partial}{\partial E_F} M_z(E_F) = \frac{1}{2e} [\sigma_{yx}(E_F) - \sigma_{xy}(E_F)] = -\frac{1}{e} \sigma_{xy}(E_F), \quad (4.46)$$

which means that the orbital magnetization changes linearly with the Fermi energy in the band gap of a Chern insulator.

In publication [BG3] the orbital magnetization has been calculated for skyrmion and antiskyrmion crystals. In a semiclassical picture, electrons are circulating around the corresponding emergent field of the texture. This brings about a topologically-induced contribution to the orbital magnetization [112, 113].

#### 4.4 Tight-binding model

One main goal of this thesis is the explanation of the topological Hall effect of electrons in skyrmion crystals which goes beyond relating the measured signal to the real-space skyrmion density as presented in the experimental section 2.4. For this reason, a model is needed that allows to access the electronic eigenstates. As derived in the previous section, the latter are essential for utilizing the Berry theory. Since the here considered magnetic quasiparticles are large compared to the lattice spacing, a sizable number of atoms has to be considered. This makes an *ab initio* approach very demanding; the method of choice is the tight-binding formalism, which is introduced in the following.

In contrast to an *ab initio* approach, a tight-binding model contains (physical) parameters. This essentially allows to disregard selected contributions to physical effects and therefore to isolate individual contributions. Here for example, the spin-orbit coupling is deliberately neglected in all calculations to isolate the topological contribution to the Hall effect of electrons in non-collinear spin textures. This makes the tight-binding method a useful tool for understanding the fundamentals of physical effects.

#### Derivation of the tight-binding Hamiltonian

The goal of the tight-binding method is to solve the stationary Schrödinger equation

$$H |\psi_{n,k}\rangle = E_{n,k} |\psi_{n,k}\rangle \quad (4.47)$$

for eigenenergies  $E_{n,k}$  and eigenfunctions  $|\psi_{n,k}\rangle$  in a simplified way. The idea is to express the wave function as a linear combination of orbitals [114–116]

$$\psi_{n,k} = \frac{1}{\sqrt{N}} \sum_{\alpha} \sum_{\mathbf{R}_i} c_{n,\alpha}(\mathbf{k}) e^{i\mathbf{k} \cdot (\mathbf{R}_i + \mathbf{t}_l)} \phi_{o,\sigma}(\mathbf{r} - \mathbf{R}_i - \mathbf{t}_l). \quad (4.48)$$

Here, the coefficients  $c_{n,\alpha}(\mathbf{k})$  have a band index  $n$  and an index  $\alpha$  comprising the indices for the basis atom  $l$ , the spin  $\sigma$ , and the orbital  $o$ . They are normalized to  $\sum |c_{n,\alpha}(\mathbf{k})|^2 = 1$ . This approach satisfies the Bloch theorem and it is assumed that the wave functions  $\phi_{o,\sigma}$  at the atom positions  $\mathbf{R}_i + \mathbf{t}_l$  are orthogonal (this can be achieved by a transformation of the initial orbitals [117]).

When the linearly combined wave function is used to solve the Schrödinger equation, the eigenenergy reads

$$\begin{aligned} E_{n,k} &= \langle \psi_{n,k} | H | \psi_{n,k} \rangle = \frac{1}{N} \sum_{\alpha,\beta} \sum_{\mathbf{R}_i, \mathbf{R}_j} c_{n,\alpha}^*(\mathbf{k}) c_{n,\beta}(\mathbf{k}) \\ &\quad \times e^{i\mathbf{k} \cdot (\mathbf{R}_i + \mathbf{t}_l - \mathbf{R}_j - \mathbf{t}_m)} \langle \phi_{o',\sigma'}(\mathbf{r} - \mathbf{R}_j - \mathbf{t}_m) | H | \phi_{o,\sigma}(\mathbf{r} - \mathbf{R}_i - \mathbf{t}_l) \rangle. \end{aligned} \quad (4.49)$$

Due to the lattice periodicity, any reference point can be chosen, e. g.  $\mathbf{R}_i = 0$ , giving  $N$  identical terms

$$E_{n,k} = \sum_{\alpha,\beta} c_{n,\alpha}^*(\mathbf{k}) c_{n,\beta}(\mathbf{k}) \underbrace{\sum_{\mathbf{R}_j} e^{-i\mathbf{k} \cdot \Delta_{jm}} \langle \phi_{o',\sigma'}(\mathbf{r} - \mathbf{R}_j - \mathbf{t}_m) | H | \phi_{o,\sigma}(\mathbf{r} - \mathbf{t}_l) \rangle}_{:= H_{\alpha,\beta}}(\mathbf{k}), \quad (4.50)$$

where  $\Delta_{jlm} = \mathbf{R}_j + \mathbf{t}_m - \mathbf{t}_l$  is the distance between two atoms: one in located in the reference cell  $\mathbf{R}_i = 0$  at  $\mathbf{t}_l$ , the other in the cell with lattice vector  $\mathbf{R}_j$  at  $\mathbf{t}_m$ . In the last equation the tight-binding Hamilton matrix  $\underline{H}$  has been introduced with elements  $H_{\alpha,\beta}$ . The Schrödinger equation has been reduced to an algebraic matrix equation

$$\underline{H} c_n(\mathbf{k}) = E_n(\mathbf{k}) c_n(\mathbf{k}). \quad (4.51)$$

### Computational details

The integrals  $\langle \phi_{\sigma',\sigma'}(\mathbf{r} - \mathbf{R}_j - \mathbf{t}_m) | H | \phi_{\sigma,\sigma}(\mathbf{r} - \mathbf{t}_l) \rangle$  can in principle be calculated from the considered orbital wave functions. However, often it is more convenient to use them as parameters which can for example be optimized by fitting the tight-binding band structure to an experimentally determined band structure (as has been done in publication [BG10] using ARPES data of a SrTiO<sub>3</sub> two-dimensional electron gas) or to an ab initio calculation. As a valid simplification, one can consider a two-center approximation neglecting integrals for which the potential of the Hamilton operator is localized on none of the two atomic positions. The calculated elements are called ‘on-site energies’ and ‘hopping amplitudes’ characterizing the interaction of orbitals from the same site or different sites, respectively.

Additionally to these terms, different effects can be considered in the tight-binding matrix. In this thesis, the aim is to make general statements on the topological Hall effect. For this reason, only the nearest-neighbor hopping of *s* orbitals and a coupling of the electrons’ spin to a magnetic texture are considered. This is the most simple setup for describing the topological Hall effect in a tight-binding model. The hopping terms reduce to expressions of the shape  $t e^{ik \cdot \Delta}$  and the Hund’s coupling (similar to a Zeeman term) at atom *i* reads  $m \boldsymbol{\sigma} \cdot \mathbf{s}_i$ , with  $\boldsymbol{\sigma}$  the vector of Pauli matrices. The ratio of  $m/t$  determines which of the two terms is dominating.

After defining the tight-binding matrix, it is diagonalized numerically to obtain the eigenenergies and the eigenfunctions via the eigenvectors  $c_{n,k}$  that consist of the coefficients  $c_{n,\alpha}(\mathbf{k})$ . These can be used to calculate the Berry curvature and the Hall conductivity, as in Eq. (4.27). As explained earlier, an advantage of this expression is that the terms  $\nabla_{k_i} H$  can be calculated analytically in advance. The corresponding speed-up in computation time is well needed: Even after utilizing this advantage, the calculation of an energy-resolved conductivity curve can take several days even on the CPU cluster of our department. The reason is the large unit cell of more than 100 atoms when considering a non-collinear spin texture.

Before closing this section, one remark appears adequate. For the definition of the hopping, two conventions can be found in the literature (cf. comparison in the program documentation of the code PythTB [118]). The convention which is presented above considers the actual distance between two atoms  $\Delta$ . Alternatively, only  $\mathbf{R}_j$ , the corresponding lattice vector (without the basis vector), can be considered for determining the phase of the hopping. This alternative convention gives the correct band structure and Hall conductivity and is therefore used in many publications. However, the *k*-space distribution of the Berry curvature is unphysical [119]. More adversely, the magnetoelectric properties in this convention are not gauge invariant, thus incorrect [118]. This comes from the fact that this convention effectively uses the full wave function for calculating



the Berry curvature instead of only the lattice periodic part. For this reason, in the here presented publications the basis vectors have always been incorporated in the hopping phases as presented above.

#### 4.5 Example: Quantum Hall effect

At this point of this thesis the used methods for the theoretical description of the emergent electrodynamics of non-collinear spin textures have been introduced and explained. As before, I conclude with one extended example which illustrates the presented theoretical method. The example of choice is the quantum Hall effect in a two-dimensional free electron gas and in graphene. It is quantified by the Berry theory approach, whose understanding is especially essential for the publications on the topological Hall effect in non-collinear spin textures ([BG2], [BG3], [BG5], [BG7], [BG8] and [BG9]) in sections 5 and 6.

The starting point of the following discussion is the conventional Hall effect [120]. This phenomenon of an occurring charge current transverse to an applied electric field under the presence of a perpendicular magnetic field can be fully described by a semi-classical approach. Once the transition is made to a two-dimensional sample, low temperatures, and high magnetic field strengths, the quantized version of the Hall effect arises. This effect can still be understood by semi-classical considerations but the essential results are nicely reproduced using the Berry theory. As a third step, graphene is investigated, for which the electrons do not behave freely. Here, the Berry theory approach can show its strengths as it allows for a straightforward calculation of the unconventional quantization of the Hall effect, which has been measured experimentally [121].

##### Conventional Hall effect

In 1879 Hall detected a voltage across a metal in perpendicular direction to an applied electric current [120]. He applied a magnetic field  $B_z$  perpendicular to this so called 'Hall bar'. In a semiclassical picture of free electrons propagating along the Hall bar, the charge carriers are deflected into the transverse direction by the Lorentz force. This leads to a charge accumulation and a counteracting electrostatic force. In equilibrium the forces compensate each other,

$$q(\mathbf{v} \times \mathbf{B}) = -q\mathbf{E}, \quad (4.52)$$

$$v_x B_z = E_y. \quad (4.53)$$

Expressing the electric field in term of a voltage  $V_H$  and the sample width  $w$ , and the longitudinal velocity in terms of the applied current density  $j$  and the carrier density  $n$

$$E_y = V_H/w, \quad j_x = n v_x q, \quad (4.54)$$

the Hall voltage can be written as

$$V_H = \frac{w B_z j_x}{n q}. \quad (4.55)$$

In terms of the resistivity [Eq. (4.22)] the Hall coefficient is normalized by the magnetic field

$$R_H = \frac{\rho_{xy}}{B_z} = \frac{1}{B_z} \frac{E_y}{j_x}. \quad (4.56)$$

This leads to

$$\rho_{xy} = R_H B_z, \quad R_H = \frac{1}{nq}. \quad (4.57)$$

The above equation implies that the Hall resistivity is proportional to the out-of-plane magnetic field and depends on electronic properties, namely the carrier density and charge; the equation holds also for holes with  $q = +e$ .

### Quantum Hall effect of free electrons

In order to calculate the Hall conductivity by means of the Berry theory in reciprocal space, first the Hamiltonian with an applied magnetic field has to be determined. The field  $\mathbf{B} = B \mathbf{e}_z$  can be described by a vector potential  $\mathbf{A} = Bx \mathbf{e}_y$  (Landau gauge), fulfilling  $\mathbf{B} = \nabla \times \mathbf{A}$ .

For free electrons with a zero-field band structure of  $E(\mathbf{k}) = \hbar^2 k^2 / (2m)$  [cf. Fig. 19(a)], the Hamiltonian reads then [122]

$$H = \frac{1}{2m} [p_x^2 + (p_y - qBx)^2], \quad (4.58)$$

whose Eigenvalues [122] [cf. Fig. 19(b)]

$$E_n = \hbar\omega \left(n + \frac{1}{2}\right), \quad n = 0, 1, 2, \dots \quad (4.59)$$

can be determined in second quantization by analogy with the harmonic oscillator: The canonical momentum  $\boldsymbol{\pi} = \mathbf{p} - q\mathbf{A}$  defines the creation and annihilation operators  $a^\dagger = \frac{R}{\sqrt{2\hbar}}(\pi_x - i\pi_y)$ ,  $a = \frac{R}{\sqrt{2\hbar}}(\pi_x + i\pi_y)$ , respectively. Here,  $\omega = qB/m$  is the cyclotron frequency and  $R = \sqrt{\hbar/qB}$  is the Larmor radius. The bands have no dispersion, implying that at zero temperature the sample becomes insulating for practically every Fermi energy. As was presented in Sec. 4.2, edge currents can occur anyway.

In a simplified picture one can introduce the edge of the sample (or more precisely the air or vacuum) as an infinitely large scalar potential, which has to be added to the Hamiltonian (4.58). This leads to a strong deformation of the energy levels near the sample's edges: The energy of every level continuously increases up to infinity. For this reason, every level below the Fermi energy cuts this particular energy close to the edge, making the sample conducting. Each energy level below the Fermi energy delivers one conduction channel.

This 'rough' version of a bulk-boundary correspondence can be expressed in terms of the reciprocal-space Berry curvatures defining integer Chern numbers. Since free electrons have been considered, there is no  $k$ -dependence in the equidistant energy spectrum [Fig. 19(b)]. As has been shown in my master thesis [75], the reciprocal-space

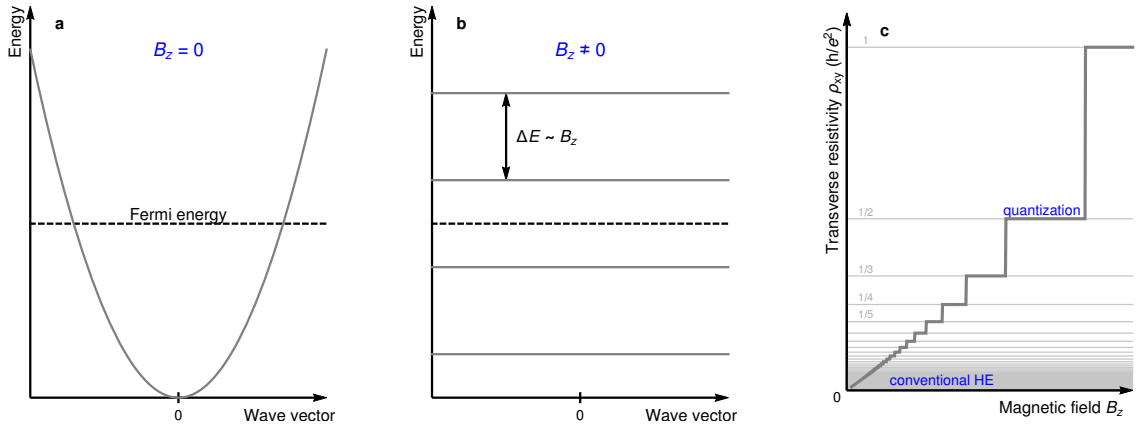


Figure 19: **Quantized Hall effect for free electrons in a two-dimensional sample.** **a** Free-electron parabola (along all wave vector directions) for  $B_z = 0$ . **b** Formed Landau levels when  $B_z$  is applied. **c** Magnetic-field dependence of the transverse resistivity  $\rho_{xy}$  for a fixed location of the Fermi energy. For large fields the signal is quantized at values of  $\frac{1}{n} \frac{h}{e^2}$ , with  $n = 1, 2, 3, \dots$ . For small fields this quantization is hard to resolve and the quantized Hall effect transitions into the conventional Hall effect. All figures show schematic representations at zero temperature. Arbitrary units have been used if not indicated otherwise.

Berry curvature  $\Omega_n^z(\mathbf{k})$  is homogeneous for every band, giving them indeed non-zero Chern numbers of

$$C_n = 1 \quad (4.60)$$

for a positive magnetic field. The Chern number of one imposes that every band below the Fermi energy contributes with one conductance quantum of  $e^2/h$  to  $\sigma_{xy}$  making the insulating bulk sample conducting at the edge, i. e., a Chern insulator.

In the considered system the transverse conductivity is given by

$$\sigma_{xy} = -\frac{e^2}{h} \sum_n^{\text{occ.}} C_n = -l \frac{e^2}{h}, \quad (4.61)$$

where  $l$  is the number of occupied bands. The negative sign is in agreement with semi-classical considerations of the conventional Hall effect: if a magnetic field is applied along the  $+z$  direction and an electron initially moves along the  $-y$  direction due to an applied field along  $+y$ , it will be deflected along the  $+x$  direction, i. e., there is an electric current flowing along the  $-x$  direction.

As follows from this consideration, free electrons in a two-dimensional system at zero temperature always exhibit a quantized Hall effect. For small fields however, the energy levels are denser in energy ( $\Delta E = \hbar\omega \propto B$ ), therefore the transverse conductivity appears to be continuous even at low temperatures. The quantized Hall effect approaches the ordinary Hall effect. Assuming a continuum of bands for small  $B$ , the number of bands below the Fermi energy (and therefore also  $\sigma_{xy}$ ) is proportional to  $1/B$ . Since in a band

gap the longitudinal conductivity vanishes, the transverse resistivity is given by

$$\rho_{xy} = -\sigma_{xy}^{-1} \propto B, \quad (4.62)$$

in agreement with the semiclassical consideration of the conventional Hall effect [cf. Eq. (4.57)]. The transition to the quantum Hall effect has been observed first in 1980 by Klaus von Klitzing [123] (Nobel prize in 1985). In the experiments  $\rho_{xy}$  increases linearly with  $B_z$  for small fields until quantized plateaus at values of  $\frac{1}{n} \frac{h}{e^2}$ , with  $n = 1, 2, 3, \dots$  are visible at higher fields, as also follows from the above calculations [cf. Fig. 19(c)].

Summarizing at this point, it has been presented that for free electrons a parabolic band dispersion condenses to equidistant Landau levels when a magnetic field is applied along the normal of the two-dimensional system [cf. Fig. 19(a) and (b)]. Those bands carry a Chern number of 1. Therefore, they contribute with one quantum of  $e^2/h$  (or  $2 \cdot e^2/h$  for spin-degenerate bands) to the transverse conductivity. The origin of the quantized Hall effect are topologically protected edge channels and the quantized Hall effect transitions into the conventional Hall effect for small fields and large temperatures [cf. Fig. 19(c)].

### Quantum Hall effect in graphene

Many innately two-dimensional systems exhibit different energy-dependent Hall signals compared to what has just been discussed. Essentially, electrons in real crystals cannot be considered as free electrons since the effective mass changes magnitude and even sign throughout the band structure. One of such examples is graphene, which is constituted by C atoms that form a two-dimensional honeycomb lattice [124] [Fig. 20(a)]. The consideration below is oriented at Ref. [BG8].

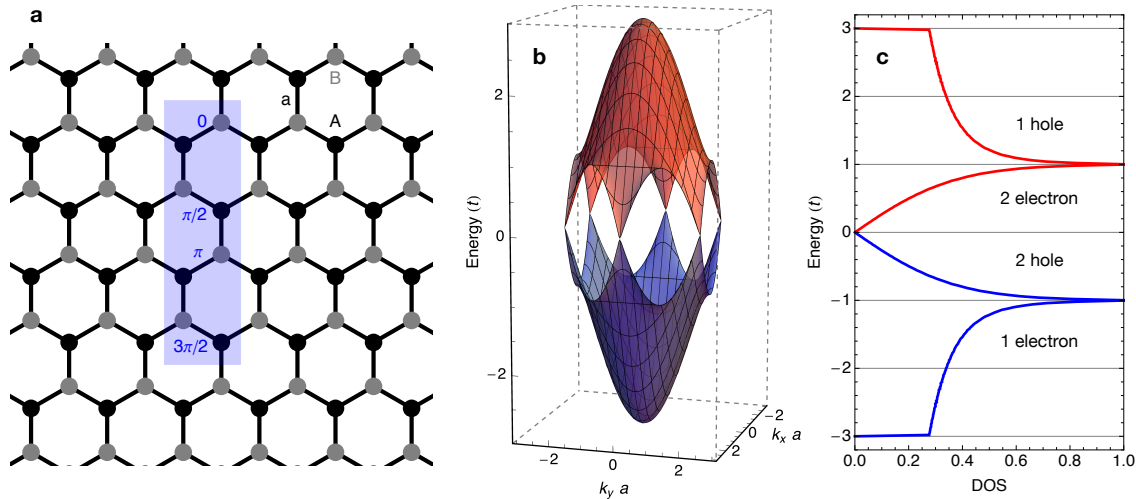


Figure 20: **Graphene.** **a** Lattice with two equivalent basis atoms A and B. If a magnetic field is considered, the theoretically relevant unit cell becomes enlarged (blue). For the hopping paths within this magnetic unit cell the phase factors are indicated. **b** Band structure in the hexagonal Brillouin zone without magnetic field. **c** Density of states for the band structure from (b). The electronic character is indicated. This figure is partially adapted from Ref. [BG8].

**Zero-field band structure.** The band structure near the Fermi level is given by two bands which intersect (neglecting a small spin-orbit gap) in the shape of a Dirac cone (linear band dispersion) [Fig. 20(b)]. These bands have  $p_z$  character, and since they hybridize equally along all directions in the plane, a tight-binding description requires only a single hopping amplitude  $t$ . Diagonalization of

$$H = t \begin{pmatrix} 0 & e^{iak_y} + e^{-ia(\frac{\sqrt{3}}{2}k_x + \frac{1}{2}k_y)} + e^{-ia(-\frac{\sqrt{3}}{2}k_x + \frac{1}{2}k_y)} \\ e^{-iak_y} + e^{ia(\frac{\sqrt{3}}{2}k_x + \frac{1}{2}k_y)} + e^{ia(-\frac{\sqrt{3}}{2}k_x + \frac{1}{2}k_y)} & 0 \end{pmatrix} \quad (4.63)$$

gives the band structure in Fig. 20(b) with the corresponding density of states in Fig. 20(c). The Fermi energy is located at  $E_F = 0$ . The tight-binding matrix  $H$  has been constructed from the nearest-neighbor-hopping terms. Each of the two atoms in the unit cell has three nearest neighbors of the other kind of basis atom. Their distance is  $a$ . Due to particle-hole symmetry of the Hamiltonian the band structure is symmetric with respect to the Fermi energy  $E_F = 0$ .

The lower band is close to a free electron parabola near the band bottom at  $-3t$  and has a saddle point (van Hove singularity) at  $-1t$ . At this energy, the constant energy cuts of the band (Fermi lines) transition from one electron pocket to two hole pockets, i. e., the whole Brillouin zone is filled except for two circular areas.

**Introduction of the magnetic field.** The external magnetic field is included by means of a Peierls substitution [125]. To account for the transverse deflection by the Lorentz force, a phase factor is added to the hopping [126]

$$e^{ik \cdot r_{ij}} \rightarrow e^{i(k \cdot r_{ij} + b_{ij})}, \quad b_{ij} = \frac{e}{\hbar} \int_{r_i \rightarrow r_j} \mathbf{A}(\mathbf{r}) \cdot d\mathbf{l}. \quad (4.64)$$

To allow for the calculation of a band structure, the phase factors have to be periodic in the unit cell. This imposes restrictions on the magnetic field strength, as will be shown in the following. In any case, instead of the structural unit cell, a larger magnetic unit cell has to be considered, as shown in Fig. 20(a).

For the calculation of the line integral, the vector potential is expressed in the gauge  $\mathbf{A}(\mathbf{r}) = B(x/\sqrt{3} - y)\mathbf{e}_x$ . For the following example only the hoppings along the direction  $a\sqrt{3}/2\mathbf{e}_x + a/2\mathbf{e}_y$  are considered. The magnetic field strength has to fulfill the relation

$$BA = \frac{p}{bq} \Phi_0 \quad (4.65)$$

in order to be compatible with the lattice. Here,  $A = 3\sqrt{3}a^2/4$  is the area of the unit cell,  $\Phi_0 = h/e$  is the flux quantum,  $b = 2$  is the number of basis atoms and  $p$  and  $q$  are coprime integers. Only if this relation is fulfilled, the phase factors can be expressed as  $0\pi\frac{p}{bq}, 2\pi\frac{p}{bq}, 4\pi\frac{p}{bq}, \dots$  for these particular hopping paths (the other hopping paths can be considered by analogy).

As an example,  $p/2q = 1/4$  as in Fig. 20 corresponds to phase factors of 0 and  $\pi$ . This set of  $p$  and  $q$  describes a magnetic field of around 39.5 kT for graphene ( $a = 0.142$  nm), which is unachievable experimentally. However, the effective magnetic field

of skyrmions is characterized by  $p \rightarrow N_{\text{Sk}}$  and  $q \rightarrow n$ , with  $n$  being the number of sites forming a skyrmion. For small skyrmions ( $n \approx 100$ ), field strengths of several thousands of Tesla can be achieved, which is why in the following example  $p/bq = 1/72$  is used. This corresponds to a field of 2193 T.

**Landau quantization and Hall conductivity.** Under the influence of this large external magnetic field, the bands of graphene are mostly flat [Fig. 21(a)]. Especially near the zero-field band structure's minimum and maximum, these Landau levels are equidistant and show no visible  $k$  dependence just like for the case of free electrons. Likewise, these bands have an almost homogeneous Berry curvature and a Chern number of 1. The Hall conductivity [Fig. 21(b)] exhibits steps of  $-e^2/h$  in this energy range, starting from zero and going back to zero, as is expected.

Near the energies of van Hove singularities of the zero-field band structure ( $E = \pm t$ ) the Landau levels exhibit  $q/b$  oscillations along the long side of the Brillouin zone (here 18 oscillations). At these energies the Hall conductivity changes sign due to a single band with an enormous Chern number of  $1 - q = -35$  which compensates the Chern numbers of all other bands.

In the range between the two characteristic energies, the bands are doubly degenerate [note, that the bands are plotted in red and blue alternately in Fig. 21(b)]. They have a combined Chern number of 2 and are not equidistant. The Hall conductivity is still quantized but takes values of  $\dots, +3e^2/h, +e^2/h, -e^2/h, -3e^2/h, \dots$ . At  $E = 0$  (the energy of the Dirac point in the zero-field band structure) the Hall conductivity changes from  $+e^2/h$  to  $-e^2/h$ . For positive energies the Hall conductivity is sign reversed with respect to the Fermi energy  $E_F = 0$ , originating in the electron-hole symmetry of this system.

**Onsager's quantization scheme.** The unconventional quantization of the Hall conductivity and the sign changes at energies of van Hove singularities and  $E_F = 0$  are strongly related to the zero-field band structure. Onsager's quantization scheme [127,128] allows to deduce the precise dependence.

As was presented before, a free electron parabola in the zero-field band structure condenses to dispersion-less equidistant bands once the magnetic field is introduced [cf. Fig. 19(a) and (b)]. One can understand the equidistant energy spacing from the constant density of states (in two-dimensions): Each Landau level is formed by an equal number of states starting from the zero-field band minimum. A Landau level forms right in the middle of the corresponding energy range, which explains why the lowest Landau level is energetically higher than the band minimum of the zero-field band structure [cf. Fig. 19(a) and (b)].

For a real material the density of states is not constant. In graphene [Fig. 20(c)] it increases starting at the band minimum. Therefore, the resulting Landau levels are forming more densely [cf. Fig. 21(a)]. Their energy can be reconstructed by integrating the density of states and placing a Landau level whenever a multiple of a field-determined constant is reached, by analogy with the case of free electrons.

This procedure is known as Onsager's quantization scheme [127,128] and has been used to generate the gray curve in Fig. 21(b), which approximates the Hall conductivity well. Energies that require a special consideration are the energies of van Hove singularities. Here, the electronic character changes from electron- to hole-like. To account for

this, a jump of  $qe^2/h$  is introduced at these particular energies. Furthermore, between  $-t$  and  $+t$  the zero-field band structure has two equivalent pockets [Fig. 20(b) and (c)]. The number of states in each of the pockets has to overcome the specific threshold for the formation of a Landau level. For this reason, two Landau levels form at the same energy and contribute with one edge channel each to the transverse conductivity.

This scheme allows for an intuitive understanding of the calculated curve and approximates it precisely, except for a few features close to the energies of the van Hove singularities [Fig. 21(b)]. These inaccuracies occur because Onsager's quantization scheme assumes perfectly flat Landau levels. For a more detailed analysis of this quantization scheme and a generalization to the topological Hall effect of electrons in non-collinear spin textures, one is referred to publication [BG8] (not explicitly included in this thesis). There, also the complicated Berry-curvature distribution in the band with the large Chern number is shown and explained.

**Relation to the conventional Hall effect.** To reestablish the relation to the conventional Hall effect, the focus is set on the energy range near the zero-field band's minimum. Assuming the synthetic case where the Fermi energy is located here, the density of states is almost constant [cf. Fig 20(c)].

Going to smaller magnetic fields, the magnetic unit cell becomes larger, in order to ensure periodicity of the Peierls phase [Eq. (4.64)]. Consequently, more Landau levels are formed, all with a Chern number of 1, each. The bands become so dense that quantized values in the conductivity disappear even for low temperatures, similar to the discussion for free electrons. In this case, the expected Hall signal is the integrated density of states multiplied by  $bq/p$ , as follows from the Onsager quantization scheme. This means that for a fixed Fermi energy

$$\rho_{xy} \propto \frac{1}{\sigma_{xy}} \propto \frac{p}{bq} \propto B \quad (4.66)$$

in the limit of small temperatures and large magnetic fields  $T/B \rightarrow \infty$ , in agreement with the conventional Hall effect [Eq. (4.57)].

**Comparison to the experiment.** In one of the earliest publications on graphene, the Hall signal is presented [121] in the energy range near the Dirac crossing, i. e., the touching point of the blue and red band in Fig. 20(b). Starting at  $E = 0$  and going to higher energies, the resistivity  $\rho_{xy}$  takes a value of  $\frac{1}{2} \frac{h}{e^2}$  and then decreases to  $\frac{1}{6} \frac{h}{e^2}, \frac{1}{10} \frac{h}{e^2}, \dots$ . This corresponds to conductivities of  $-2 \frac{e^2}{h}, -6 \frac{e^2}{h}, -10 \frac{e^2}{h}, \dots$  which were calculated in Fig. 21(b) but with a missing factor of 2. This factor comes from the spin degree of freedom which has been neglected in the calculations. In terms of a Zeeman interaction (coupling of the spin to the magnetic field), the spin splitting is negligible compared to the Landau level quantization. For this reason, all Landau levels appear to be spin degenerate in the experiment.

The transitions between the plateaus are not step-wise in the experiment because of the discussed lattice effects and (most importantly) the small but finite temperature of 1.6 K. Furthermore, the applied maximum gate voltage of  $\pm 80$  V did not allow to access the energies which correspond to the van Hove singularities. Also, in the depicted energy range (which has to be within the range of  $-t$  to  $+t$ ) many more plateaus appear

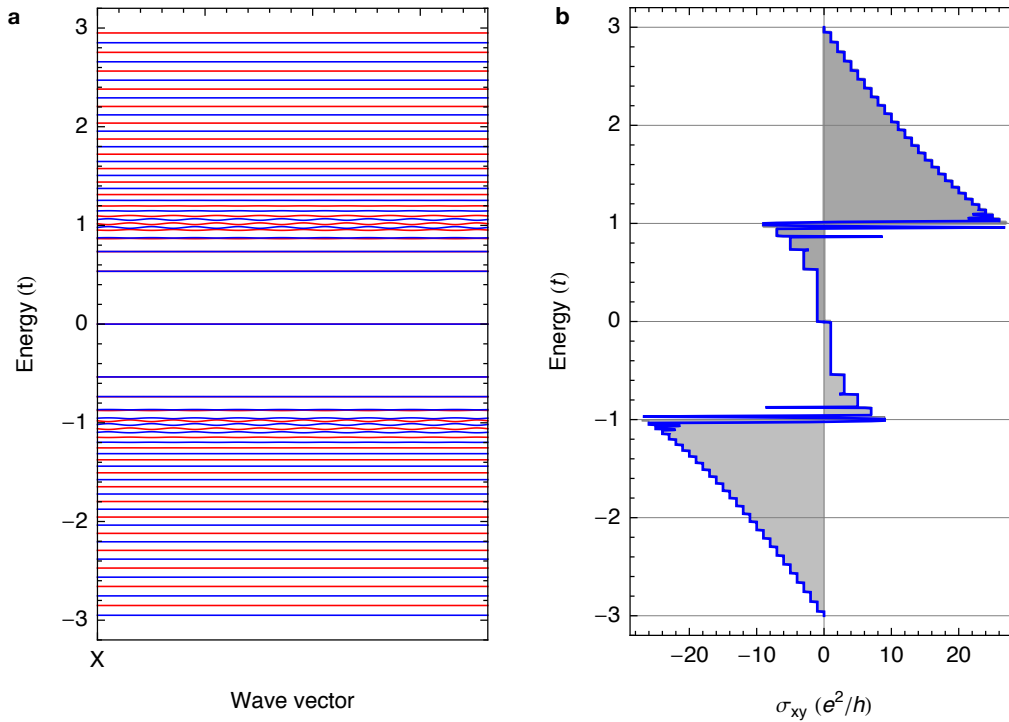


Figure 21: **Quantum Hall effect in graphene.** **a** Band structure (Landau levels are alternately depicted in red and blue) and **b** Hall conductivity versus location of the Fermi energy. Here, blue indicates the actual calculation and gray is the result of Onsager's quantization scheme (see text). This figure is partially adapted from Ref. [BG8]. The magnetic field  $B_z = 2193$  T corresponds to  $p/bq = 1/72$ .

in the experiment compared to the calculation; even though the experimental field of 9 T is large, the magnetic field was more than 200 times larger in the calculation.

Overall, the experimentally detected quantum Hall effect in graphene was well reproduced by the Berry theory approach; even an unconventional quantization could be explained. This validates its utility also for the quantification of the topological Hall effect in non-collinear spin textures, which is relevant for the publications [BG2], [BG3], [BG5], [BG7], [BG8] and [BG9].



---

## 5 Publications: Magnetic skyrmions

In the last sections, the theoretical methods for simulating magnetic textures and for describing the electronic transport properties have been introduced. In the following, seven publications will be presented and put into the context of this thesis. In the present section, the publications concerning conventional magnetic skyrmions and skyrmion crystals are discussed.

**Suppression of the skyrmion Hall effect.** The first publication [BG1] is attributed to the first goal formulated in the introduction. As presented in Sec. 3.4, a Néel skyrmion driven by spin-orbit torque suffers from a transverse deflection towards the racetrack's confinement, which is one of the major problems for the technological realization of a skyrmion-based racetrack storage device. In the publication a solution to this problem is presented: Néel skyrmions are driven by a modified spin-orbit torque so that a skyrmion Hall effect does not emerge. This increases the reliability and operation speed of a racetrack storage device drastically.

**Topological Hall effect.** Based on the mathematical concept of the Berry curvature (as presented in Sec. 4), publication [BG2] establishes an understanding of the topological Hall effect in skyrmion crystals that goes beyond justifying the charge deflection with the emergent field of the skyrmion (goal number two in the introduction). Unconventional quantization and sign changes in the signal are predicted. The latter have their origin in the energy-dependent electronic carrier characteristics.

**New hallmarks of skyrmion phases.** In publication [BG3] the orbital magnetization and the magnetoelectric polarizability have been computed for different types of skyrmion and antiskyrmion crystals, as introduced in Sec. 4.3. These quantities establish alternative hallmarks of skyrmionic phases in magnetic materials (goal number three) and even allow to distinguish different types of textures.

**Alternative magnetic quasiparticles.** The fourth goal formulated in the introduction is the prediction of alternative magnetic quasiparticles and the investigation of their emergent electrodynamic effects. In this regard, four types of textures will be discussed. The corresponding publications are presented in Sec. 6.

## 5.1 Suppression of the skyrmion Hall effect

**Skyrmions as carriers of information.** Magnetic skyrmions are considered to be the carriers of information in future data storage devices like the racetrack device. In Sec. 3.4 the current-driven motion of a Néel skyrmion in thin films has been simulated and explained. Inconvenient for applications is the skyrmion Hall effect [15, 16], that describes the transverse deflection of skyrmions towards the confinement of a racetrack when an electron current flows along the track. In real materials with a rough edge, the skyrmions will annihilate and the stored information is lost. And even when an ideally smooth edge is assumed, the maximally applicable current density is limited, resulting in a limited propulsion velocity.

**Possibilities for suppressing the skyrmion Hall effect.** To find approaches to suppress the skyrmion Hall effect one may consider the Thiele equation [identical to Eq. (3.35)]

$$-4\pi N_{\text{Sk}} b \mathbf{e}_z \times \mathbf{v} - b \underline{D} \alpha \mathbf{v} - B j \underline{I} \mathbf{s} = \nabla U(\mathbf{r}). \quad (5.1)$$

The evident solution is to consider quasiparticles with a topological charge of  $N_{\text{Sk}} = 0$ , like the antiferromagnetic skyrmion or the skyrmionium (cf. the publications in Sec. 6). Since conventional skyrmions ( $N_{\text{Sk}} = \pm 1$ ) are by far better understood experimentally, it is desirable to search for solutions also for these quasiparticles. The two-layer setup of the racetrack [as presented in Fig. 16(a)] enforces stabilized skyrmions to be of Néel type, so  $\underline{D}$  and  $\underline{I}$  are fixed as well. One is left with the manipulation of the torque-exhibiting polarization orientation  $\mathbf{s}$ . A suggested approach is the injection of spins via a magnetic layer on top of the actual racetrack layer, like in Ref. [129]. However, this method utilizes a charge current applied along the racetrack normal. For this reason, enormous currents are required to maintain this spin injection over the whole extent of the racetrack. An alternative method for injecting such spins is highly desired.

**This publication.** In the following publication “Overcoming the speed limit in racetrack devices by suppressing the skyrmion Hall effect” [BG1] an improved version of the skyrmion racetrack storage device is presented. As explained in Sec. 3.4, the conventional spin-orbit torque setup consists of a ferromagnetic layer and a heavy metal layer, where a charge current is transferred into a spin current by the spin Hall effect. The heavy metal commonly has such a high symmetry (e. g. Pt) that the spin polarization  $\mathbf{s}$  will necessarily be oriented perpendicularly to the charge current and the spin current. By considering a lower symmetric heavy metal, the spins can be oriented partially along the current direction. This changes the propulsion direction of the skyrmion (cf. Fig. 1 of the publication). At an optimal spin orientation the skyrmion Hall effect is completely suppressed, allowing to apply much higher current densities compared to the conventional system. Consequently, the skyrmions move in the middle of the racetrack at a velocity which is increased by one order of magnitude (cf. Fig. 2).

For the simulation of the skyrmion motion the LLG equation (3.16) has been solved. For the effective description of the skyrmion’s trajectory the Thiele equation (3.35) was used.

The following publication: Reprinted (whole article) with permission from (B. Göbel *et al.* Physical Review B **99**, 020405(R) (2019); Ref. [BG1]; Overcoming the speed limit in skyrmion racetrack devices by suppressing the skyrmion Hall effect). Copyright (2019) by the American Physical Society.

**Overcoming the speed limit in skyrmion racetrack devices by suppressing the skyrmion Hall effect**Börge Göbel,<sup>1,\*</sup> Alexander Mook,<sup>2</sup> Jürgen Henk,<sup>2</sup> and Ingrid Mertig<sup>1,2</sup><sup>1</sup>Max-Planck-Institut für Mikrostrukturphysik, D-06120 Halle (Saale), Germany<sup>2</sup>Institut für Physik, Martin-Luther-Universität Halle-Wittenberg, D-06099 Halle (Saale), Germany

(Received 6 July 2018; published 25 January 2019)

Magnetic skyrmions are envisioned as carriers of information in racetrack storage devices. Unfavorably, the skyrmion Hall effect hinders the fast propagation of skyrmions along an applied electric current and limits the device's maximum operation speed. In this Rapid Communication, we show that the maximum skyrmion velocity increases by a factor of 10 when the skyrmion Hall effect is suppressed, since the straight-line motion of the skyrmion allows for the application of larger driving currents. We consider a ferromagnet on a heavy-metal layer, which converts the applied charge current into a spin current by the spin Hall effect. The spin current drives the skyrmions in the ferromagnet via spin-orbit torque. We show by analytical considerations and simulations that the deflection angle decreases, when the spin current is polarized partially along the applied current direction, and derive the condition for complete suppression of the skyrmion Hall effect.

DOI: [10.1103/PhysRevB.99.020405](https://doi.org/10.1103/PhysRevB.99.020405)

**Introduction.** Over recent years, the capacity of data storage devices has steadily grown by reducing the size of magnetic bits in two-dimensional arrays [1]. The minimal size of a bit is limited by quantum effects, so new storage devices have been proposed and tested. Parkin *et al.* suggested a device that consists of quasi-one-dimensional racetracks which can be arranged to create a truly three-dimensional device with a drastically increased storage density [1–3]. Initially, walls between two ferromagnetic domains were considered as information carriers that can be written, moved, read, and deleted.

With the discovery of magnetic skyrmions [4–9] the concept of racetrack storage devices could be further improved. In a proposal by Fert *et al.* [10,11] domain walls were replaced by these whirl-like magnetic skyrmions in a ferromagnetic surrounding. Significant advantages of magnetic skyrmions as information carriers are their small size and their topological protection, quantified by an integer topological charge  $N_{\text{Sk}} = \pm 1$ .

Besides great stability the nontrivial real-space topology of a skyrmion induces emergent electrodynamic effects: spin-polarized electron currents, injected along the ferromagnetic racetrack, experience a topological Hall effect (THE) [12–20] and drive the magnetic skyrmion itself. Detrimentally, this skyrmion propagation is not parallel to the electric current direction; in most scenarios the skyrmion Hall effect (SkHE) [9,21–26] limits the maximum velocity, beyond which skyrmions annihilate at the edges of the racetrack.

To overcome this limitation, several concepts have been established. The combination of two skyrmions with opposite topological charges for example results in antiferromagnetic skyrmions [27,28], bilayer skyrmions [29,30], or  $2\pi$ -skyrmions [31–38]. Their zero topological charge gives a zero SkHE but these quasiparticles have either not been observed experimentally yet or are unstable under motion [37].

Another idea is to modify the racetrack setup. Interfacing the actual racetrack with a second ferromagnet, a spin-polarized current can be injected perpendicularly into the interface [11]. The magnetization direction can be chosen such that the skyrmion moves along the racetrack [39]. However, the spin current has to be applied over the whole racetrack, what obliterates the necessary low driving currents and the stackability of the racetrack device.

Replacing the second layer by a nonmagnetic heavy-metal (HM) layer, the spin Hall effect (SHE) converts a charge current along the HM into a spin current injected perpendicularly into the ferromagnetic layer (FM) [11] (see Fig. 1). In this Rapid Communication, we show that the skyrmion Hall angle can be engineered to zero in this setup. For HMs with reduced symmetry the generated spin current is polarized partially along the applied charge current, as recently shown in Refs. [40–43]. This reduces the skyrmion Hall angle compared to a cubic HM layer, where applied charge current, generated spin current, and the spin current's polarization are perpendicular to each other. FM and HM materials can be chosen accordingly to suppress the hindering skyrmion Hall effect completely and allow for a ten times as fast skyrmion motion compared to cubic HMs.

**Suppression of skyrmion Hall angle.** The motion of a magnetic skyrmion in a ferromagnetic thin film can be induced via two mechanisms: spin-transfer torque (STT) or spin-orbit torque (SOT). The first mechanism features in-plane injection of a spin-polarized current into the magnetic film. The electron spins align partially with the texture and transfer a torque to the magnetic texture, wherever the latter is noncollinear, in particular at a skyrmion. However, the direction of the injected spins is determined by the texture itself. Therefore the STT scenario does not allow for manipulation of the skyrmion Hall angle (angle of motion with respect to the applied current) and will inevitably suffer from the hindering transverse deflection.

We consider the second mechanism: skyrmion motion via SOT. In this scenario the FM is interfaced with a HM layer

\*bgoebel@mpi-halle.mpg.de

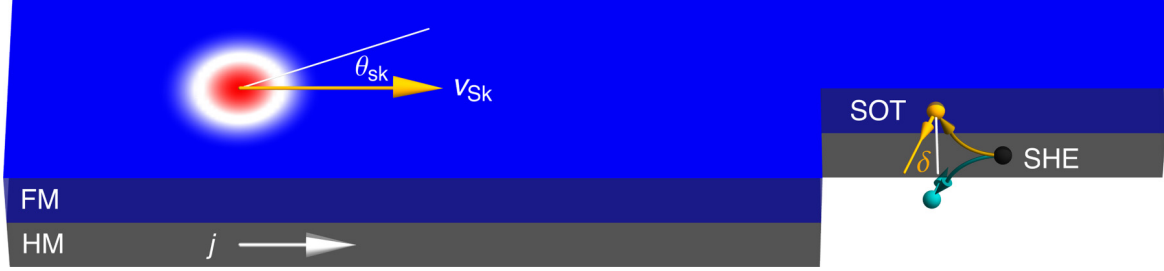


FIG. 1. Proposed mechanism to suppress the skyrmion Hall effect. A ferromagnetic layer (FM) is attached to a heavy-metal layer (HM); the interfacial DMI stabilizes Néel skyrmions (red-white circular object) in the FM. When a charge current (density  $j$ ) is applied in the HM the spin Hall effect (SHE) generates spins that are injected into the FM where they cause a SOT onto the magnetic moments. In highly symmetric materials the injected spins point into the  $\pm z$  direction (white line) and the skyrmion moves at a certain skyrmion Hall angle  $\theta_{\text{Sk}}$  (white line). In HMs with a reduced symmetry the spin polarization has an angle  $\delta$  in the  $xy$  plane and the propagation direction of the skyrmion is altered by  $\delta$  (orange). The skyrmion Hall effect is absent for  $\delta = \theta_{\text{Sk}}$  (see text).

with a nonvanishing SHE (Fig. 1). To propel the skyrmion a charge current  $j$  is injected along the HM layer ( $x$ ) where the SHE leads to perpendicular injection ( $z$ ) of spins with polarization

$$s \propto \sum_m \sigma_{zx}^m \mathbf{e}_m, \quad (1)$$

giving a spin Hall angle  $\Theta_{\text{SH}} = j_z^s/j_x$ .  $\sigma_{zx}^m$  is an element of the spin conductivity tensor ( $x$  applied current direction,  $z$  generated spin current direction,  $m = \{x, y, z\}$  direction of spin polarization), and  $\mathbf{e}_m$  is the unit vector in the  $m$  direction. For a cubic HM  $\sigma_{zx}^y \neq 0$  and  $\sigma_{zx}^x = \sigma_{zx}^z = 0$ , which means that injected spins always point into the  $\pm y$  direction (we use  $-y$  in the following). For this reason skyrmions driven by SOTs via highly symmetric HMs inhibit to manipulate the skyrmion Hall angle.

However, if the symmetry of the HM allows for  $\sigma_{zx}^x \neq 0$ , the injected spin orientation becomes  $s \propto (\sigma_{zx}^y \mathbf{e}_y + \sigma_{zx}^x \mathbf{e}_x)$ , with a deviation angle about the  $-y$  direction of

$$\delta = \arctan(\sigma_{zx}^x/\sigma_{zx}^y). \quad (2)$$

As we will show, this angle can compensate the hindering skyrmion Hall effect completely.

The collective behavior of the magnetic texture under torques follows the Landau-Lifshitz-Gilbert (LLG) equation [44–46]

$$\begin{aligned} \dot{\mathbf{m}}_i = & -\gamma_e \mathbf{m}_i \times \mathbf{B}_{i,\text{eff}} + \alpha \mathbf{m}_i \times \dot{\mathbf{m}}_i \\ & + \gamma_e \epsilon \beta [(\mathbf{m}_i \times \mathbf{s}) \times \mathbf{m}_i] - \gamma_e \epsilon' \beta (\mathbf{m}_i \times \mathbf{s}). \end{aligned} \quad (3)$$

Each magnetic moment  $\mathbf{m}_i$  precesses about the effective magnetic field  $\mathbf{B}_{i,\text{eff}} = -\delta_{m_i} F/M_s$ , which is derived from the free-energy density  $F$  [covering exchange, easy-axis anisotropy, interfacial Dzyaloshinskii-Moriya interaction (DMI), and demagnetization fields]. Damping is quantified by the material-dependent Gilbert damping parameter  $\alpha$ , and  $\gamma_e = \gamma/\mu_0 = 1.760 \times 10^{11} \text{ T}^{-1} \text{ s}^{-1}$  is the gyromagnetic ratio of an electron. The in-plane torque coefficient is  $\epsilon \beta = \frac{\hbar j \Theta_{\text{SH}}}{2ed_z M_s}$ ; we set the out-of-plane torque parameter  $\epsilon'$  to zero [47], due to its negligible influence on the skyrmion dynamics [25,39,48].

The generalized Thiele equation [49] for the SOT scenario describes effectively the center-coordinate motion of a

skyrmion [11]

$$b\mathbf{G} \times \mathbf{v} - b\underline{D}\alpha\mathbf{v} - \mathbf{BIR}(-\delta - \pi/2)\mathbf{j} = 0. \quad (4)$$

The skyrmion moves with velocity  $\mathbf{v}$  when driven by the current density  $j$ . The gyromagnetic coupling vector  $\mathbf{G} = G\mathbf{e}_z$  with  $G = -\int \mathbf{m}(\mathbf{r}) \cdot [\partial_x \mathbf{m}(\mathbf{r}) \times \partial_y \mathbf{m}(\mathbf{r})] d^2r = -4\pi N_{\text{Sk}}$  and the dissipation tensor  $\underline{D}$  with  $D_{ij} = \int \partial_{x_i} \mathbf{m}(\mathbf{r}) \cdot \partial_{x_j} \mathbf{m}(\mathbf{r}) d^2r$  (only  $D_{xx}, D_{yy}$  nonzero) determine the motion direction.  $\mathbf{R}(\phi)$  is a rotation matrix in the  $xy$  plane around the angle  $\phi$ ,  $\delta$  characterizes the injected spin orientation with respect to the  $-y$  direction, and  $B = \hbar/(2e)\Theta_{\text{SH}}$  [11,50]. The factor  $b = M_s d_z/\gamma_e$  contains the thickness of the FM  $d_z$  and its saturation magnetization  $M_s$ .  $\underline{I}$  is the tensor  $I_{ij} = \int [\partial_{x_i} \mathbf{m}(\mathbf{r}) \times \mathbf{m}(\mathbf{r})]_{x_j} d^2r$ . A Néel skyrmion (helicity  $h = 0$ ) has only  $I_{xy}$  and  $I_{yx}$  nonzero. For a different helicity this particular tensor is rotated by  $-h$ .

The Thiele equation gives a skyrmion Hall angle  $\theta_{\text{Sk}} = \arctan(v_y/v_x)$  which is zero for

$$\tan(\delta + h) = \frac{G}{\alpha D_{xx}}, \quad (5)$$

determined via  $v_y = 0$ . This tells us that an optimal spin orientation  $\delta$  or an optimal skyrmion helicity  $h$  can be found, for which the skyrmion Hall angle is absent. For  $\delta = 0$ , the above equation condenses the recent geometric considerations by Kim *et al.* [51] to a simple expression. They showed that for a mixed interfacial and bulk DMI [52,53], i.e.,  $h \neq 0, \pi/2$ , the skyrmion Hall angle can vanish. However, such skyrmions are still awaiting experimental identification.

Due to interfacial DMI the SOT scenario typically stabilizes Néel skyrmions ( $h = 0$ ). A vanishing skyrmion Hall angle is then achieved when the skyrmion Hall angle  $\arctan[G/(\alpha D_{xx})]$  of the system with  $\sigma_{zx}^x = 0$  is compensated by  $\delta = \arctan(\sigma_{zx}^x/\sigma_{zx}^y)$ :

$$\frac{\sigma_{zx}^x}{\sigma_{zx}^y} = \frac{G}{\alpha D_{xx}}. \quad (6)$$

The effective torque has been manipulated via the injected spin orientation instead of the magnetic texture itself, so that the skyrmion Hall angle is completely suppressed.

*High-speed skyrmions in micromagnetic simulations.* We verify the results of the Thiele equation using micromagnetic simulations and begin with CoPt, as considered in Ref. [11],

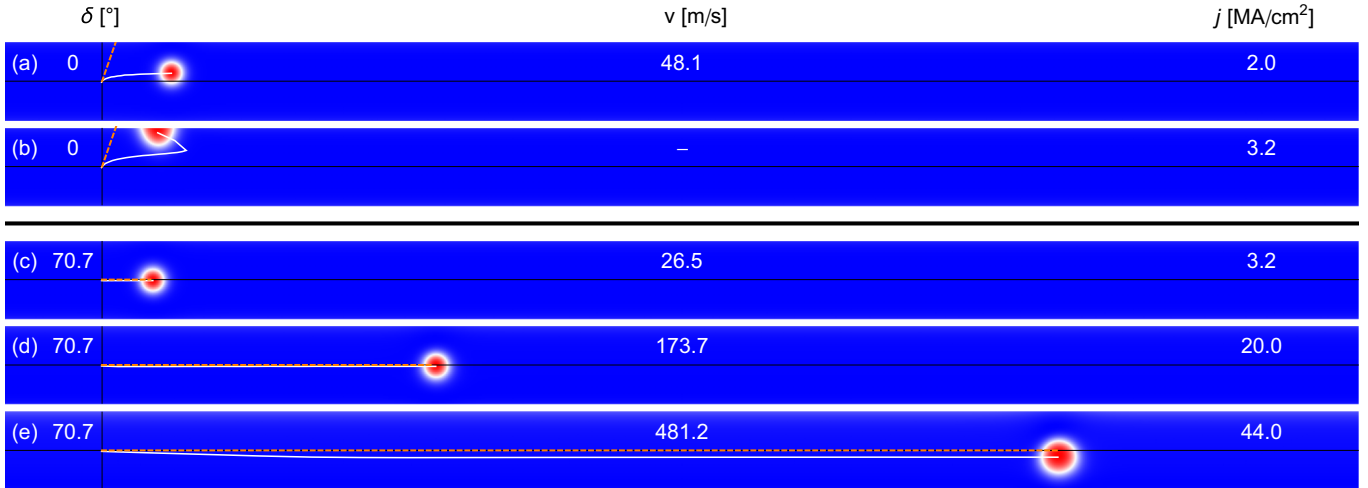


FIG. 2. Micromagnetic simulations comparing conventional and optimized setup. (a),(b) Conventional CoPt racetrack with  $\delta = 0^\circ$ . (c)–(e) Optimized racetrack with  $\delta = 70.7^\circ$ . Results of the simulations are shown after 1 ns propagation duration at different current densities  $\Theta_{\text{SH}}j$  (indicated on the right). The optimal geometry yields a stable motion for much larger current densities, allowing for faster propagation of the skyrmion. The skyrmion’s velocity in (e) is ten times as large as in the conventional scenario in (a);  $v = 481.2$  m/s compared to  $v = 48.1$  m/s. Red:  $-z$ ; blue:  $+z$  magnetization; white shows the actual trajectory and dashed orange shows the predicted trajectory from the Thiele equation without confining potential. An animated version of this figure is presented in the Supplemental Material [57].

where  $-y$  polarized spins are injected into the FM. We use MUMAX3 [54,55] to solve the LLG equation with the SOT term (3). The racetrack geometry throughout this Rapid Communication is width 40 nm, thickness  $d_z = 0.5$  nm, periodic boundary conditions in  $x$  direction, and a cell size of  $0.5 \text{ nm} \times 0.5 \text{ nm}$ . The parameters for CoPt read [11] exchange stiffness  $J = 15$  pJ/m, DMI constant  $D = 3$  mJ/m<sup>2</sup>, uniaxial anisotropy  $K_z = 0.8$  MJ/m<sup>3</sup>, saturation magnetization  $M_s = 0.58$  MA/m, and Gilbert damping  $\alpha = 0.3$ . Note that the choice of parameters does not *qualitatively* affect the skyrmion motion (as long as individual skyrmions can be stabilized). This is especially important since *ab initio* calculations predict  $D$  values that differ by up to 60% [56].

When driven by SOT a stabilized Néel skyrmion is pushed in the  $x$  direction (along the track) via the dissipative force (proportional to  $D_{xx}$ ) and is also pushed in the  $y$  direction (to the edge) by the gyrotropic force (proportional to  $N_{\text{Sk}}$ ).

The confined geometry introduces another term to the right side of the Thiele equation (4), which is the gradient  $\nabla U(y)$  of the potential energy of the skyrmion in the ferromagnetic layer. It contributes strongly at the edge of the racetrack, and repels and slightly deforms a skyrmion. Using the parameters of CoPt Néel skyrmions are stabilized with  $D_{xx} = 14.63$  and  $I_{xy} = 55.58$  nm, what gives a skyrmion Hall angle of about  $70.7^\circ$ . The skyrmions are not perfectly rotational symmetric.

In Fig. 2(a) the skyrmion is driven by a considerably low current density of  $\Theta_{\text{SH}}j = 2$  MA/cm<sup>2</sup>. In the beginning the skyrmion moves under the above angle. Increasing the  $y$  coordinate upon propagation leads to an increase of the repelling force from the confining potential. After this short acceleration phase the skyrmion moves in a steady state along the track. For current densities beyond a threshold, the gyrotropic force in the  $y$  direction is so strong that the confining potential is overcome and the skyrmion annihilates at the edge of the racetrack [Fig. 2(b)]. In this particular CoPt racetrack the applicable current density is limited to

about  $\Theta_{\text{SH}}j = 3$  MA/cm<sup>2</sup>, what limits the velocity to about 50 m/s.

Next, we consider a HM material with nonzero  $\sigma_{zx}^x$ , i.e., when an electric current is applied along the racetrack ( $x$ ) the injected spins are not polarized in the  $-y$  direction but are rotated by  $\delta$ . Choosing the tensor elements so that Eq. (6) is fulfilled, the skyrmion Hall effect is completely suppressed and the skyrmion moves in the middle of the racetrack [Fig. 2(c)]. The trajectory prediction from the Thiele equation coincides with the simulated trajectory.

The velocity of this optimized racetrack is less than that of the CoPt racetrack for the same  $j$  which follows directly from the Thiele equation,

$$v_x = \frac{B I_{xy} \cos \delta}{b \alpha D_{xx}} j. \quad (7)$$

However, skyrmions in this optimized geometry can be driven by currents 20 times as large and reach skyrmion velocities 10 times as large as for the CoPt racetrack. The result of a micromagnetic simulation for a fast-moving skyrmion is depicted in Fig. 2(e).

We showed that the skyrmion Hall angle vanishes in the optimized setup. However,  $\delta$  is given by material-specific parameters that can be tuned only slightly. Therefore, we analyze the range of current densities yielding a stable motion in dependence of  $\delta$  and find that the maximum skyrmion velocity (at maximal allowed current density) increases in every case compared to the  $\sigma_{zx}^x = 0$  velocity, even if  $\delta$  deviates from the optimal value.

The skyrmion motion is stable in the colored areas of Fig. 3(a) (solved analytically in the Supplemental Material [58]). For very low current densities the skyrmion remains stable for every spin polarization orientation since the transverse force is too weak to overcome the confining potential regardless of the propagation direction. For large  $j$  the skyrmion can only “survive” if the skyrmion Hall angle is zero. The

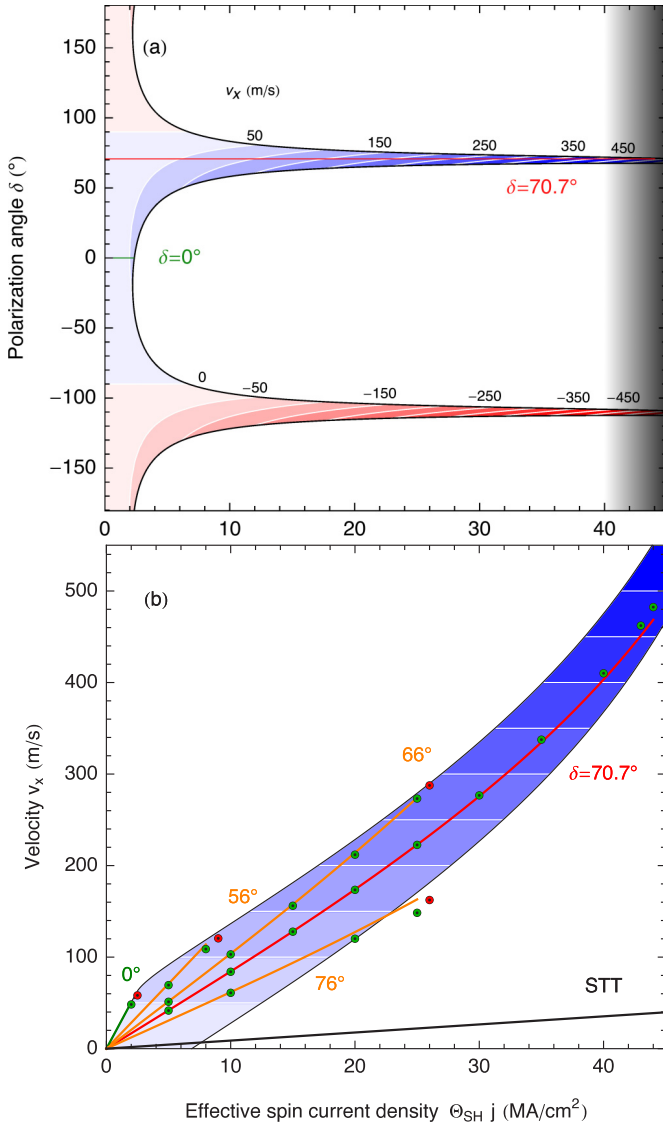


FIG. 3. Skymion velocity and stability for different HM materials. (a) The range of allowed  $\delta$  directions over  $j$  (colored area). (b) The  $j$  dependence of the velocity for selected  $\delta$ . The color in both panels corresponds to the velocity along the racetrack (blue positive, red negative; indicated with numbers). The colored lines correspond to constant  $\delta$  values (indicated). Lines and velocities have been calculated from the Thiele equation, without considering pinning effects which become negligible at large current densities. Explicit results from the micromagnetic simulations are indicated by points (green: stable motion; red: skymion annihilation). The black line (STT) is taken from Ref. [11] for comparison.

motion is reversed for  $\delta \rightarrow \delta + 180^\circ$  (sign reversal of current direction or spin conductivity tensor elements).

The velocity along the racetrack (represented by the color scale in Fig. 3) is in first approximation proportional to the applied current density  $j$  [cf. Eq. (7)]. Yet  $I_{xy}$  and  $D_{xx}$  depend on  $j$  as well. A power-law fit of these quantities (see Supplemental Material [58]) correctly reproduces the trend of the micromagnetic results [Fig. 3(b)]. Not only does the skymion velocity  $v_x$  increase with current density but also the efficiency  $v_x/j$ .

The  $j$  dependence of  $D_{xx}$  also affects the optimal  $\delta$  value [cf. Eq. (6)]. It leads to the emergence of a small skymion Hall effect for  $\delta = 70.7^\circ$  at high current densities [clearly visible in the simulation in Fig. 2(e)], while being negligible for lower current densities [Fig. 2(d)]. The optimal  $\delta$  shifts to about  $69^\circ$  for  $\Theta_{SH}j = 44 \text{ MA/cm}^2$ . In any case the maximum applicable current density is limited to  $\Theta_{SH}j \approx 45 \text{ MA/cm}^2$ . Even for the corrected  $\delta$  the skymion becomes so extended that it touches both edges of the racetrack. This limit of the maximal velocity therefore depends on the racetrack's width (here 40 nm).

The results of the micromagnetic simulations confirm the predictions of the Thiele equation quantitatively well, especially for the optimal  $\delta$ . Small deviations of analytical and numerical results are attributed to the fact that  $D_{xx}$  and  $I_{xy}$  are not only  $j$  but also  $\delta$  dependent; a skymion at the edge of the racetrack has a different shape compared to a skymion in the middle of the racetrack. For Fig. 3 we fitted only the  $j$  dependence for a fixed  $\delta = 70.7^\circ$  which already yields good agreement with the simulations.

*Discussion.* In the previous section, we proved that the skymion Hall angle can be suppressed by a nonzero  $\sigma_{zx}^x$ . To utilize the demonstrated advantage of SOT-driven skymions on a racetrack a HM with a nontrivial spin conductivity tensor has to be used. It has to generate a spin current with spins partially oriented along the charge current direction.

This nonzero  $\sigma_{zx}^x$  can be realized in nonmagnetic materials for triclinic, monoclinic, trigonal, and in tetragonal/hexagonal crystal systems, if the latter two have  $C_4$ ,  $S_4$ , and  $C_{4h}$  symmetry. Besides prohibition in all other tetragonal/hexagonal crystal systems, the element is forbidden to arise in orthorhombic and cubic crystal systems (cf. symmetry analysis of the spin conductivity tensor in Ref. [40]).

The results of Ref. [41] suggest that  $\text{Pt}_3\text{Ge}$ ,  $\text{Au}_4\text{Sc}$ , and  $(\text{Au}_{1-x}\text{Pt}_x)\text{Sc}$  may be suitable candidates for our predicted HM layer setup: they have a nonzero  $\sigma_{zx}^x$  element; e. g., for  $(\text{Au}_{0.8}\text{Pt}_{0.2})\text{Sc}$  the authors of that publication find  $\sigma_{zx}^x/\sigma_{zx}^y = 1/3$ . Moreover, these materials are nonmagnetic and consist of elements with a sizable spin-orbit coupling, which is expected to constitute interfacial DMI necessary for stabilizing Néel skymions. Even though unfavorable as a HM layer, magnetic  $\text{Mn}_3\text{Rh}$ ,  $\text{Mn}_3\text{Ir}$ , and  $\text{Mn}_3\text{Pt}$  were shown to have  $\sigma_{zx}^x/\sigma_{zx}^y$  of 1.903, 1.288, and 2.063, respectively [42,43].

There exist many materials in the above crystal systems, which can potentially have even larger ratios. Even if a setup does not fulfill the optimal condition, the merest rotation of the injected spin orientation improves the racetrack.

Summarizing, we have presented an approach to suppress the skymion Hall effect in a bilayer system via spin-orbit torques. Relation (6) comprises the parameters that determine the magnitude of the skymion Hall angle in a spin-orbit torque scenario: Gilbert damping  $\alpha$ , skymion shape  $G/D_{xx}$ , and injected spin polarization angle  $\delta$ . While the magnetic layer provides the Gilbert damping  $\alpha$ , the heavy-metal layer determines the quotient of spin Hall conductivity tensor elements  $\delta$ . The two materials have to be chosen accordingly to ensure a suppression of the SkHE.

At the current state of skymion racetrack memory development, our proposal is likely more feasible to tune the skymion Hall angle to zero compared to the concepts

presented in the Introduction. We demonstrated that by suppressing the skyrmion Hall effect skyrmion velocities of up to 500 m/s can be achieved at a reasonable  $v_x/j$  efficiency.

*Acknowledgments.* This work is supported by Priority Program SPP 1666 and SFB 762 of Deutsche Forschungsgemeinschaft (DFG).

- [1] S. S. Parkin, M. Hayashi, and L. Thomas, *Science* **320**, 190 (2008).
- [2] S. S. Parkin, Shiftable magnetic shift register and method of using the same, U.S. Patent No. 6,834,005 (21 December 2004).
- [3] S. Parkin and S.-H. Yang, *Nat. Nanotechnol.* **10**, 195 (2015).
- [4] T. H. R. Skyrme, *Nucl. Phys.* **31**, 556 (1962).
- [5] A. N. Bogdanov and D. A. Yablonskii, *Zh. Eksp. Teor. Fiz.* **95**, 178 (1989) [*Sov. Phys. JETP* **68**, 101 (1989)].
- [6] A. Bogdanov and A. Hubert, *J. Magn. Magn. Mater.* **138**, 255 (1994).
- [7] U. Röbber, A. Bogdanov, and C. Pfleiderer, *Nature (London)* **442**, 797 (2006).
- [8] S. Mühlbauer, B. Binz, F. Jonietz, C. Pfleiderer, A. Rosch, A. Neubauer, R. Georgii, and P. Böni, *Science* **323**, 915 (2009).
- [9] N. Nagaosa and Y. Tokura, *Nat. Nanotechnol.* **8**, 899 (2013).
- [10] A. Fert, V. Cros, and J. Sampaio, *Nat. Nanotechnol.* **8**, 152 (2013).
- [11] J. Sampaio, V. Cros, S. Rohart, A. Thiaville, and A. Fert, *Nat. Nanotechnol.* **8**, 839 (2013).
- [12] A. Neubauer, C. Pfleiderer, B. Binz, A. Rosch, R. Ritz, P. G. Niklowitz, and P. Böni, *Phys. Rev. Lett.* **102**, 186602 (2009).
- [13] T. Schulz, R. Ritz, A. Bauer, M. Halder, M. Wagner, C. Franz, C. Pfleiderer, K. Everschor, M. Garst, and A. Rosch, *Nat. Phys.* **8**, 301 (2012).
- [14] N. Kanazawa, Y. Onose, T. Arima, D. Okuyama, K. Ohoyama, S. Wakimoto, K. Kakurai, S. Ishiwata, and Y. Tokura, *Phys. Rev. Lett.* **106**, 156603 (2011).
- [15] M. Lee, W. Kang, Y. Onose, Y. Tokura, and N. P. Ong, *Phys. Rev. Lett.* **102**, 186601 (2009).
- [16] P. Bruno, V. K. Dugaev, and M. Taillefumier, *Phys. Rev. Lett.* **93**, 096806 (2004).
- [17] K. Hamamoto, M. Ezawa, and N. Nagaosa, *Phys. Rev. B* **92**, 115417 (2015).
- [18] B. Göbel, A. Mook, J. Henk, and I. Mertig, *Phys. Rev. B* **95**, 094413 (2017).
- [19] B. Göbel, A. Mook, J. Henk, and I. Mertig, *New J. Phys.* **19**, 063042 (2017).
- [20] B. Göbel, A. Mook, J. Henk, and I. Mertig, *Eur. Phys. J. B* **91**, 179 (2018).
- [21] J. Zang, M. Mostovoy, J. H. Han, and N. Nagaosa, *Phys. Rev. Lett.* **107**, 136804 (2011).
- [22] J. Iwasaki, M. Mochizuki, and N. Nagaosa, *Nat. Nanotechnol.* **8**, 742 (2013).
- [23] W. Jiang, X. Zhang, G. Yu, W. Zhang, X. Wang, M. B. Jungfleisch, J. E. Pearson, X. Cheng, O. Heinonen, K. L. Wang *et al.*, *Nat. Phys.* **13**, 162 (2017).
- [24] K. Litzius, I. Lemesch, B. Krüger, P. Bassirian, L. Caretta, K. Richter, F. Büttner, K. Sato, O. A. Tretiakov, J. Förster *et al.*, *Nat. Phys.* **13**, 170 (2017).
- [25] R. Tomasello, E. Martinez, R. Zivieri, L. Torres, M. Carpentieri, and G. Finocchio, *Sci. Rep.* **4**, 6784 (2014).
- [26] B. Göbel, A. Mook, J. Henk, I. Mertig, and O. A. Tretiakov, [arXiv:1811.07068](https://arxiv.org/abs/1811.07068).
- [27] X. Zhang, Y. Zhou, and M. Ezawa, *Sci. Rep.* **6**, 24795 (2016).
- [28] B. Göbel, A. Mook, J. Henk, and I. Mertig, *Phys. Rev. B* **96**, 060406(R) (2017).
- [29] J. Barker and O. A. Tretiakov, *Phys. Rev. Lett.* **116**, 147203 (2016).
- [30] X. Zhang, Y. Zhou, and M. Ezawa, *Nat. Commun.* **7**, 10293 (2016).
- [31] M. Finazzi, M. Savoini, A. R. Khorsand, A. Tsukamoto, A. Itoh, L. Duò, A. Kirilyuk, T. Rasing, and M. Ezawa, *Phys. Rev. Lett.* **110**, 177205 (2013).
- [32] F. Zheng, H. Li, S. Wang, D. Song, C. Jin, W. Wei, A. Kovács, J. Zang, M. Tian, Y. Zhang *et al.*, *Phys. Rev. Lett.* **119**, 197205 (2017).
- [33] S. Zhang, F. Kronast, G. van der Laan, and T. Hesjedal, *Nano Lett.* **18**, 1057 (2018).
- [34] A. Bogdanov and A. Hubert, *J. Magn. Magn. Mater.* **195**, 182 (1999).
- [35] M. Beg, R. Carey, W. Wang, D. Cortés-Ortuño, M. Vousden, M.-A. Bisotti, M. Albert, D. Chernyshenko, O. Hovorka, R. L. Stamps *et al.*, *Sci. Rep.* **5**, 17137 (2015).
- [36] M. Beg, M. Albert, M.-A. Bisotti, D. Cortés-Ortuño, W. Wang, R. Carey, M. Vousden, O. Hovorka, C. Ciccarelli, C. S. Spencer *et al.*, *Phys. Rev. B* **95**, 014433 (2017).
- [37] X. Zhang, J. Xia, Y. Zhou, D. Wang, X. Liu, W. Zhao, and M. Ezawa, *Phys. Rev. B* **94**, 094420 (2016).
- [38] H. Fujita and M. Sato, *Phys. Rev. B* **95**, 054421 (2017).
- [39] X. Zhang, G. Zhao, H. Fangohr, J. P. Liu, W. Xia, J. Xia, and F. Morvan, *Sci. Rep.* **5**, 7643 (2015).
- [40] M. Seemann, D. Ködderitzsch, S. Wimmer, and H. Ebert, *Phys. Rev. B* **92**, 155138 (2015).
- [41] S. Wimmer, M. Seemann, K. Chadova, D. Ködderitzsch, and H. Ebert, *Phys. Rev. B* **92**, 041101(R) (2015).
- [42] W. Zhang, W. Han, S.-H. Yang, Y. Sun, Y. Zhang, B. Yan, and S. S. Parkin, *Sci. Adv.* **2**, e1600759 (2016).
- [43] Y. Zhang, Y. Sun, H. Yang, J. Železný, S. P. P. Parkin, C. Felser, and B. Yan, *Phys. Rev. B* **95**, 075128 (2017).
- [44] L. D. Landau and E. Lifshitz, *Phys. Z. Sowjetunion* **8**, 153 (1935) [*Ukr. J. Phys.* **53**, 14 (2008)].
- [45] T. L. Gilbert, *IEEE Trans. Magn.* **40**, 3443 (2004).
- [46] J. C. Slonczewski, *J. Magn. Magn. Mater.* **159**, L1 (1996).
- [47] Note that “in-plane” and “out-of-plane” refer to the plane spanned by  $m_i$  and  $s$ . The out-of-plane torque acts like the torque from a homogeneous magnetic field which is why it does not drive a skyrmion.
- [48] W. Jiang, G. Chen, K. Liu, J. Zang, S. G. te Velthuis, and A. Hoffmann, *Phys. Rep.* **704**, 1 (2017).
- [49] A. Thiele, *Phys. Rev. Lett.* **30**, 230 (1973).
- [50] A. Hrabec, J. Sampaio, M. Belmeguenai, I. Gross, R. Weil, S. M. Chérif, A. Stashkevich, V. Jacques, A. Thiaville, and S. Rohart, *Nat. Commun.* **8**, 15765 (2017).
- [51] K.-W. Kim, K.-W. Moon, N. Kerber, J. Nothhelfer, and K. Everschor-Sitte, *Phys. Rev. B* **97**, 224427 (2018).

- [52] I. Dzyaloshinsky, *J. Phys. Chem. Sol.* **4**, 241 (1958).
- [53] T. Moriya, *Phys. Rev.* **120**, 91 (1960).
- [54] A. Vansteenkiste and B. Van de Wiele, *J. Magn. Magn. Mater.* **323**, 2585 (2011).
- [55] A. Vansteenkiste, J. Leliaert, M. Dvornik, M. Helsen, F. Garcia-Sanchez, and B. Van Waeyenberge, *AIP Adv.* **4**, 107133 (2014).
- [56] E. Simon, L. Rózsa, K. Palotás, and L. Szunyogh, *Phys. Rev. B* **97**, 134405 (2018).
- [57] See Supplemental Material at <http://link.aps.org/supplemental/10.1103/PhysRevB.99.020405> for animated version of Fig. 2.
- [58] See Supplemental Material at <http://link.aps.org/supplemental/10.1103/PhysRevB.99.020405> for derivation of the critical current density and current density dependence of  $D_{xx}$  and  $I_{xy}$ .



## 5.2 Topological Hall effect

**Phenomenological characterization.** The second main electrodynamic effect that emerges from the non-trivial real-space topology of a magnetic texture is the topological Hall effect of electrons. Summarizing the discussion so far, the Hall effect of electrons characterizes the occurrence of a transverse charge current (density  $\mathbf{j}$ ) when an electric field  $\mathbf{E}$  is applied; both quantities are not parallel to each other. An experimentally measured Hall resistivity  $\rho_{xy} = E_y/j_x$  can be decomposed into the conventional Hall effect, the anomalous Hall effect and the topological Hall effect [cf. also Fig. 22(b)]

$$\rho_{xy} = R_0^{\text{HE}} B_z + R_0^{\text{AHE}} M_z + R_0^{\text{THE}} \langle n_{\text{Sk}} \rangle. \quad (5.2)$$

The resistivity tensor element associated with the topological Hall effect is proportional to the average topological charge density  $\langle n_{\text{Sk}} \rangle$ . For this reason, the topological Hall effect can in principle be used to unambiguously detect topologically non-trivial spin textures in racetrack devices (see Appendix B).

**Electron deflection due to real-space topology.** Due to its analogy with the conventional Hall effect, the topological Hall effect can be related to an effective magnetic field, called ‘emergent field’  $\mathbf{B}_{\text{em}} = B_{\text{em}} \mathbf{e}_z \propto n_{\text{Sk}} \mathbf{e}_z$ , which accounts for the non-trivial real-space topology of a skyrmion. In a simplified picture, the traversing electrons’ spins align with the magnetic texture of the skyrmion, thereby adapting its topological properties. The conduction electrons accumulate a Berry phase in real space, which leads to

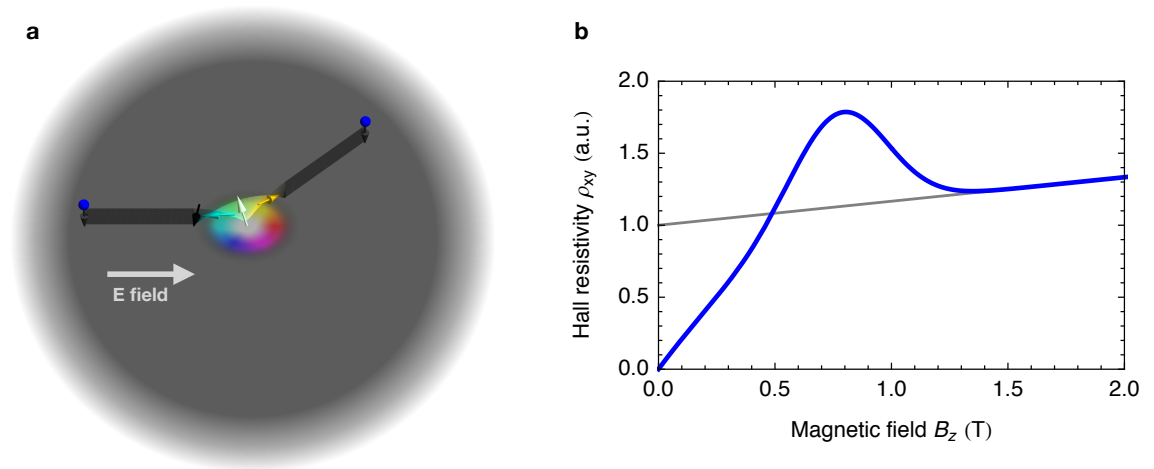


Figure 22: **Topological Hall effect of electrons.** **a** Emergent-field interpretation in the adiabatic limit. The electron spin aligns with the texture. Consequently, the electron accumulates a Berry phase and is deflected. **b** Schematic curve of a typical experimental measurement of the transverse resistivity versus the out-of-plane magnetic field. For large fields the signal exhibits a constant slope, which represents the conventional Hall effect. The curve has an offset; the sample is gradually magnetized and the anomalous Hall effect occurs. In the range between 0.5 T and 1 T a skyrmion phase is assumed to form. There, an additional contribution is present: the topological Hall effect.

a transverse deflection [130] [cf. Fig. 22(a)].

In Sec. 4.5 the conventional Hall effect was calculated for graphene using the Berry theory. The signal depends strongly on the electronic character (electron-like, hole-like), and is quantized for large fields. This motivates to utilize this reciprocal-space method also for the calculation of the topological Hall effect, for which similar phenomena are expected.

**This publication.** In the publication “Unconventional topological Hall effect in skyrmion crystals caused by the topology of the lattice” [BG2] the Berry curvature approach (Sec. 4.1) is applied to a periodic lattice of skyrmions. This treatment goes beyond the conventional interpretation of the topological Hall effect in terms of a real-space skyrmion density.

Based on the work of Hamamoto *et al.* [131] a quantized version of the topological Hall effect is found, which is most pronounced for small skyrmions whose emergent field can be as large as several thousands of Tesla. This effect is the analogue of the quantized version of the conventional Hall effect in the presence of large magnetic fields.

For a strong Hund’s coupling of electron spins and magnetic texture, a transformation is presented that shows how the reciprocal-space Berry curvature approach is equivalent to the consideration of the emergent field of the skyrmion. This transformation only holds in the adiabatic limit where the electron spin is locally aligned with the skyrmion texture.

Furthermore, it is shown that the magnitude of the topological Hall effect strongly depends on the electronic details of the skyrmion host. For simplicity a hexagonal lattice of  $s$  orbitals is considered. Without the presence of the skyrmion phase, the band structure is a single spin-degenerate band with positive effective mass near the band minimum (electron-like behavior) and a negative effective mass near the band maximum (hole-like behavior). Depending on this electronic character, the sign of the topological Hall conductivity is determined, and a sign change occurs at the energy of a van Hove singularity where the band structure has a saddle point. These findings are in analogy with the quantized Hall effect as presented in Sec. 4.5, as long as the adiabatic condition is fulfilled.

As an implication, shifting the Fermi energy (by doping or by applying a gate voltage) allows in principle to reverse the transverse electron transport. This feature may be attractive for spintronics applications. The results can be generalized to account for the multi-band dispersion relations of real materials.

In order to calculate the topological Hall conductivity the tight-binding model has been used, as introduced in Sec. 4.4. From the reciprocal-space Berry curvature the transverse Hall conductivity was then calculated using Eq. (4.27).

### Additional considerations

**Other publications.** Based on this publication, we published two more papers about the topological Hall effect of electrons in skyrmion crystals ([BG8] and [BG9]). For the course of this thesis I decided to limit myself to presenting only the most significant findings discussed in these publications.

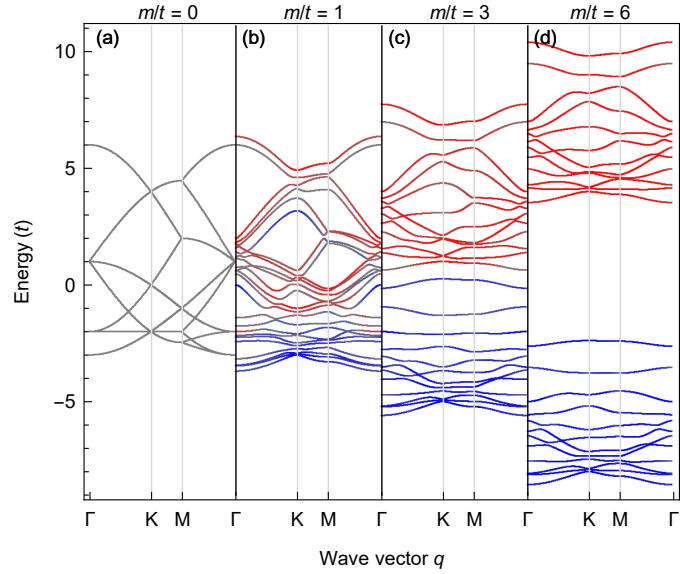


Figure 23: **Band structure for different coupling regimes.** In **a** the bands are spin degenerate and unpolarized (gray), since Hund's coupling is not considered. Upon increasing the coupling  $m$  (**b** – **d**), the spin degeneracy is lifted and the spins align locally with the skyrmion texture. Blue indicates an antiparallel alignment and red a parallel alignment for positive  $m$ . The figure considers small skyrmions on a hexagonal lattice with 12 magnetic moments in the unit cell. Reprinted from (B. Göbel *et al.*: Signatures of lattice geometry in quantum and topological Hall effect. *New Journal of Physics* **19**, 063042 (2017), DOI: <https://doi.org/10.1088/1367-2630/aa709b>; Ref. [BG8]). Published by IOP Publishing Ltd and Deutsche Physikalische Gesellschaft under the terms of the Creative Commons Attribution 3.0 license.

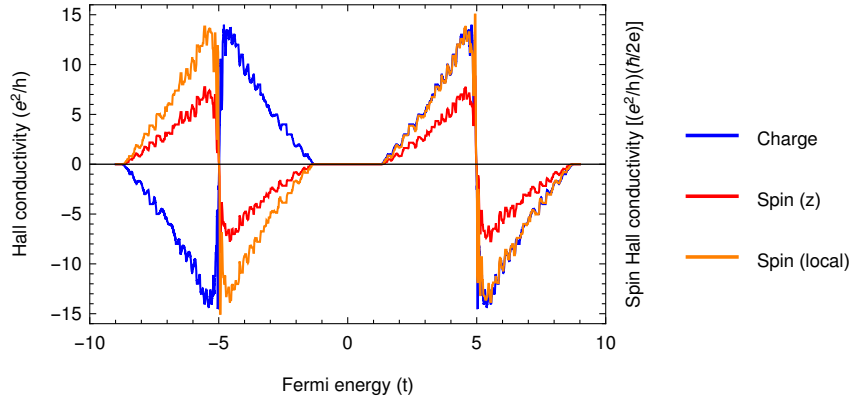


Figure 24: **Topological Hall conductivity and topological spin Hall conductivity for a skyrmion crystal.** The skyrmion (here  $N_{\text{Sk}} = -1$ ) comprises 36 atoms in the unit cell on a square lattice. Due to the large Hund's coupling,  $m = 5t$ , the bands are spin-polarized with respect to the local orientation of the magnetic texture. For the spin Hall conductivity the conventional definition (red) is compared to the definition in a local coordinate system (orange).

**Band structure and spin polarization.** A more detailed explanation of the band structure in the presented publication is given in publication [BG8]. Starting from the Hamiltonian (1) the  $s$  electrons are coupled via their spin with the skyrmion texture. Without coupling, the result would be the initial bands of the hexagonal lattice – spin-degenerate and folded back into the magnetic Brillouin zone [Fig. 23(a)]. Considering the coupling leads to a local alignment of the electron spins with the texture. In Fig. 23 the colors red (parallel) and blue (anti-parallel) signify the local spin polarization

$$P_{\text{local},n}(\mathbf{k}) = \langle n, \mathbf{k} | \text{diag}\{\boldsymbol{\sigma} \cdot \mathbf{m}_i\}_i | n, \mathbf{k} \rangle. \quad (5.3)$$

It increases when  $m/t$  is increased until an almost complete alignment is reached at approximately  $m = 5t$ . This corresponds to the adiabatic limit. The resulting bands become flatter and exhibit global band gaps near the band edges (better visible for larger skyrmions resulting in more bands). In fact, they are Landau levels with the same Chern numbers as for the quantum Hall system presented in Sec. 4.5. The edge states and the bulk-boundary correspondence have been further investigated in publication [BG8].

**Locally spin-polarized topological Hall effect.** As a subsequent result, in publication [BG9] the spin Hall conductivity has been calculated using Eq. (4.31). Instead of a global spin axis  $\sigma_\gamma$ , a local formulation has been used. The reason for this is the following: The spin Hall conductivity in the global axis definition averages the out-of-plane spin component of the arising transverse spin current over the whole bulk system. However, in typical experiments (like Kerr measurements [84] or using the inverse spin Hall effect) one measures the spins near the edge of the sample. In case of a collinear edge (as is the case for skyrmions in ferromagnets), the local formulation accounts for this by projecting the spin orientation onto the local magnetic moment and then onto the local spin orientation at the edge (here considered  $+z$ ). In case of an antiferromagnet, like in publication [BG7], the sign of the magnetization has to be reversed for one sublattice to account for the opposite edge magnetization of this sublattice.

Due to an almost complete local spin polarization for a large Hund's coupling  $m \gg t$ , the spin Hall effect is equivalent to the charge Hall effect multiplied by  $\pm\hbar/(2e)$  for the two blocks. When instead the global axis formulation (red) is used, the result is scaled by a factor  $-1 < \langle m_i^z \rangle < 1$  which does not agree with the expected accumulation at the edge. As a consequence, the local projection is reasonable, at least as long  $m \gg t$ . For weak coupling, the spin diffusion length has to be considered.

The consequence of this consideration is that skyrmion hosts exhibit a locally spin-polarized version of the topological Hall effect. This must not be confused with a topological version of a pure spin Hall effect, which is predicted for antiferromagnetic skyrmion hosts in publication [BG7].

The following publication: Reprinted (whole article) with permission from (B. Göbel *et al.* Physical Review B **95**, 094413 (2017); Ref. [BG2]; Unconventional topological Hall effect in skyrmion crystals caused by the topology of the lattice). Copyright (2017) by the American Physical Society.

# Unconventional topological Hall effect in skyrmion crystals caused by the topology of the lattice

Börge Göbel,<sup>1,\*</sup> Alexander Mook,<sup>1</sup> Jürgen Henk,<sup>2</sup> and Ingrid Mertig<sup>1,2</sup>

<sup>1</sup>Max-Planck-Institut für Mikrostrukturphysik, D-06120 Halle (Saale), Germany

<sup>2</sup>Institut für Physik, Martin-Luther-Universität Halle-Wittenberg, D-06099 Halle (Saale), Germany

(Received 11 January 2017; published 13 March 2017)

The hallmark of a skyrmion crystal (SkX) is the topological Hall effect (THE). In this article we predict and explain an unconventional behavior of the topological Hall conductivity in SkXs. In simple terms, the spin texture of the skyrmions causes an inhomogeneous emergent magnetic field whose associated Lorentz force acts on the electrons. By making the emergent field homogeneous, the THE is mapped onto the quantum Hall effect (QHE). Consequently, each electronic band of the SkX is assigned to a Landau level. This correspondence of THE and QHE allows us to explain the unconventional behavior of the THE of electrons in SkXs. For example, a skyrmion crystal on a triangular lattice exhibits a quantized topological Hall conductivity with steps of  $2 \cdot e^2/h$  below and with steps of  $1 \cdot e^2/h$  above the van Hove singularity. On top of this, the conductivity shows a prominent sign change at the van Hove singularity. These unconventional features are deeply connected to the topology of the structural lattice.

DOI: 10.1103/PhysRevB.95.094413

## I. INTRODUCTION

The quantum Hall effect (QHE) is one of the best known phenomena in condensed matter physics. It was first discussed for a two-dimensional electron gas in which the parabolic dispersion of free electrons is “compressed” into dispersionless Landau levels (LLs) [1,2]. Even before its experimental discovery [3] the QHE was described for various lattices in terms of Hofstadter butterflies [4–8]: the quantized energy levels become dispersive and the Hall conductivity  $\sigma_{xy}$  can change sign when applying a bias voltage. However, most of these manifestations of lattice topology remain to be verified by experiments. As an exception,  $\sigma_{xy}$  of graphene has been measured in a small energy window for half-filling [9]. The observed unconventional quantization—a sign change of the Hall conductivity for small variation of the bias—has been understood in terms of Chern numbers of the LLs [10,11].

Skyrmions [12] have conquered the field of magnetism since their theoretical [13–15] and experimental discoveries [16]. They are typically generated by the Dzyaloshinskii-Moriya interaction [17,18] in chiral magnets, for example in the noncentrosymmetric B20 materials, prominently represented by MnSi [16]. A skyrmion spin texture  $\mathbf{s}(\mathbf{r})$  [arrows in Fig. 1(a)] stands out from topologically trivial textures (e.g., collinear magnets or spin helices) by its topological charge

$$N_{\text{Sk}} = \frac{1}{4\pi} \int_{xy} n_{\text{Sk}}(\mathbf{r}) d^2r,$$

$$n_{\text{Sk}}(\mathbf{r}) = \mathbf{s}(\mathbf{r}) \cdot \left[ \frac{\partial \mathbf{s}(\mathbf{r})}{\partial x} \times \frac{\partial \mathbf{s}(\mathbf{r})}{\partial y} \right],$$

which is a nonzero integer;  $n_{\text{Sk}}(\mathbf{r})$  is the topological charge density. It gives rise to the topological Hall effect (THE) [19–25]: the nontrivial magnetic texture causes an emergent magnetic field  $\mathbf{B}_{\text{em}}$  which acts on the propagating electrons by its Lorentz force.

In this article we discuss an unconventional quantized THE in skyrmion crystals (SkXs): the topological Hall conductivity

exhibits a prominent change of sign as a function of bias voltage. This sign change is assigned to the *topology of the structural lattice* rather than to the nontrivial magnetic topology of the skyrmions. For this purpose, we relate the THE to the QHE as follows. The emergent field  $\mathbf{B}_{\text{em}}$  is inhomogeneous [central hexagon in Fig. 1(a)] because it is proportional to  $n_{\text{Sk}}(\mathbf{r})$ . By making  $\mathbf{B}_{\text{em}}$  homogeneous, i.e., by redistributing the magnetic flux, the THE is mapped onto a QHE on a structural lattice but in an homogeneous field [lower hexagon in Fig. 1(a)]. As a result, the quantum Hall conductivity  $\sigma_{xy}$  is quantized in the same way as for the THE: in steps of  $2 \cdot e^2/h$  below and in steps of  $1 \cdot e^2/h$  above the van Hove singularity (VHS). Most strikingly, it exhibits an abrupt change of sign when the VHS is crossed in dependence of bias. We attribute this unconventional behavior to the number and the character (electron versus hole) of the Fermi pockets. Thus, it is tightly related to the topology of the structural lattice.

The exceptional behavior, sketched in Fig. 1(b), calls for experiments on samples exhibiting a SkX phase. The Hall conductivity  $\sigma_{xy}$  in clean samples (mean free path of the electrons is larger than the skyrmion size) should be extremely sensitive to a gate voltage: the contribution of the THE to  $\sigma_{xy}$  can change sign [red versus blue curve in Fig. 1(c)]. In the following, we provide details supporting our claim.

## II. ELECTRONS IN A SKYRMION CRYSTAL

Following Ref. [24] we describe the spin-dependent electronic structure by means of the tight-binding Hamiltonian

$$H = \sum_{ij} t_{ij} c_i^\dagger c_j + m \sum_i \mathbf{s}_i \cdot (c_i^\dagger \boldsymbol{\sigma} c_i) \quad (1)$$

with constant nearest-neighbor hopping  $t_{ij} = t$  ( $i, j$  sites of the structural lattice). The electron spin is coupled to the skyrmion magnetic texture  $\{\mathbf{s}_i\}$  with strength  $m$  (measured in units of  $t$ ; second sum).  $\boldsymbol{\sigma}$  is the vector of Pauli matrices, and  $c_i^\dagger$  and  $c_i$  are spin-dependent creation and annihilation operators, respectively.

\*bgoebel@mpi-halle.mpg.de

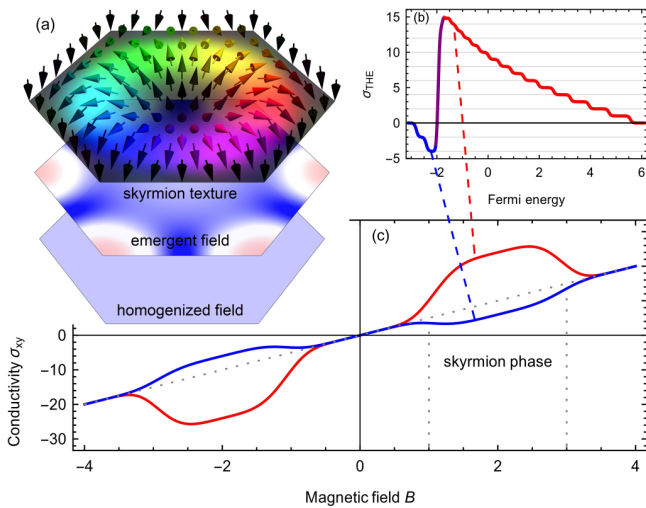


FIG. 1. Core message of the paper. (a) A skyrmion (top hexagon) generates an inhomogeneous emergent magnetic field (central hexagon; blue: positive; white: zero; red: negative). By redistributing this field such that it becomes homogeneous (lower hexagon), the topological Hall effect is mapped onto a quantum Hall effect. (b) Schematic bias dependence of the topological contribution  $\sigma_{\text{THE}}$  to the Hall conductivity  $\sigma_{xy}$ , exhibiting a sign change at the energy of a van Hove singularity (purple). (c) Magnetic-field dependence of  $\sigma_{xy}$  for a bias below (blue) and above (red) the van Hove singularity.  $\sigma_{xy}$  can show a decrease (blue) as well as an increase (red) in the skyrmion crystal phase which is present for  $1 \leq B \leq 3$  in arbitrary units.

To model a SkX (a regular array of skyrmions),  $\{s_i\}$  is assumed to be a triple- $q$  state [26], that is, a coherent superposition of three spin spirals with a prescribed wavelength  $\lambda$ . In the following, we consider a structural *triangular lattice* with lattice constant  $a$ .

The intrinsic contribution to the Hall conductivity [27]

$$\sigma_{xy}(E_F) = \frac{e^2}{h} \frac{1}{2\pi} \sum_n \int_{\text{BZ}} \Omega_n^{(z)}(\mathbf{q}) f[E_n(\mathbf{q}) - E_F] d^2q \quad (2)$$

is given by a Brillouin-zone (BZ) integral of the Berry curvature  $\Omega_n^{(z)}(\mathbf{q}) = \partial_{q_x} A_n^{(y)}(\mathbf{q}) - \partial_{q_y} A_n^{(x)}(\mathbf{q})$ . The Berry connection  $A_n(\mathbf{q}) = i \langle u_n(\mathbf{q}) | \nabla_{\mathbf{q}} | u_n(\mathbf{q}) \rangle$  is determined from the eigenvectors  $u_n(\mathbf{q})$  with energies  $E_n(\mathbf{q})$  of the Hamiltonian (1). The sum runs over all bands  $n$ ;  $e$  and  $h$  are the electron charge and Planck's constant, respectively, while  $f(E)$  is the Fermi distribution function.

At zero temperature only states below the Fermi energy  $E_F$  contribute to the transport: if  $E_F$  is located within the band gap above the  $l$ th band,  $\sigma_{xy}$  is proportional to the winding number  $w_l = \sum_{n \leq l} C_n$  [28,29] which is the accumulation of the Chern numbers

$$C_n = \frac{1}{2\pi} \int_{\text{BZ}} \Omega_n^{(z)}(\mathbf{q}) d^2q. \quad (3)$$

### III. QUANTIZED TOPOLOGICAL HALL EFFECT

For zero coupling [ $m = 0$  in Eq. (1)], the bands are spin degenerate and we obtain the band structure of a triangular

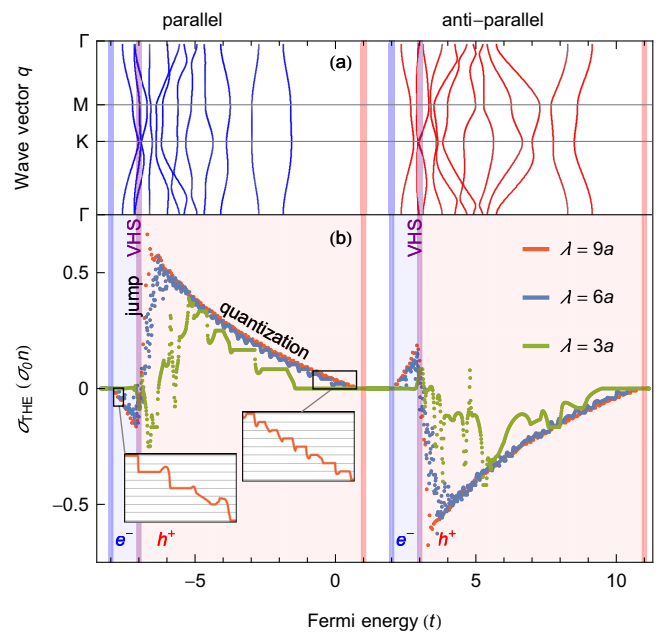


FIG. 2. Topological Hall effect in SkXs. (a) Electronic band structure of a SkX with skyrmion size  $\lambda = 3a$  for coupling strength  $m = 5t$  ( $a$  is a lattice constant). The alignment of the electron spin to the magnetic skyrmion texture is indicated by color (parallel: blue; antiparallel: red). (b) Topological Hall conductivity  $\sigma_{\text{THE}}$  versus Fermi energy for skyrmion sizes  $\lambda = 3a$  (green),  $6a$  (blue), and  $9a$  (red).  $\sigma_{\text{THE}}$  is normalized to the number  $n$  of atomic sites per skyrmion unit cell ( $\sigma_0 = e^2/h$  conductance quantum). Energy regions with electronlike ( $e^-$ , blue background) and holelike ( $h^+$ , red background) behavior are indicated (see text).

lattice. The bottom of the band is at  $-3t$ , its top at  $+6t$ ; a VHS shows up at  $E_{\text{VHS}} \equiv -2t$  [Fig. 4(b)].

For finite coupling  $m$ , the electron spin aligns with the skyrmion spin texture and the spin degeneracy is lifted. With increasing  $m$ , the band structure is split into two blocks: one with spins parallel, the other with spins antiparallel to the spin texture. In the limit  $m \rightarrow \infty$  both blocks exhibit identical dispersion relations.

The band structure for  $m = 5t$  and  $\lambda = 3a$  is depicted in Fig. 2(a). In each block, the energetically higher bands are well separated and show considerable dispersion (right part of each block). Close to the VHSs, that is at  $E = -2t \pm m$ , the bands become very narrow.

The separation into blocks is reflected in the conductivity  $\sigma_{xy}$  [Fig. 2(b)]. Since both blocks produce similar features, except for a change of sign, it is sufficient to discuss the block with lower energy. Starting from the band bottom,  $\sigma_{xy}$  is negative and decreases with energy in quanta of  $2 \cdot e^2/h$ . Close to the VHS ( $E \approx -2t - m = -7t$ ), the conductivity increases abruptly to positive values. At larger energies  $\sigma_{xy}$  drops again but in steps of  $1 \cdot e^2/h$  until it reaches zero conductance. This “quantization” region [label in Fig. 2(b)] shows up most pronounced for small skyrmions; cf.  $\lambda = 3a$  (green data set). Recall that there the bands are well separated by gaps, the associated states carry Chern number  $-1$ .

The sawtooth shape of  $\sigma_{xy}$  becomes more pronounced the larger the skyrmion size  $\lambda$ : the steps as well as the jump become

energetically more narrow because there are more bands within the same energy range [compare the green, blue, and red data sets in Fig. 2(b)].

### A. Transformation to the emergent field

In the strong-coupling limit  $m \gg t$ , the electron spin is fully aligned with the skyrmion texture and the two blocks of bands are identical but rigidly shifted in energy by the Zeeman term in the Hamiltonian. Consequently, each individual block can be discussed in terms of *spinless* electrons. However, the skyrmion texture has to be taken into account by a local gauge transformation into the reference frame of its magnetic moments [24,30,31]. The gauge field  $\mathbf{A}(\mathbf{r})$  defines the emergent magnetic field  $\mathbf{B}_{\text{em}}(\mathbf{r}) = \nabla \times \mathbf{A}(\mathbf{r})$  with  $B_{\text{em}}^{(z)}(\mathbf{r}) \propto n_{\text{Sk}}(\mathbf{r})$  [30], which is collinear (along  $z$ ) but inhomogeneous [central hexagon in Fig. 1(a)]. The gauge transformation recasts the coupling of the electron spin to the skyrmion texture to a fictitious field acting on the electron charge. Of course, both descriptions yield identical results for the THE.

In the tight-binding model, the gauge field  $\mathbf{A}(\mathbf{r})$  leads to effective complex hopping strengths [24]

$$t_{ij}^{\text{eff}} \equiv t \cos \frac{\theta_{ij}}{2} e^{i a_{ij}} \quad (4)$$

that enter the Hamiltonian of the quantum Hall effect

$$H_{\text{QH}} = \sum_{ij} t_{ij}^{\text{eff}} d_i^\dagger d_j. \quad (5)$$

$d_i^\dagger$  ( $d_i$ ) is a creation (annihilation) operator and  $\theta_{ij}$  is the angle between the spins at sites  $i$  and  $j$ . With the polar angles  $\phi_i$  and  $\phi_j$  of these spins the phase in Eq. (4) is written as [24]

$$\tan a_{ij} = - \frac{\sin(\phi_i - \phi_j)}{\cos(\phi_i - \phi_j) + \cot \frac{\theta_i}{2} \cot \frac{\theta_j}{2}}. \quad (6)$$

### B. Topological Hall effect as quantum Hall effect

The reformulation of the THE as QHE requires us to redistribute the inhomogeneous emergent field  $\mathbf{B}_{\text{em}}^{(z)}(\mathbf{r})$  into a *homogeneous* field with strength  $B$ . The topological charge of each skyrmion is conserved by the constraint  $(4\pi\hbar)^{-1} \int_{\text{uc}} B_{\text{em}}^{(z)}(\mathbf{r}) d^2r = N_{\text{Sk}}$  (uc is the unit cell of the SkX). The hopping strengths in Eq. (4) and especially the phases  $a_{ij}$  [Eq. (6)] have to be adjusted accordingly [24],

$$t_{ij}^{\text{eff}} = t \exp \left( -ie/\hbar \int_{r_i}^{r_j} \mathbf{A}(\mathbf{r}) \cdot d\mathbf{l} \right). \quad (7)$$

$d\mathbf{l}$  points along the hopping path ( $\mathbf{r}_i \rightarrow \mathbf{r}_j$ ) and  $\mathbf{A}$  is the vector potential of the homogeneous magnetic field with  $\mathbf{B} = \nabla \times \mathbf{A}$ . For our calculations we used  $\mathbf{A}(\mathbf{r}) = B \mathbf{e}_x (y - x/\sqrt{3})$ .

It is illustrative to compare the band structures for the inhomogeneous and the homogeneous emergent field (Fig. 3). The total bandwidth for the inhomogeneous emergent field (a) is increased if the term  $\cos \theta_{ij}/2$  in Eq. (4) is approximated by 1 (b); however, the shapes of the individual bands remain almost unchanged. The total bandwidth in (b) is very close to that of the LLs (c). On top of that, there is a one-to-one correspondence between the bands in (b) and the LLs (c). This is most obvious for large energies where the Chern

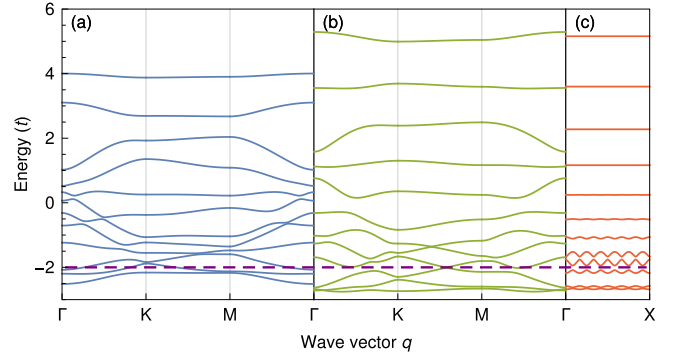


FIG. 3. Electronic band structure of a skyrmion crystal and Landau levels. (a) Band structure of a skyrmion crystal (skyrmion size  $\lambda = 3a$ , 12 sites per unit cell). (b) As (a) but with the approximation  $\cos \theta_{ij}/2 \rightarrow 1$  in Eq. (4). (c) Landau levels for a homogeneous emergent magnetic field. The five topmost bands in (a)–(c) carry Chern number  $-1$ . The energy of the van Hove singularity is indicated by the purple dashed line.

numbers ( $-1$ ) are identical as well. Hence, we conclude that the redistribution of the emergent field merely causes bandwidth broadening but conserves the topology.

We now corroborate the close relation of THE and QHE further. Constant-energy cuts (CECs) through the original band structure of the triangular lattice [ $(\alpha), \dots, (\delta)$  in Figs. 4(a) and 4(b)] at elevated energies are circular because there the band is parabolic [cf. CEC ( $\alpha$ )]. Separating occupied states in the outside from unoccupied states in the inside of the CEC, a circle is a hole pocket with negative curvature (for  $t > 0$ ). The LLs in this energy region are dispersionless, as expected for free electrons.

Constant energy cuts closer to the VHS show increased hexagonal warping [cf. CEC ( $\beta$ )]. At the VHS the CEC is a hexagon [cf. CEC ( $\gamma$ )]. Having no curvature, ( $\gamma$ ) features an infinite effective mass, with the consequence that electrons at the VHS are not affected by the emergent field. These electrons behave as in a continuum [32]; the associated band exhibits oscillations in the reduced zone scheme [Fig. 3(c)], thereby resembling the band structure of the triangular lattice [Fig. 4(b)]. Constant-energy cuts at energies below the VHS exhibit two electron orbits [cf. CEC ( $\delta$ )].

Landau levels with energies larger than that of the VHS carry Chern number  $-1$  [red peaks in Fig. 4(c)] because there is a single holelike Fermi contour [ $(\alpha)$  and ( $\beta$ ) in Fig. 4(a); the number of enclosed states is  $\zeta_h$ ]. In contrast, Landau levels below the VHS appear in pairs because there are two electronlike Fermi lines, each enclosing  $\zeta_e$  states [see ( $\delta$ )]. Thus, each pair carries twice the Chern number of free-electron-like LLs, i.e.,  $-2$  (blue peaks).

To explore the Hall conductivity in detail, we utilize an approximate *construction*. Onsager's quantization scheme [2] allows us to deduce LLs directly from the CECs of the original band structure of the triangular lattice [Fig. 4(b)]: if a LL contains  $\zeta_0$  states, the associated CEC encloses  $(j + \frac{1}{2})\zeta_0$  states ( $j$  integer). This means for CECs with two electron orbits that the total number of enclosed states reads  $2 \cdot (j + \frac{1}{2})\zeta_0$ . The character of the pockets is respected by assigning positive numbers to  $\zeta_h$  for holelike pockets (red in Fig. 4) but negative numbers to

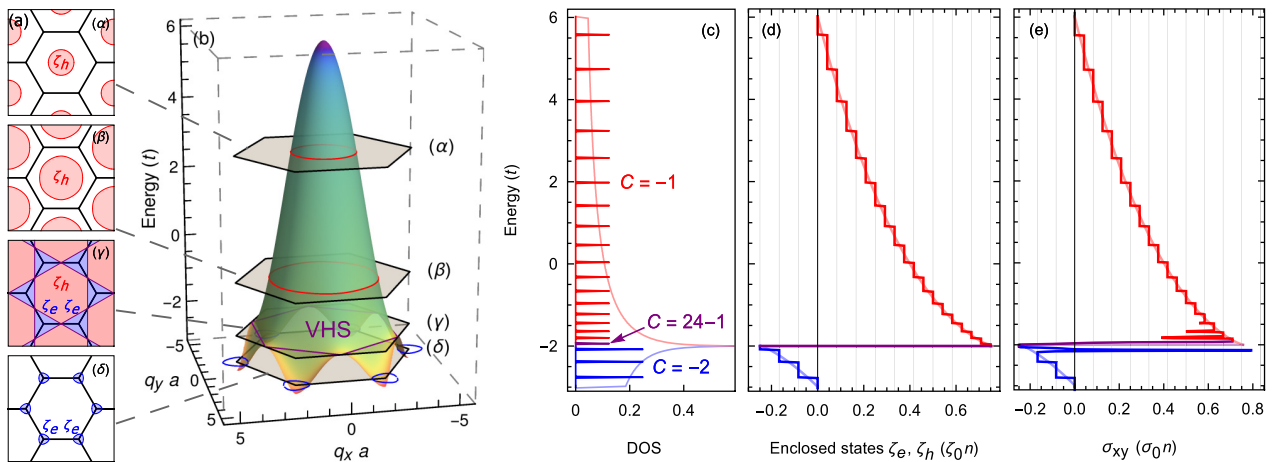


FIG. 4. Quantum Hall effect on the triangular lattice for  $n = 24$  sites in the unit cell. (a) and (b) The band structure for the triangular lattice without magnetic field is depicted in (b). Cuts at selected energies are labeled  $(\alpha), \dots, (\delta)$  and are shown in (a). The numbers  $\zeta_e$  and  $\zeta_h$  of enclosed states in the Brillouin zone (black hexagons) has to obey Onsager's quantization scheme. At the van Hove singularity [ $E_{\text{VHS}} = -2t$ , cut  $(\gamma)$ ] the constant-energy contours exhibit a Lifshitz transition. (c) Density of states (DOS) of the band structure in (b) depicted by light smooth curves. The associated Landau levels are shown by dark colors; their Chern numbers  $C$  are indicated. (d) Number of enclosed states  $\zeta_e$  and  $\zeta_h$  before (light smooth curves) and after Landau quantization (dark). (e) Transverse quantum Hall conductivity in units of  $\sigma_0 = e^2/h$ . In all panels, the character of the constant-energy pockets is indicated by color (blue: electronlike; red: holelike).

$\zeta_e$  for electronlike pockets (blue in Fig. 4) [33,34]. At the van Hove singularity which separates holelike from electronlike pockets the constructed conductivity changes sign [Fig. 4(d)].

The conductivity constructed from the number of enclosed states is remarkably similar to the quantum Hall conductivity  $\sigma_{xy}$  that has been explicitly computed from Eq. (2) for the LLs [Figs. 4(d) versus 4(e)]. The Chern numbers are proportional to the number of pockets and appear as steps in the constructed curve, although they are never explicitly used for the construction. Both curves deviate near the VHS at  $E_{\text{VHS}} = -2t$ , that is, where lattice effects are prominent; recall that the latter are neglected in Onsager's quantization scheme. The Landau levels in this energy range show oscillations [Fig. 3(c)]. Thus, the sign change of  $\sigma_{xy}$  is not located exactly at the VHS but is associated with the oscillating LL closest to the VHS.

This particular LL is composed of states with energies below *and* above the VHS; corresponding constant-energy cuts are taken below and above the cut  $(\gamma)$  [Figs. 4(a) and 4(b)], which features an open orbit with infinite mass. The distinction of the number of enclosed states and of their character—two holelike pockets below the VHS but a single electronlike pocket above the VHS—dictates a mismatch of Chern numbers. The result is a large Chern number of  $C = n - 1$  for this particular LL [magenta peak in Fig. 4(c) with  $C = +23$  for  $n = 24$ ] [10,11,33,35]. The outstanding Chern number compensates the sum of all other Chern numbers. This result is clearly a manifestation of the van Hove singularity. It is thus caused by the topology of the structural lattice: the large Chern number and the associated jump of the transverse Hall conductivity would occur at VHSs for *every* lattice.

The energy dependence of the quantum Hall conductivity  $\sigma_{xy}$  shows striking similarity to that of the topological Hall effect in skyrmion crystals. Both conductivities— $\sigma_{xy}$  of one block in Fig. 2(b) and  $\sigma_{xy}$  in Fig. 4(e)—feature steps of  $-2 \cdot e^2/h$  below the VHS, the substantial jump near the

VHS, and steps of  $-1 \cdot e^2/h$  above the VHS. Accordingly, topological and quantum Hall effect are essentially equivalent. A difference is that in the case of the THE the inhomogeneity of the emergent field “adds” dispersion to the bands [cf. Figs. 3(b) and 3(c)]. To reiterate, the effects ascribed to the topology of the structural lattice—quantization and the jump of  $\sigma_{xy}$ —are transferred from the THE to the QHE and *vice versa*. In general, topological Hall conductivities would rise abruptly at VHSs on every lattice.

#### IV. SUGGESTION FOR EXPERIMENTS

The established relation of lattice topology and bias dependence of the topological Hall conductivity calls for experimental verification. The quantized topological Hall effect can be studied in metals which exhibit a SkX phase, e.g., MnSi [16],  $\text{Fe}_{1-x}\text{Co}_x\text{Si}$  [36], and FeGe [37]. A necessary prerequisite is that the mean free path of the electrons is larger than the skyrmion size.

In samples with insignificant anomalous Hall effect, the Hall conductivity  $\sigma_{xy}$  increases with  $B$ , if  $B$  is small. A transition from a topologically trivial magnetic phase to a SkX phase would cause an abrupt change of  $\sigma_{xy}$  because the THE provides an additional contribution to  $\sigma_{xy}$  [Fig. 1(b)]. The application of a gate voltage, which allows us to scan the energy dependence of  $\sigma_{xy}$ , can make this variation either a decrease or an increase, depending on whether the Fermi energy lies below or above a VHS [red and blue lines in Fig. 1(c)].

The change of sign in  $\sigma_{xy}$  is preferably studied for large skyrmions: the sawtooth-shaped variation of the Hall conductivity becomes cultrate with increasing skyrmion size [green, blue, and red curves in Fig. 2(b)]. This behavior is, however, limited by the finite sample size because an experiment measures a conductance rather than a conductivity.



Therefore, a compromise between signal strength (favored by small skyrmions) and sharpness of the sawtooth-shaped feature (favored by large skyrmions) has to be made.

In real samples, the Hall conductivity is due to two contributions: the topological Hall effect and the anomalous Hall effect. The THE contribution to the Hall conductivity is attributed to the nontrivial topology in reciprocal space that arises from the real-space topology of the magnetic texture; spin-orbit coupling is not required. The contribution of the anomalous Hall effect relies on a nonzero Berry curvature as well but is solely induced by intrinsic spin-orbit coupling and a topologically trivial magnetic texture (like a ferromagnet); a topologically nontrivial magnetic texture is

not required. Both anomalous and topological contributions to the Hall conductivity would vary with gate voltage. Thus, the dominating contribution of the two effects should be identified in advance [38]. As real materials exhibit complicated band structures and feature intrinsic spin-orbit interaction, a combined analysis of the anomalous and the topological Hall effects seems to be worthwhile in the future.

#### ACKNOWLEDGMENTS

Fruitful discussions with Naoto Nagaosa and Tomáš Rauch are gratefully acknowledged. This work is supported by SPP 1666 of Deutsche Forschungsgemeinschaft (DFG).

- 
- [1] L. Landau, *Z. Phys.* **64**, 629 (1930).
  - [2] L. Onsager, *London, Edinburgh, Dublin Philos. Mag. J. Sci.* **43**, 1006 (1952).
  - [3] K. v. Klitzing, G. Dorda, and M. Pepper, *Phys. Rev. Lett.* **45**, 494 (1980).
  - [4] D. R. Hofstadter, *Phys. Rev. B* **14**, 2239 (1976).
  - [5] F. H. Claro and G. H. Wannier, *Phys. Rev. B* **19**, 6068 (1979).
  - [6] R. Rammal, *J. Phys.* **46**, 1345 (1985).
  - [7] F. Claro, *Phys. Status Solidi B* **104**, K31 (1981).
  - [8] D. J. Thouless, M. Kohmoto, M. P. Nightingale, and M. den Nijs, *Phys. Rev. Lett.* **49**, 405 (1982).
  - [9] K. Novoselov, A. K. Geim, S. Morozov, D. Jiang, M. Katsnelson, I. Grigorieva, S. Dubonos, and A. Firsov, *Nature (London)* **438**, 197 (2005).
  - [10] Y. Hatsugai, T. Fukui, and H. Aoki, *Phys. Rev. B* **74**, 205414 (2006).
  - [11] D. N. Sheng, L. Sheng, and Z. Y. Weng, *Phys. Rev. B* **73**, 233406 (2006).
  - [12] T. H. R. Skyrme, *Nucl. Phys.* **31**, 556 (1962).
  - [13] A. Bogdanov and D. Yablonskii, *Zh. Eksp. Teor. Fiz.* **95**, 182 (1989).
  - [14] A. Bogdanov and A. Hubert, *J. Magn. Magn. Mater.* **138**, 255 (1994).
  - [15] U. Röbner, A. Bogdanov, and C. Pfleiderer, *Nature (London)* **442**, 797 (2006).
  - [16] S. Mühlbauer, B. Binz, F. Jonietz, C. Pfleiderer, A. Rosch, A. Neubauer, R. Georgii, and P. Böni, *Science* **323**, 915 (2009).
  - [17] I. Dzyaloshinsky, *J. Phys. Chem. Solids* **4**, 241 (1958).
  - [18] T. Moriya, *Phys. Rev.* **120**, 91 (1960).
  - [19] A. Neubauer, C. Pfleiderer, B. Binz, A. Rosch, R. Ritz, P. G. Niklowitz, and P. Böni, *Phys. Rev. Lett.* **102**, 186602 (2009).
  - [20] T. Schulz, R. Ritz, A. Bauer, M. Halder, M. Wagner, C. Franz, C. Pfleiderer, K. Everschor, M. Garst, and A. Rosch, *Nat. Phys.* **8**, 301 (2012).
  - [21] N. Kanazawa, Y. Onose, T. Arima, D. Okuyama, K. Ohoyama, S. Wakimoto, K. Kakurai, S. Ishiwata, and Y. Tokura, *Phys. Rev. Lett.* **106**, 156603 (2011).
  - [22] M. Lee, W. Kang, Y. Onose, Y. Tokura, and N. P. Ong, *Phys. Rev. Lett.* **102**, 186601 (2009).
  - [23] Y. Li, N. Kanazawa, X. Z. Yu, A. Tsukazaki, M. Kawasaki, M. Ichikawa, X. F. Jin, F. Kagawa, and Y. Tokura, *Phys. Rev. Lett.* **110**, 117202 (2013).
  - [24] K. Hamamoto, M. Ezawa, and N. Nagaosa, *Phys. Rev. B* **92**, 115417 (2015).
  - [25] J. L. Lado and J. Fernández-Rossier, *Phys. Rev. B* **92**, 115433 (2015).
  - [26] T. Okubo, S. Chung, and H. Kawamura, *Phys. Rev. Lett.* **108**, 017206 (2012).
  - [27] N. Nagaosa, J. Sinova, S. Onoda, A. MacDonald, and N. Ong, *Rev. Mod. Phys.* **82**, 1539 (2010).
  - [28] Y. Hatsugai, *Phys. Rev. B* **48**, 11851 (1993).
  - [29] Y. Hatsugai, *Phys. Rev. Lett.* **71**, 3697 (1993).
  - [30] K. Everschor-Sitte and M. Sitte, *J. Appl. Phys.* **115**, 172602 (2014).
  - [31] K. Ohgushi, S. Murakami, and N. Nagaosa, *Phys. Rev. B* **62**, R6065(R) (2000).
  - [32] W. Y. Hsu and L. M. Falicov, *Phys. Rev. B* **13**, 1595 (1976).
  - [33] M. Arai and Y. Hatsugai, *Phys. Rev. B* **79**, 075429 (2009).
  - [34] I. M. Lifshitz, M. Ya. Azbel, and M. I. Kaganov, *Sov. Phys. JETP* **4**, 41 (1957) [*J. Exptl. Theoret. Phys. (U.S.S.R.)* **31**, 63 (1956)].
  - [35] M. Arai and Y. Hatsugai, *Phys. E* **42**, 740 (2010).
  - [36] X. Yu, Y. Onose, N. Kanazawa, J. Park, J. Han, Y. Matsui, N. Nagaosa, and Y. Tokura, *Nature (London)* **465**, 901 (2010).
  - [37] X. Yu, N. Kanazawa, Y. Onose, K. Kimoto, W. Zhang, S. Ishiwata, Y. Matsui, and Y. Tokura, *Nat. Mater.* **10**, 106 (2011).
  - [38] J. Matsuno, N. Ogawa, K. Yasuda, F. Kagawa, W. Koshibae, N. Nagaosa, Y. Tokura, and M. Kawasaki, *Sci. Adv.* **2**, e1600304 (2016).

### 5.3 Magnetolectric effect and orbital magnetization

**Alternative hallmarks of skyrmionic phases.** Besides the skyrmion Hall effect and the topological Hall effect of electrons, other geometrically induced phenomena have been proposed or detected in skyrmionic phases.

The orbital magnetization was predicted for materials hosting a magnetic texture with a finite topological charge [112]. As explained in the last section, the topological real-space properties of a skyrmion manifest themselves as an effective magnetic field. Just like the topological Hall effect is explainable by analogy with the conventional Hall effect in the presence of an actual magnetic field, a topologically induced orbital magnetization arises by analogy with the conventional orbital magnetization (briefly discussed in Sec. 4.3). So far, this quantity remains unobserved experimentally.

As a second phenomenon, a magnetolectric effect has been observed in the skyrmion hosts  $\text{Cu}_2\text{OSeO}_3$  [52, 132] and  $\text{GaV}_4\text{S}_8$  [133, 134]. However, its origin is attributed to the multiferroic nature of these materials and not to the presence of skyrmions. Still, as explained in Sec. 4.3, spin textures with a finite toroidal moment (like Bloch skyrmions) allow for a transverse magnetolectric effect in any case. This motivates to find a magnetolectric contribution of geometric origin that occurs even in non-multiferroic materials.

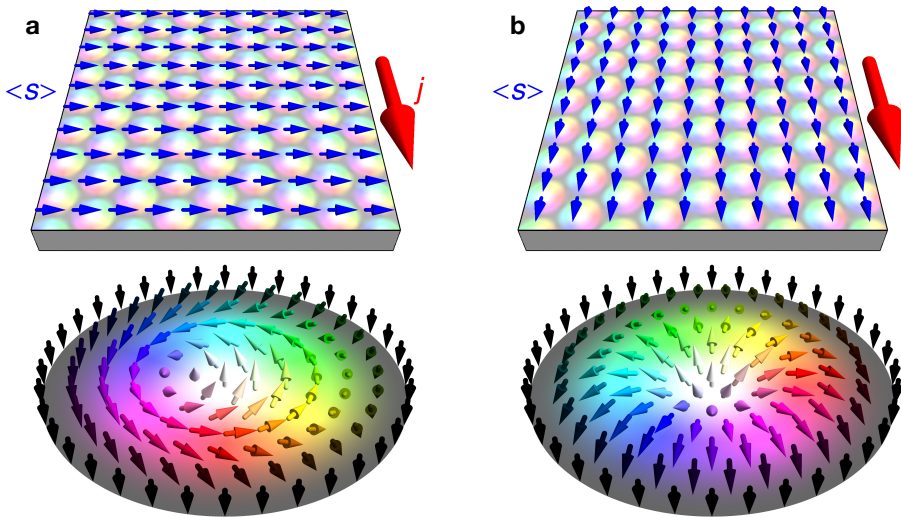


Figure 25: **Edelstein effect in skyrmion crystals.** In metals an applied electric field generates a current (density  $j$ ). Due to the Edelstein effect, a non-equilibrium spin accumulation  $\langle s \rangle$  arises. The shape of the  $\underline{\alpha}$  tensor determines the angle under which these quantities emerge. **a** For a Bloch skyrmion  $j$  and  $\langle s \rangle$  are perpendicular to each other, **b** for a Néel skyrmion they are (anti-)parallel.

**This publication.** In the following publication “Magnetolectric effect and orbital magnetization in skyrmion crystals: Detection and characterization of skyrmions” [BG3] the two above discussed effects have been quantified for different types of skyrmion crystals using a tight-binding model (Sec. 4.3).

For the orbital magnetization we explain its dependence on the properties of the electronic band structure, similar to the discussion of the topological Hall effect in the before presented publication [BG2]. Furthermore, we find that the orbital magnetization

is proportional to the topological charge of the texture, similar to the topological Hall conductivity.

As the main result, we predict a magnetolectric effect which arises in any skyrmion-hosting material; the contribution arises solely due to the geometric properties of the skyrmion. As expected from the geometric considerations in Sec. 4.3, the transverse tensor element is proportional to the toroidal moment of the skyrmion: a Bloch skyrmion has a finite toroidal moment and a Néel skyrmion's toroidal moment vanishes by symmetry. As a consequence, these two types of skyrmions can be distinguished by their transverse magnetolectric polarizability  $\alpha_{xy}$ . Knowledge of the full  $\underline{\alpha}$  tensor allows to determine the helicity of an unknown skyrmion unambiguously.

Since many skyrmion hosts are metallic, it is important to clarify the meaning of  $\underline{\alpha}$  for these materials. It cannot characterize a magnetolectric effect since an electric polarization is ill-defined in a metal. Instead, the intrinsic Edelstein effect is quantified. The electric field generates a current which, in turn, generates a non-equilibrium spin accumulation  $\langle s \rangle$  (similar to a magnetization). As Onsager reciprocal effect, the inverse Edelstein effect describes the emergence of a charge current (time derivative of  $\mathbf{P}$ ) upon spin pumping (time derivative of  $\mathbf{B}$ ). The nomenclature of this effect is quite intricate: an Edelstein effect is commonly defined for systems with time-reversal symmetry, which is however broken in any magnetic material. For this reason, the described effect has also been labeled 'new magnetolectric effect' [135] or simply 'magnetolectric effect in metals' [108]. We decided to stick with this nomenclature in the following publication. The effect has originally been predicted for metals with coplanar toroidal spin textures [108], and has been confirmed in UNi<sub>4</sub>B [135] experimentally.

The following publication: Reprinted (whole article) with permission from (B. Göbel *et al.* Physical Review B **99**, 060406(R) (2019); Ref. [BG3]; Magnetolectric effect and orbital magnetization in skyrmion crystals: Detection and characterization of skyrmions). Copyright (2019) by the American Physical Society.

## Magnetoelectric effect and orbital magnetization in skyrmion crystals: Detection and characterization of skyrmions

Börge Göbel,<sup>1,\*</sup> Alexander Mook,<sup>1</sup> Jürgen Henk,<sup>2</sup> and Ingrid Mertig<sup>1,2</sup>

<sup>1</sup>Max-Planck-Institut für Mikrostrukturphysik, D-06120 Halle (Saale), Germany

<sup>2</sup>Institut für Physik, Martin-Luther-Universität Halle-Wittenberg, D-06099 Halle (Saale), Germany



(Received 26 October 2017; revised manuscript received 16 May 2018; published 13 February 2019)

Skyrmions are small magnetic quasiparticles, which are uniquely characterized by their topological charge and their helicity. In this Rapid Communication, we show via calculations how both properties can be determined without relying on real-space imaging. The orbital magnetization and topological Hall conductivity measure the arising magnetization due to the circulation of electrons in the bulk and the occurrence of topologically protected edge channels due to the emergent field of a skyrmion crystal. Both observables quantify the topological Hall effect and distinguish skyrmions from antiskyrmions by sign. Additionally, we predict a magnetoelectric effect in skyrmion crystals, which is the generation of a magnetization (polarization) by application of an electric (magnetic) field. This effect is quantified by spin toroidization and magnetoelectric polarizability. The dependence of the transverse magnetoelectric effect on the skyrmion helicity fits that of the classical toroidal moment of the spin texture and allows one to differentiate skyrmion helicities: It is largest for Bloch skyrmions and zero for Néel skyrmions. We predict distinct features of the four observables that can be used to detect and characterize skyrmions in experiments.

DOI: [10.1103/PhysRevB.99.060406](https://doi.org/10.1103/PhysRevB.99.060406)

*Introduction.* Skyrmionics has attracted enormous interest over the recent years, as skyrmions [1–5]—small magnetic quasiparticles that are topologically protected—are aspirants to be “bits” in future data storage devices [6–16]. The integral of the local spin chirality

$$n_{\text{Sk}}(\mathbf{r}) = \mathbf{s}(\mathbf{r}) \cdot \left( \frac{\partial \mathbf{s}(\mathbf{r})}{\partial x} \times \frac{\partial \mathbf{s}(\mathbf{r})}{\partial y} \right) \quad (1)$$

of a skyrmion with magnetic texture  $\mathbf{s}(\mathbf{r})$  tells the skyrmion number  $N_{\text{Sk}} = \pm 1$  [17,18], that is, the topological invariant which characterizes skyrmions and antiskyrmions [19–22], respectively. On top of this,  $n_{\text{Sk}}(\mathbf{r})$  induces a topological Hall effect (THE) [23–34], which is an additional contribution to the Hall effect [35] of electrons in skyrmion crystals (SkXs, a periodic array of skyrmions; Fig. 1).

Another quantity related to the magnetic texture is the orbital magnetization, which is explained in a semiclassical picture by the circulation of conduction electrons in the presence of spin-orbit coupling (SOC) [36–41]. Recently, it has been shown that spin chirality, for example, in SkXs, can as well induce an orbital magnetization, even without SOC [42–44].

In this Rapid Communication, we establish a complete scheme (Fig. 1) for identifying the type of SkX in an experiment, without reverting to real-space imaging (e.g., Lorentz microscopy [45]). The TH conductivity and the orbital magnetization describe the THE and are proportional to  $N_{\text{Sk}}$ ; therefore they differentiate skyrmions from antiskyrmions. Furthermore, we predict a magnetoelectric effect in SkXs, which is within experimental reach; the magnetoelectric po-

larizability [46–48] and the spin toroidization [49,50] allow one to determine the skyrmion helicity, by which Néel skyrmions are differentiated from Bloch skyrmions. While the THE quantities are based on reciprocal space Berry curvature, the magnetoelectric effect is characterized by the mixed Berry curvature analogs (Fig. 1).

*Model and methods.* We consider a two-dimensional square lattice with a fixed skyrmion texture  $\{s_i\}$  (unit length,  $i$  lattice site). The resulting skyrmions and antiskyrmions can have various helicities [cf. Figs. 1(c)–1(e)].

The electrons in the SkX are described by a tight-binding Hamiltonian

$$H = \sum_{ij} t c_i^\dagger c_j + m \sum_i s_i \cdot (c_i^\dagger \boldsymbol{\sigma} c_i) \quad (2)$$

( $c_i^\dagger$  and  $c_j$  creation and annihilation operators, respectively), with Hund’s rule coupling. The electron spins interact with the magnetic texture ( $m$  coupling energy;  $s_i$  unit vector;  $\boldsymbol{\sigma}$  vector of Pauli matrices), which could be created by localized  $d$  electrons that are not explicitly featured in this one-orbital Hamiltonian.

From the eigenvalues  $E_n(\mathbf{k})$  and eigenvectors  $|u_n(\mathbf{k})\rangle$  of the Hamiltonian (2) we calculate the  $\mathbf{k}$  space and the mixed Berry curvature for band  $n$ ,

$$\Omega_n^{(ij)}(\mathbf{k}) = -2 \text{Im} \langle \partial_{k_i} u_n(\mathbf{k}) | \partial_{k_j} u_n(\mathbf{k}) \rangle, \quad (3a)$$

$$D_n^{(ij)}(\mathbf{k}) = -2 \text{Im} \langle \partial_{k_i} u_n(\mathbf{k}) | \frac{1}{m} \partial_{s_j} u_n(\mathbf{k}) \rangle, \quad (3b)$$

respectively. With

$$v_{nl}^{(j)}(\mathbf{k}) \equiv \langle u_n(\mathbf{k}) | \partial_{k_j} H(\mathbf{k}) | u_l(\mathbf{k}) \rangle, \quad (4a)$$

$$s_{nl}^{(j)}(\mathbf{k}) \equiv \langle u_n(\mathbf{k}) | \sigma_j | u_l(\mathbf{k}) \rangle \quad (4b)$$

\*Corresponding author: [bgoebel@mpi-halle.mpg.de](mailto:bgoebel@mpi-halle.mpg.de)

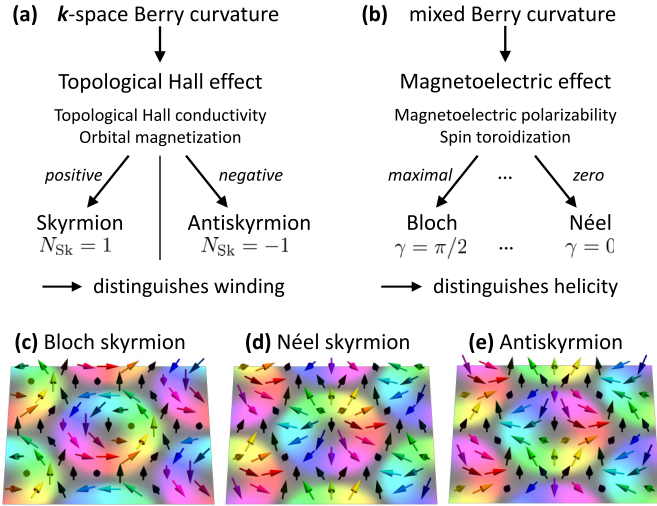


FIG. 1. Core message of this Rapid Communication. (a) Skyrmions and antiskyrmions are distinguished by the topological Hall effect. (b) The helicity of skyrmions (e.g., Bloch and Néel skyrmions) is differentiated by the magnetoelectric effect. With these quantities, (c) Bloch skyrmions, (d) Néel skyrmions, and (e) antiskyrmions can be distinguished. The color scale in (c)–(e) indicates the in-plane orientation of the spins (arrows).

( $j = x, y, z$ ), we arrive at

$$\Omega_n^{(ij)}(\mathbf{k}) = -2 \operatorname{Im} \sum_{l \neq n} \frac{v_{nl}^{(i)}(\mathbf{k}) v_{ln}^{(j)}(\mathbf{k})}{[E_n(\mathbf{k}) - E_l(\mathbf{k})]^2}, \quad (5a)$$

$$D_n^{(ij)}(\mathbf{k}) = -2 \operatorname{Im} \sum_{l \neq n} \frac{v_{nl}^{(i)}(\mathbf{k}) s_{ln}^{(j)}(\mathbf{k})}{[E_n(\mathbf{k}) - E_l(\mathbf{k})]^2}. \quad (5b)$$

Integration over the occupied states [shorthand notation  $\int_{\text{occ}}(\cdot) \equiv \sum_n \int(\cdot) \Theta(E_n(\mathbf{k}) - E_F) d^2k$  with  $E_F$  Fermi energy and  $\Theta$  Fermi distribution at zero temperature] yields the conductivity  $\sigma_{ij}$  [51] and the magnetoelectric polarizability  $\alpha_{ij}$  [47–49],

$$\sigma_{ij}(E_F) = -\frac{e^2}{h} \frac{1}{2\pi} \int_{\text{occ}} \Omega_n^{(ij)}(\mathbf{k}), \quad (6a)$$

$$\alpha_{ij}(E_F) = g\mu_B \frac{e}{(2\pi)^2} \int_{\text{occ}} D_n^{(ij)}(\mathbf{k}). \quad (6b)$$

From the orbital magnetic moment [36,37]

$$\mathbf{m}_n(\mathbf{k}) = -\frac{e}{2\hbar} \operatorname{Im} \sum_{l \neq n} \frac{v_{nl}(\mathbf{k}) \times v_{ln}(\mathbf{k})}{E_n(\mathbf{k}) - E_l(\mathbf{k})}, \quad (7)$$

we calculate the orbital magnetization [39],

$$M_z(E_F) = \frac{1}{(2\pi)^2} \int_{\text{occ}} m_n^{(z)}(\mathbf{k}) + \frac{e}{\hbar} \frac{1}{(2\pi)^2} \times \int_{\text{occ}} \frac{\Omega_n^{(xy)}(\mathbf{k}) - \Omega_n^{(yx)}(\mathbf{k})}{2} [E_F - E_n(\mathbf{k})]; \quad (8)$$

likewise, from the spin toroidal moment,

$$\mathbf{t}_n(\mathbf{k}) = \frac{g\mu_B}{2} \operatorname{Im} \sum_{l \neq n} \frac{v_{nl}(\mathbf{k}) \times s_{ln}}{E_n(\mathbf{k}) - E_l(\mathbf{k})}, \quad (9)$$

the spin toroidization, as recently shown by Gao *et al.* [49],

$$T_z(E_F) = \frac{1}{(2\pi)^2} \int_{\text{occ}} t_n^{(z)}(\mathbf{k}) - g\mu_B \frac{1}{(2\pi)^2} \times \int_{\text{occ}} \frac{D_n^{(xy)}(\mathbf{k}) - D_n^{(yx)}(\mathbf{k})}{2} [E_F - E_n(\mathbf{k})]. \quad (10)$$

The terms with  $m_n^{(z)}$  and  $t_n^{(z)}$  capture the intrinsic contributions of each Bloch electron, while the other terms account for the Berry curvatures  $\Omega_n^{(ij)}$  and  $D_n^{(ij)}$ , which modify the density of states [39].

*Topological Hall effect as a quantum Hall effect.* Before discussing the novel results concerning the energy-dependent orbital magnetization, magnetoelectric polarizability, and spin toroidization, a sketch of the band formation and the TH conductivity is adequate; cf. Refs. [30,31].

For  $m = 0$  in the Hamiltonian (2), the so-called zero-field band structure is spin degenerate because there is neither spin-orbit coupling nor coupling to the SkX magnetic texture.

If  $m$  is turned on, the spin degeneracy is lifted and the electron spins tend to align locally parallel or antiparallel with the magnetic texture. At  $m \approx 5t$  the spin alignment is almost complete and two blocks with  $n_b$  (number of sites forming a SkX unit cell) bands each are formed: one for parallel (higher energies) and one for antiparallel alignment (lower energies); see Fig. 2(a).

In the limit  $m \rightarrow \infty$  the alignment is perfect and the electron spins follow the skyrmion texture adiabatically. Both blocks are identical but shifted in energy. Roughly speaking, besides the rigid shift by  $\pm m$ , the nontrivial Zeeman term leads to a “condensation” of bands [identified as Landau levels (LLs) in what follows].

The perfect alignment for  $m \rightarrow \infty$  motivates the transformation of the Hamiltonian (2): A local spin rotation diagonalizes the Zeeman term [29–31,52] and alters the hopping term (the hopping strengths  $t_{ij}$  become complex  $2 \times 2$  matrices). Since the system can be viewed as consisting of two (uncoupled) spin species, it is sufficient to consider only one species. The resulting Hamiltonian describes a spin-polarized version of the quantum Hall effect (QHE). Since we discuss charge conductivities, the diagonal Zeeman term is dropped and we arrive at the Hamiltonian

$$H_{\parallel} = \sum_{ij} t_{ij}^{(\text{eff})} \tilde{c}_i^{\dagger} \tilde{c}_j \quad (11)$$

of a quantum Hall (QH) system (spinless electrons on a lattice) [53–59]. The effective hopping strengths  $t_{ij}^{(\text{eff})}$  describe the coupling of the electron charges with a collinear inhomogeneous magnetic field,

$$B_{\text{em}}^{(z)}(\mathbf{r}) \propto n_{\text{Sk}}(\mathbf{r}). \quad (12)$$

This emergent field [17,18] is given by the spin chirality (1), that is, the real-space Berry curvature in the continuous limit [17,18]. The parallel (antiparallel) alignment of the electron spins, corresponding to the upper (lower) block in the band structure for  $m \rightarrow \infty$ , manifests itself in the sign of the nonzero average of  $B_{\text{em}}$ .

For finite  $m$ , the mapping of the THE onto the QHE—and the one-to-one identification of bands and LLs—is reasonable as long as the band blocks are separated, i.e., for  $m \geq 4t$  [60].

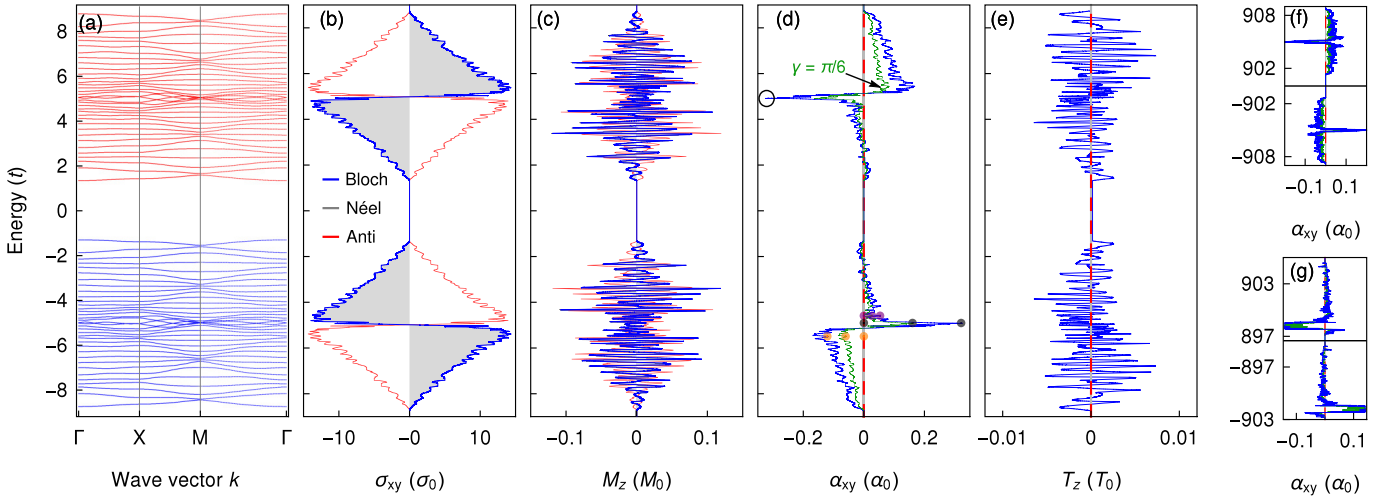


FIG. 2. Properties of a skyrmion crystal. Parameters read  $n_b = 36$  (sites in the skyrmion unit cell), coupling  $m = 5t$ . A Bloch ( $N_{\text{Sk}} = +1$ ,  $\gamma = \pi/2$ ; topological charge and helicity), a Néel ( $N_{\text{Sk}} = +1$ ,  $\gamma = 0$ ), and an antiskyrmion ( $N_{\text{Sk}} = -1$ ,  $\gamma = 0$ ) are compared. (a) Band structure, (b) TH conductivity  $\sigma_{xy}$ , (c) orbital magnetization  $M_z$ , (d) magnetolectric polarizability  $\alpha_{xy}$ , and (e) spin toroidization  $T_z$  are separated into blocks in which the electron spins are aligned parallel [red in (a)] or antiparallel (blue) with the skyrmion magnetic texture ( $\sigma_0 \equiv e^2/h$ ,  $M_0 \equiv te/\hbar$ ,  $\alpha_0 \equiv g\mu_B e/at$ , and  $T_0 \equiv g\mu_B/a$ ;  $a$  is the lattice constant). The band structure is identical for all skyrmion types. In (d) results for an intermediate skyrmion with  $\gamma = \pi/6$  are shown in addition (green). Colored dots refer to Fig. 3. (f)  $\alpha_{xy}$  in the strong-coupling limit  $m = 900t$  and (g) for larger skyrmions  $n_b = 48$  on a different lattice (triangular).

The LL character of the bands arises in Chern numbers and in the TH conductivity [Fig. 2(b)]. Bands of the upper (lower) block carry Chern numbers of  $+1$  ( $-1$ ) due to the positive (negative) average emergent field. As a result, the TH conductivity is quantized in steps of  $e^2/h$ . At the shifted van Hove singularity (VHS)  $E_{\text{VHS}} = \pm m$ , the TH conductivity changes sign in a narrow energy window.

The quantization and the sign change are closely related to the zero-field band structure [30,31,61]. At the VHS the character of the Fermi lines changes from electron- to holelike. The bands close to the VHS are simultaneously formed from electron- and holelike states, leading to a large Chern number that causes this jump.

Having sketched the influences of the zero-field band structure on the THE, we derive consequences for the orbital magnetization.

*Orbital magnetization.* The block separation manifests itself in the orbital magnetization (8) as well. Its energy dependence within the lower block is similar to that in the upper one but with opposite sign [Fig. 2(c)]; the latter is explained by the alignment of the electron spin with the magnetic texture.

$M_z(E_F)$  shows rapid oscillations with zero crossings within the band gaps, which is explicated as follows. The emergent field leads to a rotation of an electron wave packet around its center of mass. The first term in Eq. (8), given by  $\mathbf{m}_n(\mathbf{k})$ , changes continuously within the bands but is constant within the band gaps. In contrast, the phase-space correction due to the Berry curvature [39] (second term) varies continuously in energy. Its slope in the band gaps is determined by the TH conductivity,

$$\frac{\partial}{\partial E_F} M_z(E_F) = \frac{1}{2e} [\sigma_{yx}(E_F) - \sigma_{xy}(E_F)]. \quad (13)$$

Both gauge-invariant contributions are similar in absolute value but differ in sign. Consequently, their small difference leads to one oscillation per band.

For a better understanding we relate the orbital magnetization in a SkX to that of the associated QH system with (almost) dispersionless bands [62–64]. Besides the oscillations we identify a continuous envelope function [62] (Fig. S1 in the Supplemental Material [65]). In the SkX this envelope is “deformed” due to the inhomogeneity of the emergent field. Nevertheless, the spectrum of the QH system is quite similar to that of the SkX.

The influences of the two terms in Eq. (8) show up “undistorted” in the QH system. The orbital magnetic moment per band (entering the first term) decreases (increases) stepwise at energies below (above) the shifted zero-field VHSs at  $E_{\text{VHS}} \equiv \pm m$  [cf. Fig. S1(c)]. There is no sign change at the VHSs, in contrast to the TH conductivity. Still, a zero-field explanation holds as  $\mathbf{M}$  is also based on the  $\mathbf{k}$ -space Berry curvature. At energies below a VHS, LLs are formed from electronlike orbits with a fixed common circular direction. At energies above a VHS, holelike orbits are formed in addition. Since these exhibit the opposite circular direction, they contribute with opposite sign. Both contributions result in an extremum at the VHS.

The size and shape of the orbits dictate the magnitude of the contributions of each band. Therefore, on one hand, the oscillation amplitudes in Figs. 2(c) and S1(b) [corresponding to the step heights in Fig. S1(c)] increase with increasing energy distance of the Fermi energy and band edges. On the other hand, the oscillation amplitudes vanish at the VHS. Recall that the Fermi lines have zero curvature at this particular energy.

When exchanging skyrmions with antiskyrmions the sign of the emergent field changes and so does the sign of both the TH conductivity and the orbital magnetization in Figs. 2(b) and 2(c), as both characterize the THE. These quantities

distinguish skyrmions from antiskyrmions but cannot distinguish Bloch and Néel skyrmions.

**Magnetolectric polarizability.** The independence of all above quantities on the skyrmions' helicity calls for further characterization: This is met by the magnetolectric effect described by magnetolectric polarizability and spin toroidization. Both quantities are derived from the mixed Berry curvature  $D_n^{(ij)}$ . If the Fermi energy lies between two Landau levels, the system is insulating. In this case, the transverse magnetolectric polarizability

$$\alpha_{xy} = \left. \frac{\partial M_y}{\partial E_x} \right|_{B=0} = \left. \frac{\partial P_x}{\partial B_y} \right|_{E=0} \quad (14)$$

quantifies the magnetolectric coupling [46] to in-plane fields that are applied to a sample in the SkX phase: An in-plane magnetization  $\mathbf{M}$  (polarization  $\mathbf{P}$ ) can be modified by an orthogonal in-plane electric field  $\mathbf{E}$  (magnetic field  $\mathbf{B}$  [66]). If the Fermi energy lies within a Landau level, the system is metallic and cannot exhibit a polarization. Nevertheless, an in-plane magnetization can be produced by perpendicular in-plane currents that are brought about by an applied electric field. This so-called magnetolectric effect in metals is equivalent to an intrinsic Edelstein effect [67] and was predicted [48] and confirmed experimentally for UNi<sub>4</sub>B [68], which shows a coplanar toroidal order. The Onsager reciprocal effect is the inverse Edelstein effect: the generation of a current via the injection of a nonequilibrium spin polarization.

For a Bloch SkX, the spectrum of the magnetolectric polarizability  $\alpha_{xy}(E_F)$ , Eq. (6b), shows a sign reversal of the two separated blocks [Fig. 2(d)]. Although  $\alpha_{xy}$  exhibits plateaus, it is not quantized. Around the VHS the curve shows a sharp peak (circle).

For  $m \gg t$  the spectrum of each block becomes symmetric [Fig. 2(f)]. Within a block the sign of  $\alpha_{xy}$  mostly remains, in contrast to  $\sigma_{xy}$ . The monotonicity, however, is reversed above the VHS, the reason being the exchange of  $v_{ln}$  and  $s_{ln}$  in Eqs. (5a) and (5b). While the sign of the velocity is given by the electron or hole character, the spin is aligned with the magnetic texture, irrespective of the electronic character of band  $l$ . The mixing of electron and hole states in a small energy window about  $E_{VHS}$  leads to a collapse of  $\alpha_{xy}$  with a reversed sign for this small energy region. This energy window corresponds to the jump in  $\sigma_{xy}$ .

**Spin toroidization.** As the magnetolectric polarizability is related to the TH conductivity, the spin toroidization (10) is related to the orbital magnetization. It comprises two terms: one given by the spin toroidal moments  $\mathbf{t}_n$ , and the other by the phase-space correction due to the mixed Berry curvature. In analogy to Eq. (13), its slope

$$\frac{\partial}{\partial E_F} T_z(E_F) = \frac{1}{2e} [\alpha_{yx}(E_F) - \alpha_{xy}(E_F)]$$

is given by the magnetolectric polarizability in the band gap [49].

$T_z(E_F)$  oscillates rapidly for the Bloch SkX [Fig. 2(e)]. In the strong-coupling limit  $m \gg t$  the shape of the oscillations becomes more pronounced.

**Relation to skyrmion helicity.** Changing continuously the skyrmion helicity, from Bloch to Néel skyrmions,  $\alpha_{xy}$  and  $T_z$  are reduced by a Fermi-energy-independent factor

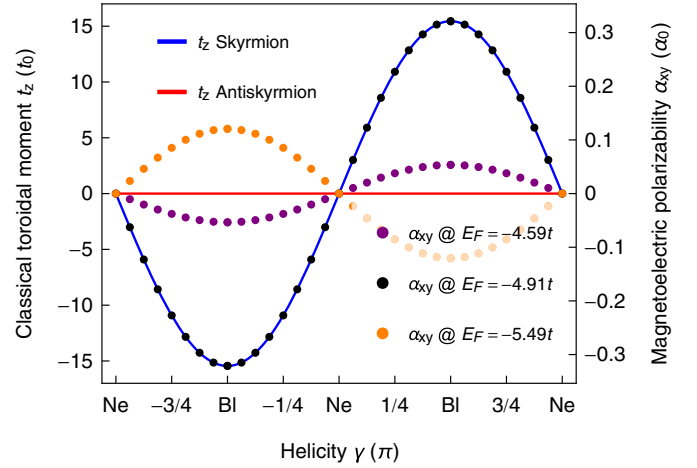


FIG. 3. Dependence of the classical toroidal moment  $t_z$  (blue, red) and the magnetolectric polarizability  $\alpha_{xy}$  on the helicity of a skyrmion for selected Fermi energies  $E_F$  [distinguished by color, as indicated; also marked in Fig. 2(d)].  $t_z$  is proportional to  $\alpha_{xy}$ , with the proportionality factor depending on  $E_F$ .  $t_0 \equiv g\mu_B a$ ,  $\alpha_0 \equiv g\mu_B e/at$ .

[Fig. 3 and green curve in Fig. 2(d)]; both quantities vanish for Néel SkXs by symmetry. We find that this factor is quantified by the classical toroidal moment [48]

$$\mathbf{t} = \frac{g\mu_B}{2} \sum_i \mathbf{r}_i \times \mathbf{s}_i \propto \sin(\gamma) \mathbf{e}_z \quad (15)$$

( $\mathbf{r}_i$  position of spin  $\mathbf{s}_i$  with respect to the skyrmion center).  $\mathbf{t}$  is a pure real-space quantity given by the skyrmion helicity  $\gamma$  (blue line in Fig. 3). This easily accessible quantity successfully reproduces the functional dependence of  $\alpha_{xy}$  (and also of  $T_z$ ) on the helicity but fails to reproduce the proportionality factor because it does not depend on  $E_F$ . Being a classical quantity,  $\mathbf{t}$  cannot explain the shape of  $\alpha_{xy}(E_F)$  and  $T_z(E_F)$ .

For a Bloch skyrmion ( $\gamma = \pi/2$ ) the full  $\alpha$  tensor is antisymmetric ( $\alpha_{xy} = -\alpha_{yx}$ ) and has no longitudinal components. A Néel skyrmion ( $\gamma = 0$ ) exhibits only a longitudinal effect  $\alpha_{xx} = \alpha_{yy}$  identical to  $\alpha_{xy}$  of the Bloch skyrmion, since all spins are rotated by  $\pi/2$  around the  $z$  axis [69]. For antiskyrmions Eq. (15) always gives zero. This is why the  $\alpha$  tensor is symmetric and  $T_z$  is zero in this case. Rotation of the sample always allows one to diagonalize the tensor for antiskyrmion crystals since  $\gamma$  merely orients the two principal axes of an antiskyrmion, for which the texture points into opposite directions giving opposite longitudinal effects  $\alpha_{xx} = -\alpha_{yy}$ .

The full tensor of the texture-induced magnetolectric polarizability for a structural square lattice reads

$$\alpha(E_F) = \alpha_{xy}^{\text{Bloch}}(E_F) \begin{pmatrix} \cos(\gamma) & \sin(\gamma) \\ -N_{\text{Sk}} \sin(\gamma) & N_{\text{Sk}} \cos(\gamma) \end{pmatrix}.$$

The measurement of all tensor elements allows one to determine topological charge  $N_{\text{Sk}}$  and helicity  $\gamma$  of an unknown skyrmion.

**Conclusion.** In this Rapid Communication, we established a complete scheme for the characterization of the skyrmion crystals' topological charge and helicity (Fig. 1). Our findings on the topological Hall effect and the magnetolectric effect are explained by quite simple pictures: a quantum Hall

system and the classical toroidal moment of a spin texture, respectively.

Our prediction of the helicity-dependent magnetoelectric effect allows one to discriminate Néel and Bloch skyrmions, without reverting to real-space imaging of their magnetic texture (which is in particular difficult for skyrmions arising at interfaces). For an electric field of  $10^8$  V/m an additional in-plane magnetic moment of one-hundredth of  $g\mu_B$  is induced per atom [70]. The collapse of  $\alpha_{xy}$  near van Hove singularities is a significant feature and could establish a new hallmark of the SkX phase: It is observable by shifting the Fermi energy (e.g., by a gate voltage or by chemical doping).

As shown in Figs. 2(f) and 2(g) as well as in the Supplemental Material [65], the main claims of this Rapid Communication depend qualitatively neither on skyrmion size, strength of the exchange interaction, nor on the lattice geometry. The established scheme for discrimination (Fig. 1) is a general result, which is not limited to specific materials. All presented quantities arise solely due to coupling of

“spinful” electrons with the skyrmion texture and vanish in the absence of skyrmions. The skyrmion-induced contributions are distinguishable from the corresponding nonskyrmionic counterparts, e.g., the anomalous Hall effect in the presence of spin-orbit coupling, the “conventional” magnetization, and the “conventional” magnetoelectric effect in multiferroic materials [14,71–73]).

An experimental proof of the predicted magnetoelectric effect can be done simplest for a nonmultiferroic material with a crystal symmetry that allows only for Bloch skyrmions (e.g., MnSi) [74]. The transverse magnetoelectric effect arises purely due to toroidal order of the SkX and should be measurable in an isolated manner in such a material. The experiment can be conducted in analogy to that of Ref. [68], in which the metallic coplanar toroidal magnet UNi<sub>4</sub>B was investigated.

*Acknowledgments.* We are grateful to Yukitoshi Motome, Gerrit E. W. Bauer, and Annika Johansson for fruitful discussions. This work is supported by Priority Program SPP 1666 and SFB 762 of Deutsche Forschungsgemeinschaft (DFG).

- 
- [1] T. H. R. Skyrme, *Nucl. Phys.* **31**, 556 (1962).  
 [2] A. N. Bogdanov and D. A. Yablonskii, *Zh. Eksp. Teor. Fiz.* **95**, 178 (1989) [*Sov. Phys. JETP* **68**, 101 (1989)].  
 [3] A. Bogdanov and A. Hubert, *J. Magn. Magn. Mater.* **138**, 255 (1994).  
 [4] U. Röbber, A. Bogdanov, and C. Pfleiderer, *Nature (London)* **442**, 797 (2006).  
 [5] S. Mühlbauer, B. Binz, F. Jonietz, C. Pfleiderer, A. Rosch, A. Neubauer, R. Georgii, and P. Böni, *Science* **323**, 915 (2009).  
 [6] A. Fert, V. Cros, and J. Sampaio, *Nat. Nanotechnol.* **8**, 152 (2013).  
 [7] R. Wiesendanger, *Nat. Rev. Mater.* **1**, 16044 (2016).  
 [8] N. Romming, C. Hanneken, M. Menzel, J. E. Bickel, B. Wolter, K. von Bergmann, A. Kubetzka, and R. Wiesendanger, *Science* **341**, 636 (2013).  
 [9] P.-J. Hsu, A. Kubetzka, A. Finco, N. Romming, K. von Bergmann, and R. Wiesendanger, *Nat. Nanotechnol.* **12**, 123 (2017).  
 [10] X. Zhang, M. Ezawa, and Y. Zhou, *Sci. Rep.* **5**, 9400 (2015).  
 [11] X. Zhang, Y. Zhou, M. Ezawa, G. Zhao, and W. Zhao, *Sci. Rep.* **5**, 11369 (2015).  
 [12] W. Jiang, P. Upadhyaya, W. Zhang, G. Yu, M. B. Jungfleisch, F. Y. Fradin, J. E. Pearson, Y. Tserkovnyak, K. L. Wang, O. Heinonen *et al.*, *Science* **349**, 283 (2015).  
 [13] O. Boulle, J. Vogel, H. Yang, S. Pizzini, D. de Souza Chaves, A. Locatelli, T. O. Menteş, A. Sala, L. D. Buda-Prejbeanu, O. Klein *et al.*, *Nat. Nanotechnol.* **11**, 449 (2016).  
 [14] S. Seki, X. Yu, S. Ishiwata, and Y. Tokura, *Science* **336**, 198 (2012).  
 [15] S. Woo, K. Litzius, B. Krüger, M.-Y. Im, L. Caretta, K. Richter, M. Mann, A. Krone, R. M. Reeve, M. Weigand *et al.*, *Nat. Mater.* **15**, 501 (2016).  
 [16] B. Göbel, A. Mook, J. Henk, and I. Mertig, *Phys. Rev. B* **99**, 020405(R) (2019).  
 [17] N. Nagaosa and Y. Tokura, *Nat. Nanotechnol.* **8**, 899 (2013).  
 [18] K. Everschor-Sitte and M. Sitte, *J. Appl. Phys.* **115**, 172602 (2014).  
 [19] A. K. Nayak, V. Kumar, T. Ma, P. Werner, E. Pippel, R. Sahoo, F. Damay, U. K. Röbber, C. Felser, and S. S. Parkin, *Nature (London)* **548**, 561 (2017).  
 [20] M. Hoffmann, B. Zimmermann, G. P. Müller, D. Schürhoff, N. S. Kiselev, C. Melcher, and S. Blügel, *Nat. Commun.* **8**, 308 (2017).  
 [21] S. Huang, C. Zhou, G. Chen, H. Shen, A. K. Schmid, K. Liu, and Y. Wu, *Phys. Rev. B* **96**, 144412 (2017).  
 [22] B. Göbel, A. Mook, J. Henk, I. Mertig, and O. A. Tretiakov, *arXiv:1811.07068*.  
 [23] A. Neubauer, C. Pfleiderer, B. Binz, A. Rosch, R. Ritz, P. G. Niklowitz, and P. Böni, *Phys. Rev. Lett.* **102**, 186602 (2009).  
 [24] T. Schulz, R. Ritz, A. Bauer, M. Halder, M. Wagner, C. Franz, C. Pfleiderer, K. Everschor, M. Garst, and A. Rosch, *Nat. Phys.* **8**, 301 (2012).  
 [25] N. Kanazawa, Y. Onose, T. Arima, D. Okuyama, K. Ohoyama, S. Wakimoto, K. Kakurai, S. Ishiwata, and Y. Tokura, *Phys. Rev. Lett.* **106**, 156603 (2011).  
 [26] M. Lee, W. Kang, Y. Onose, Y. Tokura, and N. P. Ong, *Phys. Rev. Lett.* **102**, 186601 (2009).  
 [27] Y. Li, N. Kanazawa, X. Z. Yu, A. Tsukazaki, M. Kawasaki, M. Ichikawa, X. F. Jin, F. Kagawa, and Y. Tokura, *Phys. Rev. Lett.* **110**, 117202 (2013).  
 [28] P. Bruno, V. K. Dugaev, and M. Taillefumier, *Phys. Rev. Lett.* **93**, 096806 (2004).  
 [29] K. Hamamoto, M. Ezawa, and N. Nagaosa, *Phys. Rev. B* **92**, 115417 (2015).  
 [30] B. Göbel, A. Mook, J. Henk, and I. Mertig, *Phys. Rev. B* **95**, 094413 (2017).  
 [31] B. Göbel, A. Mook, J. Henk, and I. Mertig, *New J. Phys.* **19**, 063042 (2017).  
 [32] J. L. Lado and J. Fernández-Rossier, *Phys. Rev. B* **92**, 115433 (2015).  
 [33] P. B. Ndiaye, C. A. Akosa, and A. Manchon, *Phys. Rev. B* **95**, 064426 (2017).  
 [34] B. Göbel, A. Mook, J. Henk, and I. Mertig, *Eur. Phys. J. B* **91**, 179 (2018).



- [35] E. H. Hall, *Am. J. Math.* **2**, 287 (1879).
- [36] M.-C. Chang and Q. Niu, *Phys. Rev. B* **53**, 7010 (1996).
- [37] A. Raoux, F. Piéchon, J.-N. Fuchs, and G. Montambaux, *Phys. Rev. B* **91**, 085120 (2015).
- [38] J.-P. Hanke, F. Freimuth, A. K. Nandy, H. Zhang, S. Blügel, and Y. Mokrousov, *Phys. Rev. B* **94**, 121114 (2016).
- [39] D. Xiao, J. Shi, and Q. Niu, *Phys. Rev. Lett.* **95**, 137204 (2005).
- [40] T. Thonhauser, D. Ceresoli, D. Vanderbilt, and R. Resta, *Phys. Rev. Lett.* **95**, 137205 (2005).
- [41] D. Ceresoli, T. Thonhauser, D. Vanderbilt, and R. Resta, *Phys. Rev. B* **74**, 024408 (2006).
- [42] M. d. S. Dias, J. Bouaziz, M. Bouhassoune, S. Blügel, and S. Lounis, *Nat. Commun.* **7**, 13613 (2016).
- [43] M. d. S. Dias and S. Lounis, *Proc. SPIE* **10357**, 103572A (2017).
- [44] F. R. Lux, F. Freimuth, S. Blügel, and Y. Mokrousov, *Communications Physics* **1**, 60 (2018).
- [45] X. Yu, Y. Onose, N. Kanazawa, J. Park, J. Han, Y. Matsui, N. Nagaosa, and Y. Tokura, *Nature (London)* **465**, 901 (2010).
- [46] A. M. Essin, J. E. Moore, and D. Vanderbilt, *Phys. Rev. Lett.* **102**, 146805 (2009).
- [47] A. M. Essin, A. M. Turner, J. E. Moore, and D. Vanderbilt, *Phys. Rev. B* **81**, 205104 (2010).
- [48] S. Hayami, H. Kusunose, and Y. Motome, *Phys. Rev. B* **90**, 024432 (2014).
- [49] Y. Gao, D. Vanderbilt, and D. Xiao, *Phys. Rev. B* **97**, 134423 (2018).
- [50] N. A. Spaldin, M. Fiebig, and M. Mostovoy, *J. Phys.: Condens. Matter* **20**, 434203 (2008).
- [51] N. Nagaosa, J. Sinova, S. Onoda, A. MacDonald, and N. Ong, *Rev. Mod. Phys.* **82**, 1539 (2010).
- [52] K. Ohgushi, S. Murakami, and N. Nagaosa, *Phys. Rev. B* **62**, 0605(R) (2000).
- [53] D. R. Hofstadter, *Phys. Rev. B* **14**, 2239 (1976).
- [54] F. H. Claro and G. H. Wannier, *Phys. Rev. B* **19**, 6068 (1979).
- [55] R. Rammal, *J. Phys.* **46**, 1345 (1985).
- [56] F. Claro, *Phys. Status Solidi B* **104**, K31 (1981).
- [57] D. J. Thouless, M. Kohmoto, M. P. Nightingale, and M. den Nijs, *Phys. Rev. Lett.* **49**, 405 (1982).
- [58] Y. Hatsugai, T. Fukui, and H. Aoki, *Phys. Rev. B* **74**, 205414 (2006).
- [59] D. N. Sheng, L. Sheng, and Z. Y. Weng, *Phys. Rev. B* **73**, 233406 (2006).
- [60] Please note that in real materials  $m \leq 10t$ .
- [61] B. Göbel, A. Mook, J. Henk, and I. Mertig, *Phys. Rev. B* **96**, 060406(R) (2017).
- [62] O. Gat and J. E. Avron, *Phys. Rev. Lett.* **91**, 186801 (2003).
- [63] Z. Wang and P. Zhang, *Phys. Rev. B* **76**, 064406 (2007).
- [64] Z. Yuan, Z. Wang, Z. Fu, S. Li, and P. Zhang, *Sci. China: Phys., Mech. Astron.* **55**, 1791 (2012).
- [65] See Supplemental Material at <http://link.aps.org/supplemental/10.1103/PhysRevB.99.060406> for orbital magnetization of the quantum Hall system and discussion of the four observables for different SkXs.
- [66] The magnetic field  $\mathbf{B}$  is applied in addition to the field that is needed to stabilize the SkX phase.
- [67] V. M. Edelstein, *Solid State Commun.* **73**, 233 (1990).
- [68] H. Saito, K. Uenishi, N. Miura, C. Tabata, H. Hidaka, T. Yanagisawa, and H. Amitsuka, *J. Phys. Soc. Jpn.* **87**, 033702 (2018).
- [69] Similar to superexchange-driven magnetoelectricity in magnetic vortices [75].
- [70] We used  $\alpha_{xy} = 0.1g\mu_B e/at$  and typical values of  $t = 1$  eV and  $a = 1$  nm. The electrical field corresponds to the insulating case and has to be replaced by the corresponding electrical currents if the Fermi energy is located within a band.
- [71] S. Seki, S. Ishiwata, and Y. Tokura, *Phys. Rev. B* **86**, 060403 (2012).
- [72] I. Kézsmárki, S. Bordács, P. Milde, E. Neuber, L. Eng, J. White, H. M. Rønnow, C. Dewhurst, M. Mochizuki, K. Yanai *et al.*, *Nat. Mater.* **14**, 1116 (2015).
- [73] E. Ruff, S. Widmann, P. Lunkenheimer, V. Tsurkan, S. Bordács, I. Kézsmárki, and A. Loidl, *Sci. Adv.* **1**, e1500916 (2015).
- [74] A. Leonov, T. Monchesky, N. Romming, A. Kubetzka, A. Bogdanov, and R. Wiesendanger, *New J. Phys.* **18**, 065003 (2016).
- [75] K. T. Delaney, M. Mostovoy, and N. A. Spaldin, *Phys. Rev. Lett.* **102**, 157203 (2009).



---

## 6 Publications: Beyond skyrmions

In this section the stabilization of alternative magnetic quasiparticles and their emergent electrodynamic effects are discussed (goal number 4 from the introduction). Four publications are presented corresponding to the quasiparticles depicted in Fig. 3 of the introduction: biskyrmion, bimeron, skyrmionium and antiferromagnetic skyrmion.

First, in publication [BG4] the merging process of two skyrmions with reversed in-plane magnetizations is investigated. In case of a partial overlap, a biskyrmion with a topological charge  $N_{\text{Sk}} = \pm 2$  is constituted. Thereafter, a theoretical study on magnetic bimerons is presented (publication [BG5]). These particles can be viewed as spin-rotated versions of magnetic skyrmions ( $N_{\text{Sk}} = \pm 1$ ) which can be stabilized in in-plane magnetized samples. In publication [BG6] the magnetic skyrmionium is considered as carrier of information in a racetrack device. This object can be described as a skyrmion with a second skyrmion with reversed magnetization positioned in its center, giving the skyrmionium a topological charge of  $N_{\text{Sk}} = 0$ . In the fourth publication [BG7] the existence of a periodic lattice of antiferromagnetic skyrmions is predicted. These objects also carry a topological charge of  $N_{\text{Sk}} = 0$  but the subskyrmions are ‘intertwined’, existing on two sublattices.

**Emergent electrodynamics.** All of the considered magnetic quasiparticles are combinations of two simpler topologically non-trivial spin textures. This brings about different emergent electrodynamic effects compared to those of conventional skyrmions.

For the topological Hall effect of electrons the discussion is straight forward. As long as a spin texture has a finite topological charge, a topological Hall effect occurs. For this reason, the bimeron ( $N_{\text{Sk}} = \pm 1$ ) and the biskyrmion ( $N_{\text{Sk}} = \pm 2$ ) exhibit a topological Hall effect but not the antiferromagnetic skyrmion or the skyrmionium (both  $N_{\text{Sk}} = 0$ ). Still, due to the spatial separation of the two subskyrmions that constitute a skyrmionium, we observe a local version of the topological Hall effect in publication [BG6] allowing for an electrical detection of these objects in a racetrack device. For antiferromagnetic skyrmions this is not possible, since the topological charge densities of the two subskyrmions are mutually compensated locally. Instead, we establish the topological spin Hall effect as a hallmark of this topological phase in publication [BG7].

On the contrary, the skyrmion Hall effect in the spin-orbit torque scenario (as presented in Sec. 3.4) is not directly coupled to the topological charge of a spin texture. This can already be understood by recalling the result of publication [BG1] from the previous section, where the skyrmion Hall effect was suppressed for a Néel skyrmion by manipulation of the orientation of the injected spins. Even if one considers the conventional spin injection, like for a Co/Pt bilayer, the skyrmion Hall angle is not exclusively determined by the topological charge. Admittedly, it is correct that antiferromagnetic skyrmions and skyrmioniums (both  $N_{\text{Sk}} = 0$ ) do not exhibit such a transverse deflection with respect to the applied driving current but non-symmetric  $\underline{D}$  tensors and non-antisymmetric  $\underline{I}$  tensors can suppress such an effect as well, as can be seen in the Thiele equation

$$-4\pi N_{\text{Sk}} b \mathbf{e}_z \times \mathbf{v} - b \underline{D} \alpha \mathbf{v} - B \mathbf{j} \underline{I} \mathbf{s} = \nabla U(\mathbf{r}). \quad (6.1)$$

Especially when a magnetic quasiparticle lacks rotational symmetry, like in the case of the biskyrmion or the bimeron, the current-driven motion exhibits a different angular dependence as in the skyrmionic case.

## 6.1 Magnetic biskyrmions in centrosymmetric nanodisks

**Combining two skyrmions to form a biskyrmion.** Conceptionally speaking, an intuitive way to combine magnetic skyrmions is to stabilize two of them in a sample and make them merge partially. Already from geometrical arguments it becomes apparent that the skyrmion helicity is crucial for this merging process: If both skyrmions have the same helicity, the magnetic moments between the two skyrmions' centers point into opposite in-plane directions. This configuration is very unfavorable concerning the dominant ferromagnetic exchange interaction leading to a strong repulsive interaction between the two quasiparticles. In order to be geometrically compatible, the in-plane components of the magnetic moments between the skyrmions' centers have to be parallel to each other, which is only achieved if the helicities of both skyrmions differ by  $\pi$ .

**Preliminary studies.** A so-called 'biskyrmion' consists of two Bloch skyrmions with helicities  $\pm\pi/2$  that exhibit a considerable overlap. Such a merged spin texture has been observed experimentally, for example in layered manganite  $\text{La}_{2-2x}\text{Sr}_{1+2x}\text{Mn}_2\text{O}_7$  [136]; cf. Fig. 26. The stabilizing mechanism cannot be the DMI, since this interaction strictly favors one type of skyrmion with a fixed helicity (cf. Sec. 2.3). The detrimental interaction is indeed forbidden in  $\text{La}_{2-2x}\text{Sr}_{1+2x}\text{Mn}_2\text{O}_7$ , since it is centrosymmetric.

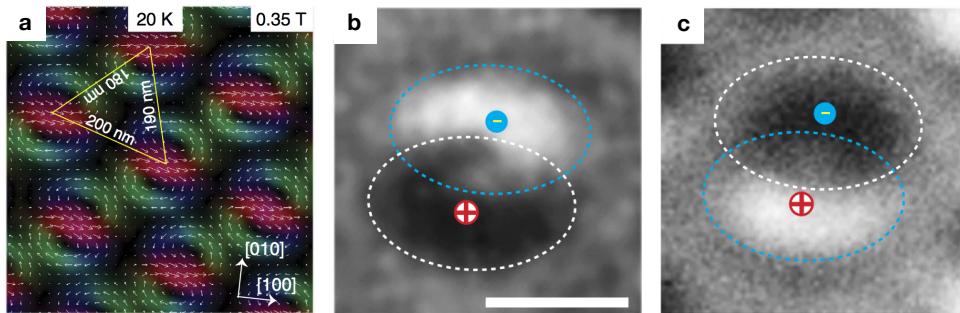


Figure 26: **Lorentz TEM images of a biskyrmion lattice.** **a** The color encodes the in-plane orientation of the biskyrmion lattice. The information is extracted from the over-focused and under-focused images, shown in pannels **b** and **c** for an individual biskyrmion. Adapted by the permission from Springer Nature Terms and Conditions for RightsLink Permissions Springer Nature Customer Service Centre GmbH: Macmillan Publishers Limited Nature Communications Biskyrmion states and their current-driven motion in a layered manganite, X. Z. Yu *et al.* 2014; Ref. [136].

A possible stabilizing mechanism is the frustration of exchange interactions. As presented in Sec. 2.3, this mechanism does not favor a specific skyrmion helicity. Consequently, the two skyrmions can coexist and merge, as presented in the theoretical work by Zhang *et al.* [137]. However, as described earlier, even conventional skyrmions due to frustration have never been observed experimentally. Also, the biskyrmions from the experiments have a strictly fixed helicity of  $\pm\pi/2$ . For this reason, frustrated exchange interactions are unlikely the stabilizing mechanism of biskyrmions in nature. Therefore, alternative mechanisms have to be considered to explain the biskyrmion stabilization.

**This publication.** A more realistic mechanism for the stabilization of biskyrmions is the dipole-dipole interaction. As is shown in the following publication “Forming individual magnetic biskyrmions by merging two skyrmions in a centrosymmetric nanodisk” [BG4], this interaction stabilizes Bloch skyrmions with helicities  $\pm\pi/2$  likewise and even favors their spatial overlap energetically. The predicted effective interaction is verified by micromagnetic simulations of a nanodisk. The main result of the publication is the controlled generation of individual biskyrmions by writing two individual Bloch skyrmions in the first step.

For the micromagnetic simulations of the magnetic textures, the LLG equation (3.16) has been propagated. The effective description utilized the Thiele equation (3.35).

**Conclusion.** Up to now, biskyrmions have only been found as periodic lattices. The presented publication predicts the existence of individual biskyrmions. It lays the foundation for utilizing biskyrmions in spintronic devices. Just like a skyrmion, the biskyrmion exhibits emergent electrodynamic effects, namely the topological Hall effect and the skyrmion Hall effect. Since the topological charge has a finite value of  $\pm 2$ , biskyrmions have the same advantages but also disadvantages as skyrmions on first sight. However, the missing rotational symmetry finds expression in the utility as well: the orientation of a biskyrmion provides another degree of freedom which can be used to store information. Also, anisotropic features of the current-driven motion should be investigated in the future.

It is worth mentioning that in two recent publications the experimental observations of biskyrmion crystals have been contested. Two groups have shown that the Lorentz TEM images from Ref. [136] (cf. Fig. 26) and other works do not necessarily show biskyrmions but can also arise if topologically trivial bubbles (called ‘type-II bubbles’ or ‘hard bubbles’ in these publications) are viewed at an angle [138, 139]. Alternative observation techniques would have to be considered in order to be sure of the existence of magnetic biskyrmion crystals in these materials. In the predicted setup of the following publication [BG4] the magnetic material is only a few nm thick. Therefore, a biskyrmion-like image in a Lorentz TEM measurement would irrevocably prove the stabilization of the proposed individual biskyrmions.

Reprinted from (B. Göbel *et al.*: Forming individual magnetic biskyrmions by merging two skyrmions in a centrosymmetric nanodisk. *Scientific Reports* 9, 9521 (2019), DOI: <https://doi.org/10.1038/s41598-019-45965-8>; Ref. [BG4]).  
Published by Springer Nature under the terms of the Creative Commons Attribution 4.0 license.

# SCIENTIFIC REPORTS

OPEN

## Forming individual magnetic biskyrmions by merging two skyrmions in a centrosymmetric nanodisk

Börge Göbel<sup>1</sup>, Jürgen Henk<sup>2</sup> & Ingrid Mertig<sup>1,2</sup>

When two magnetic skyrmions – whirl-like, topologically protected quasiparticles – form a bound pair, a biskyrmion state with a topological charge of  $N_{\text{sk}} = \pm 2$  is constituted. Recently, especially the case of two partially overlapping skyrmions has brought about great research interest. Since for its formation the individual skyrmions need to possess opposite in-plane magnetizations, such a biskyrmion cannot be stabilized by the Dzyaloshinskii-Moriya-interaction (DMI), which is the interaction that typically stabilizes skyrmions in non-centrosymmetric materials and at interfaces. Here, we show that these biskyrmions can be stabilized by the dipole-dipole interaction in centrosymmetric materials in which the DMI is forbidden. Analytical considerations indicate that the bound state of a biskyrmion is energetically preferable over two individual skyrmions. As a result, when starting from two skyrmions in a micromagnetic simulation, a biskyrmion is formed upon relaxation. We propose a scheme that allows to control this biskyrmion formation in nanodisks and analyze the individual steps.

Magnetic skyrmions<sup>1–3</sup> are whirl-like magnetic quasiparticles on the sub-micrometer scale, first observed in  $\text{MnSi}^2$  as periodic arrays (so-called skyrmion crystals or lattices). Later, also isolated skyrmions have been found in ferromagnetic  $\text{Fe}_{0.5}\text{Co}_{0.5}\text{Si}$  films<sup>4</sup>. Each skyrmion is characterized by a topological charge

$$N_{\text{sk}} = \frac{1}{4\pi} \int \mathbf{m}(\mathbf{r}) \cdot \left[ \frac{\partial \mathbf{m}(\mathbf{r})}{\partial x} \times \frac{\partial \mathbf{m}(\mathbf{r})}{\partial y} \right] d^2r \quad (1)$$

of  $\pm 1$  [ $\mathbf{m}(\mathbf{r})$  is the magnetization], which imposes an energy barrier that protects a skyrmion from annihilating to the ferromagnetic groundstate. Their high stability and small sizes make skyrmions candidates for the carriers of information in future storage devices<sup>5,6</sup>. For example, skyrmions can be written and deleted, driven by electric currents and read in thin films<sup>6–11</sup>.

An object which is closely related to the skyrmion is the biskyrmion, a term that describes two skyrmions in a bound state. Like the skyrmion<sup>12</sup> it was initially proposed in nuclear physics<sup>13,14</sup>. In the context of magnetism the term ‘biskyrmion’ has been used for two skyrmions in a bilayer quantum Hall system<sup>15</sup>, for two asymmetric skyrmions in the cone phase of a chiral helimagnet which exhibit an attractive interaction<sup>16,17</sup>, and – as observed for the first time in 2014<sup>18</sup> – a composition of two partially overlapping skyrmions with opposite in-plane magnetizations (Fig. 1b)<sup>18–23</sup>. Still, all of these objects are geometrically distinct. In the remainder of this paper the term ‘biskyrmion’ refers always to the latter object: a pair of partially overlapping skyrmions with a helicity difference of  $\pi$  that has attracted an enormous research interest since its initial discovery.

Although merged, each skyrmion forming the biskyrmion can still be identified and their shifted centers indicate a merely partial overlap. For this reason, each skyrmion contributes with its topological charge of  $\pm 1$  to the biskyrmion’s topological charge of  $N_{\text{sk}} = \pm 2$ . Periodic arrays of such biskyrmions (biskyrmion crystals) have first been observed in the centrosymmetric layered manganite  $\text{La}_{2-2x}\text{Sr}_{1+2x}\text{Mn}_2\text{O}_7$ <sup>18</sup>, other centrosymmetric biskyrmion hosts followed recently<sup>19–22</sup>.

If *individual* biskyrmions could be stabilized, they could be used to store information just like conventional skyrmions. However, up to now, individual biskyrmions have only been predicted in frustrated magnets<sup>23</sup> — even

<sup>1</sup>Max-Planck-Institut für Mikrostrukturphysik, Halle (Saale), 06120, Germany. <sup>2</sup>Martin-Luther-Universität Halle-Wittenberg, Institut für Physik, Halle (Saale), 06099, Germany. Correspondence and requests for materials should be addressed to B.G. (email: [bgoebel@mpi-halle.mpg.de](mailto:bgoebel@mpi-halle.mpg.de))

the existence of conventional skyrmions in these materials<sup>24–26</sup> remains to be proven experimentally. These considerations suggest to investigate centrosymmetric materials with dominating dipole-dipole interaction, like in the experimental observations of biskyrmion crystals, to find also individual biskyrmions. In these materials the constituents of biskyrmions — skyrmionic bubbles — have been found already decades ago<sup>27,28</sup>.

In this Paper, we propose a scheme for creating biskyrmions in a controlled manner. In a first step, we derive an attractive skyrmion-skyrmion interaction which is necessary for the formation of a biskyrmion, using an analytical model. Thereafter, we show by micromagnetic simulations for a nanodisk geometry that two Bloch skyrmions with opposite in-plane magnetizations can be written at opposite sides of a nanodisk. We simulate the resultant motion of such skyrmions upon relaxation and derive their equations of motion analytically. After relaxation we find that both skyrmions have merged to a stable biskyrmion state (Fig. 1). The importance of the skyrmions' helicities for this process is discussed. We summarize our findings and give an outlook.

## Results

**Analytical superposition of two skyrmions.** As presented in the introduction, it is an established fact that non-collinear spin textures like skyrmions can be stabilized by the dipole-dipole interaction<sup>3</sup>. Therefore, it is well conceivable that also two skyrmions with reversed in-plane magnetizations can be stabilized in the same sample by this mechanism. The question is now how these skyrmions interact. As we will show, already considering a short-range approximation of the dipole-dipole interaction leads to the conclusion that the two skyrmions attract each other, thereby allowing to form a biskyrmion. This finding is later confirmed by micromagnetic simulations where the full dipole-dipole interaction is considered and a biskyrmion state is metastabilized.

To find the attractive interaction between two skyrmions with opposite in-plane magnetizations, we superpose such two (fixed) skyrmions at a distance of  $\Delta r$  analytically. For simplicity we neglect shape deformations of the skyrmions (such deformations are accounted for by the micromagnetic simulations later in this paper). The magnetic textures  $\mathbf{m}(\mathbf{r}) = (\sin\Theta\cos\Phi, \sin\Theta\sin\Phi, \cos\Theta)$  are imposed onto a two-dimensional square lattice with lattice constant  $a$ .

The spherical coordinates of the magnetic moments of an individual skyrmion read  $\Phi = \arctan(my/x) + \gamma$  and  $\Theta = 2\arctan(\sqrt{x^2 + y^2}/r_0)$ ;  $r_0$  determines the size of the skyrmion. The helicity  $\gamma$  of the skyrmion manifests itself in the in-plane components via  $\Phi = m\phi + \gamma$ . Here,  $\phi$  is the polar angle of the position vector with respect to the skyrmion's center and  $m = +1$  is the vorticity, which defines the sense of in-plane spin rotation. In case of a Bloch skyrmion we have  $m = 1$  and  $\gamma = \pm\pi/2$ , i. e., the polar angle of the spin orientation  $\Phi$  has a fixed offset to the polar angle  $\phi$  of the position  $\mathbf{r}$  with respect to the skyrmion's center. The topological charge  $N_{\text{sk}} = p \cdot m = \pm 1$  of a skyrmion depends on the skyrmion's polarity  $p = \pm 1$ . In this Paper, we consider skyrmions in a ferromagnetic surrounding, magnetized along  $-z$ , which gives a polarity and topological charge of  $+1$ .

One way to superpose two skyrmions is adding their polar angles and multiplying the arguments of their arctan function for the azimuthal angle,

$$\begin{aligned}\Phi &= \arctan\left(\frac{y - \Delta y/2}{x - \Delta x/2}\right) + \arctan\left(\frac{y + \Delta y/2}{x + \Delta x/2}\right) + (\gamma_d - \alpha), \\ \Theta &= 2\arctan\left[\frac{1}{r_0^2}\sqrt{(x - \Delta x/2)^2 + (y - \Delta y/2)^2} \cdot \sqrt{(x + \Delta x/2)^2 + (y + \Delta y/2)^2}\right].\end{aligned}\quad (2)$$

The condition  $|\mathbf{m}| = 1$  holds for all  $\mathbf{r}$ . Here,  $\Delta\mathbf{r} = (\Delta x, \Delta y, 0) = \Delta r(\cos\alpha, \sin\alpha, 0)$  is the displacement vector of the two skyrmions with helicities  $\gamma_d$  and  $\gamma_d + \pi$ . For an inter-skyrmion distance of  $\Delta r \gg r_0$  we find two isolated skyrmions, for  $\Delta r \approx 2r_0$  the solution is a biskyrmion state with two skyrmions overlapping partially, and for  $\Delta r = 0$  a higher-order skyrmion is formed. In any case, the total topological charge is  $N_{\text{sk}} = +2$ .

**Attractive skyrmion-skyrmion interaction.** We clarify now which term in the lattice Hamiltonian causes an attractive interaction of the two skyrmions, what can lead to the formation of a biskyrmion. The exchange interaction  $H_{\text{ex}} = -\frac{1}{2}\sum_{ij} J_{ij}\mathbf{m}_i \cdot \mathbf{m}_j$  is independent of  $\Delta r$  and independent of the skyrmions' sizes and shapes. Hence, the exchange interaction alone will not stabilize a biskyrmion. This finding is in line with the fact that even conventional skyrmions cannot be stabilized by a bare exchange interaction, unless further (frustrated) exchange interactions are considered; then, the interaction constants  $J_{ij}$  have different signs for nearest and second-nearest neighbor spins. The same requirement holds for biskyrmions<sup>23</sup>.

In most materials, skyrmions are stabilized by the Dzyaloshinskii-Moriya interaction (DMI)<sup>29,30</sup>  $H_{\text{DMI}} = \frac{1}{2}\sum_{ij} \mathbf{D}_{ij} \cdot (\mathbf{m}_i \times \mathbf{m}_j)$  that originates from spin-orbit coupling and a broken inversion symmetry. The DMI vectors  $\mathbf{D}_{ij} = -\mathbf{D}_{ji}$  whose directions are prescribed by the crystal symmetry determine the type of metastable spin texture<sup>31</sup>. For all types of DMI the energy contributions of the two skyrmions with reversed in-plane magnetizations — what is necessary for the formation of the here considered biskyrmion — cancel. As a result,  $H_{\text{DMI}}$  is independent of  $\Delta r$  and does not allow for the formation of a biskyrmion. Even more detrimental, at least one of the two skyrmions would annihilate in a simulation.

An interaction that is present in all magnetic materials, but often 'overshadowed' by the DMI in non-centrosymmetric materials, is the dipole-dipole interaction

$$H_{\text{dp}} = -\frac{1}{2}\sum_{ij} \frac{\mu_0}{4\pi|\mathbf{r}_{ij}|^3} [3(\mathbf{m}_i \cdot \mathbf{r}_{ij})(\mathbf{m}_j \cdot \mathbf{r}_{ij}) - \mathbf{m}_i \cdot \mathbf{m}_j].\quad (3)$$

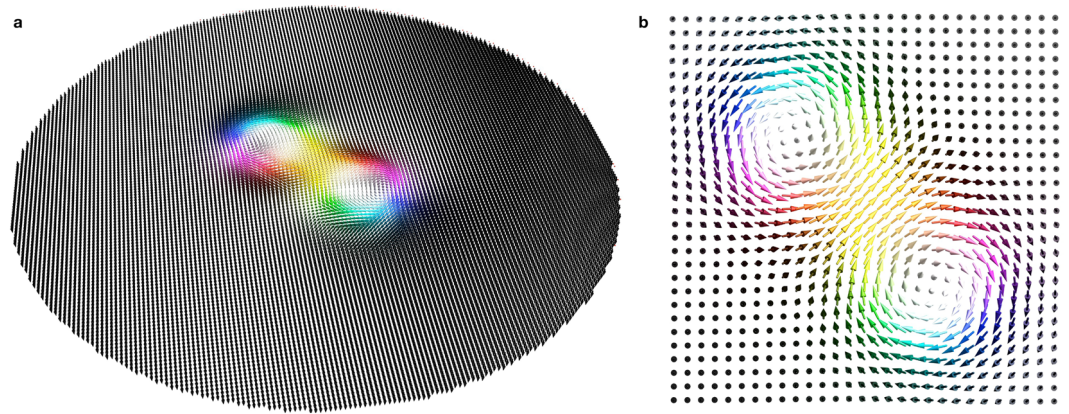


**Figure 1.** Magnetic biskyrmion. **(a)** Spin texture of a magnetic biskyrmion in the considered nanodisk resulting from a micromagnetic simulation (also presented in Fig. 5). The orientation of the individual magnetic moments is represented by a Lorentz transmission electron microscopy (LTEM) color scheme. **(b)** Close-up of the center region of **(a)**. The biskyrmion consists of two overlapping skyrmions with helicities  $\pm\pi/2$ , respectively. In the two panels only every fourth or sixteenth magnetic moment from the simulation is displayed, respectively, for better visibility.

In case the DMI is forbidden, like in centrosymmetric materials, this interaction can stabilize not only skyrmions<sup>32–35</sup> but also biskyrmions, as will be presented later in this paper by micromagnetic simulations. To establish an intuitive understanding of the attractive skyrmion-skyrmion interaction, which is necessary for the formation of a biskyrmion, we consider a short-range approximation of the dipole-dipole interaction for the calculations in this section. Note however, that this approximation is accompanied by a loss of information<sup>36</sup>. Even the lowest energy state of the considered model would relax to a collinear ferromagnetic configuration if only the short-range approximation was considered in a simulation in which shape relaxation is allowed. Since Derrick's theorem<sup>37</sup> implies the absence of local energy minima for non-collinear spin textures for this reduced type of dipole-dipole interaction<sup>38</sup>, we cannot make statements on the metastability of a certain configuration. However, comparing the energies of states described by the model in Eq. (2) allows to extract an attractive skyrmion-skyrmion interaction. The actual proof of metastability are the micromagnetic simulations of the three-dimensional system with the full dipole-dipole interaction shown later in this paper. A three-dimensional consideration is essential since non-collinear spin textures are only metastable once the sample is thicker than a critical value<sup>28,39</sup>.

To extract the attractive interaction we consider in this section only nearest-neighbor interactions in a two-dimensional square lattice. In this case the second term in Eq. (3) merely rescales the exchange interaction, thereby rendering only the first term relevant

$$H_{\text{dp,approx}} \propto -\sum_{ij} (\mathbf{m}_i \cdot \hat{\mathbf{r}}_{ij})(\mathbf{m}_j \cdot \hat{\mathbf{r}}_{ij}), \quad (4)$$

where  $\hat{\mathbf{r}}_{ij}$  is a unit vector which is parallel to either  $\mathbf{e}_x$  or  $\mathbf{e}_y$ . This interaction can be interpreted as a special easy-plane anisotropy. It favors parallel spins energetically. Such an alignment is approximately fulfilled for the overlap region of the two skyrmions (that is the center of the biskyrmion). As a result, two skyrmions in centrosymmetric materials attract each other.

We find that partially overlapping Bloch skyrmions ( $\gamma = \pm\pi/2$ ) at a displacement angle of  $\alpha = \pm\pi/4$  or  $\pm 3\pi/4$  have the lowest energy of all states described by Eq. (2) with respect to the short-range approximation of the dipole-dipole interaction. The energy minimum occurs at an inter-skyrmion distance of  $\Delta r \approx 2r_0$ , which is a biskyrmion state (Fig. 2a). The helicity dependence (Fig. 2b) has a cosine shape making the Bloch skyrmion energetically most favorable. This helicity dependence is not unique to the biskyrmion state; a similar dependence is found for a single skyrmion. The  $\alpha$  dependence (Fig. 2c; global rotation of the texture) originates from the underlying lattice. As a consequence it has a period of  $\pi/2$  with respect to  $\alpha$  for the square lattice. Different lattices have energy minima at other angles, e. g.  $\alpha = \pm\pi/6, \pm 3\pi/6$  and  $\pm 5\pi/6$  for a hexagonal lattice.

So far, we have shown that two skyrmions with reversed in-plane magnetizations attract each other in centrosymmetric systems without DMI but with dipole-dipole interaction. The resulting biskyrmion is expected to be of Bloch type and to form at an angle of  $45^\circ$  with respect to the underlying lattice. In the following, micromagnetic simulations will be used to analyze how these two specific skyrmions can be stabilized in a three-dimensional sample considering the full dipole-dipole interaction. We will show that all three results from the analytic model are confirmed in the simulation: the skyrmions attract each other to form a biskyrmion characterized by  $\gamma_e = \pm\pi/2$  and  $\alpha = \pm\pi/4, \pm 3\pi/4$ .

**Setup for the micromagnetic simulations.** To support the above analytical considerations, we performed micromagnetic simulations for a thin magnetic nanodisk with out-of-plane anisotropy. These disks have been in the focus of skyrmion-related research in many recent publications<sup>40–45</sup>. The considered disk and its



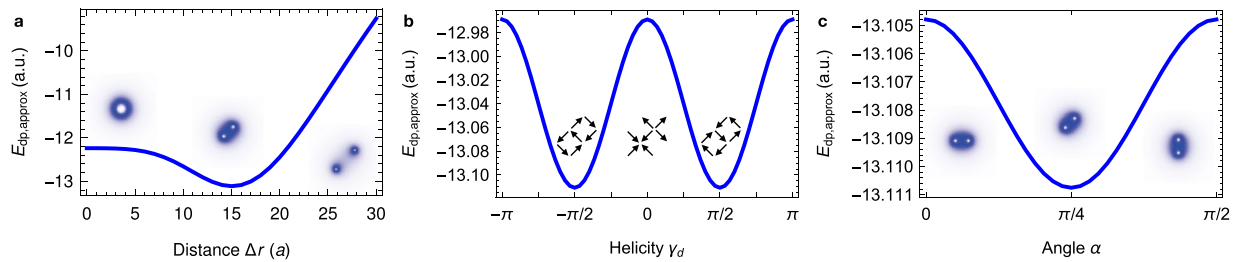


**Figure 2.** Formation of a biskyrmion by the dipole-dipole interaction. (a) Approximated dipole-dipole interaction energy [Eq. (4)] versus distance of the two skyrmions in the model [Eq. (2)]. Insets visualize the energy density for an  $N_{\text{sk}} = 2$  skyrmion with  $\Delta r = 0$  (left), a biskyrmion with  $\Delta r = 15a$  (center), and for two skyrmions with  $\Delta r = 30a$  (right);  $a$  is the lattice constant. Here,  $\alpha = \pi/4$  and  $\gamma_d = \pi/2$ . The size parameter is  $r_0 = 8a$  in all panels. (b) Helicity dependence of the approximated dipole-dipole energy for the biskyrmion with  $\Delta r = 15a$  and  $\alpha = \pi/4$ . Insets show the in-plane magnetization, representing two superposed Bloch skyrmions for  $\gamma_d = \pm\pi/2$  and Néel skyrmions for  $\gamma_d = 0$ . In all cases the two skyrmions have helicities  $\gamma_d$  and  $\gamma_d + \pi$ , respectively. (c) Approximated dipole-dipole energy for the biskyrmion with  $\Delta r = 15a$  and  $\gamma_d = \pi/2$  versus the biskyrmion orientation angle  $\alpha$ . Insets visualize the energy density.

surfaces exhibit negligibly small DMI, so that only the dipole-dipole interaction (included in the demagnetization field) could stabilize a biskyrmion.

The micromagnetic simulations were performed using the Mumax3 code<sup>46,47</sup>. Therein, the Landau-Lifshitz-Gilbert equation (LLG)<sup>48–50</sup> with parameters similar to those in ref.<sup>35</sup> is solved for each discretized magnetic moment  $\mathbf{m}_i$ ; see Methods.

Initially, two energetically degenerate metastable skyrmions with helicities  $\pm\pi/2$  are ‘written’ symmetrically to the nanodisk’s center. Upon relaxation they are pushed to the center by their attractive interaction and the confinement potential of the nanodisk. When the skyrmions reach the energetically optimal distance, a biskyrmion has formed. We proceed by discussing the individual steps in detail and begin with the mechanism for writing the skyrmions.

**Generation of isolated skyrmions.** The vanishing DMI complicates a controlled writing of skyrmions in centrosymmetric materials, since there is no energetically preferred chirality: injecting spins oriented along  $\mathbf{z}$  via spin torque, as commonly done in DMI-dominated systems<sup>6</sup>, produces a topologically trivial bubble (the in-plane spin components point toward the disk’s center; they are oriented nearly parallel). Evidently, in order to write two skyrmions off-center without DMI the aimed-for texture has to be induced explicitly. In other words, deterministic instead of stochastic writing has to be considered. This is especially important since the two skyrmions need to have opposite helicities.

We consider two smaller disks attached to the nanodisk (Fig. 3a). These additional disks host stable in-plane vortex configurations<sup>51,52</sup>, similar to refs.<sup>53–56</sup>. The opposite helicities of the vortices, which are switchable e. g., by a magnetic field<sup>57–60</sup>, determine the helicity of the two emerging Bloch skyrmions. If an electric current  $\mathbf{j}_{\text{write}}$  is applied in perpendicular direction (here:  $\mathbf{j}_{\text{write}} = 7 \times 10^8 \text{ A/cm}^2 \mathbf{e}_z$  applied for 200 ps), the spin of the flowing electrons is aligned with the vortex (as long as the coupling is sufficiently large) and injected into the underlying nanodisk; there a skyrmion is formed via spin torque.

The writing process is visualized in Fig. 3b–g. Starting from a ferromagnetic state, a skyrmionium-like configuration (a skyrmion with reversed skyrmion-like magnetization in its center<sup>61–63</sup>) is written (b–d). Since the ‘central’ reversed skyrmion is very small, it quickly annihilates (<100 ps) so that a skyrmion with a topological charge of  $N_{\text{sk}} = +1$  remains at each side of the disk (e). On the time scale of 1 ns their sizes relax (f, g).

While the writing mechanism considered here appears convenient, other approaches are suited for an experimental realization as well; in the following, we give an incomplete list.

Merons (vortices with out-of-plane spins in their center) in the writing devices work equally well. The same holds for skyrmions. All of the considered textures have a similar in-plane magnetization which seems to be the most important component for skyrmion generation in centrosymmetric materials; due to the fact that the dipole-dipole interaction is achiral, a suitable in-plane magnetization has to be ‘imprinted’ in order to ‘generate’ a topological charge.

In a recent publication<sup>63</sup> we have presented a mechanism for writing skyrmioniums via a photosensitive switch<sup>64</sup>: a laser triggers a radial current in a ring of a heavy metal, thereby generating an in-plane toroidal spin polarization via the spin Hall effect. This toroidal spin profile is then injected into the magnetic nanodisk, very similar to the vortex-writing device but for a ring geometry instead of a disk geometry. Depending on the chosen parameters, this method works for writing skyrmions as well. The sign of the applied bias voltage controls the spin polarization’s orientation and thus the writing of either  $+\pi/2$  or  $-\pi/2$  Bloch skyrmions.

As a third option, one may consider spatiotemporally tuned electron sources<sup>65</sup>. The type of induced Bloch skyrmion can be controlled via the propagation direction of the electrons (beam applied from above or below the nanodisk).

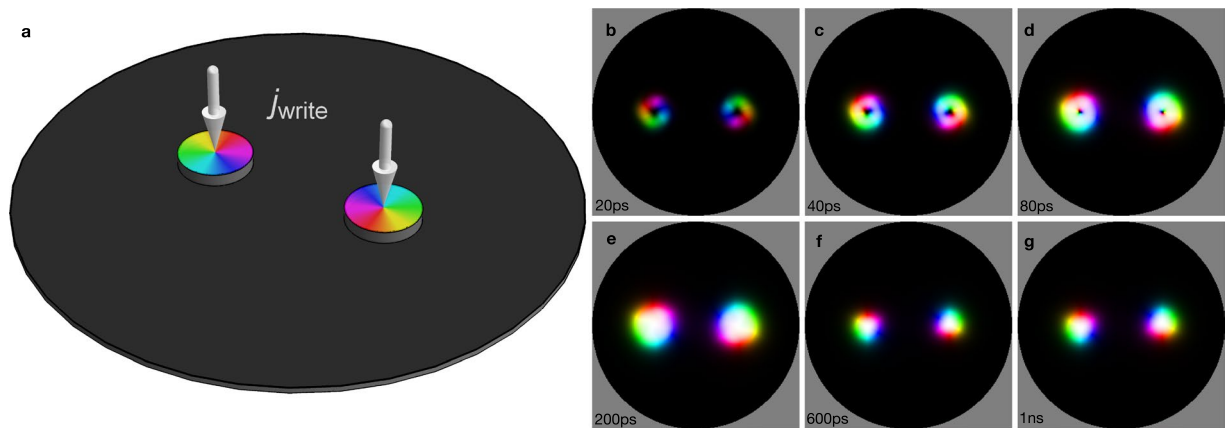


**Figure 3.** Writing two Bloch skyrmions with opposite helicities into a nanodisk. (a) Thin nanodisk with two smaller writing disks that host vortex textures (colored) with opposite helicities. The writing process is triggered by spin-polarized current densities  $\mathbf{j}_{\text{write}}$  which are applied for 200 ps. (b–g) Snapshots during the generation of two skyrmions. The color scale is the same as in Fig. 1. An animated version is accessible in Supplementary Video 1.

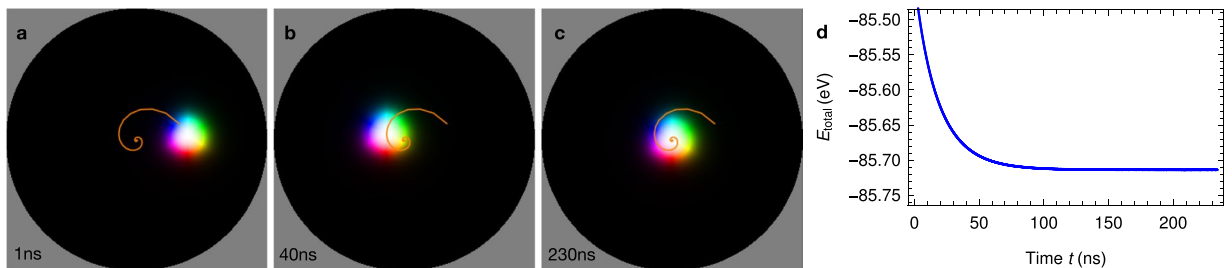


**Figure 4.** Motion of a single skyrmion within a nanodisk. (a–c) Snapshots and trajectory (orange line) of a single skyrmion in the nanodisk at indicated times. (d) Temporal progression of the system’s total energy. An animated version is accessible in Supplementary Video 2.

**Motion of a single skyrmion.** Before discussing the formation of biskyrmions, we address the motion of a single skyrmion within the nanodisk. After relaxation of shape and size, a skyrmion starts to move toward the center of the nanodisk in a counter-clockwise spiral trajectory (orange in Fig. 4a–c). Initially, the skyrmion is accelerated but is subsequently decelerated when the skyrmion’s center is close to the nanodisk’s center. The helicity of the skyrmion remains unchanged during the evolution.

The spiral trajectory is understood by considering the Thiele equation<sup>66,67</sup>

$$b \mathbf{G} \times \mathbf{v} - b \underline{D} \alpha \mathbf{v} + F_{\text{int}}(r) \frac{\mathbf{r}}{r} = 0. \tag{5}$$

In this effective ‘center-of-mass-like’ description of magnetic quasiparticles with velocity  $\mathbf{v}$  all internal degrees of freedom have been integrated out. The spatial details of the skyrmion are ‘condensed’ in the gyromagnetic coupling vector  $\mathbf{G} = -4\pi N_{\text{sk}} \mathbf{e}_z$  and in the dissipative tensor  $\underline{D}$  with elements  $D_{ij} = \int \partial_i \mathbf{m}(\mathbf{r}) \cdot \partial_j \mathbf{m}(\mathbf{r}) d^2r$ . Only  $D_{xx} = D_{yy}$  are nonzero.  $b = M_s d_z / \gamma_e$  is determined by the saturation magnetization  $M_s$ , the disk thickness  $d_z$  and the gyromagnetic ratio of an electron  $\gamma_e$ . Due to the disk geometry the force  $F_{\text{int}}$ , that covers interactions of the considered quasiparticle with other quasiparticles or with the edge of the sample, is radially symmetric. The Thiele equation in polar coordinates

$$4\pi N_{\text{sk}} b (r \dot{\phi} \mathbf{e}_r - \dot{r} \mathbf{e}_\phi) - \alpha D_{xx} b (\dot{r} \mathbf{e}_r + r \dot{\phi} \mathbf{e}_\phi) + F_{\text{int}}(r) \mathbf{e}_r = 0 \tag{6}$$

yields

$$\begin{aligned} \dot{r} &= \frac{F_{\text{int}}(r)}{(\alpha D_{xx})^2 b + (4\pi N_{\text{sk}})^2 b} \alpha D_{xx}, \\ \dot{\phi} &= \frac{F_{\text{int}}(r)}{(\alpha D_{xx})^2 b + (4\pi N_{\text{sk}})^2 b} \frac{-4\pi N_{\text{sk}}}{r}. \end{aligned} \tag{7}$$

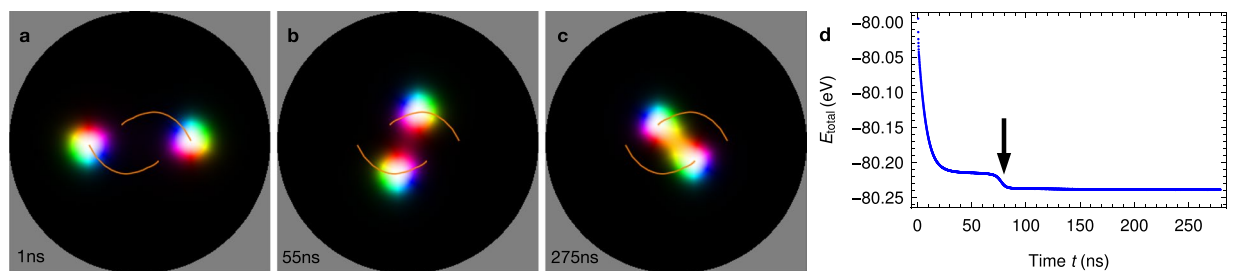


**Figure 5.** Formation of a biskyrmion. (a–c) Snapshots and trajectories (orange) of two Bloch skyrmions with opposite helicities. (d) Temporal progression of the system’s total energy. The pronounced drop (indicated by an arrow) corresponds to the energy minimum in Fig. 2a: a stable biskyrmion is formed at that point in time. An animated version is accessible in Supplementary Video 3.

Since  $F_{\text{int}}(r) < 0$ , a skyrmion moves to the nanodisk’s center along a counter-clockwise spiral trajectory ( $\dot{r} < 0$ ,  $\dot{\phi} > 0$ ). When it approaches the center, the angular velocity decreases since  $F_{\text{int}}(r)$  drops faster to 0 than  $1/r$ . The transverse component of the spiral motion is a consequence of the skyrmion’s topological charge. Like any quasiparticle with nontrivial real-space topology a skyrmion does not move parallel to the propelling force — let it be due to a current or the skyrmion–edge interaction<sup>3,8,9,31,67,68</sup> — and thus exhibits a skyrmion Hall effect. The corresponding transverse force is similar to the Magnus force for classical particles<sup>3,69</sup>.

**Formation of biskyrmions.** The formation of a biskyrmion starts with two Bloch skyrmions with opposite helicities of  $\gamma = \pm\pi/2$ , as stabilized in Fig. 3. Since both skyrmions have identical dissipative tensors  $\underline{D}$  and topological charges  $N_{\text{sk}} = +1$ , the equations of motion (7) hold for both quasiparticles. They move on a spiral trajectory towards the nanodisk’s center. However, the skyrmion-skyrmion interaction has to be considered in  $F_{\text{int}}$ . This force changes sign when both skyrmions come close to each other, corresponding to the energy minimum in Fig. 2a; it is zero at a finite distance of the two skyrmions.

This behavior is well visible in the results of micromagnetic simulations (Fig. 5). After the writing period (relaxation after  $\approx 1$  ns as presented in Fig. 3), both skyrmions start to exhibit a spiral motion to the center as in the case of a single skyrmion. Once both skyrmions start to overlap the spiral motion stops and a biskyrmion is formed. During the formation process the topological charge remains  $N_{\text{sk}} = +2$  within an error of less than 1.5% (the topological charge is not integer due to the discreteness of the underlying lattice).

The biskyrmion configuration is remarkably stable. The energy drops significantly once the two skyrmions are close to each other (Fig. 5d). This drop corresponds to the energy minimum established in the analytic model (Fig. 2a). In the final phase of the propagation the biskyrmion aligns with one of the crystallographic directions  $\alpha = 45^\circ, 135^\circ, 225^\circ$  or  $315^\circ$ , visible as energy minimum in Fig. 2c (here:  $\alpha = 135^\circ$ ). Once the system is close to the energy minimum  $F_{\text{int}}$  is far from being rotational symmetric and the equations of motion derived from the Thiele equation do not hold anymore. By comparing the energy scales of Figs. 2a,c it becomes apparent that the reorientation of the biskyrmion plays a role after the optimal distance of the two skyrmions has been reached. The distinguished axis of the biskyrmion can in principle be imposed by the initial positions of the skyrmions. If the two writing disks are closer together the biskyrmion can end for example at  $\alpha = 45^\circ$  (Fig. S1 of the Supplementary Information).

Starting with two skyrmions with *identical* helicity (i. e. by switching one of the two writing vortices) a mostly static behavior is observed (Fig. S2 of the Supplementary Information). This is readily explained by the stronger repulsion of skyrmions with the same helicity in comparison to those with opposite helicities. Due to the disk geometry both skyrmions experience a force towards the center, resulting in a zero of  $F_{\text{int}}$  at larger distances compared to the biskyrmion system. The (final) steady state — two skyrmions without considerable overlap — has a sizably higher energy than the biskyrmion state (cf. Fig. S2d and Fig. 5d). Starting from this particular configuration a biskyrmion does not form since one skyrmion would have to reverse its helicity. That, however, requires to overcome an energy barrier similar to that in Fig. 2b, corresponding to a Néel skyrmion state.

In refs.<sup>16,17</sup> it was shown that asymmetric skyrmion tubes (e. g. in the cone phase of chiral magnetic materials) can exhibit an attractive interaction despite their equal helicities. The resulting non-overlapping pair of skyrmions is stabilized by a different mechanism and at a larger inter-skyrmion distance compared to the type of biskyrmion discussed in the present paper. Nevertheless, the skyrmion-skyrmion pair was labeled ‘biskyrmion’ in ref.<sup>16</sup> due to the topological equivalence ( $N_{\text{sk}} = \pm 2$ ) of both textures. Yet, both are geometrically distinct objects.

## Discussion

Here, we have demonstrated that the dipole-dipole interaction in centrosymmetric magnetic systems can stabilize *isolated biskyrmions*, in the sense of a pair of partially overlapping skyrmions with reversed in-plane magnetizations. We propose methods for writing two Bloch skyrmions with opposite helicities at opposite sides of a nanodisk. After spiral propagation of each skyrmion towards the nanodisk’s center, an *isolated biskyrmion* is formed due to the attractive interaction that originates in the dipole-dipole interaction. These ingredients provide a step towards utilizing biskyrmions as carriers of information in spintronics devices.

To the best of our knowledge, only biskyrmion *lattices* have been found experimentally so far<sup>18–22</sup>, and even for them the interpretation of the presented Lorentz transmission electron microscopy images is under serious debate. In two recent publications it was shown that tubes of topologically trivial bubbles (called type-II or hard bubbles) can appear as biskyrmion-like features when observed under an angle<sup>70,71</sup>. Since thin magnetic disks are considered in the present work, potential real-space images can hardly be misinterpreted, and therefore our prediction may be decisive for showing that biskyrmions can exist at all.

Besides their potential for applications, biskyrmions are also worth being investigated from a fundamental point of view. Their nontrivial real-space topology, manifested in the topological charge of  $N_{\text{sk}} = \pm 2$ , imposes emergent electrodynamic effects: just like conventional skyrmions, biskyrmions exhibit a skyrmion Hall effect<sup>3,8,9,67,68</sup> and a topological Hall effect<sup>3,10,11,72–78</sup>. In other words, under the effect of a spin-polarized current the biskyrmion and the current electrons are deflected into transverse directions. Our study motivates future in-depth analyses of similarities and differences of these Hall effects for skyrmions and biskyrmions.

One fundamental aspect that distinguishes biskyrmions from skyrmions is their missing rotational symmetry. The orientation of a biskyrmion could be exploited to store multiple bits per biskyrmion. Here, the underlying cubic lattice yields four energetically degenerate orientations  $\alpha$  and allows for quaternary instead of binary logic. It is conceivable to store data in an array of nanodisks instead of in a racetrack device.

## Methods

For the micromagnetic simulations the Landau-Lifshitz-Gilbert equation<sup>48–50</sup>

$$\dot{\mathbf{m}}_i = -\gamma_e \mathbf{m}_i \times \mathbf{B}_{i,\text{eff}} + \alpha_g \mathbf{m}_i \times \dot{\mathbf{m}}_i + \gamma_e \varepsilon \beta [(\mathbf{m}_i \times \mathbf{s}_i) \times \mathbf{m}_i] \quad (8)$$

is solved using Mumax3<sup>46,47</sup>.

The first term describes the precession of each magnetic moment around its instantaneous effective magnetic field  $\mathbf{B}_{\text{eff}}^i = -\delta_{\mathbf{m}_i} F / M_s$ . This field, derived from the free energy density  $F$ , takes into account exchange interaction, uniaxial anisotropy, Zeeman energy, and the demagnetization field accounting for the dipole-dipole interaction.

The second term, introduced phenomenologically, considers that the magnetic moments tend to align along their effective magnetic field. The strength of this damping is quantified by the Gilbert damping constant  $\alpha_g$ .

The third term accounts for the coupling of the magnetic moments with injected spin-polarized currents. The in-plane torque coefficient  $\varepsilon \beta = \hbar P j / 2 e d_z M_s$  depends on the current's spin polarization  $P$  and the current density  $j$ . The spatial distribution of the injected spins  $\{\mathbf{s}_i\}$  is given by the vortex textures in the writing disks. An out-of-plane torque has been neglected since it is usually small and merely rescales the external magnetic field.  $\gamma_e = 1.760 \times 10^{11} \text{ T}^{-1} \text{ s}^{-1}$  is the gyromagnetic ratio of an electron.

We use parameters that stabilize stray-field skyrmions, similar to those in ref.<sup>35</sup>: exchange  $A = 15 \text{ pJ/m}$ , uniaxial anisotropy in  $z$  direction  $K_z = 1.2 \text{ MJ/m}^3$ , external field  $\mathbf{B} = -40 \text{ mT} \mathbf{e}_z$  (along the ferromagnetic orientation), saturation magnetization  $M_s = 1.4 \text{ MA/m}$ , and Gilbert damping  $\alpha_g = 0.3$ . The disk has a radius of 150 nm and a thickness of  $d_z = 3 \text{ nm}$ . For the simulations we used discrete magnetization cells of size  $1 \text{ nm} \times 1 \text{ nm} \times 1 \text{ nm}$ . The DMI has been set to zero. We checked that a small DMI constant (interfacial DMI  $D = 0.1 \text{ mJ/m}^2$ ) does not qualitatively affect the results of the simulations shown in Fig. 5; for larger values of  $D$  one of the two skyrmions would annihilate and a biskyrmion would not form.

As stated in the main text, a spin-polarized current of  $\mathbf{j}_{\text{write}} P = 7 \times 10^8 \text{ A/cm}^{-2} \mathbf{e}_z$  with a spin polarization orientation  $\{\mathbf{s}_i\}$ , given by an in-plane vortex texture

$$\mathbf{s}_i = \pm (-y, x \mp \Delta x/2, 0) / \sqrt{(x_i \pm \Delta x/2)^2 + y^2}, \quad (9)$$

writes well-defined skyrmions into the nanodisk, if the current is applied for 200 ps. The two signs correspond to the left and right writing disks, respectively. The writing disks have a radius of 25 nm each and their centers are at a distance of 120 nm. The writing disks and the process of spin polarization have not been simulated explicitly but are condensed into the spin-polarization parameter  $P$  which scales the necessary applied current density.

**Accession codes.** The code Mumax3 is accessible at <https://github.com/mumax3/releases/tag/v3.9.3>.

## References

- Bogdanov, A. N. & Yablonskii, D. Thermodynamically stable vortices in magnetically ordered crystals. the mixed state of magnets. *Zh. Eksp. Teor. Fiz* **95**, 178 (1989).
- Mühlbauer, S. *et al.* Skyrmion lattice in a chiral magnet. *Science* **323**, 915–919, <https://doi.org/10.1126/science.1166767> (2009).
- Nagaosa, N. & Tokura, Y. Topological properties and dynamics of magnetic skyrmions. *Nat. Nanotechnol.* **8**, 899–911, <https://doi.org/10.1038/nnano.2013.243> (2013).
- Yu, X. *et al.* Real-space observation of a two-dimensional skyrmion crystal. *Nature* **465**, 901–904, <https://doi.org/10.1038/nature09124> (2010).
- Parkin, S. S. P. Shiftable magnetic shift register and method of using the same US Patent 6,834,005 (2004).
- Sampaio, J., Cros, V., Rohart, S., Thiaville, A. & Fert, A. Nucleation, stability and current-induced motion of isolated magnetic skyrmions in nanostructures. *Nat. Nanotechnol.* **8**, 839, <https://doi.org/10.1038/nnano.2013.210> (2013).
- Romming, N. *et al.* Writing and deleting single magnetic skyrmions. *Science* **341**, 636–639, <https://doi.org/10.1126/science.1240573> (2013).
- Jiang, W. *et al.* Direct observation of the skyrmion Hall effect. *Nat. Phys.* **13**, 162–169, <https://doi.org/10.1038/nphys3883> (2017).
- Litzius, K. *et al.* Skyrmion Hall effect revealed by direct time-resolved x-ray microscopy. *Nat. Phys.* **13**, 170–175, <https://doi.org/10.1038/nphys4000> (2017).
- Maccariello, D. *et al.* Electrical detection of single magnetic skyrmions in metallic multilayers at room temperature. *Nat. Nanotechnol.* **13**, 233–237 <https://doi.org/10.1038/s41565-017-0044-4> (2018).

11. Hamamoto, K., Ezawa, M. & Nagaosa, N. Purely electrical detection of a skyrmion in constricted geometry. *Appl. Phys. Lett.* **108**, 112401, <https://doi.org/10.1063/1.4943949> (2016).
12. Skyrme, T. H. R. A non-linear field theory. *Proc. Royal Soc. Lond. A: Math. Phys. Eng. Sci.* **260**, 127–138 (1961).
13. Biedenharn, L., Sorace, E. & Tarlini, M. Topological concepts in nuclear physics: The deuteron as a bi-skyrmion. In *Symmetries in Science II*, 51–59 (Springer, 1986).
14. Schramm, A. J., Dothan, Y. & Biedenharn, L. C. A calculation of the deuteron as a biskyrmion. *Phys. Lett. B* **205**, 151–155, [https://doi.org/10.1016/0370-2693\(88\)91638-3](https://doi.org/10.1016/0370-2693(88)91638-3) (1988).
15. Hasebe, K. & Ezawa, Z. Grassmannian fields and doubly enhanced skyrmions in the bilayer quantum Hall system at  $\nu=2$ . *Phys. Rev. B* **66**, 155318, <https://doi.org/10.1103/PhysRevB.66.155318> (2002).
16. Leonov, A., Monchesky, T., Loudon, J. & Bogdanov, A. Three-dimensional chiral skyrmions with attractive interparticle interactions. *J. Physics: Condens. Matter* **28**, 35LT01, <https://doi.org/10.1088/0953-8984/28/35/35LT01> (2016).
17. Du, H. *et al.* Interaction of individual skyrmions in a nanostructured cubic chiral magnet. *Phys. Rev. Lett.* **120**, 197203, <https://doi.org/10.1103/PhysRevLett.120.197203> (2018).
18. Yu, X. *et al.* Biskyrmion states and their current-driven motion in a layered manganite. *Nat. Commun.* **5**, 3198, <https://doi.org/10.1038/ncomms4198> (2014).
19. Wang, W. *et al.* A centrosymmetric hexagonal magnet with superstable biskyrmion magnetic nanodomains in a wide temperature range of 100–340 K. *Adv. Mater.* **28**, 6887–6893, <https://doi.org/10.1002/adma.201600889> (2016).
20. Peng, L. *et al.* Real-space observation of nonvolatile zero-field biskyrmion lattice generation in MnNiGa magnet. *Nano Lett.* **17**, 7075–7079, <https://doi.org/10.1021/acs.nanolett.7b03792> (2017).
21. Zuo, S. *et al.* Direct observation of the topological spin configurations mediated by the substitution of rare-earth element  $\gamma$  in MnNiGa alloy. *Nanoscale* **10**, 2260–2266, <https://doi.org/10.1039/C7NR08997J> (2018).
22. Peng, L. *et al.* Multiple tuning of magnetic biskyrmions using *in situ* L-TEM in centrosymmetric MnNiGa alloy. *J. Physics: Condens. Matter* **30**, 065803, <https://doi.org/10.1088/1361-648X/aaa527> (2018).
23. Zhang, X. *et al.* Skyrmion dynamics in a frustrated ferromagnetic film and current-induced helicity locking-unlocking transition. *Nat. Commun.* **8**, 1717, <https://doi.org/10.1038/s41467-017-01785-w> (2017).
24. Okubo, T., Chung, S. & Kawamura, H. Multiple-q states and the skyrmion lattice of the triangular-lattice heisenberg antiferromagnet under magnetic fields. *Phys. Rev. Lett.* **108**, 017206, <https://doi.org/10.1103/PhysRevLett.108.017206> (2012).
25. Leonov, A. & Mostovoy, M. Multiply periodic states and isolated skyrmions in an anisotropic frustrated magnet. *Nat. Commun.* **6**, 8275, <https://doi.org/10.1038/ncomms9275> (2015).
26. Göbel, B., Mook, A., Henk, J. & Mertig, I. Antiferromagnetic skyrmion crystals: Generation, topological Hall, and topological spin Hall effect. *Phys. Rev. B* **96**, 060406(R), <https://doi.org/10.1103/PhysRevB.96.060406> (2017).
27. Malozemoff, A. & Slonczewski, J. *Magnetic Domain Walls in Bubble Materials* (Academic press, 1979).
28. Eschenfelder, A. H. *Magnetic bubble technology* (Springer-Verlag Berlin Heidelberg New York, 1980).
29. Dzyaloshinsky, I. A thermodynamic theory of “weak” ferromagnetism of antiferromagnetics. *J. Phys. Chem. Solids* **4**, 241–255, [https://doi.org/10.1016/0022-3697\(58\)90076-3](https://doi.org/10.1016/0022-3697(58)90076-3) (1958).
30. Moriya, T. Anisotropic superexchange interaction and weak ferromagnetism. *Physical Review* **120**, 91, <https://doi.org/10.1103/PhysRev.120.91> (1960).
31. Göbel, B., Mook, A., Henk, J., Mertig, I. & Tretiakov, O. A. Magnetic bimerons as skyrmion analogues in in-plane magnets. *Phys. Rev. B* **99**, 060407(R), <https://doi.org/10.1103/PhysRevB.99.060407> (2019).
32. Lin, Y., Grundy, P. & Giess, E. Bubble domains in magnetostatically coupled garnet films. *Appl. Phys. Lett.* **23**, 485–487, <https://doi.org/10.1063/1.1654968> (1973).
33. Takao, S. A study of magnetization distribution of submicron bubbles in sputtered Ho-Co thin films. *J. Magn. Magn. Mater.* **31**, 1009–1010, [https://doi.org/10.1016/0304-8853\(83\)90772-2](https://doi.org/10.1016/0304-8853(83)90772-2) (1983).
34. Jiang, W. *et al.* Blowing magnetic skyrmion bubbles. *Science* **349**, 283–286, <https://doi.org/10.1126/science.aaa1442> (2015).
35. Büttner, F., Lemesh, I. & Beach, G. S. Theory of isolated magnetic skyrmions: From fundamentals to room temperature applications. *Sci. Reports* **8**, 4464, <https://doi.org/10.1038/s41598-018-22242-8> (2018).
36. Aharoni, A. *et al.* *Introduction to the Theory of Ferromagnetism*, vol. 109 (Clarendon Press, 2000).
37. Derrick, G. Comments on nonlinear wave equations as models for elementary particles. *J. Math. Phys.* **5**, 1252–1254 (1964).
38. Rajaraman, R. *Solitons and instantons* (North Holland, 1987).
39. Gioia, G. & James, R. D. Micromagnetics of very thin films. *Proc. Royal Soc. London. Ser. A: Math. Phys. Eng. Sci.* **453**, 213–223, <https://doi.org/10.1098/rspa.1997.0013> (1997).
40. Guslienko, K. Y. Skyrmion state stability in magnetic nanodots with perpendicular anisotropy. *IEEE Magn. Lett.* **6**, 4000104, <https://doi.org/10.1109/LMAG.2015.2413758> (2015).
41. Vidal-Silva, N., Riveros, A. & Escrig, J. Stability of Néel skyrmions in ultra-thin nanodots considering Dzyaloshinskii-Moriya and dipolar interactions. *J. Magn. Magn. Mater.* **443**, 116–123, <https://doi.org/10.1016/j.jmmm.2017.07.049> (2017).
42. Riveros, A., Vidal-Silva, N., Tejo, F. & Escrig, J. Analytical and numerical  $K_1$ - $B$  phase diagrams for cobalt nanostructures: Stability region for a Bloch skyrmion. *J. Magn. Magn. Mater.* **460**, 292–296, <https://doi.org/10.1016/j.jmmm.2018.04.018> (2018).
43. Guslienko, K. Y. Néel skyrmion stability in ultrathin circular magnetic nanodots. *Applied Physics Express* **11**, 063007, <https://doi.org/10.7567/APEX.11.063007> (2018).
44. Tejo, F., Riveros, A., Escrig, J., Guslienko, K. & Chubykalo-Fesenko, O. Distinct magnetic field dependence of Néel skyrmion sizes in ultrathin nanodots. *Sci. Reports* **8**, 6280, <https://doi.org/10.1038/s41598-018-24582-x> (2018).
45. Castro, M. A. & Allende, S. Skyrmion core size dependence as a function of the perpendicular anisotropy and radius in magnetic nanodots. *J. Magn. Magn. Mater.* **417**, 344–348, <https://doi.org/10.1016/j.jmmm.2016.05.095> (2016).
46. Vansteenkiste, A. & Van de Wiele, B. MuMax: a new high-performance micromagnetic simulation tool. *J. Magn. Magn. Mater.* **323**, 2585–2591, <https://doi.org/10.1016/j.jmmm.2011.05.037> (2011).
47. Vansteenkiste, A. *et al.* The design and verification of MuMax3. *AIP Adv.* **4**, 107133, <https://doi.org/10.1063/1.4899186> (2014).
48. Landau, L. D. & Lifshitz, E. On the theory of the dispersion of magnetic permeability in ferromagnetic bodies. *Phys. Z. Sowjetunion* **8**, 101–114 (1935).
49. Gilbert, T. L. A phenomenological theory of damping in ferromagnetic materials. *IEEE Transactions on Magn.* **40**, 3443–3449, <https://doi.org/10.1109/TMAG.2004.836740> (2004).
50. Slonczewski, J. C. Current-driven excitation of magnetic multilayers. *J. Magn. Magn. Mater.* **159**, L1–L7, [https://doi.org/10.1016/0304-8853\(96\)00062-5](https://doi.org/10.1016/0304-8853(96)00062-5) (1996).
51. Cowburn, R., Koltsov, D., Adeyeye, A., Welland, M. & Tricker, D. Single-domain circular nanomagnets. *Phys. Rev. Lett.* **83**, 1042, <https://doi.org/10.1103/PhysRevLett.83.1042> (1999).
52. Shinjo, T., Okuno, T., Hassdorf, R., Shigeto, K. & Ono, T. Magnetic vortex core observation in circular dots of permalloy. *Science* **289**, 930–932, <https://doi.org/10.1126/science.289.5481.930> (2000).
53. Sun, L. *et al.* Creating an artificial two-dimensional skyrmion crystal by nanopatterning. *Phys. Rev. Lett.* **110**, 167201, <https://doi.org/10.1103/PhysRevLett.110.167201> (2013).
54. Miao, B. *et al.* Experimental realization of two-dimensional artificial skyrmion crystals at room temperature. *Phys. Rev. B* **90**, 174411, <https://doi.org/10.1103/PhysRevB.90.174411> (2014).

55. Gilbert, D. A. *et al.* Realization of ground-state artificial skyrmion lattices at room temperature. *Nat. Commun.* **6**, 8462, <https://doi.org/10.1038/ncomms9462> (2015).
56. Loreto, R. *et al.* Creation, transport and detection of imprinted magnetic solitons stabilized by spin-polarized current. *J. Magn. Magn. Mater.* **455**, 25–31, <https://doi.org/10.1016/j.jmmm.2017.04.074> (2018).
57. Taniuchi, T., Oshima, M., Akinaga, H. & Ono, K. Vortex-chirality control in mesoscopic disk magnets observed by photoelectron emission microscopy. *J. Appl. Phys.* **97**, 10J904, <https://doi.org/10.1063/1.1862032> (2005).
58. Gaididei, Y., Sheka, D. D. & Mertens, F. G. Controllable switching of vortex chirality in magnetic nanodisks by a field pulse. *Appl. Phys. Lett.* **92**, 012503, <https://doi.org/10.1063/1.2829795> (2008).
59. Konoto, M. *et al.* Formation and control of magnetic vortex chirality in patterned micromagnet arrays. *J. Appl. Phys.* **103**, 023904, <https://doi.org/10.1063/1.2828177> (2008).
60. Yakata, S., Miyata, M., Nonoguchi, S., Wada, H. & Kimura, T. Control of vortex chirality in regular polygonal nanomagnets using in-plane magnetic field. *Appl. Phys. Lett.* **97**, 222503, <https://doi.org/10.1063/1.3521407> (2010).
61. Bogdanov, A. & Hubert, A. The stability of vortex-like structures in uniaxial ferromagnets. *J. Magn. Magn. Mater.* **195**, 182–192, [https://doi.org/10.1016/S0304-8853\(98\)01038-5](https://doi.org/10.1016/S0304-8853(98)01038-5) (1999).
62. Zhang, X. *et al.* Control and manipulation of a magnetic skyrmionium in nanostructures. *Phys. Rev. B* **94**, 094420, <https://doi.org/10.1103/PhysRevB.94.094420> (2016).
63. Göbel, B., Schäffer, A. F., Berakdar, J., Mertig, I. & Parkin, S. S. P. Electrical writing, deleting, reading, and moving of magnetic skyrmioniums in a racetrack device. *arXiv preprint:1902.06295* (2019).
64. Yang, Y. *et al.* Ultrafast magnetization reversal by picosecond electrical pulses. *Science Advances* **3**, e1603117, <https://doi.org/10.1126/sciadv.1603117> (2017).
65. Schäffer, A. F., Dürr, H. A. & Berakdar, J. Ultrafast imprinting of topologically protected magnetic textures via pulsed electrons. *Appl. Phys. Lett.* **111**, 032403, <https://doi.org/10.1063/1.4991521> (2017).
66. Thiele, A. Steady-state motion of magnetic domains. *Phys. Rev. Lett.* **30**, 230, <https://doi.org/10.1103/PhysRevLett.30.230> (1973).
67. Göbel, B., Mook, A., Henk, J. & Mertig, I. Overcoming the speed limit in skyrmion racetrack devices by suppressing the skyrmion Hall effect. *Phys. Rev. B* **99**, 020405(R), <https://doi.org/10.1103/PhysRevB.99.020405> (2019).
68. Zang, J., Mostovoy, M., Han, J. H. & Nagaosa, N. Dynamics of skyrmion crystals in metallic thin films. *Phys. Rev. Lett.* **107**, 136804, <https://doi.org/10.1103/PhysRevLett.107.136804> (2011).
69. Everschor-Sitte, K. & Sitte, M. Real-space Berry phases: Skyrmion soccer. *J. Appl. Phys.* **115**, 172602, <https://doi.org/10.1063/1.4870695> (2014).
70. Loudon, J. C. *et al.* Do images of biskyrmions show type-II bubbles? *Adv. Mater.* **1806598**, <https://doi.org/10.1002/adma.201806598> (2019).
71. Yao, Y. *et al.* Magnetic hard nanobubble: A possible magnetization structure behind the bi-skyrmion. *Appl. Phys. Lett.* **114**, 102404, <https://doi.org/10.1063/1.5083971> (2019).
72. Bruno, P., Dugaev, V. & Taillefumier, M. Topological Hall effect and Berry phase in magnetic nanostructures. *Phys. Rev. Lett.* **93**, 096806, <https://doi.org/10.1103/PhysRevLett.93.096806> (2004).
73. Neubauer, A. *et al.* Topological Hall effect in the A phase of MnSi. *Phys. Rev. Lett.* **102**, 186602, <https://doi.org/10.1103/PhysRevLett.102.186602> (2009).
74. Hamamoto, K., Ezawa, M. & Nagaosa, N. Quantized topological Hall effect in skyrmion crystal. *Phys. Rev. B* **92**, 115417, <https://doi.org/10.1103/PhysRevB.92.115417> (2015).
75. Göbel, B., Mook, A., Henk, J. & Mertig, I. Unconventional topological Hall effect in skyrmion crystals caused by the topology of the lattice. *Phys. Rev. B* **95**, 094413, <https://doi.org/10.1103/PhysRevB.95.094413> (2017).
76. Göbel, B., Mook, A., Henk, J. & Mertig, I. Signatures of lattice geometry in quantum and topological Hall effect. *New J. Phys.* **19**, 063042, <https://doi.org/10.1088/1367-2630/aa709b> (2017).
77. Göbel, B., Mook, A., Henk, J. & Mertig, I. The family of topological Hall effects for electrons in skyrmion crystals. *The Eur. Phys. J. B* **91**, 179, <https://doi.org/10.1140/epjb/e2018-90090-0> (2018).
78. Nakazawa, K., Bibes, M. & Kohnno, H. Topological Hall effect from strong to weak coupling. *J. Phys. Soc. Jpn.* **87**, 033705, <https://doi.org/10.7566/JPSJ.87.033705> (2018).

## Acknowledgements

B.G. is thankful to Alexander F. Schäffer regarding discussions about Mumax and possible alternative writing approaches. This work is supported by Priority Program SPP 1666 and SFB 762 of Deutsche Forschungsgemeinschaft (DFG).

## Author Contributions

B.G. initiated the project and performed the calculations. B.G. wrote the manuscript with the help of J.H. All authors discussed the results and commented on the manuscript.

## Additional Information

**Supplementary information** accompanies this paper at <https://doi.org/10.1038/s41598-019-45965-8>.

**Competing Interests:** The authors declare no competing interests.

**Publisher's note:** Springer Nature remains neutral with regard to jurisdictional claims in published maps and institutional affiliations.



**Open Access** This article is licensed under a Creative Commons Attribution 4.0 International License, which permits use, sharing, adaptation, distribution and reproduction in any medium or format, as long as you give appropriate credit to the original author(s) and the source, provide a link to the Creative Commons license, and indicate if changes were made. The images or other third party material in this article are included in the article's Creative Commons license, unless indicated otherwise in a credit line to the material. If material is not included in the article's Creative Commons license and your intended use is not permitted by statutory regulation or exceeds the permitted use, you will need to obtain permission directly from the copyright holder. To view a copy of this license, visit <http://creativecommons.org/licenses/by/4.0/>.

© The Author(s) 2019

## 6.2 Magnetic bimerons as in-plane analogues of skyrmions

As the next magnetic quasiparticle the bimeron is discussed. This spin texture consists of a meron and an antimeron with reversed net magnetizations. Both objects have the same topological charge of  $N_{\text{Sk}} = 1/2$  or  $N_{\text{Sk}} = -1/2$ , depending of their polarity. They can be seen as half a skyrmion or antiskyrmion, respectively; the spins are oriented in the plane far from the objects' centers [see Fig. 27(a)]. While a meron and an antimeron cannot exist in a ferromagnetic background, a bimeron can [see Fig. 27(b)]. It has a topological charge of  $N_{\text{Sk}} = \pm 1$ . Similar to skyrmions, different types of bimerons can be defined. Besides changing the helicity of the bimeron, also the connecting vector of meron and antimeron can be rotated around the bimeron's center; in contrast to a skyrmion, a bimeron is not rotationally symmetric.

Besides its interpretation as an object constructed from two subparticles, a bimeron can also be understood as a skyrmion whose magnetic moments have been rotated around an in-plane axis (very similar to the rotation of every moment around the out-of-plane axis upon changing a skyrmion's helicity). Both rotations leave the topological charge (and even its density) invariant. For this reason, the bimeron can also be understood as a skyrmion in an in-plane magnetized sample (Fig. 27).

**Preliminary studies.** Bimeron spin textures have first been stabilized theoretically by Kharkov *et al.* [140] in thin films with in-plane anisotropy. The authors considered frustrated exchange interactions as the stabilizing mechanism. As shown in Sec. 2.3 this interaction is not chiral, which means that the corresponding energy is invariant under

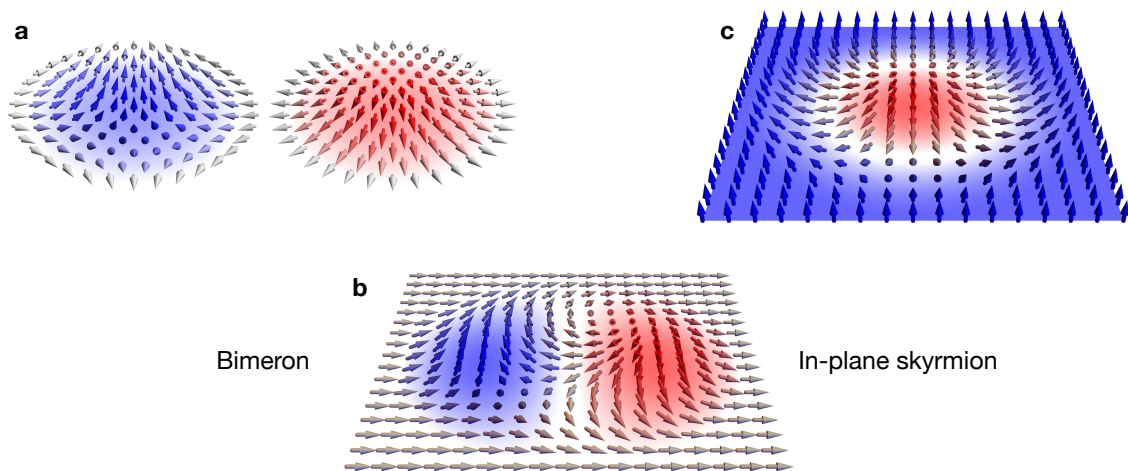


Figure 27: **Magnetic bimeron.** **a** A pair of meron and antimeron with reversed out-of-plane magnetizations. **b** The combination of these two textures constitutes a bimeron. Alternatively, the present texture can be understood as an in-plane skyrmion, since it can be generated by rotating all magnetic moments of a conventional skyrmion **c** by  $90^\circ$  around an in-plane axis. The net magnetization and the surrounding of the bimeron point into an in-plane direction. Panels b and c: Reprinted (figure) with permission from (B. Göbel *et al.* Physical Review B **99**, 060407(R) (2019); Ref. [BG3]); Magnetic bimerons as skyrmion analogues in in-plane magnets. Copyright (2019) by the American Physical Society.

common rotations of all spins' orientations around any global axis. This includes the out-of-plane axis, (a continuous change of the helicity) and in-plane axes (the transformation of a skyrmion to a bimeron).

A few papers present experimental results, which are loosely related to magnetic bimerons. Perhaps most relevant is Ref. [141], where the existence of skyrmion tubes, which lay in an in-plane direction, is presented. These tubes are meandering and cut off after only a few nanometers. The cross-section magnetization then looks just like a bimeron. However, this texture is not continued trivially along the third dimension. It is not a bimeron tube but a short skyrmion tube.

The lack of an experimental observation of bimerons and the fact that theoretical predictions consider only frustrated exchange (a stabilizing mechanism which remains unproven experimentally even for conventional skyrmions) imply that new mechanisms for stabilizing bimerons have to be predicted.

**This publication.** In the following publication “Magnetic bimerons as skyrmion analogues in in-plane magnets” [BG5] the idea of the common spin rotation is adapted. It allows to straightforwardly explain why bimerons can be stabilized by the frustrated exchange interactions as in Ref. [140] and allows for a generalization to other stabilizing mechanisms. One main result is the proposal of a novel DMI setup [Fig. 1(c) of the publication] that stabilizes bimerons and bimeron crystals.

Furthermore, the geometric argumentation allows to predict a Hall effect, which is of purely topological origin (cf. Fig. 2 of the publication). The spin rotation gives a bimeron a net magnetization in the plane and leads to a stabilization under the presence of an external magnetic field which also points in the plane. For this reason, the  $xy$  elements of the anomalous Hall effect and the conventional Hall effect vanish. However, the spin rotation leaves the emergent field of the spin texture invariant, which is why a topological Hall effect still emerges.

The behavior under spin torques is presented in Fig. 3 of the publication and can be understood from the geometric consideration as well. The main results are that bimerons can be utilized as carriers of information in racetrack-storage devices, just like skyrmions, but that they can be written and moved also by different spin orientations. This allows to use new materials in devices.

The stability of the magnetic textures has been identified using Monte Carlo simulations (Sec. 3.1). The topological Hall effect has been calculated using the Berry theory (Sec. 4.2) for a tight-binding model (Sec. 4.4). The current-driven motion was simulated by propagating the LLG equation using mumax3 and by considering the Thiele equation (3.35) for an effective description. For the micromagnetic simulations the modified DMI configurations, corresponding to bimerons and antiskyrmions, had to be implemented in the code.

The following publication: Reprinted (whole article) with permission from (B. Göbel *et al.* Physical Review B **99**, 060407(R) (2019); Ref. [BG5]; Magnetic bimerons as skyrmion analogues in in-plane magnets). Copyright (2019) by the American Physical Society.



## Magnetic bimerons as skyrmion analogues in in-plane magnets

Börge Göbel,<sup>1,\*</sup> Alexander Mook,<sup>2</sup> Jürgen Henk,<sup>2</sup> Ingrid Mertig,<sup>1,2</sup> and Oleg A. Tretiakov<sup>3,4,5</sup><sup>1</sup>Max-Planck-Institut für Mikrostrukturphysik, D-06120 Halle (Saale), Germany<sup>2</sup>Institut für Physik, Martin-Luther-Universität Halle-Wittenberg, D-06099 Halle (Saale), Germany<sup>3</sup>School of Physics, The University of New South Wales, Sydney 2052, Australia<sup>4</sup>Institute for Materials Research and Center for Science and Innovation in Spintronics, Tohoku University, Sendai 980-8577, Japan<sup>5</sup>National University of Science and Technology MISiS, Moscow 119049, Russia

(Received 8 November 2018; published 25 February 2019)

A magnetic bimeron is a pair of two merons and can be understood as the in-plane magnetized version of a skyrmion. Here we theoretically predict the existence of single magnetic bimerons as well as bimeron crystals, and compare the emergent electrodynamics of bimerons with their skyrmion analogues. We show that bimeron crystals can be stabilized in frustrated magnets and analyze what crystal structure can stabilize bimerons or bimeron crystals via the Dzyaloshinskii-Moriya interaction. We point out that bimeron crystals, in contrast to skyrmion crystals, allow for the detection of a pure topological Hall effect. By means of micromagnetic simulations, we show that bimerons can be used as bits of information in in-plane magnetized racetrack devices, where they allow for current-driven motion for torque orientations that leave skyrmions in out-of-plane magnets stationary.

DOI: [10.1103/PhysRevB.99.060407](https://doi.org/10.1103/PhysRevB.99.060407)

Over the last years magnetic skyrmions [Fig. 1(a) top] [1–6] have attracted immense research interest, as these small spin textures  $\mathbf{m}(\mathbf{r})$  possess strong stability, characterized by a topological charge  $N_{\text{Sk}} = \pm 1$ . Skyrmions offer a topological contribution to the Hall effect [7–18], commonly measured in skyrmion crystals, and can be stabilized as individual quasiparticles in collinear ferromagnets. They can be driven by currents in thin films [6, 19–26] allowing for spintronics applicability. The stabilizing interaction in most systems is the Dzyaloshinskii-Moriya interaction (DMI) [27, 28], while theoretical simulations also point to other stabilizing mechanisms, e.g., frustrated exchange interactions [29, 30]. Textures with a half-integer topological charge, like merons and antimerons (or vortices and antivortices), have also been subject of intense research [31–33].

Magnetic bimerons [34–37] [Fig. 1(a) bottom] are the combination of two merons [red and blue] and can be understood as in-plane magnetized versions of magnetic skyrmions [38]. Instead of the out-of-plane component of the magnetization it is an in-plane component which is radial symmetric about the quasiparticle's center; being aligned with the saturation magnetization of the ferromagnet at the outer region of the bimeron and pointing into the opposite direction in the center. Recently, Kharkov *et al.* showed that isolated bimerons can be stabilized in an easy-plane magnet by frustrated exchange interactions [34]. In DMI dominated systems (as is the case for all experimentally known skyrmion-host materials) bimerons have only been shown to exist as unstable transition states [35, 36].

In this Rapid Communication, we show that bimerons in frustrated magnets can also be stabilized in an array, the

bimeron crystal. Furthermore, we propose a structural configuration that allows for DMI stabilizing isolated bimerons and bimeron crystals. We compare fundamental properties of skyrmions and bimerons and find that both show the same topological Hall effect, whereas the bimeron allows for a *pure* detection, that is without superposition of the anomalous and ordinary Hall effects. Elaborating on the spintronics applicability of bimerons in in-plane racetrack memory devices, we find that bimerons can be driven by spin currents, similar to skyrmions. However, they extend the class of materials and spin-torque configurations for building spintronics devices.

*Stabilization of bimerons and bimeron crystals.* A bimeron [see Fig. 1(a) bottom] (or a vortex-antivortex pair) consists of two subtextures: a meron and an antimeron (or a vortex and an antivortex), with mutually reversed  $z$  components of the magnetic moments  $\{\mathbf{m}_i\}$ . Still, the bimeron itself is the quasiparticle in in-plane magnets, since merons and antimerons can not exist individually in a ferromagnet. The topological charge density

$$n_{\text{Sk}}(\mathbf{r}) = \frac{1}{4\pi} \mathbf{m}(\mathbf{r}) \cdot \left[ \frac{\partial \mathbf{m}(\mathbf{r})}{\partial x} \times \frac{\partial \mathbf{m}(\mathbf{r})}{\partial y} \right] \quad (1)$$

is distributed radially symmetrically around the center of the bimeron and integrates to  $N_{\text{Sk}} = \pm 1$ ; meron and antimeron carry a topological charge of  $\pm 1/2$  each [39].

The recurring idea of this paper is a geometric comparison of skyrmions, bimerons, and antiskyrmions: all three magnetic textures are related by a rotation of each spin around an in-plane axis (in this paper always  $y$ ). A bimeron is constructed by rotating each spin of a skyrmion by  $90^\circ$  [cf. Fig. 1(a)]; for an antiskyrmion the spins have to be rotated by another  $90^\circ$ .

To find stable bimerons or bimeron crystals, one can therefore start from any system that stabilizes skyrmions and rotate every vectorial term in the Hamiltonian. The most effortless approach is to consider skyrmions stabilized by frustrated

\*Corresponding author: [bgoebel@mpi-halle.mpg.de](mailto:bgoebel@mpi-halle.mpg.de)

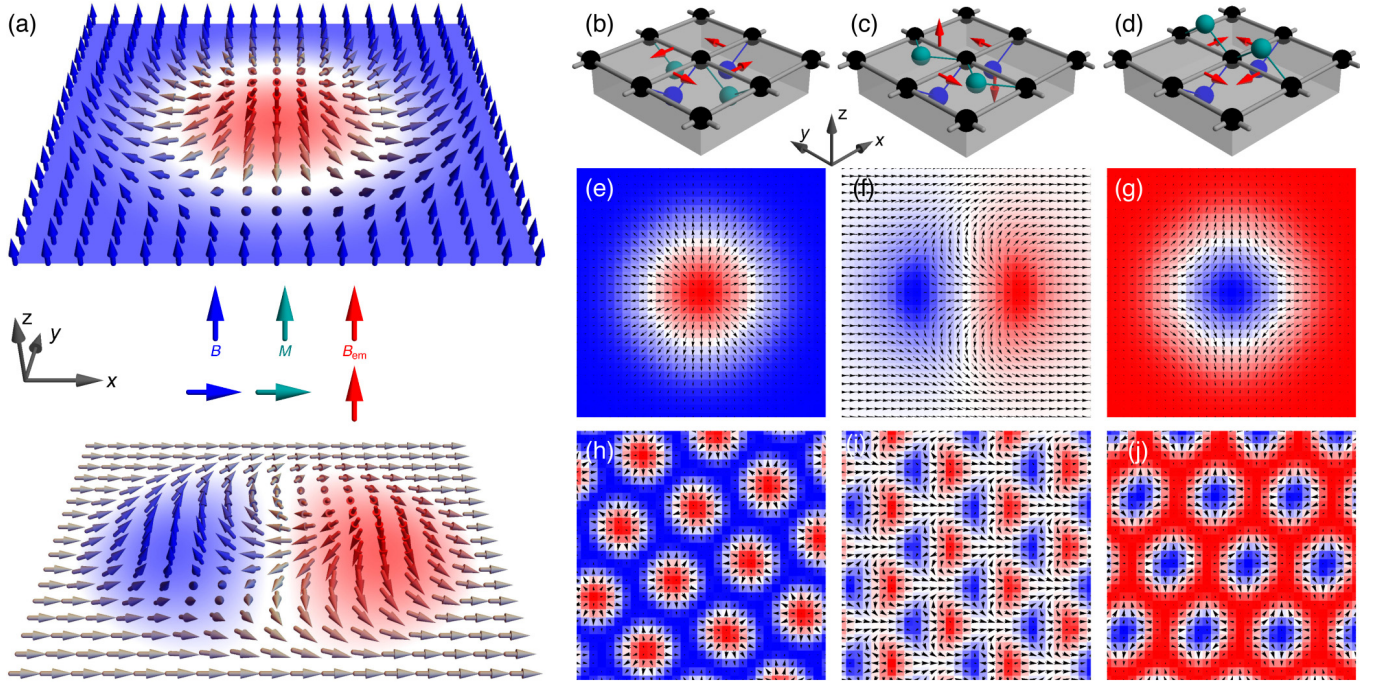


FIG. 1. Magnetic textures. (a) If the magnetic moments of a magnetic skyrmion (top) are rotated by  $90^\circ$  around the  $y$  axis the resulting texture is a magnetic bimeron (bottom), which requires a stabilizing magnetic field  $\mathbf{B}$  and has net magnetization  $\mathbf{M}$ , both rotated in the same way. The emergent field  $\mathbf{B}_{\text{em}}$  remains out-of plane. (b)–(d) show the necessary geometry of magnetic atoms (black) and heavy metal atoms (blue, green) to generate the DMI vectors (red), which stabilize (e)–(g) isolated skyrmions, bimerons and antiskyrmions, respectively. (h)–(j) show periodic arrays. The color in the magnetic textures indicates the out-of plane component of the magnetization (blue: positive, red: negative). (a) shows schematic representations. (e)–(g) are relaxed metastable textures from propagating the LLG equation in a ferromagnetic background at zero temperature for the parameters:  $D = J/3$ ,  $|\mathbf{K}| = |\mathbf{B}| = J/15$  (here  $J$  is the nearest-neighbor exchange constant) and Gilbert damping  $\alpha = 0.01$ . (h)–(j) are results of Monte Carlo simulations at zero temperature, with  $D = J$ ,  $|\mathbf{B}| = |\mathbf{K}| = 0.3J$ . Magnetic field  $\mathbf{B}$  and easy-axis anisotropy  $\mathbf{K}$  point along  $z$  for the skyrmion,  $x$  for the bimeron and  $-z$  for the antiskyrmion; the corresponding DMI vectors have been used.

exchange  $-J_{ij}\mathbf{m}_i \cdot \mathbf{m}_j$ . If the *scalar* constants  $J_{ij}$  for nearest and next-nearest neighbor interactions have opposite signs the ground state of the system can be a spin-spiral phase [29]. When an external magnetic field  $\mathbf{B}$  and easy-axis anisotropy  $\mathbf{K}$  are present pointing out-of-plane, skyrmions and skyrmion crystals may be stabilized.

Following this idea, bimerons and bimeron crystals are stabilized in a system where both  $\mathbf{B}$  and  $\mathbf{K}$  are rotated in-plane [cf. Fig. 1(a)]. Then, the Hamiltonian

$$H = -\frac{1}{2} \sum_{i,j} J_{ij} \mathbf{m}_i \cdot \mathbf{m}_j - \sum_i \mathbf{B} \cdot \mathbf{m}_i - \frac{1}{2} \sum_i \sum_{A \in \{x,y,z\}} K_A (m_i^A)^2$$

gives the same energy as for the skyrmion phase before the rotation. The results of Monte Carlo simulations confirming this finding are presented in Ref. [40]. The analogy of the two systems does also hold for other typical phases: for low fields, we find a spin-spiral state, for medium fields the bimeron crystal and for high fields the system is fully magnetized. At the transition, we find isolated bimerons in an in-plane magnetized background.

To illustrate the geometric equivalence of bimeron and skyrmion we used an easy-axis anisotropy along an in-plane

direction, even though such quantity is commonly small. Our results also hold for systems without anisotropy or with an easy-plane anisotropy (as in Ref. [34], where isolated metastable bimerons have been considered), since the applied magnetic field makes the two in-plane directions inequivalent (see Ref. [40]).

At the present state of research almost all experimentally detected skyrmions are generated by the Dzyaloshinskii-Moriya interaction (DMI) [27,28]

$$H_{\text{DMI}} = \frac{1}{2} \sum_{i,j} \mathbf{D}_{ij} \cdot (\mathbf{m}_i \times \mathbf{m}_j). \quad (2)$$

It is a relativistic energy contribution due to spin-orbit coupling and broken inversion symmetry. The DMI vectors  $\mathbf{D}_{ij}$  obey Moriya's symmetry rules [28] and can be estimated from the Levy-Fert rule [41];  $\mathbf{D}_{ij}$  points into the direction  $\mathbf{r}_{i \rightarrow j} \times \mathbf{r}_{i \rightarrow \text{HM}}$ , i. e., it is perpendicular to the plane of the two lattice sites  $i, j$  and the nearest heavy-metal atom (HM). Similar to the frustrated exchange interactions the DMI leads to spin canting, but since it is vectorial it strictly dictates the type of magnetic texture: Skyrmions can not be turned into bimerons by rotating  $\mathbf{B}$  and  $\mathbf{K}$  only. The  $\mathbf{D}_{ij}$  have to be adjusted as well [42].

At interfaces of layered systems [Fig. 1(b)] heavy-metal atoms (green and blue) induce DMI vectors between

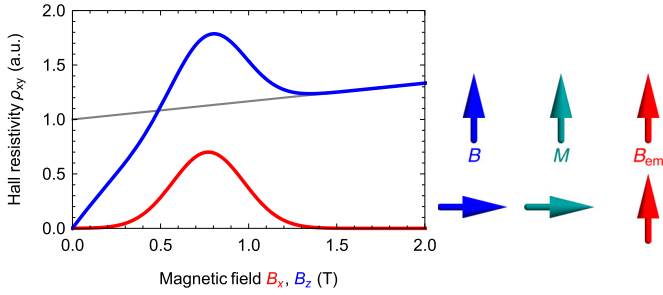


FIG. 2. Hall resistivity (schematic). We compare the signal for a bimeron (red) and a skymion (blue). While the signal is purely of topological origin in the bimeron phase (here stable for magnetic fields in  $x$  direction between 0.5 and 1 T), it is superimposed by the ordinary Hall (cf. slope of the gray curve) and the anomalous Hall effect (offset of the gray curve) for the skymion (here the stabilizing field is applied along  $z$ ).

neighboring magnetic atoms (black). Typically, the DMI vectors form a toroidal arrangement and produce Néel skyrmions (e) or Néel skyrmion crystals (h). Rotating the HM atoms around the bond in  $y$  direction, the  $D_{ij}$  are rotated in the same way according to the Levy-Fert rule. If now external field and anisotropy are oriented along the  $x$  direction, as in the frustrated exchange case, bimerons or bimeron crystals are stabilized for the same parameters (in magnitude) as for the skyrmion phase, see Figs. 1(f) and 1(i). This approach is confirmed by Monte Carlo simulations and atomistic simulations of the Landau-Lifshitz-Gilbert equation (LLG) [43,44] (see Ref. [40]). To complete this picture, we point out that for the stabilization of antiskyrmions [(g) and (j)] the indicated HM atoms (green) have to be rotated another  $90^\circ$  around the bond in  $y$  direction (d)—a configuration recently found experimentally [45] in the Heusler alloy  $\text{Mn}_{1.4}\text{Pt}_{0.9}\text{Pd}_{0.1}\text{Sn}$ . The corresponding DMI is called “anisotropic” [46–48].

Summarizing up to this point we predict the existence of isolated bimerons and bimeron crystals by frustrated exchange and DMI. Next, we discuss implications of the in-plane magnetized bulk systems and thin films with bimerons for electronic properties and spintronic applications.

*Pure topological Hall effect of electrons.* When an electric field  $\mathbf{E}$  is applied to a metal, a current  $\mathbf{j}$  flows according to Ohm’s law  $\mathbf{E} = \rho\mathbf{j}$ . For a skyrmion crystal the transverse element of the resistivity tensor

$$\rho_{xy} = \rho_{xy}^{\text{HE}} + \rho_{xy}^{\text{AHE}} + \rho_{xy}^{\text{THE}} \quad (3)$$

is decomposed into an ordinary Hall contribution [49] due to an external magnetic field  $\rho_{xy}^{\text{HE}} \propto B_z$ , an anomalous Hall contribution [50] due to spin-orbit coupling and a net magnetization  $\rho_{xy}^{\text{AHE}} \propto M_z$  [51], and a topological Hall contribution due to the local topological charge density [Eq. (1)] that acts like an emergent field  $\rho_{xy}^{\text{THE}} \propto \langle B_{\text{em},z} \rangle \propto N_{\text{Sk}}$ . For skyrmions,  $\mathbf{B}$ ,  $\mathbf{M}$ , and  $\langle \mathbf{B}_{\text{em}} \rangle$  point along the  $z$  direction.

For a bimeron, the spin rotation renders the  $z$  component of magnetic quantities zero,  $B_z = M_z = 0$  [cf. Fig. 1(a)], but since  $n_{\text{Sk}}$  is invariant under global spin rotation  $B_{\text{em},z}$  remains. For this reason, *only* the topological Hall effect emerges in a sample with bimerons (see Fig. 2). This hallmark for real-space topology can be detected in an isolated manner

making bimeron crystals a playground for investigating fundamental physics. In Ref. [40], we numerically validate the equivalence of the topological Hall effect for skyrmion and bimeron crystals following Refs. [13,15–18,52], in which the energy-dependent conductivity is discussed.

*Current-driven motion in thin film.* In Ref. [37], the rotation of an annihilating vortex-antivortex pair in in-plane magnets without DMI has been analyzed. We are now able to discuss the current-driven propagation of *metastable* bimerons. In the following, we show that bimerons can be utilized as topologically protected information carriers in in-plane magnetized thin films and discuss similarities and differences to skyrmion racetrack devices [20,53–56].

In the spin-transfer torque (STT) scenario [20], a current  $\mathbf{j}$  of spin-polarized electrons is applied along the ferromagnet. Since the electron spin at site  $i$  is given by the magnetic texture itself, the torque is rotated in the same way as the magnetization, which leads to identical motion of bimerons and skyrmions under STT.

A more efficient way to drive skyrmions is the spin-orbit torque (SOT) scenario [20]: spins are injected perpendicularly to the ferromagnetic film, via (i) a spin-polarized current traversing a second ferromagnetic layer with a distinct magnetization  $s_{\text{in}}$  or via (ii) a charge current in an adjacent heavy-metal layer, which is transformed into a spin current by the spin Hall effect ( $s_{\text{in}} \parallel \mathbf{y}$  in cubic systems). The perpendicularly injected spins are independent of the magnetization in the actual racetrack layer, and large torques can be generated.

The motion of magnetic textures in nanostructured samples is simulated within the micromagnetic approach, that models magnetic textures on a larger length scale compared to the atomistic simulations presented in Fig. 1. We solve the LLG equation (see Ref. [40]) for each micromagnetic moment  $\mathbf{m}_i$  with the in-plane spin torque [57] proportional to

$$\frac{jP}{d_z M_s} [(\mathbf{m}_i \times \mathbf{s}_{\text{in}}) \times \mathbf{m}_i], \quad (4)$$

where  $d_z$  is the layer thickness,  $M_s$  is the saturation magnetization, and  $P$  is the spin polarization of a perpendicular current  $j$  for (i) or spin Hall angle for (ii). For comparability the parameters of Co/Pt are taken from Ref. [20] (they are specified in Ref. [40]). The DMI that stabilizes bimerons is derived from the vectors of Fig. 1(c)

$$\epsilon_{\text{DMI}} = D \left( m_z \frac{\partial m_x}{\partial x} - m_x \frac{\partial m_z}{\partial x} + m_x \frac{\partial m_y}{\partial y} - m_y \frac{\partial m_x}{\partial y} \right)$$

and was implemented in MUMAX3 [58,59].

For the SOT scenario (i), skyrmions in a  $z$  magnetized ferromagnet can be driven by injected spins  $s_{\text{in}} \perp z$ . Due to the global rotation of spins a bimeron in an  $x$  magnetized ferromagnet can be driven by spins  $s_{\text{in}} \perp x$  and remain stationary for  $s_{\text{in}} \parallel x$ , see Fig. 3(a).

Towards utilization in a racetrack device the current-driven motion ( $\mathbf{j} \parallel \mathbf{x}$ ) is the most relevant aspect of SOTs. Using a cubic heavy metal material for scenario (ii) (e.g., Pt), i. e.,  $s_{\text{in}} \parallel \mathbf{y}$ , skyrmions and bimerons are propelled equally in a system with their favoring easy-axis anisotropy ( $K_z > 0$  for the skyrmion and  $K_x > 0$  for the bimeron) and DMI [Fig. 1(b) for the skyrmion and Fig. 1(c) for the bimeron], as long as the demagnetization field is neglected, cf. Fig. 3(b). In this case

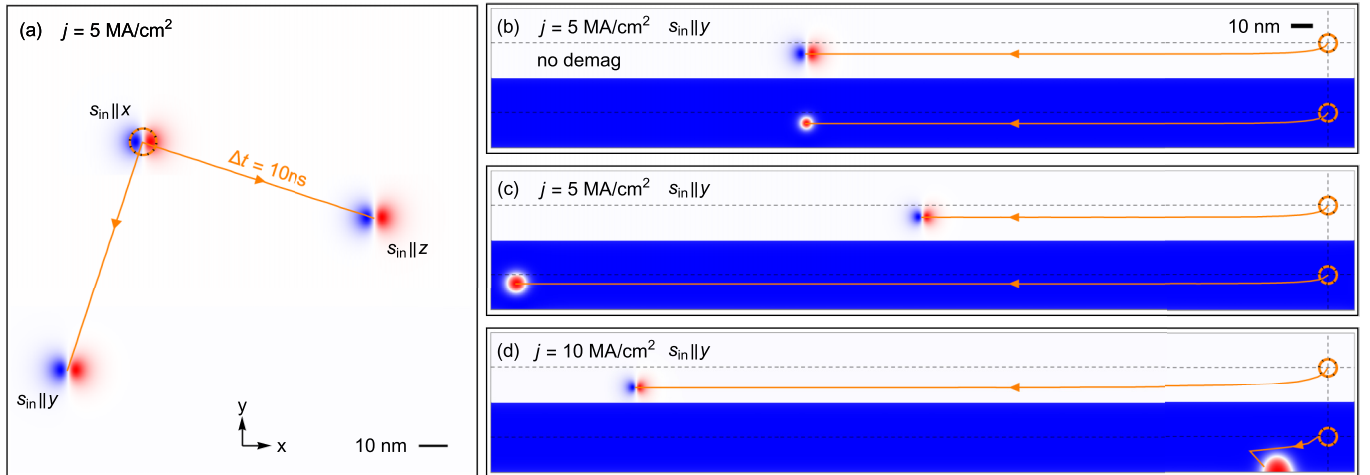


FIG. 3. Current-driven motion of magnetic bimerons and skyrmions. (a) Superposition of three results of micromagnetic simulations of a bimeron in an in-plane magnet with periodic boundary conditions starting from the orange circle (top left). The bimerons are driven by SOT type (i) (injected spins  $s_{in} \parallel x, y, z$  as indicated). (b) Bimeron (top) and skyrmion (bottom) in a racetrack geometry driven by SOT type (ii) (current along the track  $j_x = 5 \text{ MA/cm}^2$ , injected spins  $s_{in} \parallel y$ ). The demagnetization field is set to zero. (c) Like (b) but with demagnetization field. (d) Like (c) but at double the current density. In all panels, the trajectory (orange) of the center of the bimeron or skyrmion is indicated; the figures show the results after 10-ns propagation time, except for (d) bottom, where the skyrmion already annihilates after 0.5 ns.

both quasiparticles experience the same forces and behave equally under the influence of temperature.

The demagnetization field acts effectively as an inhomogeneous in-plane magnetic field for *both* textures, leading to an increase of the skyrmion size and a decrease of the bimeron size. Consequently the skyrmion velocity is larger than that of the bimeron [cf. Fig. 3(c) and see Ref. [40] for a complementary Thiele equation analysis]. Still, the bimeron can reach similar velocities as the skyrmion since the bimeron allows for larger applied currents densities. While a bimeron is still stable at  $j = 10 \text{ MA/cm}^2$ , the skyrmion is already annihilated at the edge of the racetrack for  $j \gtrsim 6.25 \text{ MA/cm}^2$  [cf. Fig. 3(d)]. Both quasiparticles can reach velocities of around 50 m/s although the skyrmion moves more efficiently for the presented parameters. In Ref. [40], we show that current-driven motion is also possible for a material with an easy-plane anisotropy ( $K_z < 0$ ), when a magnetic field is applied in-plane to generate a preferred direction.

*Conclusion and perspective.* In this Rapid Communication, we have demonstrated how to generate isolated bimerons and bimeron crystals via DMI and frustrated exchange interactions. Since the magnetic moments of a bimeron are merely rotated moments of a skyrmion, the topological properties of the two objects are unchanged and the topological Hall effects due to both of them are identical. Nevertheless, the fact that all magnetic quantities (net magnetization and stabilizing field) are rotated, while the emergent field is not, allows for the pure and therefore unambiguous detection of the topological Hall effect in bimeron systems, and for the development of future spintronic devices based on this effect.

We have shown that magnetic materials with in-plane magnetization can be used to build racetrack storage devices with magnetic bimerons as carriers of information. In these materials, the current-induced dynamics of bimerons can be accomplished similarly to that of skyrmions in conventional racetracks. Furthermore, in-plane ferromagnets allow us to

use different orientations of injected spins for the propulsion of bimerons as well as for their generation (for  $s_{in} \parallel x$  in analogy to Refs. [20,60]). A technological advantage of these materials is the stackability of the quasi-one-dimensional racetracks, since the dipolar energy of two in-plane magnets is smaller than that of two out-of-plane magnets. The smaller stray fields in a bimeron-based racetrack allow for a denser array of tracks in three dimensions and thus a higher storage density.

The established analogy between skyrmions and bimerons can be carried over to all types of skyrmion-related spin textures such as higher-order skyrmions [30,61], biskyrmions [62,63], multi- $\pi$  skyrmions [64–67], bobbbers [68,69], and topologically trivial bubbles. Regarding applicability in spintronics the antiferromagnetic skyrmions [70–76] that become antiferromagnetic bimerons (two mutually reversed bimerons on different sublattices), stand above all, since they allow for SOT-driven dynamics precisely in the middle of the racetrack at speeds of up to several km/s. Very recently the existence of such bimerons has been confirmed experimentally in synthetic antiferromagnets [77].

*Note added.* After the submission of this Paper a vortex-antivortex crystal has been observed by Lorentz transmission electron microscopy in  $\text{Co}_8\text{Zn}_9\text{Mn}_3$  [78]. These textures have been predicted earlier [79] and are topologically (but not geometrically) equivalent to bimeron crystals.

We are grateful to Steffen Trimper and Stuart S. P. Parkin for fruitful discussions. This work is supported by Priority Program SPP 1666 and SFB 762 of Deutsche Forschungsgemeinschaft (DFG). O.A.T. acknowledges support by the Grants-in-Aid for Scientific Research (Grants No. 17K05511 and No. 17H05173) from MEXT (Japan), by the grant of the Center for Science and Innovation in Spintronics (Core Research Cluster), Tohoku University, and by JSPS and RFBR under the Japan-Russian Research Cooperative Program.

- [1] T. H. R. Skyrme, *Nucl. Phys.* **31**, 556 (1962).
- [2] A. N. Bogdanov and D. A. Yablonskii, *Zh. Eksp. Teor. Fiz.* **95**, 178 (1989) [*Sov. Phys. JETP* **68**, 101 (1989)].
- [3] A. Bogdanov and A. Hubert, *J. Magn. Magn. Mater.* **138**, 255 (1994).
- [4] U. Röbber, A. Bogdanov, and C. Pfleiderer, *Nature (London)* **442**, 797 (2006).
- [5] S. Mühlbauer, B. Binz, F. Jonietz, C. Pfleiderer, A. Rosch, A. Neubauer, R. Georgii, and P. Böni, *Science* **323**, 915 (2009).
- [6] N. Nagaosa and Y. Tokura, *Nat. Nanotechnol.* **8**, 899 (2013).
- [7] P. Bruno, V. K. Dugaev, and M. Taillefumier, *Phys. Rev. Lett.* **93**, 096806 (2004).
- [8] A. Neubauer, C. Pfleiderer, B. Binz, A. Rosch, R. Ritz, P. G. Niklowitz, and P. Böni, *Phys. Rev. Lett.* **102**, 186602 (2009).
- [9] T. Schulz, R. Ritz, A. Bauer, M. Halder, M. Wagner, C. Franz, C. Pfleiderer, K. Everschor, M. Garst, and A. Rosch, *Nat. Phys.* **8**, 301 (2012).
- [10] N. Kanazawa, Y. Onose, T. Arima, D. Okuyama, K. Ohoyama, S. Wakimoto, K. Kakurai, S. Ishiwata, and Y. Tokura, *Phys. Rev. Lett.* **106**, 156603 (2011).
- [11] M. Lee, W. Kang, Y. Onose, Y. Tokura, and N. P. Ong, *Phys. Rev. Lett.* **102**, 186601 (2009).
- [12] Y. Li, N. Kanazawa, X. Z. Yu, A. Tsukazaki, M. Kawasaki, M. Ichikawa, X. F. Jin, F. Kagawa, and Y. Tokura, *Phys. Rev. Lett.* **110**, 117202 (2013).
- [13] K. Hamamoto, M. Ezawa, and N. Nagaosa, *Phys. Rev. B* **92**, 115417 (2015).
- [14] J. L. Lado and J. Fernández-Rossier, *Phys. Rev. B* **92**, 115433 (2015).
- [15] B. Göbel, A. Mook, J. Henk, and I. Mertig, *Phys. Rev. B* **95**, 094413 (2017).
- [16] B. Göbel, A. Mook, J. Henk, and I. Mertig, *New J. Phys.* **19**, 063042 (2017).
- [17] P. B. Ndiaye, C. A. Akosa, and A. Manchon, *Phys. Rev. B* **95**, 064426 (2017).
- [18] G. Yin, Y. Liu, Y. Barlas, J. Zang, and R. K. Lake, *Phys. Rev. B* **92**, 024411 (2015).
- [19] F. Jonietz, S. Mühlbauer, C. Pfleiderer, A. Neubauer, W. Münzer, A. Bauer, T. Adams, R. Georgii, P. Böni, R. A. Duine *et al.*, *Science* **330**, 1648 (2010).
- [20] J. Sampaio, V. Cros, S. Rohart, A. Thiaville, and A. Fert, *Nat. Nanotechnol.* **8**, 839 (2013).
- [21] J. Zang, M. Mostovoy, J. H. Han, and N. Nagaosa, *Phys. Rev. Lett.* **107**, 136804 (2011).
- [22] J. Iwasaki, M. Mochizuki, and N. Nagaosa, *Nat. Nanotechnol.* **8**, 742 (2013).
- [23] W. Jiang, X. Zhang, G. Yu, W. Zhang, X. Wang, M. B. Jungfleisch, J. E. Pearson, X. Cheng, O. Heinonen, K. L. Wang *et al.*, *Nat. Phys.* **13**, 162 (2017).
- [24] K. Litzius, I. Lemesh, B. Krüger, P. Bassirian, L. Caretta, K. Richter, F. Büttner, K. Sato, O. A. Tretiakov, J. Förster *et al.*, *Nat. Phys.* **13**, 170 (2017).
- [25] R. Tomasello, E. Martinez, R. Zivieri, L. Torres, M. Carpentieri, and G. Finocchio, *Sci. Rep.* **4**, 6784 (2014).
- [26] B. Göbel, A. Mook, J. Henk, and I. Mertig, *Phys. Rev. B* **99**, 020405(R) (2019).
- [27] I. Dzyaloshinsky, *J. Phys. Chem. Solids* **4**, 241 (1958).
- [28] T. Moriya, *Phys. Rev.* **120**, 91 (1960).
- [29] T. Okubo, S. Chung, and H. Kawamura, *Phys. Rev. Lett.* **108**, 017206 (2012).
- [30] A. Leonov and M. Mostovoy, *Nat. Commun.* **6**, 8275 (2015).
- [31] A. M. Kosevich, B. Ivanov, and A. Kovalev, *Phys. Rep.* **194**, 117 (1990).
- [32] F. G. Mertens and A. R. Bishop, in *Nonlinear Science at the Dawn of the 21st Century* (Springer, Heidelberg-Berlin, Germany, 2000), pp. 137–170.
- [33] E. Kamenetskii, in *Electromagnetic, Magnetostatic, and Exchange-Interaction Vortices in Confined Magnetic Structures* (Transworld Research Network, Kerala, India, 2008).
- [34] Y. A. Kharkov, O. P. Sushkov, and M. Mostovoy, *Phys. Rev. Lett.* **119**, 207201 (2017).
- [35] C. Heo, N. S. Kiselev, A. K. Nandy, S. Blügel, and T. Rasing, *Sci. Rep.* **6**, 27146 (2016).
- [36] X. Zhang, M. Ezawa, and Y. Zhou, *Sci. Rep.* **5**, 9400 (2015).
- [37] S. Komineas, *Phys. Rev. Lett.* **99**, 117202 (2007).
- [38] Note that recently the term “bimeron” has also been used for elongated skyrmions [80–82], instead of the original object, found in dual layer two-dimensional electron gases and quantum Hall systems [83–87]. Throughout this paper we always refer to the latter.
- [39] O. A. Tretiakov and O. Tchernyshyov, *Phys. Rev. B* **75**, 012408 (2007).
- [40] See Supplemental Material <http://link.aps.org/supplemental/10.1103/PhysRevB.99.060407> for a numerical validation of several claims made in the main text, which includes Refs. [13,15,20,26,30,43,44,50,57,88–91].
- [41] A. Fert and P. M. Levy, *Phys. Rev. Lett.* **44**, 1538 (1980).
- [42] Note that in magnets with in-plane anisotropy and conventional interfacial DMI [Fig. 1(b)] asymmetric skyrmions are stabilized [92]. These objects are intermediate states between skyrmions and bimerons with nonvanishing in-plane and out-of-plane net magnetization.
- [43] L. D. Landau and E. Lifshitz, *Phys. Z. Sowjetunion* **8**, 153 (1935) [*Ukr. J. Phys.* **53**, 14 (2008)].
- [44] T. L. Gilbert, *IEEE Trans. Magn.* **40**, 3443 (2004).
- [45] A. K. Nayak, V. Kumar, T. Ma, P. Werner, E. Pippel, R. Sahoo, F. Damay, U. K. Röbber, C. Felser, and S. S. Parkin, *Nature (London)* **548**, 561 (2017).
- [46] U. Güngördü, R. Nepal, O. A. Tretiakov, K. Belashchenko, and A. A. Kovalev, *Phys. Rev. B* **93**, 064428 (2016).
- [47] S. Huang, C. Zhou, G. Chen, H. Shen, A. K. Schmid, K. Liu, and Y. Wu, *Phys. Rev. B* **96**, 144412 (2017).
- [48] M. Hoffmann, B. Zimmermann, G. P. Müller, D. Schürhoff, N. S. Kiselev, C. Melcher, and S. Blügel, *Nat. Commun.* **8**, 308 (2017).
- [49] E. H. Hall, *Am. J. Math.* **2**, 287 (1879).
- [50] N. Nagaosa, J. Sinova, S. Onoda, A. H. MacDonald, and N. P. Ong, *Rev. Mod. Phys.* **82**, 1539 (2010).
- [51] Over the recent years an additional contribution to the Hall resistivity  $\rho_{xy}$  has been predicted which is neither proportional to  $M$  nor  $N_{sk}$ ; it is only determined by the SOC [93]. Even though this effect cannot be excluded, all Hall measurements in skyrmion crystals are well approximated by Eq. (3) to the best of our knowledge.
- [52] B. Göbel, A. Mook, J. Henk, and I. Mertig, *Eur. Phys. J. B* **91**, 179 (2018).
- [53] A. Fert, V. Cros, and J. Sampaio, *Nat. Nanotechnol.* **8**, 152 (2013).
- [54] S. S. Parkin, Shiftable magnetic shift register and method of using the same, US Patent No. 6,834,005, 2004.

- [55] S. S. Parkin, M. Hayashi, and L. Thomas, *Science* **320**, 190 (2008).
- [56] S. Parkin and S.-H. Yang, *Nat. Nanotechnol.* **10**, 195 (2015).
- [57] J. C. Slonczewski, *J. Magn. Magn. Mater.* **159**, L1 (1996).
- [58] A. Vansteenkiste and B. Van de Wiele, *J. Magn. Magn. Mater.* **323**, 2585 (2011).
- [59] A. Vansteenkiste, J. Leliaert, M. Dvornik, M. Helsen, F. Garcia-Sanchez, and B. Van Waeyenberge, *AIP Adv.* **4**, 107133 (2014).
- [60] N. Romming, C. Hanneken, M. Menzel, J. E. Bickel, B. Wolter, K. von Bergmann, A. Kubetzka, and R. Wiesendanger, *Science* **341**, 636 (2013).
- [61] R. Ozawa, S. Hayami, and Y. Motome, *Phys. Rev. Lett.* **118**, 147205 (2017).
- [62] X. Yu, Y. Tokunaga, Y. Kaneko, W. Zhang, K. Kimoto, Y. Matsui, Y. Taguchi, and Y. Tokura, *Nat. Commun.* **5**, 3198 (2014).
- [63] L. Peng, Y. Zhang, W. Wang, M. He, L. Li, B. Ding, J. Li, Y. Sun, X.-G. Zhang, J. Cai *et al.*, *Nano Lett.* **17**, 7075 (2017).
- [64] A. Bogdanov and A. Hubert, *J. Magn. Magn. Mater.* **195**, 182 (1999).
- [65] X. Zhang, J. Xia, Y. Zhou, D. Wang, X. Liu, W. Zhao, and M. Ezawa, *Phys. Rev. B* **94**, 094420 (2016).
- [66] F. Zheng, H. Li, S. Wang, D. Song, C. Jin, W. Wei, A. Kovács, J. Zang, M. Tian, Y. Zhang *et al.*, *Phys. Rev. Lett.* **119**, 197205 (2017).
- [67] S. Zhang, F. Kronast, G. van der Laan, and T. Hesjedal, *Nano Lett.* **18**, 1057 (2018).
- [68] F. N. Rybakov, A. B. Borisov, S. Blügel, and N. S. Kiselev, *Phys. Rev. Lett.* **115**, 117201 (2015).
- [69] F. Zheng, F. N. Rybakov, A. B. Borisov, D. Song, S. Wang, Z.-A. Li, H. Du, N. S. Kiselev, J. Caron, A. Kovács *et al.*, *Nat. Nanotechnol.* **13**, 451 (2018).
- [70] J. Barker and O. A. Tretiakov, *Phys. Rev. Lett.* **116**, 147203 (2016).
- [71] X. Zhang, Y. Zhou, and M. Ezawa, *Nat. Commun.* **7**, 10293 (2016).
- [72] X. Zhang, Y. Zhou, and M. Ezawa, *Sci. Rep.* **6**, 24795 (2016).
- [73] P. F. Bessarab, D. Yudin, D. R. Gulevich, P. Wadley, M. Titov, and O. A. Tretiakov, [arXiv:1709.04454](https://arxiv.org/abs/1709.04454).
- [74] B. Göbel, A. Mook, J. Henk, and I. Mertig, *Phys. Rev. B* **96**, 060406(R) (2017).
- [75] L. Shen, J. Xia, G. Zhao, X. Zhang, M. Ezawa, O. A. Tretiakov, X. Liu, and Y. Zhou, *Phys. Rev. B* **98**, 134448 (2018).
- [76] C. A. Akosa, O. A. Tretiakov, G. Tatara, and A. Manchon, *Phys. Rev. Lett.* **121**, 097204 (2018).
- [77] A. G. Kolesnikov, V. S. Plotnikov, E. V. Pustovalov, A. S. Samardak, L. A. Chebotkevich, A. V. Ognev, and O. A. Tretiakov, *Sci. Rep.* **8**, 15794 (2018).
- [78] X. Yu, W. Koshibae, Y. Tokunaga, K. Shibata, Y. Taguchi, N. Nagaosa, and Y. Tokura, *Nature (London)* **564**, 95 (2018).
- [79] Y. Gaididei, O. M. Volkov, V. P. Kravchuk, and D. D. Sheka, *Phys. Rev. B* **86**, 144401 (2012).
- [80] M. Ezawa, *Phys. Rev. B* **83**, 100408 (2011).
- [81] H. Du, W. Ning, M. Tian, and Y. Zhang, *Phys. Rev. B* **87**, 014401 (2013).
- [82] R. L. Silva, L. D. Secchin, W. A. Moura-Melo, A. R. Pereira, and R. L. Stamps, *Phys. Rev. B* **89**, 054434 (2014).
- [83] K. Moon, H. Mori, K. Yang, S. M. Girvin, A. H. MacDonald, L. Zheng, D. Yoshioka, and S.-C. Zhang, *Phys. Rev. B* **51**, 5138 (1995).
- [84] K. Yang and A. H. MacDonald, *Phys. Rev. B* **51**, 17247(R) (1995).
- [85] L. Brey, H. A. Fertig, R. Côté, and A. H. MacDonald, *Phys. Rev. B* **54**, 16888 (1996).
- [86] J. Bourassa, B. Roostaeei, R. Côté, H. A. Fertig, and K. Mullen, *Phys. Rev. B* **74**, 195320 (2006).
- [87] R. Côté, W. Luo, B. Petrov, Y. Barlas, and A. H. MacDonald, *Phys. Rev. B* **82**, 245307 (2010).
- [88] I. A. Ado, O. A. Tretiakov, and M. Titov, *Phys. Rev. B* **95**, 094401 (2017).
- [89] A. Thiele, *Phys. Rev. Lett.* **30**, 230 (1973).
- [90] O. A. Tretiakov, D. Clarke, G.-W. Chern, Y. B. Bazaliy, and O. Tchernyshyov, *Phys. Rev. Lett.* **100**, 127204 (2008).
- [91] D. J. Clarke, O. A. Tretiakov, G.-W. Chern, Y. B. Bazaliy, and O. Tchernyshyov, *Phys. Rev. B* **78**, 134412 (2008).
- [92] A. Leonov and I. Kézsmárki, *Phys. Rev. B* **96**, 014423 (2017).
- [93] H. Chen, Q. Niu, and A. MacDonald, *Phys. Rev. Lett.* **112**, 017205 (2014).

### 6.3 Magnetic skyrmioniums in racetrack applications

Quasiparticles with a vanishing topological charge are highly attractive for racetrack applications since they do not exhibit a skyrmion Hall effect, even in the conventional SOT geometry. To construct a quasiparticle with a vanishing topological charge, two skyrmions with topological charges  $+1$  and  $-1$  may be combined.

One way is to write a skyrmion in the center of the second skyrmion with the opposite polarity. The resulting ‘skyrmionium’ can be stabilized by DMI just like a skyrmion; this has been known even before the initial detection of conventional skyrmions [142]. Analyzing the magnetic moments starting from the edge and going to the center of this magnetic object, the azimuthal angle changes for example from  $0$  to  $\pi$  to  $2\pi$ , hence the skyrmionium is also referred to as ‘ $2\pi$  skyrmion’.

**Experimental discovery.** Besides the DMI, the confining potential in nanodisks or nanorods helps stabilizing these quasiparticles as has been shown experimentally in Ref. [143] [Fig. 28(b)]. In these geometries the texture is often called ‘target skyrmion’. For these objects, the azimuthal angle does not change by a full  $2\pi$  and therefore the topological charge is not exactly zero. However, these objects resemble ideal skyrmioniums to a large degree. Actual skyrmioniums, which are addressable individually, have been realized experimentally by laser pulses [63] and were observed in ferromagnetic films on top of topological insulators [144] [Fig. 28(a)]. This motivates to consider skyrmionium-based racetrack storage devices, in which the bits move parallel to the current, directly in the middle of the racetrack.

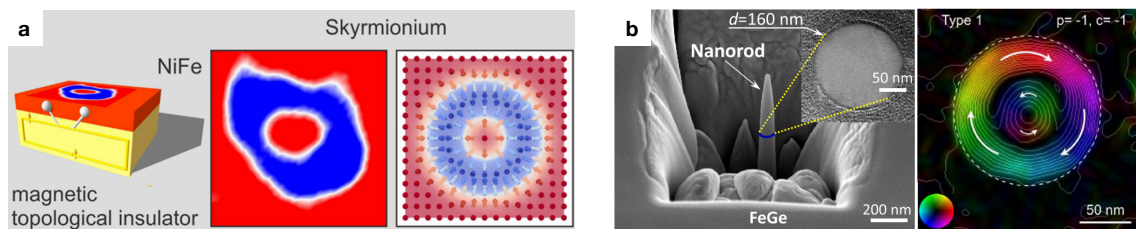


Figure 28: **Magnetic skyrmioniums in experiments.** **a** A skyrmionium stabilized in NiFe interfaced with a topological insulator. **b** A target skyrmion in a nanorod. Panel a: Reprinted (adapted) with permission from (S. Zhang *et al.*: Real-Space Observation of Skyrmionium in a Ferromagnet-Magnetic Topological Insulator Heterostructure. *Nano Letters* **18**, 1057 (2018); Ref. [144]). Copyright (2018) American Chemical Society. Panel b: Reprinted from (F. Zheng *et al.*: Direct Imaging of a Zero-Field Target Skyrmion and Its Polarity Switch in a Chiral Magnetic Nanodisk. *Physical Review Letters* **119**, 197205 (2017); Ref. [143]). Published by the American Physical Society under the terms of the Creative Commons Attribution 4.0 International license.

**This publication.** In the following publication “Electrical writing, deleting, reading, and moving of magnetic skyrmioniums in a racetrack device” [BG6] all four constituents of a racetrack-storage device have been simulated.

The writing and deleting processes are realized by the injection of a toroidal spin configuration for an ultra-short time span. This SOT-based mechanism is induced by a current pulse which is triggered by a laser (Fig. 1 of the publication). This step has been

simulated by Alexander Schäffer. The main advantage of the ultra-fast generation of skyrmioniums is that the driving current may remain applied while the bits are written or deleted. A sequence of skyrmioniums moves perfectly in the middle of the racetrack due to the vanishing topological charge (Fig. 4 of the publication). For this consideration I have conducted micromagnetic simulations using mumax3 to solve the LLG equation (Sec. 3.2; together with Alexander Schäffer) and analyzed the trajectory with the Thiele equation (3.35).

For the reading process I have conducted calculations of the topological Hall effect. The opposite topological charges of the two sub-skyrmions lead to a cancellation of the topological Hall effect globally, as follows from a calculation using the Berry-curvature approach. However, for the detection of magnetic quasiparticles in a racetrack, only the deflected electrons in a finite area are relevant. This was calculated using a Landauer-Büttiker formalism, as introduced in Appendix B.

The general idea of this method is that four leads are attached to the racetrack: two along the longitudinal directions to apply the current, and two on the sides for the detection of the transverse voltage. The voltages  $U_i$  and currents  $I_i$  at the four leads are related by a system of linear equations

$$I_m = \frac{e^2}{h} \sum_n T_{mn} U_n, \quad (6.2)$$

where  $\underline{T}$  is the transition matrix, which has been computed using the code Kwant [145]. The transverse resistance is given by  $R_{xy} = \Delta U_{\text{trans}} / I_{\text{long}}$ . As can be seen in Fig. 5 of the publication, despite its vanishing topological charge, a skyrmionium exhibits a pronounced signal in the topological Hall resistivity. This allows for an unambiguous detection and even for a distinction from other non-collinear spin textures. An electrical detection should therefore be feasible just like for conventional skyrmions as presented in Ref. [14] (cf. Fig. 13 presented in the experimental review section).

Reprinted from (B. Göbel *et al.*: Electrical writing, deleting, reading, and moving of magnetic skyrmioniums in a racetrack device. *Scientific Reports* 9, 12119 (2019), DOI: <https://doi.org/10.1038/s41598-019-48617-z>; Ref. [BG6]).  
Published by Springer Nature under the terms of the Creative Commons Attribution 4.0 license.



OPEN

# Electrical writing, deleting, reading, and moving of magnetic skyrmioniums in a racetrack device

Börge Göbel<sup>1</sup>, Alexander F. Schäffer<sup>2</sup>, Jamal Berakdar<sup>2</sup>, Ingrid Mertig<sup>1,2</sup> & Stuart S. P. Parkin<sup>1</sup>

**A magnetic skyrmionium (also called  $2\pi$ -skyrmion) can be understood as a skyrmion—a topologically nontrivial magnetic whirl—which is situated in the center of a second skyrmion with reversed magnetization. Here, we propose a new optoelectrical writing and deleting mechanism for skyrmioniums in thin films, as well as a reading mechanism based on the topological Hall voltage. Furthermore, we point out advantages for utilizing skyrmioniums as carriers of information in comparison to skyrmions with respect to the current-driven motion. We simulate all four constituents of an operating skyrmionium-based racetrack storage device: creation, motion, detection and deletion of bits. The existence of a skyrmionium is thereby interpreted as a '1' and its absence as a '0' bit.**

Magnetic skyrmions<sup>1–3</sup> are whirl-like quasiparticles that are under consideration as carriers of information in modern data storages: Sampaio *et al.*<sup>4</sup> proposed to write and move skyrmions in thin film nanowires what constitutes a derivative of a racetrack storage device, initially proposed for domain walls in a ferromagnetic thin films<sup>5–7</sup>. The low driving current, small size and high stability of skyrmions, combined with the stackability of these tracks into three dimensions may lead to the development of highly efficient magnetic memory-storage devices with capacities that rival those of magnetic hard-disk drives, satisfying the ever-growing demand for data storage.

Since the initial discovery of skyrmions in the form of periodic lattices in bulk single crystals of MnSi<sup>2</sup>, scientific effort has led to promising advances towards the utilization of isolated skyrmions as information carriers<sup>4,8–13</sup>. Still, one major issue for driving skyrmions on a racetrack is the skyrmion Hall effect<sup>3,11,14,15</sup> originating from the real-space topological properties of skyrmions. A skyrmion carries a topological charge of  $N_{\text{sk}} \pm 1$ , defined as the integral over the topological charge density

$$n_{\text{sk}}(\mathbf{r}) = \frac{1}{4\pi} \mathbf{m}(\mathbf{r}) \cdot \left[ \frac{\partial \mathbf{m}(\mathbf{r})}{\partial x} \times \frac{\partial \mathbf{m}(\mathbf{r})}{\partial y} \right], \quad (1)$$

where  $\mathbf{m}(\mathbf{r})$  is the unit vector magnetization field. Skyrmions driven by spin-polarized electrical currents are not propelled parallel to the racetrack. They experience a transverse deflection towards the edge of the racetrack where they may be confined. This effect is detrimental for racetrack applications.

Theoretical suggestions for suppressing the skyrmion Hall effect are to manipulate the driving torque orientation<sup>16–19</sup> or to use antiferromagnetic skyrmions with a vanishing topological charge<sup>20–23</sup> instead of skyrmions. However, both approaches have not yet been realized experimentally.

Here, we utilize another type of magnetic quasi-particle (Fig. 1a) with a zero topological charge: the skyrmionium (also called a  $2\pi$ -skyrmion)<sup>24–34</sup>. The skyrmionium has been observed experimentally created by laser pulses<sup>27</sup>, as target skyrmionium in nanodiscs<sup>28</sup> and very recently in a thin ferromagnetic film on top of a topological insulator<sup>29</sup>. A magnetic skyrmionium (Fig. 1b) can be described as a skyrmion, with a second skyrmion situated in the center. The inner skyrmion has a reversed polarity and deforms the outer skyrmion to a ring.

Here, we show that skyrmioniums can be used as carriers of information in a racetrack storage device (Fig. 1a): the existence of a skyrmionium is interpreted as a '1' bit, while its absence is a '0' bit. Based on recent progresses in optically generated current pulses<sup>35</sup> we propose a way to write and delete magnetic skyrmioniums on the

<sup>1</sup>Max-Planck-Institut für Mikrostrukturphysik, D-06120, Halle, Saale, Germany. <sup>2</sup>Institut für Physik, Martin-Luther-Universität Halle-Wittenberg, D-06099, Halle, Saale, Germany. Börge Göbel and Alexander F. Schäffer contributed equally. Correspondence and requests for materials should be addressed to B.G. (email: [bgoebel@mpi-halle.mpg.de](mailto:bgoebel@mpi-halle.mpg.de)) or A.F.S. (email: [alexander.schaeffer@physik.uni-halle.de](mailto:alexander.schaeffer@physik.uni-halle.de))

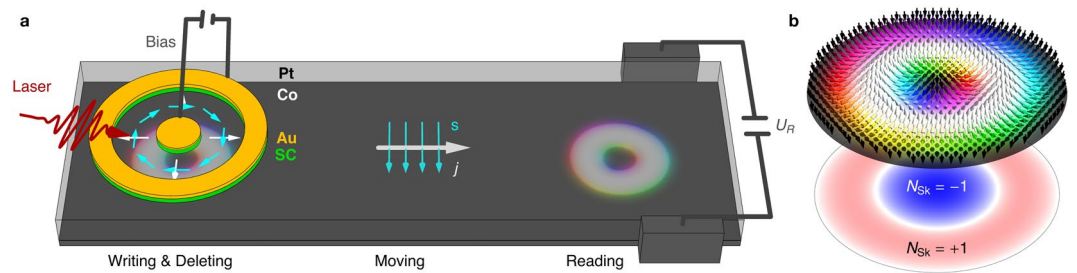


**Figure 1.** Skyrmionium-based racetrack storage device. **(a)** Schematic presentation of the proposed device including the four constituents: writing, deleting, moving and reading. A skyrmionium, the circular object in the Co layer (gray), is written or deleted by a photosensitive switch built from gold (Au) and a semi-conductor (SC). A radial current (white) is triggered upon illuminating the antenna with a fs-laser pulse due to the applied bias voltage. The current mainly flows in the Pt layer (transparent) where the SHE injects spins (cyan) into the Co layer that are oriented perpendicularly to the plane normal and current directions. Depending on the polarity of the gate voltage, the sign of the optically activated current pulse and the orientation of the polarization are determined, so that a skyrmionium can be written or deleted. To move the skyrmionium a uniform current density  $j$  is applied along the track, again generating spins  $s$  that exert a SOT onto the skyrmionium. When a skyrmionium is located near the two leads on the right, a Hall voltage  $U_R$  can be measured, allowing for a distinct detection of a skyrmionium bit. **(b)** (top) Magnetic texture of a skyrmionium, and (bottom) topological charge density  $n_{sk}$  with opposite signs for the inner skyrmion and the outer ring.

picosecond timescale, so that the current-induced skyrmionium flow—without the detrimental skyrmion Hall effect—can remain steady while writing. Also we show that skyrmioniums can be detected electrically by their topological Hall signal, that arises from the local topological charge density (Fig. 1b bottom), even though the global topological charge vanishes.

## Results

**Skyrmionium racetrack.** In the following, we simulate and analyze point by point the four essential constituents to operate a racetrack-storage device based on magnetic skyrmioniums. First, we show via micromagnetic simulations how skyrmioniums can be written and deleted by optically excited localized current pulses. Thereafter, we present advantages in the current-driven motion of skyrmioniums compared to that of conventional skyrmions; we explain the simulated results by an effective description using the Thiele equation. Ultimately, we show via Landauer-Büttiker calculations that the local separation of the two sub-skyrmions of a skyrmionium can be exploited to electrically detect skyrmioniums even though they exhibit no topological Hall voltage when integrated over the whole sample.

For the device (Fig. 1a) we consider a magnetic layer on a heavy metal: here we exemplarily select Co (gray) on Pt (transparent), as in refs<sup>4,26</sup>. In this setup an applied charge current density  $j$  (white) within the Pt layer is translated into a spin current by the considerable spin Hall effect that has been observed in Pt. The spin current flows perpendicularly to the plane into the Co potentially hosting skyrmioniums. The spin polarization  $s$  (cyan) is perpendicular to  $j$  and the plane normal, thereby leading to a spin-orbit torque<sup>36</sup> (SOT) that can propel a skyrmionium.

On top of the basic racetrack that is formed from the Pt/Co bilayer a photosensitive switch<sup>37</sup> is fabricated that can switch the magnetization as experimentally shown in ref.<sup>35</sup>. A circular gold disk inside a gold ring is isolated from the metallic racetrack by an underlying semiconducting layer (green) so that a bias voltage can be applied between the inner and outer gold electrodes (Corbino geometry). The semiconductor is electrically activated by fs-laser pulses which generate a radially symmetric current pulse profile  $j = j_{write} \frac{r_0}{r} \hat{e}_r$  (white) in the Pt-layer. By analogy with the explanation given above, this leads to a toroidal spin polarization profile  $s(r) \parallel \pm \hat{e}_\phi$  (cyan) of the spin currents (parallel to  $\hat{e}_z$ ) that diffuse into the Co layer to create or delete the skyrmionium. To model the skyrmionium generation, deletion and motion we use a micromagnetic framework based on the Landau-Lifshitz-Gilbert (LLG) equation<sup>36,38,39</sup>. For details and simulation parameters see Methods.

For the reading process we utilize the local topological properties of a skyrmionium. The non-zero topological charge density  $n_{sk}$  leads to a deflection of electrons into a transverse direction. A Hall voltage  $U_R$  builds up that can be measured by attaching two small leads (gray) to the sides of the device.

**Optoelectrical writing of skyrmioniums.** Several mechanisms for writing skyrmions have been proposed, such as the application of spin-polarized currents<sup>40</sup>, laser beams<sup>27</sup> and electron beams<sup>41,42</sup>. These mechanisms can potentially be adapted to generate also skyrmioniums. It has been predicted that skyrmioniums can be generated by alternating the out-of-plane orientation of an external magnetic field<sup>30</sup> or by the perpendicular injection of spin currents<sup>26,31</sup>.

We propose a faster writing mechanism, where spins are injected from the perpendicular direction for an ultrashort duration. We consider a SOT-driven approach based on a nanostructured skyrmionium manipulation unit as sketched in Fig. 1a. Optically excited radially symmetric charge currents (white) in the Pt-layer lead to out-of-plane spin currents with a controllable toroidal spin polarization configuration (cyan): For opposite signs of the applied bias-voltage opposite spin polarizations are achieved ( $\pm \hat{e}_\phi$ ). According to Yang *et al.*<sup>35</sup> current den-

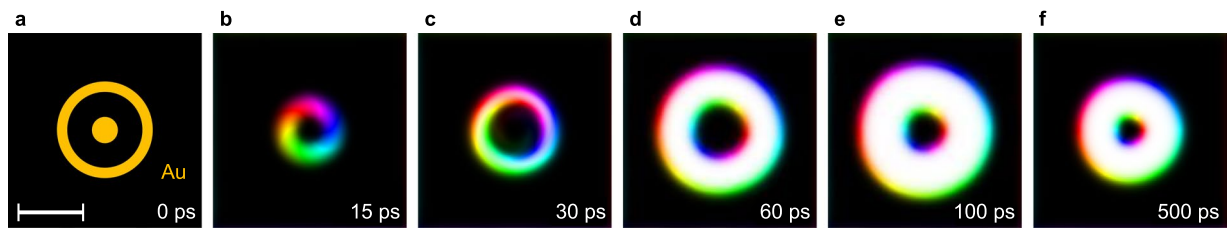


**Figure 2.** Writing skyrmioniums by optically excited current pulses. (a) The starting point is a ferromagnet magnetized along  $-z$ . The orange areas indicate the gold nanostructures that generate a current pulse of 9 ps duration (FWHM) with  $j_{\max}(t = 15 \text{ ps}) = 2 \times 10^{13} \text{ A/m}^2$  at the disk. (b) After the spin current has induced a skyrmionium-shaped excitation the quasiparticle relaxes in (c–f). The color code is the same as in Fig. 1. An animated version is accessible in Supplementary Video 1. For sample and beam parameters see text and Methods. The scale bar corresponds to 50 nm.

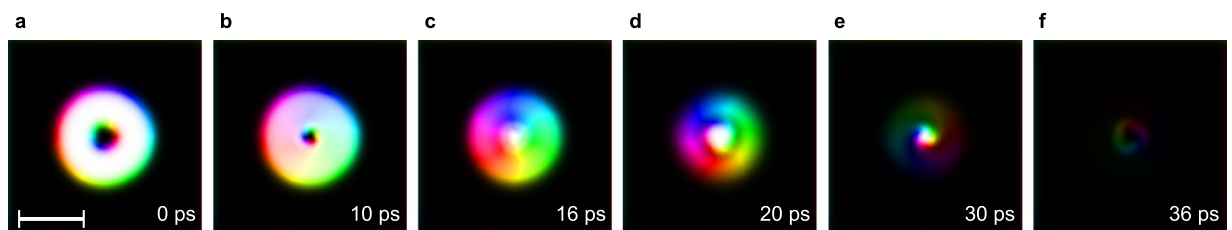


**Figure 3.** Deleting skyrmioniums by optically excited current pulses. (a) We start from the skyrmionium stabilized in Fig. 2 and generate a spin current with opposite polarization ( $\hat{e}_\varphi$ ) compared to the writing process achieved by switching the sign of the bias voltage. (b,c) The domain wall unwinds the inner skyrmion leading to its collapse. (d–f) Subsequently, the skyrmion-like configuration contracts and dissolves. An animated version is accessible in Supplementary Video 2. The scale bar corresponds to 50 nm.

sities on the order of  $j_{\max} = 2 \times 10^{13} \text{ A/m}^2$  could be created for a pulse duration of 9 ps full width at half maximum (FWHM). These values were adapted in our proposed optoelectrical writing and deleting process of a single skyrmionium. They cannot be reached by a conventional perpendicular spin current injection. The diameter of the inner disk of the photosensitive switch is 20 nm and the outer ring's inner diameter is 60 nm in order to match the skyrmionium's dimension. These dimensions are at the limit of what is possible today using conventional lithographic processes.

Starting from an initially uniform magnetization pointing into the  $-z$  direction (Fig. 2a), the system is excited by an out-of-plane spin current with toroidal polarization. Because of the ultrashort current pulses of 9 ps (FWHM) the excitation itself is non-adiabatic and the magnetic texture will relax on a longer time scale.

During the current-pulse (Fig. 2b, maximum current at 15 ps) the magnetization in the excited ring-shaped region begins to align with the spin current's polarization, i.e. along  $-\hat{e}_\varphi$ . The amplitude of the current as well as its location needs to be tuned in such a way, that it will effectively switch a ring-shaped domain of a suitable size (Fig. 2c). Subsequently not only spin waves propagate radially, but also the central circular region remaining in its initial orientation starts to pulsate (Fig. 2c–f). Associated with this, the domain wall between the central  $-z$  region and the intermediate  $+z$  region is rotating such that a central Néel-skyrmion is generated, thereby, in total, constituting a skyrmionium. The slowest relaxation is the adjustment of the skyrmionium's size, taking place after the central fluctuations decay. The shrinking towards the final diameter (around 80 nm) lasts for  $\sim 500$  ps (Fig. 2e,f).

**Optoelectrical deleting of skyrmioniums.** Deleting a non-collinear magnetic texture means turning it into a ferromagnetic state. Since no stabilizing external magnetic field is applied to the racetrack, the magnetization can in principle point into both out-of-plane directions. The uncontrolled annihilation of a skyrmionium can therefore easily lead to a local reversal of the magnetization direction, i. e., the formation of a domain. Therefore '1' bits need to be turned into '0' bits in a controlled way; no ferromagnetic domains must form. An efficient way is to invert the writing mechanism by reversing the bias voltage, which goes along with a change of the spin current's polarization from  $-\hat{e}_\varphi$  to  $+\hat{e}_\varphi$ .

The annihilation process is shown in Fig. 3. The generated spin current effectively unwinds the skyrmionium structure step by step. First, the rotation of the domain wall leads to the dissolving of the central  $-z$  domain (Fig. 3a–c). Second, the remaining skyrmion-like configuration contracts (Fig. 3d,e) until it collapses (Fig. 3f). The system relaxes towards the ferromagnetic state in less than 40 ps.

**Current-driven motion of skyrmioniums.** Skyrmions and skyrmioniums can be driven by spin torques. As discussed above, we use a two-layer setup that utilizes SOT, which means  $s||-y$  for  $j||x$ . This mechanism has

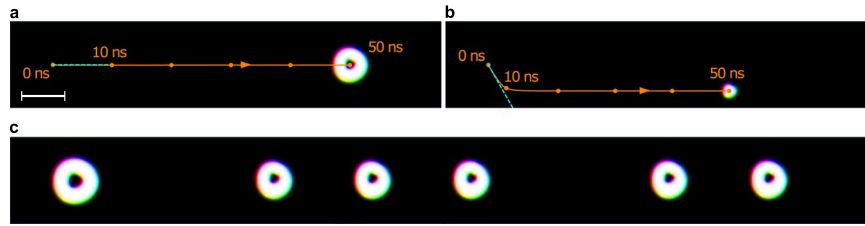


**Figure 4.** Current-driven motion of skyrmioniums. (a) A skyrmionium in a racetrack is driven by SOT: applied current density  $j_x \Theta_{SH} = 0.6 \text{ MA/cm}^2$ , injected spins are oriented along  $-y$ . (b) The motion of a skyrmion is shown for comparison. In both cases the image is taken after 50 ns of propagation time. The orange curve shows the trajectory of the quasiparticles' centers (starting point is indicated by 0 ns). The blue line indicates the motion direction under the skyrmion Hall angle, calculated from the Thiele equation (see text). (c) The results of a 'writing-under-current' simulation are shown after 35 ns propagation time in a racetrack with a doubled length. Due to the stronger current ( $j_x \Theta_{SH} = 2.0 \text{ MA/cm}^2$ ) the skyrmioniums are slightly deformed. Skyrmioniums are written after 0 ns, 5 ns, 15 ns, 20 ns, 25 ns, and 35 ns. The last skyrmionium is not yet fully relaxed. An animated version of the skyrmionium-sequence generation is accessible in the Supplementary Video 3. The scale bar corresponds to 100 nm.

been proven to be far more efficient compared to propagation induced by spin-polarized currents applied within the ferromagnetic layer (spin-transfer torque)<sup>4,26</sup>.

In our simulations (Fig. 4a,b) a reference skyrmion (Fig. 4b) first moves to the edge partially along the  $-y$  direction of the racetrack for about 10 ns and then moves at a steady velocity along the confining edge along the  $+x$  direction. The skyrmionium (Fig. 4a) on the other hand is propelled almost instantly to the steady state velocity and moves in the middle of the racetrack along  $+x$ .

The results of micromagnetic simulations can most easily be understood by an effective center-of-mass description of magnetic quasiparticles (velocity  $\mathbf{v}$ ): the Thiele equation (in units of force)<sup>4,19,26,43</sup>

$$b \mathbf{G} \times \mathbf{v} - b \underline{D} \alpha \mathbf{v} + B \underline{I} \mathbf{s} = \nabla U(y). \quad (2)$$

The properties of the respective quasiparticle are condensed into the gyromagnetic coupling vector  $\mathbf{G} = G \mathbf{e}_z$  with  $G = -4\pi N_{sk}$ , and the dissipative tensor  $\underline{D}$  determined by  $D_{ij} = \int \partial_i \mathbf{m}(\mathbf{r}) \cdot \partial_j \mathbf{m}(\mathbf{r}) d^2 r$ . Only  $D_{xx}$  and  $D_{yy}$  are nonzero. The tensor  $\underline{I}$  is calculated from  $I_{ij} = \int [\partial_i \mathbf{m}(\mathbf{r}) \times \mathbf{m}(\mathbf{r})]_j d^2 r$  and has only nonzero  $xy$  and  $yx$  elements for the stabilized Néel skyrmion (the type of skyrmion is determined by the Dzyaloshinskii-Moriya interaction (DMI)<sup>44,45</sup> arising at the interface between the Pt and Co layers) and skyrmionium. This tensor describes the interaction of injected spins  $\mathbf{s}$  and the magnetic texture. The constants are  $b = M_s d_z / \gamma_e$  and  $B = \hbar / (2e) \Theta_{SH}$ .

While neglecting the racetrack potential  $U$  (minimum in the middle of the racetrack), both textures experience a skyrmion Hall angle of  $\theta_{sk} = \arctan(G/D_{xx}\alpha)$ , which gives an angle of  $-60.5^\circ$  for the skyrmion and  $0^\circ$  for the skyrmionium with respect to the  $+x$  direction, in agreement with the first period of the simulation (blue dashed lines in Fig. 4a,b). The magnetic quasiparticles move at a velocity of

$$v_x = \frac{B}{b} \frac{I_{xy}}{D_{xx}} \frac{1}{\alpha} j_x - \tan \theta_{sk} v_y \quad (3)$$

along the racetrack. If the current density  $j_x$  is small enough, a skyrmion moves to the edge of the racetrack due to its topological charge, until the gradient potential of the racetrack edge compensates the transverse force. In this case the longitudinal velocity is increased, because the second term vanishes. Due to  $\theta_{sk} = 0$  a skyrmionium on the other hand moves instantly at a constant velocity, which is given by the first term of Eq. 3.

In agreement with ref.<sup>26</sup> we find a slightly increased skyrmionium velocity ( $|v_x^{st}| = 13.8 \text{ m/s}$ ) compared to the skyrmion velocity ( $|v_x^{st}| = 13.2 \text{ m/s}$ ) even in the steady state, which is explained by  $v_x \propto I_{xy}/D_{xx}$  in Eq. 3. In infinitely wide racetracks this ratio is equal for skyrmions and skyrmioniums. In finite tracks however, the confining potential deforms the magnetic quasiparticles slightly, altering the above ratio. Since skyrmioniums are larger than skyrmions, they experience a stronger deformation which manifests itself in a slightly increased  $I_{xy}/D_{xx}$  ratio.

The striking advantage of skyrmioniums as carriers of information compared to skyrmions becomes apparent in the first 10 ns of their motion after a current pulse is applied. During this period of time the skyrmionium already moves at maximum speed in the middle of the track, thereby allowing the writing of several skyrmioniums in sequence while the driving current is still applied (Fig. 4c).

Similarly to the skyrmion-skyrmion interaction<sup>46</sup>, also the interaction between skyrmioniums is decreasing exponentially with the distance between them (see Supplementary Fig. S1). A repulsion of the quasiparticles is mainly limited to the case of a spatial overlap of the spin textures, therefore leaving the inter-skyrmionium distance in Fig. 4c constant during the considered time period.

In Fig. 4c we apply a current density of  $j \Theta_{SH} = 2.0 \text{ MA/cm}^2$ . The skyrmionium moving at 46.28 m/s is no longer rotationally symmetric: Its inner part is pushed to the top while the outer ring is dragged to the bottom of the racetrack, in accordance with the opposite skyrmion Hall effects that originate in the opposite partial topological charges of the two skyrmionium parts.

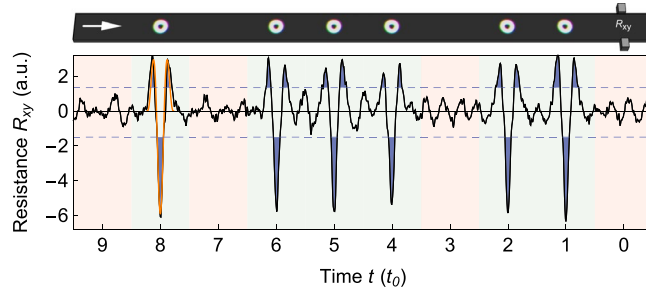


**Figure 5.** Electrical reading of skyrmioniums. The black curve shows the calculated transverse resistance signal when the skyrmionium sequence (top panel) passes the leads. In the presence of a skyrmionium between the leads (green background) a distinct pattern is found that exceeds two thresholds (dashed lines) three times. In good approximation the signal is proportional to the integrated topological charge density between the leads (orange). If no skyrmionium is present (red) the curve fluctuates around zero. Parameters: skyrmionium radius: 40 sites, track width:  $120 \times 2000$  sites, bit width: 240 sites, lead width: 29 sites,  $m/t = 5$ ,  $E_F = -8.5 t$ .

The maximal current density that can be applied to skyrmions and skyrmioniums is limited to around the same value. When the driving current is too large skyrmioniums self destruct because the forces pushing the two parts of the skyrmionium in opposite directions become too large<sup>26</sup> (For an analysis of the current dependence of the skyrmionium velocity and stability see Supplementary Fig. S2). On the other hand skyrmions are annihilated at the edge. For skyrmioniums the steady state velocity can be increased up to around 140 m/s. Alternatively, skyrmioniums can also be driven by spin waves<sup>32,33</sup>.

**Electrical reading of skyrmioniums.** Due to its distinct magnetization a skyrmionium can easily be detected by out-of-plane measurements. However, electrical in-plane measurement can be included in the racetrack geometry more easily. For this reason we consider detection of skyrmioniums via the Hall voltage as has been done experimentally for conventional skyrmions<sup>9</sup>.

When a small reading current  $I$  is applied along the track, the Hall resistivity is given by anomalous Hall and topological Hall contributions. The anomalous contribution is proportional to the net magnetization of the texture between the two detecting leads. For this reason every non-collinear magnetic texture is easily detected by the anomalous Hall effect. However, the signal is rather similar for different textures. Skyrmioniums cannot unambiguously be distinguished from skyrmions or even domain walls. This problem is resolved by the additional topological contribution to the Hall effect.

The topological Hall effect<sup>3,9,10,47–52</sup> is a hallmark of the skyrmion phase: Traversing electrons are deflected into a transverse direction, since their spins (partially) align with the non-collinear texture and a Berry phase is accumulated. The topological charge density acts like a fictitious magnetic field, called an emergent field<sup>3</sup>. We show that even though a skyrmionium has a zero topological charge it exhibits a distinct topological Hall signal that allows for a failsafe detection of skyrmioniums as ‘1’ bits in comparison to other non-collinear textures that may appear as defects in imperfect racetracks.

We calculate the Hall resistance for skyrmioniums in a racetrack by means of the Landauer-Büttiker formalism<sup>53,54</sup>, by analogy with refs<sup>10,52</sup> where skyrmions have been considered (see Methods for details). To model the interaction of electrons with the magnetic texture we considered a tight-binding model, which features nearest-neighbor hopping (amplitude  $t$ ; creation and annihilation operator  $c_i^\dagger, c_i$ ) and a Hund’s coupling term (amplitude  $m$ , vector of Pauli matrices  $\sigma$ )

$$H = \sum_{\langle i,j \rangle} t c_i^\dagger c_j + m \sum_i \mathbf{m}_i \cdot (c_i^\dagger \boldsymbol{\sigma} c_i). \quad (4)$$

Without the presence of skyrmioniums the Hamiltonian for the ferromagnet gives the energy bands  $E = 2t[\cos(k_x a) + \cos(k_y a)] \pm m$ . Since skyrmions are detected most easily for low carrier concentrations<sup>10</sup>, we set the Fermi energy of the system close to the lower band edge, where the electrons behave like free electrons ( $E_F = -8.5 t$  for  $m = 5 t$ ).

Since  $N_{\text{sk}} = 0$  the topological Hall effect vanishes globally: The inner part of the skyrmion deflects electrons to the bottom, while the outer ring redirects electrons into the opposite direction. Fortunately, this spatial separation of the two opposing contributions leads to a non-zero signal in a local measurement (Fig. 5). The topological Hall resistance  $R_{xy} = (U_{\text{up}} - U_{\text{down}})/I$  is determined by the difference in voltage  $U$  at the two leads normalized by the reading current.

Whenever a skyrmionium approaches the contacts, at first only electrons deflected by the outer ring are detected. Later, when the skyrmionium is right between the leads, the inner part dominates the electron deflection and the effective charge accumulation is reversed. Finally, upon leaving the vicinity of the contacts, only the outer ring contributes to the signal. This leads to a characteristic curve that is well approximated (orange) by the topological charge density between the leads for a skyrmionium at position  $x$

$$R_{xy}(x) \propto \int_y \int_{-x_0}^{x_0} n_{\text{sk}}(x - x', y') dx' dy'. \quad (5)$$

Electrons that traverse the spin texture are deflected by the locally nonzero emergent field of the skyrmionium  $\mathbf{B}_{\text{em}} \propto n_{\text{sk}} \mathbf{e}_z$  to the leads (voltage  $U_{\text{up}}$  and  $U_{\text{down}}$ ) of finite width ranging from  $x = -x_0$  to  $+x_0$ . Note, that for  $x_0 \rightarrow \infty$  the result of zero global resistivity is recovered, independent of the position of the skyrmionium.

## Discussion

In this Paper we simulated the four fundamental constituents of a racetrack storage device utilizing magnetic skyrmioniums as carriers of information.

For the writing and deleting mechanism we proposed a new method that utilizes the optoelectrical control of localized spin currents and their polarizations. Based on previous experimental advances we designed a nanostructured geometry enabling the writing or deleting of single skyrmionium bits, depending on the sign of the bias voltage. Since the writing process is ultrafast, skyrmioniums can be written while the driving current is applied even at the maximal velocity of the bits along the track of around 140 m/s (Fig. 4c). The reliability of this deterministic method is emphasized by the result, that an excitation with the ‘wrong’ gate voltage cannot change an existing bit (see Supplementary Videos 4 and 5). In that case the spin current’s associated chirality is not suited to wind or unwind the present configuration, respectively. Furthermore, even when room temperature fluctuations (see Methods for details) are accounted for, the proposed manipulation technique still works (see Supplementary Fig. S3 and Videos 6 and 7) what makes the presented mechanism highly attractive over other proposals. Also, we checked the range of parameters characterizing the optoelectrical writing mechanism that allow for a controlled generation of skyrmioniums (cf. Supplementary Fig. S4).

We analyzed the motion of skyrmioniums under application of electrical currents in the Pt layer where a spin current is injected perpendicularly into the Co layer (SOT). Due to their vanishing topological charge, skyrmioniums move in the middle of the racetrack and reach a steady state of motion almost instantly.

Reading magnetic skyrmioniums is possible via measurements of the Hall voltage. A local drop in the net magnetization leads to the emergence of an anomalous Hall effect and the segregation of the two skyrmionic subsystems even allows for the detection of a topological contribution: While the outer ring deflects electrons into one transverse direction, the inner ring redirects electrons into the other direction. Since the detecting leads are of finite size, one observes an oscillating Hall signal when the skyrmionium moves through them allowing for a highly reliable reading process.

Compared to skyrmions the main advantages of utilizing skyrmioniums as bits of information are (a) the slightly higher velocity (effect increases for narrower racetracks), (b) the absence of an acceleration phase ( $v_x$  is instantly proportional to  $j_x$ ; this effect is more prominent for a wider track), and (c) the skyrmionium moves always in the middle of the track. Advantages (b) and (c) are essential for an effective reading process, allow for changes in the moving direction and—combined with the ultrafast writing speed of the presented optoelectrical approach—allow for a convenient ‘writing-while-moving’ as well as ‘deleting-while-moving’ functionality of a skyrmionium racetrack (cf. Fig. 4c).

In conclusion, writing and reading of magnetic skyrmioniums in thin films can be exploited to allow for the operation of an efficient skyrmionium-based racetrack storage device. In contrast to other magnetic quasiparticles, that are predicted to move without a skyrmion Hall effect, skyrmioniums have already been detected in experiments. Our proposals will expedite the development of a working data storage device based on magnetic quasiparticles.

## Methods

**Micromagnetic simulations.** We use the GPU-accelerated micromagnetic software package Mumax3<sup>55,56</sup> to solve the LLG equation with the SOT term for every magnetic moment  $\mathbf{m}_i$  of the discretized magnetization<sup>36,38,39</sup>

$$\dot{\mathbf{m}}_i = -\gamma_e \mathbf{m}_i \times \mathbf{B}_{i,\text{eff}} + \alpha \mathbf{m}_i \times \dot{\mathbf{m}}_i + \gamma_e \epsilon \beta [(\mathbf{m}_i \times \mathbf{s}) \times \mathbf{m}_i]. \quad (6)$$

Here,  $\gamma_e = 1.760 \times 10^{11} \text{T}^{-1} \text{s}^{-1}$  is the gyromagnetic ratio of an electron. The in-plane torque coefficient is  $\epsilon \beta = \frac{\hbar^2 \Theta_{\text{SH}}}{2ed_s M_s}$ ; the out-of-plane torque parameter is set zero as it is small and does not drive the quasiparticles. The space- and time-dependent effective magnetic field

$$\mathbf{B}_{\text{eff}}^i = -\frac{\delta F[\mathbf{m}]}{M_s \delta \mathbf{m}_i} \quad (7)$$

is derived from the system’s total free energy density  $F$ , given as the sum of exchange interaction, magnetocrystalline anisotropy, the demagnetization field, Zeeman energy, and DMI.

To generate skyrmioniums we use a modified photosensitive switch setup as shown in Fig. 1a, motivated by the experimental results from Yang *et al.*<sup>35</sup>. As discussed in the main text an optoelectrically induced spin current is superposed on the uniform spin current, which drives the skyrmioniums along the racetrack. For the simulations we assumed a Gaussian envelope in time according to ref.<sup>35</sup>.

Additionally, for the room temperature simulations an effective thermal field is included as

$$\mathbf{B}_{\text{therm}}^i = \eta \sqrt{\frac{2\alpha \mu_0 k_B T}{M_s \gamma \Delta V \Delta t}}, \quad (8)$$

where  $\eta$  is a random vector generated according to a standard normal distribution for each simulation cell and changed after every time step.  $k_B$  is Boltzmann’s constant,  $T$  the temperature,  $\Delta V$  the simulation cells’ size and  $\Delta t$  the time simulation’s step. The thermal fluctuations due to the room-temperature ambience lead to deformations of the skyrmionium structure, but the switching mechanism still works successfully.

The system of Co/Pt is described by the following parameters<sup>4,26</sup>: saturation magnetization  $M_s = 0.58$  MA/m, exchange stiffness  $A = 15$  pJ/m, interfacial DMI  $D = 3.5$  mJ/m<sup>2</sup>, uniaxial anisotropy in  $z$ -direction  $K_z = 0.8$  MJ/m<sup>3</sup>, Gilbert damping parameter  $\alpha = 0.3$  and the spin Hall angle  $\Theta_{SH} = 0.4$ . We simulate a Co nanowire racetrack of width 150 nm and thickness  $d_z = 1$  nm, and discretize the magnetization in cubic cells of size 1 nm<sup>3</sup>.

We use these values for comparability with refs<sup>4,26</sup>, while noting that the DMI constant<sup>57</sup> and the spin Hall angle<sup>58</sup> are still under debate. For the here presented parameters a skyrmionium is stable for DMI strengths between 3.3 mJ/m<sup>2</sup> and 3.7 mJ/m<sup>2</sup> (cf. Supplementary Fig. S5). In this context we note, that the effective DMI constant can be tuned, for instance as in a Pt/Co/Ir setup presented in ref.<sup>59</sup> or by utilizing a different bilayer system, what is possible since our predictions are generally applicable and not limited to Co/Pt interfaces.

**Topological Hall effect calculations.** To calculate the topological Hall resistivity we consider the tight-binding Hamiltonian (Eq. 4) on a finite square lattice that forms the racetrack, as in Fig. 5. We apply four leads to the track: to the left and right to inject a small reading current, i. e.,  $I_l = -I_r = I$  and  $V_l = -V_r$ , and up and down to detect the voltage due to the transverse deflection and accumulation of the electrons, i. e.,  $I_u = I_d = 0$  and  $V_u$  and  $V_d$ . The transverse resistance follows directly from these voltages and currents, see text. To calculate the relationship between the currents and voltages we use a Landauer-Büttiker approach<sup>53,54</sup>, by analogy with refs<sup>10,52</sup>, where skyrmions have been investigated. For the calculations we use the transport simulation package Kwant<sup>60</sup>.

We solve the set of linear equations  $\{m, n\} = \{l, r, u, d\}$

$$I_m = \frac{e^2}{h} \sum_n T_{mn} V_n, \quad (9)$$

containing the transition matrix

$$T_{mn} = \text{Tr}(\Gamma_m G_{mn} \Gamma_n G_{mn}^\dagger), \quad (10)$$

for the current  $I$  and non-fixed voltages  $V_u$  and  $V_d$ . Here, the retarded Green's function

$$\mathbf{G} = (E - H - \sum_i \Sigma_i)^{-1} \quad (11)$$

and  $\Gamma_i = i(\Sigma_i - \Sigma_i^\dagger)$  enter ( $E$  energy,  $H$  tight-binding Hamiltonian).  $\Sigma_i$  is the self energy of the  $i$  th lead.

Analyzing the results for different geometric parameters we find that skyrmioniums need to have a minimal size so that the topological charge density is well resembled. The leads should not be too large (optimally below half the skyrmionium radius) since they integrate the locally distinct signal making it broader and ambiguous. The distance between two bits can be small but then their signals begin to overlap, hampering an unambiguous detection. A minimal distance is given by  $2(r_0 + x_0)$ , which is the width of the predicted signal (orange). In '0' bit regions oscillations of the signal around zero are visible originating from backscattering of electrons from the racetrack edges. This unfavorable effect decreases for wider tracks.

## References

- Bogdanov, A. & Yablonskii, D. Thermodynamically stable vortices in magnetically ordered crystals. the mixed state of magnets. *Zh. Eksp. Teor. Fiz* **95**, 182 (1989).
- Mühlbauer, S. *et al.* Skyrmion lattice in a chiral magnet. *Science* **323**, 915–919 (2009).
- Nagaosa, N. & Tokura, Y. Topological properties and dynamics of magnetic skyrmions. *Nature Nanotechnol.* **8**, 899–911 (2013).
- Sampaio, J., Cros, V., Rohart, S., Thiaville, A. & Fert, A. Nucleation, stability and current-induced motion of isolated magnetic skyrmions in nanostructures. *Nature Nanotechnol.* **8**, 839 (2013).
- Parkin, S. S. P. Shiftable magnetic shift register and method of using the same. US Patent 6,834,005 (2004).
- Parkin, S. S. P., Hayashi, M. & Thomas, L. Magnetic domain-wall racetrack memory. *Science* **320**, 190–194 (2008).
- Parkin, S. S. P. & Yang, S.-H. Memory on the racetrack. *Nature Nanotechnol.* **10**, 195–198 (2015).
- Romming, N. *et al.* Writing and deleting single magnetic skyrmions. *Science* **341**, 636–639 (2013).
- Maccariello, D. *et al.* Electrical detection of single magnetic skyrmions in metallic multilayers at room temperature. *Nature Nanotechnol.* **13**, 233–237 (2018).
- Hamamoto, K., Ezawa, M. & Nagaosa, N. Purely electrical detection of a skyrmion in constricted geometry. *Appl. Phys. Lett.* **108**, 112401 (2016).
- Jiang, W. *et al.* Direct observation of the skyrmion Hall effect. *Nat. Phys.* **13**, 162–169 (2017).
- Kang, W., Huang, Y., Zhang, X., Zhou, Y. & Zhao, W. Skyrmionelectronics: An overview and outlook. *Proceedings of the IEEE* **104**, 2040–2061 (2016).
- Kang, W. *et al.* Voltage controlled magnetic skyrmion motion for racetrack memory. *Sci. Rep.* **6**, 23164 (2016).
- Zang, J., Mostovoy, M., Han, J. H. & Nagaosa, N. Dynamics of skyrmion crystals in metallic thin films. *Phys. Rev. Lett.* **107**, 136804 (2011).
- Litzius, K. *et al.* Skyrmion Hall effect revealed by direct timeresolved x-ray microscopy. *Nat. Phys.* **13**, 170–175 (2017).
- Zhang, X. *et al.* Skyrmion-skyrmion and skyrmion-edge repulsions in skyrmion-based racetrack memory. *Sci. Rep.* **5**, 7643 (2015).
- Kim, K.-W., Moon, K.-W., Kerber, N., Nothhelfer, J. & Everschor-Sitte, K. Asymmetric skyrmion Hall effect in systems with a hybrid Dzyaloshinskii-Moriya interaction. *Phys. Rev. B* **97**, 224427 (2018).
- Büttner, F., Limesch, I. & Beach, G. S. Theory of isolated magnetic skyrmions: From fundamentals to room temperature applications. *Sci. Rep.* **8**, 4464 (2018).
- Göbel, B., Mook, A., Henk, J. & Mertig, I. Overcoming the speed limit in skyrmion racetrack devices by suppressing the skyrmion Hall effect. *Phys. Rev. B* **99**, 020405(R) (2019).
- Barker, J. & Tretiakov, O. A. Static and dynamical properties of antiferromagnetic skyrmions in the presence of applied current and temperature. *Phys. Rev. Lett.* **116**, 147203 (2016).
- Zhang, X., Zhou, Y. & Ezawa, M. Magnetic bilayer-skyrmions without skyrmion Hall effect. *Nature Commun.* **7**, 10293 (2016).
- Zhang, X., Zhou, Y. & Ezawa, M. Antiferromagnetic skyrmion: stability, creation and manipulation. *Sci. Rep.* **6**, 24795 (2016).
- Göbel, B., Mook, A., Henk, J. & Mertig, I. Antiferromagnetic skyrmion crystals: Generation, topological Hall, and topological spin Hall effect. *Phys. Rev. B* **96**, 060406(R) (2017).

24. Bogdanov, A. & Hubert, A. The stability of vortex-like structures in uniaxial ferromagnets. *J. Magn. Magn. Mater.* **195**, 182–192 (1999).
25. Beg, M. *et al.* Ground state search, hysteretic behaviour, and reversal mechanism of skyrmionic textures in confined helimagnetic nanostructures. *Sci. Rep.* **5**, 17137 (2015).
26. Zhang, X. *et al.* Control and manipulation of a magnetic skyrmionium in nanostructures. *Phys. Rev. B* **94**, 094420 (2016).
27. Finazzi, M. *et al.* Laser-induced magnetic nanostructures with tunable topological properties. *Phys. Rev. Lett.* **110**, 177205 (2013).
28. Zheng, F. *et al.* Direct imaging of a zero-field target skyrmion and its polarity switch in a chiral magnetic nanodisk. *Phys. Rev. Lett.* **119**, 197205 (2017).
29. Zhang, S., Kronast, F., van der Laan, G. & Hesjedal, T. Real-space observation of skyrmionium in a ferromagnet-magnetic topological insulator heterostructure. *Nano Lett.* **18**, 1057–1063 (2018).
30. Hagemeister, J., Siemens, A., Rózsa, L., Vedmedenko, E. Y. & Wiesendanger, R. Controlled creation and stability of  $k\pi$  skyrmions on a discrete lattice. *Phys. Rev. B* **97**, 174436 (2018).
31. Kolesnikov, A. G., Stebliy, M. E., Samardak, A. S. & Ognev, A. V. Skyrmionium–high velocity without the skyrmion Hall effect. *Sci. Rep.* **8**, 16966 (2018).
32. Li, S. *et al.* Dynamics of a magnetic skyrmionium driven by spin waves. *Appl. Phys. Lett.* **112**, 142404 (2018).
33. Shen, M., Zhang, Y., Ou-Yang, J., Yang, X. & You, L. Motion of a skyrmionium driven by spin wave. *Appl. Phys. Lett.* **112**, 062403 (2018).
34. Pylypovskiy, O. V. *et al.* Chiral skyrmion and skyrmionium states engineered by the gradient of curvature. *Phys. Rev. Appl.* **10**, 064057 (2018).
35. Yang, Y. *et al.* Ultrafast magnetization reversal by picosecond electrical pulses. *Sci. Adv.* **3**, e1603117 (2017).
36. Slonczewski, J. C. Current-driven excitation of magnetic multilayers. *J. Magn. Magn. Mater.* **159**, L1–L7 (1996).
37. Ketchen, M. *et al.* Generation of subpicosecond electrical pulses on coplanar transmission lines. *Appl. Phys. Lett.* **48**, 751–753 (1986).
38. Landau, L. D. & Lifshitz, E. On the theory of the dispersion of magnetic permeability in ferromagnetic bodies. *Phys. Z. Sowjetunion* **8**, 101–114 (1935).
39. Gilbert, T. A Lagrangian formulation of the gyromagnetic equation of the magnetization field. *Phys. Rev.* **100**, 1243 (1955).
40. Fert, A., Cros, V. & Sampaio, J. Skyrmions on the track. *Nature Nanotechnol.* **8**, 152–156 (2013).
41. Schäffer, A. F., Dürr, H. A. & Berakdar, J. Ultrafast imprinting of topologically protected magnetic textures via pulsed electrons. *Appl. Phys. Lett.* **111**, 032403 (2017).
42. Schäffer, A. F., Dürr, H. A. & Berakdar, J. Ultrafast nanoscale magnetic switching via intense picosecond electron bunches. *In Ultrafast Nonlinear Imaging and Spectroscopy V* **10380**, 103800G (2017).
43. Thiele, A. Steady-state motion of magnetic domains. *Phys. Rev. Lett.* **30**, 230 (1973).
44. Dzyaloshinsky, I. A thermodynamic theory of weak ferromagnetism of antiferromagnetics. *J. Phys. Chem. Sol.* **4**, 241–255 (1958).
45. Moriya, T. Anisotropic superexchange interaction and weak ferromagnetism. *Phys. Rev.* **120**, 91 (1960).
46. Schäffer, A. F., Rózsa, L., Berakdar, J., Vedmedenko, E. Y. & Wiesendanger, R. Stochastic dynamics and pattern formation of geometrically confined skyrmions. *Commun. Phys.* **2**, 72 (2019).
47. Bruno, P., Dugaev, V. & Taillefumier, M. Topological Hall effect and Berry phase in magnetic nanostructures. *Phys. Rev. Lett.* **93**, 096806 (2004).
48. Neubauer, A. *et al.* Topological Hall effect in the a phase of MnSi. *Phys. Rev. Lett.* **102**, 186602 (2009).
49. Hamamoto, K., Ezawa, M. & Nagaosa, N. Quantized topological Hall effect in skyrmion crystal. *Phys. Rev. B* **92**, 115417 (2015).
50. Göbel, B., Mook, A., Henk, J. & Mertig, I. Unconventional topological Hall effect in skyrmion crystals caused by the topology of the lattice. *Phys. Rev. B* **95**, 094413 (2017).
51. Göbel, B., Mook, A., Henk, J. & Mertig, I. Signatures of lattice geometry in quantum and topological Hall effect. *New J. Phys.* **19**, 063042 (2017).
52. Yin, G., Liu, Y., Barlas, Y., Zang, J. & Lake, R. K. Topological spin Hall effect resulting from magnetic skyrmions. *Phys. Rev. B* **92**, 024411 (2015).
53. Landauer, R. Spatial variation of currents and fields due to localized scatterers in metallic conduction. *IBM Journal of Research and Development* **1**, 223–231 (1957).
54. Büttiker, M. Absence of backscattering in the quantum Hall effect in multiprobe conductors. *Phys. Rev. B* **38**, 9375 (1988).
55. Vansteenkiste, A. & Van de Wiele, B. Mumax: a new highperformance micromagnetic simulation tool. *J. Magn. Magn. Mater.* **323**, 2585–2591 (2011).
56. Vansteenkiste, A. *et al.* The design and verification of mumax3. *AIP Adv.* **4**, 107133 (2014).
57. Simon, E., Rózsa, L., Palotás, K. & Szunyogh, L. Magnetism of a co monolayer on pt (111) capped by overlayers of 5 d elements: A spin-model study. *Phys. Rev. B* **97**, 134405 (2018).
58. Tao, X. *et al.* Self-consistent determination of spin Hall angle and spin diffusion length in pt and pd: The role of the interface spin loss. *Science Adv.* **4**, eaat1670 (2018).
59. Moreau-Luchaire, C. *et al.* Additive interfacial chiral interaction in multilayers for stabilization of small individual skyrmions at room temperature. *Nature Nanotechnol.* **11**, 444 (2016).
60. Groth, C. W., Wimmer, M., Akhmerov, A. R. & Waintal, X. Kwant: a software package for quantum transport. *New J. Phys.* **16**, 063065 (2014).

## Acknowledgements

This work is supported by Priority Program SPP 1666, CRC/TRR 227 and SFB 762 of Deutsche Forschungsgemeinschaft (DFG).

## Author Contributions

B.G. and A.S. initiated research and planned the project. J.B., I.M. and S.P. supervised the project. B.G. conducted calculations of the topological Hall effect and analyzed the Thiele equation. A.S. did the micromagnetic simulations. B.G. and A.S. wrote the manuscript. All authors discussed the results and commented on the manuscript.

## Additional Information

**Supplementary information** accompanies this paper at <https://doi.org/10.1038/s41598-019-48617-z>.

**Competing Interests:** The authors declare no competing interests.

**Publisher's note:** Springer Nature remains neutral with regard to jurisdictional claims in published maps and institutional affiliations.





**Open Access** This article is licensed under a Creative Commons Attribution 4.0 International License, which permits use, sharing, adaptation, distribution and reproduction in any medium or format, as long as you give appropriate credit to the original author(s) and the source, provide a link to the Creative Commons license, and indicate if changes were made. The images or other third party material in this article are included in the article's Creative Commons license, unless indicated otherwise in a credit line to the material. If material is not included in the article's Creative Commons license and your intended use is not permitted by statutory regulation or exceeds the permitted use, you will need to obtain permission directly from the copyright holder. To view a copy of this license, visit <http://creativecommons.org/licenses/by/4.0/>.

© The Author(s) 2019

## 6.4 Antiferromagnetic skyrmion crystals and topological spin Hall effect

**Theoretical prediction.** At the present state of research antiferromagnetic skyrmions are perhaps the most promising candidates for improved bits in racetrack storage devices. These quasiparticles consist of two copies of conventional skyrmions with mutually reversed spins, living on separate layers [Fig. 29(a); initially proposed by Zhang *et al.* [146] and Barker *et al.* [147]] or sublattices [Fig. 29(b); first introduced by Zhang *et al.* [148]].

**Current-driven motion without skyrmion Hall effect.** The two subskyrmions constituting the antiferromagnetic skyrmion have opposite polarities resulting in a compensated  $N_{\text{Sk}} = 0$  for the here considered object. When an antiferromagnetic skyrmion is driven by a current via spin torques, both subparticles will experience the same drag force but opposite transverse forces (determined by their opposite topological charges  $N_{\text{Sk}}$ ); cf. Fig. 29(c). For this reason, the antiferromagnetic skyrmion will move perfectly in the middle of the racetrack without skyrmion Hall effect. Since the two skyrmions are ‘intertwined’ (and not separated from each other like for the skyrmionium), much larger current densities can be applied. Antiferromagnetic skyrmions are predicted to move more than an order of magnitude faster compared to conventional skyrmions in the conventional SOT geometry [149].

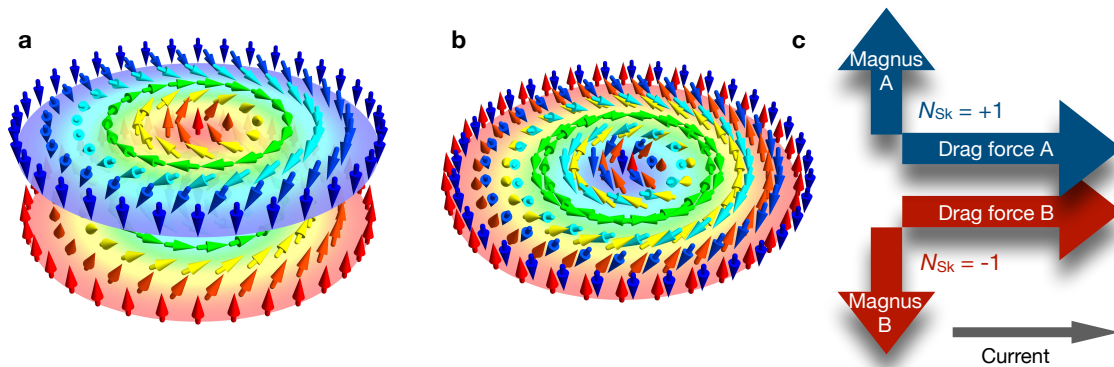


Figure 29: **Antiferromagnetic skyrmion.** **a** shows the considered quasiparticle as bilayer skyrmion, and **b** as two ‘intertwined’ skyrmions on individual sublattices. **c** visualizes the compensation of the skyrmion Hall effect. For both sublattices the drag forces (or dissipative forces) are oriented parallel while the transverse forces (here often called Magnus forces) cancel due to the sign reversed topological charges  $N_{\text{Sk}}$ . Consequently, an antiferromagnetic skyrmion will move parallel to an applied current.

**This publication.** In the following publication “Antiferromagnetic skyrmion crystals: Generation, topological Hall, and topological spin Hall effect” [BG7] we predict a new state of matter: the antiferromagnetic skyrmion crystal. Up to this publication, only individual antiferromagnetic skyrmions had been proposed.

The difficulty in producing these objects is that the vectorial quantity that characterizes the generating mechanism has to be oriented oppositely for the two subskyrmions.

This is especially difficult to fulfill since an externally applied magnetic field is necessary for the formation of antiferromagnetic skyrmion crystals, as suggested by the experiences with conventional skyrmion crystals. In fact, the field cannot change its orientation on the length scale of the lattice constant, which would be necessary for the stabilization of a pair of skyrmions living on two intertwined sublattices. For this reason, we propose to mimic a staggered magnetic field by growing a potential antiferromagnetic skyrmion layer on top of a collinear antiferromagnet. This way, the exchange interaction between the layers has the same mathematical expression as the required Zeeman term. Monte Carlo simulations (cf. Sec. 3.1) have been performed to confirm the idea numerically.

Antiferromagnetic skyrmion crystals have never been observed in an experiment and even isolated antiferromagnetic skyrmions in a synthetic antiferromagnet had never been seen at the moment of publication of the presented paper (they have been observed just recently, see note added). Even if antiferromagnetic skyrmion crystals were present in a material, a main challenge is to realize their existence. The topological charge density and the magnetization density are both compensated on the length scale of the lattice constant. This renders typical observation techniques like the Lorentz TEM or a registration by the Hall signal suboptimal, especially for ‘real’ antiferromagnetic skyrmions living in the same layer.

The second main claim of the following publication is the prediction of a topologically induced version of the spin Hall effect, complementary to Ref. [150]. Instead of a transverse charge current, a (locally aligned) pure spin current arises. The explanation is similar to the cancellation of the skyrmion Hall effect: two transverse charge currents emerge, which are oriented oppositely and cancel. However, they are (locally) spin polarized oppositely as well, which is why they add up with respect to the spin degree of freedom [cf. Fig. 4(b) of the following publication]. This hallmark of the antiferromagnetic skyrmion crystal phase may be utilized to detect these highly desired spin textures in experiments. The topological version of the spin Hall effect was calculated by analogy with Sec. 4.3.

**Note added.** Shortly before the submission of this thesis, antiferromagnetic skyrmions have finally been observed by magnetic force microscopy (MFM) in Pt/Co/Ru multilayers [151]. The Ru acts as a bias layer that leads to an antiferromagnetic coupling of the magnetic layers. For this reason, the system can be considered a synthetic antiferromagnet. Due to the spatial separation of the magnetic layers, the dipolar fields are not compensated and the object can be detected via real-space techniques. The favorable emergent electrodynamics remains to be observed. Our presented contribution to this field may help to find also native antiferromagnetic skyrmions in an innately antiferromagnetic material.

The following publication: Reprinted (whole article) with permission from (B. Göbel *et al.* Physical Review B **96**, 060406(R) (2017); Ref. [BG7]; Antiferromagnetic skyrmion crystals: Generation, topological Hall, and topological spin Hall effect). Copyright (2017) by the American Physical Society.

## Antiferromagnetic skyrmion crystals: Generation, topological Hall, and topological spin Hall effect

Börge Göbel,<sup>1,\*</sup> Alexander Mook,<sup>1</sup> Jürgen Henk,<sup>2</sup> and Ingrid Mertig<sup>1,2</sup>

<sup>1</sup>Max-Planck-Institut für Mikrostrukturphysik, D-06120 Halle (Saale), Germany

<sup>2</sup>Institut für Physik, Martin-Luther-Universität Halle-Wittenberg, D-06099 Halle (Saale), Germany

(Received 20 April 2017; revised manuscript received 15 June 2017; published 9 August 2017)

Skyrmions are topologically nontrivial, magnetic quasiparticles that are characterized by a topological charge. A regular array of skyrmions, a skyrmion crystal (SkX), features the topological Hall effect (THE) of electrons, which, in turn, gives rise to the Hall effect of the skyrmions themselves. It is commonly believed that *antiferromagnetic* skyrmion crystals (AFM-SkXs) lack both effects. In this Rapid Communication, we present a generally applicable method to create stable AFM-SkXs by growing a two-sublattice SkX onto a collinear antiferromagnet. As an example we show that both types of skyrmion crystals, conventional and antiferromagnetic, exist in honeycomb lattices. While AFM-SkXs with equivalent lattice sites do not show a THE, they exhibit a topological spin Hall effect. On top of this, AFM-SkXs on inequivalent sublattices exhibit a nonzero THE, which may be utilized in spintronics devices. Our theoretical findings call for experimental realization.

DOI: [10.1103/PhysRevB.96.060406](https://doi.org/10.1103/PhysRevB.96.060406)

**Introduction.** Skyrmions [1–5] are small magnetic quasiparticles, which are usually caused by the Dzyaloshinskii-Moriya interaction [6,7], but they have been produced by other mechanisms [8], like frustrated exchange interactions [9], as well. While single skyrmions are envisioned to be used as “bits” in data storage devices [10–19], which provide durability of data due to topological protection [8], skyrmion *crystals* (SkXs), regular arrays of skyrmions, are best known for exhibiting the topological Hall effect (THE) of electrons [20–29], which, in turn, gives rise to the skyrmion Hall effect (SkHE; also present in isolated skyrmions) [8,30–32].

From the perspective of applications in data storage devices, the SkHE is undesirable. Thus, the concept of antiferromagnetic (AFM) skyrmions has been developed [33–36]: skyrmions on two sublattices in which the spins on one sublattice are reversed. As a result, both THE and SkHE vanish [33]. Because no periodic antiferromagnetic skyrmion crystal (AFM-SkX) is known yet, surrogate systems consisting of two skyrmion layers with opposite winding have been investigated [37,38].

In this Rapid Communication, we predict the generation of stable AFM-SkXs by coupling a bipartite skyrmion material to a collinear antiferromagnetic layer [Fig. 1(b)]. The interlayer interaction acts as a staggered magnetic field, which flips the spins of the SkX on one sublattice. The approach is generally applicable, as it can turn *every* established phase of conventional SkXs into an AFM-SkX phase, irrespective of the skyrmion-generating mechanism. As an example, we apply the method to frustrated spins on a honeycomb lattice, i.e., two triangular sublattices that exhibit SkXs via frustrated exchange interactions (cf. Ref. [9]).

If both sublattices of the AFM-SkX are equivalent, there is no THE. However, we find a topological spin Hall effect (TSHE). Since the TSHE arises in a single two-dimensional layer, it is clearly distinguished from that in the surrogate system discussed in Refs. [37,38]. For inequivalent sublattices the THE becomes also nonzero, which may become considerable

for applications once the predicted existence of AFM-SkXs has been realized experimentally.

**Generation of AFM skyrmion crystals.** First, we present our approach to create a stable AFM-SkX starting from a known SkX phase. We take two copies of that two-dimensional system and couple them to a collinear antiferromagnet. This inverts the spins of one sublattice and yields a stable AFM-SkX with the parameters of the initial SkX. This approach is generally applicable, as it does not depend on the SkX-generating mechanism.

As an example we take a honeycomb lattice featuring two triangular sublattices, A and B, which both exhibit a SkX generated by frustrated exchange interactions [9]. The sublattice skyrmions are stabilized by an external magnetic

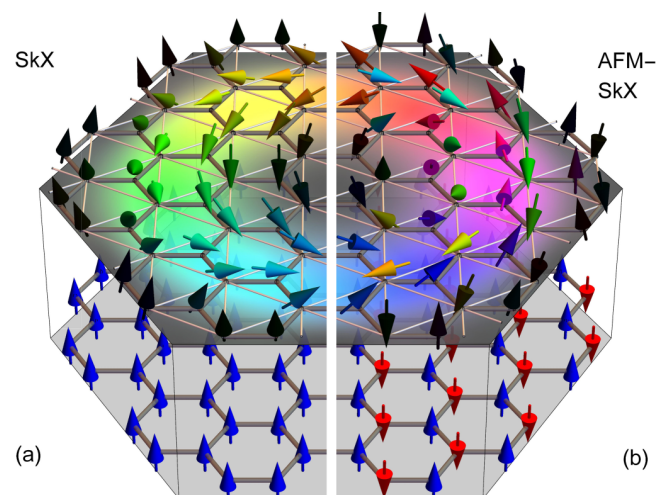


FIG. 1. (a) Skyrmion and (b) antiferromagnetic skyrmion crystal on a honeycomb lattice. The spins at each site are represented by arrows. The lower hexagon represents (a) a ferromagnet and (b) a collinear antiferromagnet, on which the (antiferromagnetic) skyrmion layer has been deposited. Gray lines, forming the honeycomb lattice, represent exchange interactions with constant  $J_1^{AB}$ ; see text. White thin lines visualize the exchange coupling within a sublattice (among second-nearest sites)  $J_1$ .

\*bgoebel@mpi-halle.mpg.de

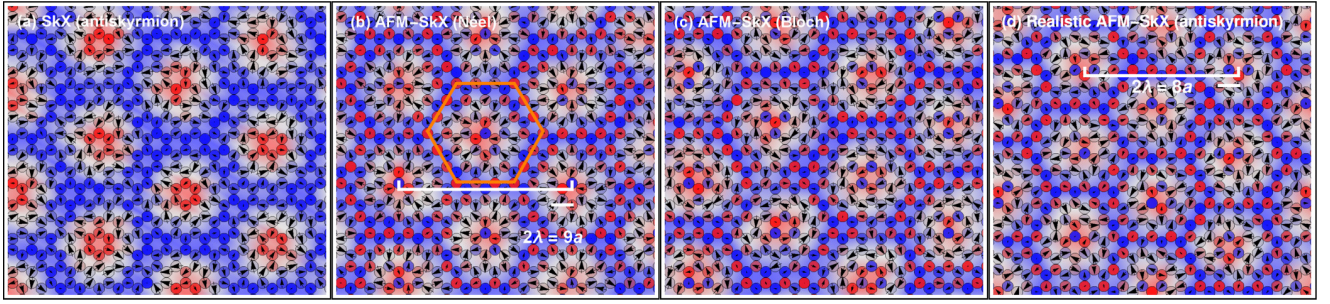


FIG. 2. Antiferromagnetic skyrmion crystals on a honeycomb lattice of size  $\lambda = 4.5a$  [see (b);  $a$  lattice constant] characterized by vorticity  $v$  and helicity  $\gamma$  (azimuth of a spin  $\Phi = v\phi + \gamma$ , where  $\phi$  is the azimuth of the position vector with respect to the skyrmions center). Blue (red) circles denote a positive (negative)  $z$  component of the spins, whereas arrows represent their in-plane components (modulus and direction). (a) Crystal of antiskyrmions ( $v = -1$ ;  $\gamma \approx -\pi/3$ ). (b) Crystal of antiferromagnetic Néel-type skyrmions (sublattice skyrmions  $v = +1$ ;  $\gamma \approx \frac{\pi}{2} \pm \frac{\pi}{2}$ ). (c) Crystal of antiferromagnetic Bloch-type skyrmions (sublattice skyrmions  $v = +1$ ;  $\gamma \approx \pi \pm \frac{\pi}{2}$ ). Parameters:  $J_1 = 1.63042J$ ;  $J_3 = -J$ , and  $k_B T = 2.5J$ ; for (a)  $J_1^{AB} = +0.05J$  and  $B_A = +B_B = 0.9J$ , while for (b) and (c)  $J_1^{AB} = -0.05J$  and  $B_A = -B_B = 0.9J$ . This staggered magnetic field corresponds to a coupling to a collinear antiferromagnet with strength  $0.9J$ . Cluster size:  $36 \times 36$  sites per sublattice. (d) Realistic antiferromagnetic antiskyrmion crystal. Parameters:  $J_1 = 0.42J$ ;  $J_3 = -0.665J$ ;  $J_1^{AB} = -1.751J$  on a  $32 \times 32$  cluster;  $T$  and  $B$  are as in (b) and (c). The size of the antiferromagnetic skyrmions is reduced ( $\lambda = 4a$ ).

field and by thermal fluctuations; they can be understood as the superposition of three energetically degenerate spin spirals; one of them forms the ground state for zero temperature and no magnetic field. To make the sublattice SkXs match we add a weak intersublattice coupling (results for a realistic intersublattice coupling are shown thereafter).

The system is described by the Hamiltonian [9]

$$H_{MC} = -\frac{1}{2} \sum_{i,j} J_{ij} \mathbf{s}_i \cdot \mathbf{s}_j - \sum_i s_i^z B_i, \quad (1)$$

in which  $J_{ij}$  are Heisenberg exchange constants ( $i$  and  $j$  site indices). We take into account nearest-neighbor ( $J_1$ ) and third-nearest-neighbor ( $J_3$ ) exchange within each sublattice and add intersublattice coupling  $J_1^{AB}$ . The Zeeman term provides coupling to the external magnetic field  $B_i$  along the  $z$  direction. All energies are given in units of a global constant  $J$ . The magnetic configuration  $\{s_i\}$  is computed by classical Monte Carlo simulations ( $s_i$  spin of unit length).

As a prerequisite, a weak intersublattice coupling  $J_1^{AB} \ll J$  (see caption of Fig. 1) ensures that the skyrmion-center locations of A and B adjust to each other. In this way the lattice constant of the SkX and the magnetic phase diagram remain almost unchanged (with respect to the uncoupled SkXs [9]). An exemplary result for a conventional SkX is shown in Fig. 2(a).

To create an AFM-SkX the spins of one sublattice have to be reversed, which would require an unrealistic staggered magnetic field  $B_A = -B_B$ . Instead, we mimic it by placing the skyrmion lattice on a collinear antiferromagnet with strong out-of-plane uniaxial anisotropy [Fig. 1(b)]. For matching sublattices the intersublattice coupling  $J_1^{AB}$  has to be chosen to be negative. The resulting AFM-SkXs on top of an antiferromagnet [Fig. 1(b)] have the same energy and exhibit the same geometry [compare Fig. 2(a) with Figs. 2(b) and 2(c)] as the SkXs [Fig. 1(a)].

Special properties of the SkXs attributed to frustration survive our approach: helicity (i.e., Néel- or Bloch-type skyrmions), winding (i.e., skyrmions or antiskyrmions with

topological charge  $\mp 1$ ), and skyrmion-center locations are not fixed for both SkXs and AFM-SkXs (Fig. 2).

In real materials the sublattices A and B are strongly coupled;  $J_1^{AB} \gg 0$ . Nevertheless, our simulations show that AFM-SkXs can still be stabilized [Fig. 2(d)], but the lattice constant, stabilizing field, and temperature of the initial sublattice skyrmions cannot be carried over to the resulting AFM-SkX.

In summary, AFM-SkXs can be produced by coupling a two-sublattice SkX to an antiferromagnetic layer [Fig. 1(b)]. This approach is valid irrespective of the physical mechanism that stabilizes the SkX (frustration [9], Dzyaloshinskii-Moriya interaction [39], or anisotropy [40]). The novel AFM-SkX state motivates us to calculate the THE and TSHE.

*Electron transport in (AFM) skyrmion crystals.* In a tight-binding model the interaction of electrons with an (AFM) skyrmion texture  $\{s_i\}$  is described by the Hamiltonian [29]

$$H = \sum_{ij} t_{ij} c_i^\dagger c_j + m \sum_i s_i \cdot (c_i^\dagger \boldsymbol{\sigma} c_i), \quad (2)$$

where  $c_i^\dagger$  and  $c_i$  creation and annihilation operators, respectively, and  $\boldsymbol{\sigma}$  is the vector of Pauli matrices. The hopping from site  $i$  to site  $j$  is quantified by  $t_{ij}$ , and the coupling to the skyrmion texture is quantified by  $m$ .

The transverse charge conductivity  $\sigma_{xy}$  at the Fermi energy  $E_F$  is calculated from the Kubo formula [41]

$$\sigma_{xy}(E_F) = \frac{e^2}{h} \frac{1}{2\pi} \sum_n \int_{BZ} \Omega_n^{(z)}(\mathbf{k}) f(E_{nk} - E_F) d^2k, \quad (3)$$

where BZ indicates the Brillouin zone and  $\mathbf{k}$  is the wave vector. The sum runs over all bands  $n$ .  $f(E)$  is the Fermi distribution function at temperature  $T$ ;  $e$ ,  $h$ , and  $k_B$  denote the electron charge, the Planck constant, and the Boltzmann constant, respectively. The Berry curvature (a general version which also describes spin transport),

$$\Omega_n(\mathbf{k}) = i \sum_{m \neq n} \frac{\langle u_{nk} | \nabla_{\mathbf{k}} \mathcal{M} H_{\mathbf{k}} | u_{mk} \rangle \times \langle u_{mk} | \nabla_{\mathbf{k}} H_{\mathbf{k}} | u_{nk} \rangle}{(E_{nk} - E_{mk})^2},$$

is determined from the eigenvectors  $u_{nk}$  with eigenenergies  $E_{nk}$  of the  $k$ -dependent Hamiltonian  $H_k$  [42]. For the topological Hall conductivity  $\sigma_{xy}$  in skyrmion textures, the  $(2n) \times (2n)$  matrix  $\mathcal{M}$  is a unit matrix. If  $E_F$  lies within the band gap above the  $n$ th band,  $\sigma_{xy}$  is proportional to the winding number [43,44],  $w_n = \sum_{m \leq n} C_m$ , which is the accumulation of the integer Chern numbers  $C_m = \frac{1}{2\pi} \int_{\text{BZ}} \Omega_m^{(z)}(\mathbf{k}) d^2k$ .

For the spin conductivity,  $\mathcal{M} = \text{diag}(s_1 \cdot \sigma, \dots, s_n \cdot \sigma)$  accounts for the alignment of the electron spin with the skyrmion texture. Additionally, Eq. (3) has to be multiplied by  $\hbar/(2e)$  to reflect spin instead of charge transport. For the spin conductivity in AFM-SkXs the signs of the entries are reversed for the sublattice with negative net magnetization since a locally parallel aligned spin means spin up or down in the respective sublattice.

In the following, we utilize skyrmion textures on the honeycomb lattice that enter Eq. (2) by superposing three spin spirals, as in Ref. [9] [Fig. 1(a)]. An AFM-SkX is then constructed by reversing the spins in one of the sublattices [Fig. 1(b)]. These textures are idealized versions of those generated from  $H_{\text{MC}}$  (Fig. 2).

*Topological Hall effects in skyrmion crystals.* For the THE in a SkX [Fig. 1(a)], we consider two generic cases: (i) nearest-neighbor hopping strength  $t_1 = t$  and second-nearest neighbor hopping strength  $t_2 = 0$  and (ii)  $t_1 = 0$  and  $t_2 = t$  (compare the insets in Fig. 3).

For large coupling  $m$  to the skyrmion texture ( $m = 5t$  in Fig. 3), the band structure is energetically split into two blocks (rigidly shifted by  $\pm m$ ). In each of the blocks, the electron spin is aligned parallel (lower block) or antiparallel (upper block) to the texture. As a result, the respective

energy-dependent transverse conductivities have opposite sign and exhibit (almost) identical shapes [26].

The above qualitative picture is nicely reproduced by the computed THE of case (i) [black line in Fig. 3(a); cf. Ref. [27]]. Within each block, the conductivity curve is antisymmetric because the sublattices are equivalent. The bands of the lower (upper) block carry Chern number  $-1$  ( $+1$ ), except for bands close to a van Hove singularity of the zero-field band structure (at  $\pm m \pm t$ ), as is explained in Refs. [26,27] (at the associated energies the Fermi lines change their character from electron to hole pockets). The latter bands compensate the accumulated large Chern numbers of all other bands in their block and bring about a sign change in  $\sigma_{xy}$ .

For case (ii) (two uncoupled triangular sublattices [26]), we find the separation into two blocks as well. Every band is almost degenerate [minimal splitting due to  $E(\mathbf{k}) \neq E(-\mathbf{k})$  for bands of both sublattices; see Fig. S2 in the Supplemental Material [45]]. Thus, the conductivity shows steps in units of  $2e^2/h$  [Fig. 3(b)], which is twice as large as in case (i).

The alignment of the spins (parallel or antiparallel) with the skyrmion texture results in a transverse spin-polarized current [46]. The magnitude of the spin conductivity corresponds to the charge conductivity (in the block-separated case for large coupling  $m$ ). Spin and charge current are inseparable.

*Topological spin Hall effect in AFM skyrmion crystals.* We proceed with the generic cases for the AFM-SkXs [Fig. 1(b)]. Case (i) exhibits no considerable transverse transport because the emergent field fluctuates around zero, yielding zero net field. In case (ii) the topological Hall conductivity is zero as well; this is explained by the two sublattices having opposite emergent fields. However, we find a topological spin Hall effect.

The bands of case (ii) are twofold degenerate because the sublattices are equivalent [ $E^A(\mathbf{k}) = E^B(\mathbf{k})$ ]. The spin is aligned parallel (lower block) or antiparallel (upper block) to the texture of the respective sublattice. Since the sublattices are decoupled ( $t_1 = 0$ ), the electrons are localized exclusively in either sublattice. This causes a spin-up current (from the sublattice with positive net magnetization) and a spin-down current (from the other sublattice, with negative net magnetization). Hence, a TSHE occurs which is identical to the (spin-polarized) THE in the SkX [Figs. 4(b) and 4(c); compare the blue and orange lines in Fig. 3(b)]. For the AFM-SkX we find a pure spin current; the THE is zero.

In each of the bulk-band gaps the number of right-propagating edge states is identical to that of left-propagating ones [Fig. 4(a)]: there is no charge transport, i.e., no THE. Since the edge states “live” on different sublattices, they carry opposite spin because their spins are aligned with the associated sublattice texture. The emergent fields of the individual sublattices have opposite signs; thus, they deflect electrons of *opposite spin into opposite directions* [Fig. 4(b)]. The result is a TSHE. Recall that in a SkX the identical emergent fields of the sublattices deflect electrons of the *same spin in the same direction* [Fig. 4(c)]; hence, the spin conductivities for AFM-SkX and SkX are identical, but in the AFM-SkX there is no effective transverse charge current.

For intermediate and more general cases, i.e.,  $t_1 \neq 0$  and  $t_2 \neq 0$ , the results lie between cases (i) and (ii) (see Fig. S1 in

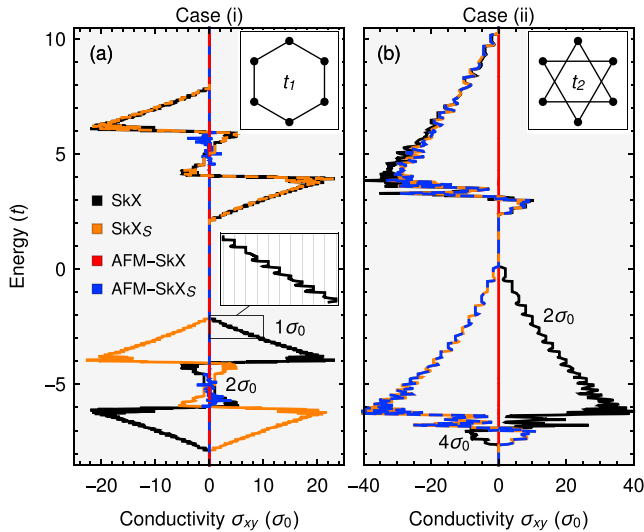


FIG. 3. Topological Hall conductivities in skyrmion crystals [black: charge conductivity (SkX); orange: spin conductivity (SkX<sub>S</sub>)] and in antiferromagnetic skyrmion crystals [red: charge conductivity (AFM-SkX); blue: spin conductivity (AFM-SkX<sub>S</sub>)] with 72 sites in the unit cell. The tight-binding parameters read (a)  $t_1 = t$ ;  $t_2 = 0$  [case (i)] and (b)  $t_1 = 0$ ;  $t_2 = t$  [case (ii)]; the coupling to the skyrmion texture equals  $m = 5t$ . The hopping strengths are sketched in the insets. Conductivities are quantized in units of  $\sigma_0 = e^2/h$  (charge) and  $\sigma_0 = e/(4\pi)$  (spin) (see Refs. [26,27]).

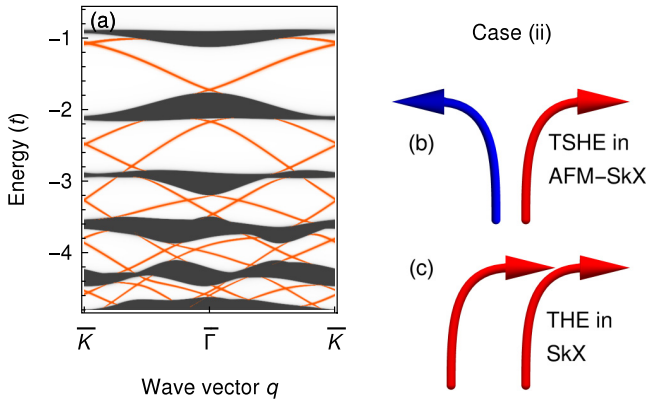


FIG. 4. Topological spin Hall effect in an antiferromagnetic skyrmion crystal of generic case (ii) with 32 sites in the unit cell. (a) Electronic structure at the edge of the semi-infinite sample computed by Green's function renormalization [47,48]. Black: bulk states, orange: edge states. (b) Deflection of electrons with opposite spins (blue and red arrows) in an AFM-SkX (schematic). (c) Deflection of electrons with equal spins in a SkX.

the Supplemental Material [49]). The TSHE in an AFM-SkX is nonzero as long as  $t_2 > 0$ . The THE is zero in any case.

Summarizing, one finds a THE of spin-polarized electrons in SkXs [Fig. 1(a)] and a TSHE in AFM-SkXs [Fig. 1(b)], which are, the analogs to Hall and spin Hall physics in a single two-dimensional layer, as distinguished from the surrogate multilayer system of Refs. [37,38].

*Topological Hall effect in asymmetric AFM skyrmion crystals.* Having discussed generic cases, we proceed with sublattice-asymmetric AFM-SkXs (e.g., in crystals consisting of two different elements), which is modeled by setting  $t_2^A \neq t_2^B$  and by differing on-site energies,  $\delta\epsilon = \epsilon^A - \epsilon^B \neq 0$ . The topological Hall conductivity exhibits the band-block separation [Figs. 5(a) and 5(b)] and is nonzero in any case.

To clarify these findings we consider the tight-binding Hamiltonian (2) without spin texture ( $m = 0$ ), with parameters as in Fig. 5(b) (uncoupled sublattices). The density of states (DOS) of the resulting two bands (one band per sublattice) is shown in Fig. 5(c). Comparing SkX and AFM-SkX, the sublattice skyrmions on sublattice A (green curve) have the same winding, while for sublattice B (blue) they have opposite winding. Therefore, in regions in which the two zero-field bands (green and blue) do not overlap in energy, the topological Hall conductivities of a SkX and an AFM-SkX are identical.

The contribution of the narrow band (blue) has to be subtracted (added) from (to) the conductivity corresponding to the green band for the AFM-SkX (SkX) because of the opposite (identical) winding of the sublattice skyrmion (see Ref. [27]).

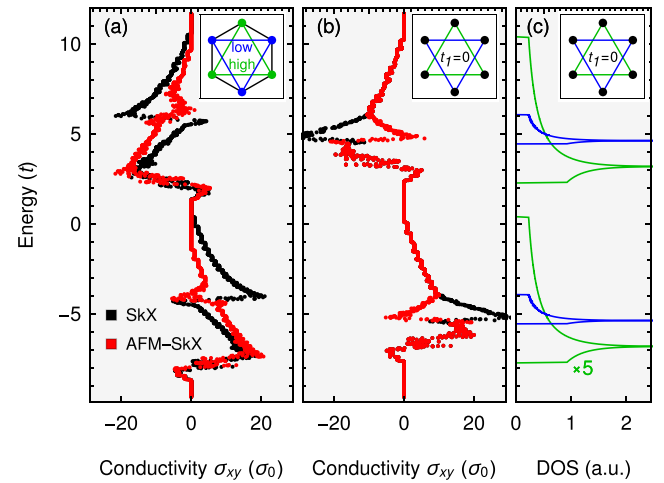


FIG. 5. Topological Hall conductivity (SkX: black; asymmetric AFM-SkX: red; in units of  $\sigma_0 = e^2/h$ ). (a) Conductivity  $\sigma_{xy}$  versus energy for differing on-site energies and second-nearest-neighbor strengths:  $t_1 = 0.75t$ ;  $t_2^A = 0.2t \neq t_2^B = t$ ;  $\delta\epsilon = 2t$ . (b) Same as (a) but with  $\delta\epsilon = 0$  and  $t_1 = 0$ . The coupling to the skyrmion texture is  $m = 5t$  in all cases. (c) DOS of the zero-field band structure for the parameters of (b).

For nonzero  $t_1$  and  $\delta\epsilon$  [Fig. 5(a)] a sublattice separation of the bands is no longer given, but the conductivity does not change qualitatively. It is even possible that the topological Hall conductivity of an AFM-SkX exceeds that of a SkX (see Fig. S3 in the Supplemental Material [50]).

*Conclusion.* In this Rapid Communication, we predicted the generation of stable antiferromagnetic skyrmion crystals. These systems can, in principle, be realized on *any* bipartite lattice, provided the individual sublattices exhibit a conventional skyrmion crystal (irrespective of the generating mechanism), by growing it on a collinear antiferromagnet [Fig. 1(b)].

For equivalent sublattices, there is no topological Hall effect but a topological spin Hall effect. Furthermore, asymmetric antiferromagnetic skyrmion crystals (i.e., with inequivalent sublattices) exhibit a topological Hall effect. These findings are valid also for metastable single antiferromagnetic skyrmions (see Refs. [33–35]). Very recently, ferrimagnetic skyrmions have been found in GdFeCo films [51]. The magnetic moments of the two sublattices are inequivalent, and a topological Hall effect is measurable, which corroborates our analysis.

Besides the potential of *stable* AFM-SkXs for applications, the Hamiltonian  $H_{MC}$  of Eq. (1) motivates further theoretical investigations. An example is transport via magnons, studied in stable magnetic configurations. One may compare the topological magnon Hall effects in skyrmion crystals [52] with that in antiferromagnetic skyrmion crystals.

*Acknowledgment.* This work is supported by Priority Program SPP 1666 of Deutsche Forschungsgemeinschaft (DFG).

[1] T. H. R. Skyrme, *Nucl. Phys.* **31**, 556 (1962).

[2] A. Bogdanov and D. Yablonskii, *Zh. Eksp. Teor. Fiz.* **95**, 182 (1989).

[3] A. Bogdanov and A. Hubert, *J. Magn. Magn. Mater.* **138**, 255 (1994).

- [4] U. Röbber, A. Bogdanov, and C. Pfleiderer, *Nature (London)* **442**, 797 (2006).
- [5] S. Mühlbauer, B. Binz, F. Jonietz, C. Pfleiderer, A. Rosch, A. Neubauer, R. Georgii, and P. Böni, *Science* **323**, 915 (2009).
- [6] I. Dzyaloshinsky, *J. Phys. Chem. Sol.* **4**, 241 (1958).
- [7] T. Moriya, *Phys. Rev.* **120**, 91 (1960).
- [8] N. Nagaosa and Y. Tokura, *Nat. Nanotechnol.* **8**, 899 (2013).
- [9] T. Okubo, S. Chung, and H. Kawamura, *Phys. Rev. Lett.* **108**, 017206 (2012).
- [10] A. Fert, V. Cros, and J. Sampaio, *Nat. Nanotechnol.* **8**, 152 (2013).
- [11] R. Wiesendanger, *Nat. Rev. Mater.* **1**, 16044 (2016).
- [12] N. Romming, C. Hanneken, M. Menzel, J. E. Bickel, B. Wolter, K. von Bergmann, A. Kubetzka, and R. Wiesendanger, *Science* **341**, 636 (2013).
- [13] P.-J. Hsu, A. Kubetzka, A. Finco, N. Romming, K. von Bergmann, and R. Wiesendanger, *Nat. Nanotechnol.* **12**, 123 (2017).
- [14] X. Zhang, M. Ezawa, and Y. Zhou, *Sci. Rep.* **5**, 9400 (2015).
- [15] X. Zhang, Y. Zhou, M. Ezawa, G. Zhao, and W. Zhao, *Sci. Rep.* **5**, 11369 (2015).
- [16] W. Jiang, P. Upadhyaya, W. Zhang, G. Yu, M. B. Jungfleisch, F. Y. Fradin, J. E. Pearson, Y. Tserkovnyak, K. L. Wang, O. Heinonen *et al.*, *Science* **349**, 283 (2015).
- [17] O. Bouille, J. Vogel, H. Yang, S. Pizzini, D. de Souza Chaves, A. Locatelli, T. O. Menteş, A. Sala, L. D. Buda-Prejbeanu, O. Klein *et al.*, *Nat. Nanotechnol.* **11**, 449 (2016).
- [18] S. Seki, X. Yu, S. Ishiwata, and Y. Tokura, *Science* **336**, 198 (2012).
- [19] S. Woo, K. Litzius, B. Krüger, M.-Y. Im, L. Caretta, K. Richter, M. Mann, A. Krone, R. M. Reeve, M. Weigand *et al.*, *Nat. Mater.* **15**, 501 (2016).
- [20] A. Neubauer, C. Pfleiderer, B. Binz, A. Rosch, R. Ritz, P. G. Niklowitz, and P. Böni, *Phys. Rev. Lett.* **102**, 186602 (2009).
- [21] T. Schulz, R. Ritz, A. Bauer, M. Halder, M. Wagner, C. Franz, C. Pfleiderer, K. Everschor, M. Garst, and A. Rosch, *Nat. Phys.* **8**, 301 (2012).
- [22] N. Kanazawa, Y. Onose, T. Arima, D. Okuyama, K. Ohoyama, S. Wakimoto, K. Kakurai, S. Ishiwata, and Y. Tokura, *Phys. Rev. Lett.* **106**, 156603 (2011).
- [23] M. Lee, W. Kang, Y. Onose, Y. Tokura, and N. P. Ong, *Phys. Rev. Lett.* **102**, 186601 (2009).
- [24] Y. Li, N. Kanazawa, X. Z. Yu, A. Tsukazaki, M. Kawasaki, M. Ichikawa, X. F. Jin, F. Kagawa, and Y. Tokura, *Phys. Rev. Lett.* **110**, 117202 (2013).
- [25] P. Bruno, V. K. Dugaev, and M. Taillefumier, *Phys. Rev. Lett.* **93**, 096806 (2004).
- [26] B. Göbel, A. Mook, J. Henk, and I. Mertig, *Phys. Rev. B* **95**, 094413 (2017).
- [27] B. Göbel, A. Mook, J. Henk, and I. Mertig, *New J. Phys.* **19**, 063042 (2017).
- [28] P. B. Ndiaye, C. A. Akosa, and A. Manchon, *Phys. Rev. B* **95**, 064426 (2017).
- [29] K. Hamamoto, M. Ezawa, and N. Nagaosa, *Phys. Rev. B* **92**, 115417 (2015).
- [30] J. Zang, M. Mostovoy, J. H. Han, and N. Nagaosa, *Phys. Rev. Lett.* **107**, 136804 (2011).
- [31] W. Jiang, X. Zhang, G. Yu, W. Zhang, X. Wang, M. B. Jungfleisch, J. E. Pearson, X. Cheng, O. Heinonen, K. L. Wang *et al.*, *Nat. Phys.* **13**, 162 (2017).
- [32] K. Litzius, I. Lemesch, B. Krüger, P. Bassirian, L. Caretta, K. Richter, F. Büttner, K. Sato, O. A. Tretiakov, J. Förster *et al.*, *Nat. Phys.* **13**, 170 (2017).
- [33] J. Barker and O. A. Tretiakov, *Phys. Rev. Lett.* **116**, 147203 (2016).
- [34] X. Zhang, Y. Zhou, and M. Ezawa, *Sci. Rep.* **6**, 24795 (2016).
- [35] H. Fujita and M. Sato, *Phys. Rev. B* **95**, 054421 (2017).
- [36] C. Jin, C. Song, J. Wang, and Q. Liu, *Appl. Phys. Lett.* **109**, 182404 (2016).
- [37] X. Zhang, Y. Zhou, and M. Ezawa, *Nat. Commun.* **7**, 10293 (2016).
- [38] P. M. Buhl, F. Freimuth, S. Blügel, and Y. Mokrousov, *Phys. Status Solidi RRL* **11**, 1700007 (2017).
- [39] S. D. Yi, S. Onoda, N. Nagaosa, and J. H. Han, *Phys. Rev. B* **80**, 054416 (2009).
- [40] A. Leonov and M. Mostovoy, *Nat. Commun.* **6**, 8275 (2015).
- [41] N. Nagaosa, J. Sinova, S. Onoda, A. MacDonald, and N. Ong, *Rev. Mod. Phys.* **82**, 1539 (2010).
- [42] M. Gradhand, D. Fedorov, F. Pientka, P. Zahn, I. Mertig, and B. Györfy, *J. Phys. Condens. Matter* **24**, 213202 (2012).
- [43] Y. Hatsugai, *Phys. Rev. B* **48**, 11851 (1993).
- [44] Y. Hatsugai, *Phys. Rev. Lett.* **71**, 3697 (1993).
- [45] See Supplemental Material at <http://link.aps.org/supplemental/10.1103/PhysRevB.96.060406> for band structures of the SkX and AFM-SkX.
- [46] G. Yin, Y. Liu, Y. Barlas, J. Zang, and R. K. Lake, *Phys. Rev. B* **92**, 024411 (2015).
- [47] J. Henk and W. Schattke, *Comput. Phys. Commun.* **77**, 69 (1993).
- [48] A. Bödicker, W. Schattke, J. Henk, and R. Feder, *J. Phys. Condens. Matter* **6**, 1927 (1994).
- [49] See Supplemental Material at <http://link.aps.org/supplemental/10.1103/PhysRevB.96.060406> for topological (spin) Hall conductivities for the case  $t_1 = t_2 = t/2$ .
- [50] See Supplemental Material at <http://link.aps.org/supplemental/10.1103/PhysRevB.96.060406> for topological Hall conductivities for the case  $t_2^A = -t_2^B$ .
- [51] S. Woo, K. M. Song, X. Zhang, Y. Zhou, M. Ezawa, S. Finizio, J. Raabe, J. W. Choi, B.-C. Min, H. C. Koo *et al.*, [arXiv:1703.10310](https://arxiv.org/abs/1703.10310).
- [52] A. Mook, B. Göbel, J. Henk, and I. Mertig, *Phys. Rev. B* **95**, 020401(R) (2017).



---

## 7 Conclusion and perspectives

In this thesis the stabilization and the emergent electrodynamics of topologically non-trivial spin textures have been investigated. A major part was attributed to magnetic skyrmions. The formation of these small magnetic whirls as well as periodic lattices of skyrmions, stabilized by different mechanisms, has been simulated by means of Monte Carlo, atomistic and micromagnetic simulations. For periodic lattices, the topological Hall effect and the magnetoelectric effect have been analyzed using a Berry theory approach. For individual skyrmions, a Landauer-Büttiker approach was utilized. In both cases a transverse deflection of electrons has been observed. Furthermore, the current-driven motion of skyrmions has been simulated using a micromagnetic approach and analyzed using an effective equation of motion. Another major part of this thesis was concerned with alternative quasiparticles that can be understood as the combination of two subparticles (skyrmions or merons): biskyrmions, bimerons, skyrmioniums and antiferromagnetic skyrmions have been stabilized and their emergent electrodynamic effects have been compared to those of skyrmions.

**Achievements.** In the introduction four goals have been formulated. In the following, the main findings, presented in this thesis, are listed:

1. Established new ways to suppress the skyrmion Hall effect and to accelerate the current-driven motion of skyrmions in racetrack devices
  - A new method to completely suppress the skyrmion Hall effect was proposed and simulated in publication [BG1]. Considering low-symmetric heavy metal materials as the generator of a spin-orbit torque, the injected spin polarization orientation can be manipulated. By suppressing the skyrmion Hall effect, the maximum velocity of skyrmions could be increased by one order of magnitude compared to the conventional racetrack geometry.
2. Gained a profound understanding of the topological Hall effect that goes beyond relating the measured signal with the skyrmion density
  - In agreement with Ref. [131] it was established that the Berry theory can be utilized to quantify the topological Hall effect of electrons in skyrmion crystals (by analogy with the description of the quantized Hall effect). As a new result, in publication [BG2] it was presented that the topological Hall effect strongly depends on the details of the band structure. In particular, the transverse conductivity can change its sign.
  - In the non-adiabatic limit, the emerging current is not fully spin polarized anymore. This leads to a decoupled occurrence of a topological (charge) Hall effect and a topological spin Hall effect (presented in the not explicitly included publication [BG9]).
3. Established new hallmarks of magnetic skyrmions accessible in experiments
  - The discussion of the orbital magnetization in skyrmion crystals in Ref. [112] was generalized in publication [BG3] and its energy dependence was investigated. This quantity can be used to detect skyrmions and to distinguish them from antiskyrmions by their topological charge.

- 
- A geometrically induced magnetoelectric effect in skyrmion crystals was predicted in publication [BG3]. This quantity can be utilized to detect skyrmions and to determine the skyrmions' helicity. For metallic skyrmion hosts, an intrinsic version of the Edelstein effect was proposed.
4. Predicted alternative non-collinear spin textures and compared their emergent electrodynamic effects to those of skyrmions
- Individual magnetic biskyrmions have been stabilized in centrosymmetric materials in publication [BG4]. These objects can be understood as two partially overlapping skyrmions with reversed in-plane magnetizations. The dipole-dipole interaction has been found to be the stabilizing mechanism.
  - The prediction of magnetic bimerons ('in-plane rotated' skyrmions) [140] has been generalized in publication [BG5]. As new states of matter, individual bimerons have been predicted and a stabilizing DMI has been proposed. Furthermore, a purely topological Hall effect as well as the possibility to consider new geometries to drive these magnetic quasiparticles by spin torques have been predicted.
  - For the magnetic skyrmionium (a skyrmion within another skyrmion with mutually reversed spins) a racetrack storage device has been fully simulated in publication [BG6], including the creation, deletion, motion and detection processes of the bits. As new findings, a locally occurring topological Hall effect and an optoelectrical writing mechanism have been predicted.
  - As a new state of matter, the antiferromagnetic skyrmion crystal has been predicted in publication [BG7]. It consists of two conventional skyrmion crystals with mutually reversed spins existing on two separate sublattices. In agreement with Ref. [150], the topological version of a pure spin Hall effect has been established as the hallmark of this state of matter.

**Techniques.** Summarizing the results of this PhD thesis, several new topologically non-trivial spin textures and emergent electrodynamic effects have been predicted and a deeper understanding of existing phenomena has been established. In the process I have on one hand considered analytical models (e. g. the Thiele equation) and on the other hand used and developed computer codes for the simulations. Less demanding calculations have been conducted using Wolfram's Mathematica. For the more demanding calculations I have adapted the Monte Carlo code (*fortran90*) of our group [74] to the considered systems and implemented the computation of Hall conductivity, spin Hall conductivity, orbital magnetization and magnetoelectric polarizability in the tight-binding code (*fortran90*) of the group [116]. For the Landauer-Büttiker simulations I used the open-source code Kwant [145] (*python*) and for the micromagnetic simulations I used and modified the GPU-accelerated environment mumax3 [43, 44] (nvidia's language *cuda* and google's language *go*).

**Outlook.** In the publication section 6 several skyrmion-related magnetic quasiparticles have been introduced. For future projects it seems promising to investigate more alternative spin textures and to systematically characterize them. Antiskyrmions [41] and higher-order skyrmions [32, 152] for example are not rotational symmetric. This may

---

lead to an anisotropic current-driven motion. Also, more complicated combinations of two skyrmions like ferrimagnetic skyrmions [51,153], antiferromagnetic skyrmioniums [154,155], and antiferromagnetic bimerons [156] have been discussed in the literature and are worth a further investigation. Up to now, the main focus of research was attributed to quasi two-dimensional spin textures but non-trivial continuations of skyrmions like chiral bobbars [157,158], hopfions [159,160] or three-dimensional monopole crystals [161,162] govern interesting electrodynamic effects as well.

Furthermore, we have recently shown in an experimental collaboration [BG13] that typical antiskyrmion hosts can stabilize also skyrmions by dipole-dipole interactions. This finding suggests spintronic devices based on switching between these topologically distinct objects.

Concerning an imminent technological realization of a racetrack storage device, it is perhaps most convenient to rely on conventional skyrmions since they are best understood experimentally. As explained, the Thiele equation allows to understand different possibilities to suppress the skyrmion Hall effect for these particles. The last possibility which remains to be investigated is to manipulate the confining potential of the racetrack. Here, different predictions exist, like the addition of a high-anisotropy material at the racetrack's edges [163] or by utilizing repulsive or attractive defect atoms [164]. In this way, the skyrmion Hall effect is not suppressed but its disadvantage on the applicability is diminished; room for improvement is still available. A combination of the different proposed concepts to suppress the skyrmion Hall effect may be the expedient solution in the end, which eventually allows to realize an operating skyrmion racetrack storage device in the real world. The discovery of skyrmioniums [144] and, very recently, also antiferromagnetic skyrmions in synthetic antiferromagnets [151] motivates to pursue this avenue as well, exploiting the favorable emergent electrodynamics of these objects.

In terms of driving non-collinear spin textures, one is not limited to applying electric currents or spin currents. It has for example been shown that skyrmions can be driven by a temperature gradient [165], by an anisotropy gradient [166], or by spin waves [58]. In publication [BG11] we have established the opposite effect: the topological version of a magnon Hall effect. Just like for electrons in a skyrmion crystal, also magnons experience a transverse deflection due to the non-trivial real-space topology of skyrmions. In fact, there exists an analogy between electrons and magnons, as we have shown in publication [BG12], which allows to understand the emergence of this effect quite elegantly. A further investigation of magnon-mediated effects in non-collinear spin textures seems to be worthwhile in the future. Another aspect is to take also the lattice degree of freedom into account and to investigate how phonons affect the presented emergent electrodynamics.

Lastly, it is worth mentioning, that the introduced mathematical concepts for computing the Hall effect, magnetoelectric effect and orbital magnetization are not limited to systems with non-collinear spin textures. The presented approach is applicable even for non-magnetic systems: In the experimental collaboration [BG10] we have calculated the extrinsic Edelstein effect (which is formulated by analogy with the magnetoelectric effect in metals) for the two-dimensional electron gas at the interface of SrTiO<sub>3</sub> and AlO<sub>x</sub> after fitting a tight-binding model to the band structure determined by ARPES measurements. This mapping allowed to explain the origin of a measured enormous spin to charge conversion efficiency – highly relevant for future spintronic devices.

---

## List of publications

- [BG1] **B. Göbel**, A. Mook, J. Henk, I. Mertig  
Overcoming the speed limit in skyrmion racetrack devices by suppressing the skyrmion Hall effect.  
*Phys. Rev. B* **99**, 020405(R) (2019).
- [BG2] **B. Göbel**, A. Mook, J. Henk, I. Mertig  
Unconventional topological Hall effect in skyrmion crystals caused by the topology of the lattice.  
*Phys. Rev. B* **95**, 094413 (2017).
- [BG3] **B. Göbel**, A. Mook, J. Henk, I. Mertig  
Magnetoelectric effect and orbital magnetization in skyrmion crystals: Detection and characterization of skyrmions.  
*Phys. Rev. B* **99**, 060406(R) (2019).
- [BG4] **B. Göbel**, J. Henk, I. Mertig  
Forming magnetic biskyrmions by merging two skyrmions in a centrosymmetric nanodisk.  
*Sci. Reports* **9**, 9521 (2019).
- [BG5] **B. Göbel**, A. Mook, J. Henk, I. Mertig, O. A. Tretiakov  
Magnetic bimerons as skyrmion analogues in in-plane magnets.  
*Phys. Rev. B* **99**, 060407(R) (2019).
- [BG6] **B. Göbel\***, A. F. Schäffer\*, J. Berakdar, I. Mertig, S. S. P. Parkin  
Electrical writing, reading, and moving of magnetic skyrmioniums in a racetrack device.  
*Sci. Reports* **9**, 12119 (2019).
- [BG7] **B. Göbel**, A. Mook, J. Henk, I. Mertig  
Antiferromagnetic skyrmion crystals: Generation, topological Hall, and topological spin Hall effect.  
*Phys. Rev. B* **96**, 060406(R) (2017).
- [BG8] **B. Göbel**, A. Mook, J. Henk, I. Mertig  
Signatures of lattice geometry in quantum and topological Hall effect.  
*New J. Phys.* **19**, 063042 (2017).
- [BG9] **B. Göbel**, A. Mook, J. Henk, I. Mertig  
The family of topological Hall effects for electrons in skyrmion crystals.  
*Euro. Phys. J. B* **91**, 179 (2018).
- [BG10] D. C. Vaz\*, P. Noël\*, A. Johansson\*, **B. Göbel\***, F. Bruno, G. Singh, S. McKeown-Walker, F. Trier, A. Sander, P. Bruneel, M. Vivek, M. Gabay, N. Bergeal, F. Baumberger, H. Okuno, A. Barthélémy, A. Fert, L. Vila, I. Mertig, J.-P. Attané, M. Bibes  
Mapping spin-charge conversion to the band structure in a topological oxide two-dimensional electron gas.  
*Nature Materials* (published online 09.09.2019).

- 
- [BG11] A. Mook, **B. Göbel**, J. Henk, I. Mertig  
Magnon transport in noncollinear spin textures: Anisotropies and topological magnon Hall effects.  
*Phys. Rev. B* **95**, 020401(R) (2017).
- [BG12] A. Mook, **B. Göbel**, J. Henk, I. Mertig  
Taking an electron-magnon duality shortcut from electron to magnon transport.  
*Phys. Rev. B* **97**, 140401(R) (2018).

### Submitted manuscripts

- [BG13] J. Jena\*, **B. Göbel**\*, T. Ma, V. Kumar, R. Saha, I. Mertig, C. Felser, S. S. P. Parkin  
Discovery of elliptical-skyrmion chiral twins in an anti-skyrmion system.
- [BG14] **B. Göbel**, A. Mook, J. Henk, I. Mertig  
Compensated Quantum and Topological Hall Effects of Electrons in Polyatomic Stripe Lattices.

\* These authors contributed equally.

### Copyright

Publication [BG1]: Reprinted (whole article) with permission from (B. Göbel *et al.* Physical Review B **99**, 020405(R) (2019); Overcoming the speed limit in skyrmion racetrack devices by suppressing the skyrmion Hall effect. Copyright (2019) by the American Physical Society.

Publication [BG2]: Reprinted (whole article) with permission from (B. Göbel *et al.* Physical Review B **95**, 094413 (2017); Unconventional topological Hall effect in skyrmion crystals caused by the topology of the lattice. Copyright (2017) by the American Physical Society.

Publication [BG3]: Reprinted (whole article) with permission from (B. Göbel *et al.* Physical Review B **99**, 060407(R) (2019); Magnetic bimerons as skyrmion analogues in in-plane magnets. Copyright (2019) by the American Physical Society.

Publication [BG4]: Published under the terms of the Creative Commons CC BY 4.0 license.

Publication [BG5]: Reprinted (whole article) with permission from (B. Göbel *et al.* Physical Review B **99**, 060407(R) (2019); Magnetic bimerons as skyrmion analogues in in-plane magnets. Copyright (2019) by the American Physical Society.

Publication [BG6]: Published under the terms of the Creative Commons CC BY 4.0 license.

Publication [BG7]: Reprinted (whole article) with permission from (B. Göbel *et al.* Physical Review B **96**, 060406(R) (2017); Antiferromagnetic skyrmion crystals: Generation, topological Hall, and topological spin Hall effect. Copyright (2017) by the American Physical Society.

---

## Appendix

### A Derivation of the Hall conductivity by the Boltzmann equation

The following derivation is oriented at Refs. [74, 167, 168].

All physical systems in the following are two-dimensional, which is why the following derivation of the Hall conductivity considers the charge current density in two dimensions

$$\mathbf{j} = \frac{q}{(2\pi)^2} \sum_n \int_{\text{BZ}} \mathbf{r} f \, d^2k.$$

The distribution function  $f$  is decomposed into the local equilibrium function  $f^0(\mathbf{r}, \mathbf{k}, t)$  and its deviation in linear response  $\delta f(\mathbf{r}, \mathbf{k}, t)$

$$f = f^0 + \delta f.$$

Also, the definition of the group velocity  $\mathbf{v} = \hbar^{-1} \frac{\partial E_n(\mathbf{k})}{\partial \mathbf{k}}$  and  $\dot{\mathbf{k}} = q/\hbar \mathbf{E}$  under  $\mathbf{B} = 0$  are used to arrive at

$$\mathbf{j} = \frac{q}{(2\pi)^2} \sum_n \int_{\text{BZ}} \left( \mathbf{v} - \frac{q}{\hbar} \mathbf{E} \times \boldsymbol{\Omega}_n(\mathbf{k}) \right) (f^0 + \delta f) \, d^2k.$$

Now it is assumed that  $\delta f$  is proportional to the electron scattering with other particles, quasiparticles or impurities (called collision integral)

$$\delta f(\mathbf{r}, \mathbf{k}, t) = -\tau(\mathbf{k}) \left. \frac{\partial f(\mathbf{r}, \mathbf{k}, t)}{\partial t} \right|_{\text{collision}}.$$

The proportionality factor is the relaxation time  $\tau(\mathbf{k})$ . The collision integral is estimated by the Boltzmann equation [168] for a stationary and homogeneous distribution function

$$\left. \frac{\partial f(\mathbf{r}, \mathbf{k}, t)}{\partial t} \right|_{\text{collision}} = \dot{\mathbf{k}} \cdot \frac{\partial f(\mathbf{k})}{\partial \mathbf{k}}.$$

Combining the two above equations and using  $\dot{\mathbf{k}} = q/\hbar \mathbf{E}$  under  $\mathbf{B} = 0$  [cf. Eq. (4.24)] gives

$$\delta f = -q\tau \frac{\mathbf{E}}{\hbar} \cdot \frac{\partial f(\mathbf{k})}{\partial \mathbf{k}}.$$

The derivative of the distribution function can be expressed as an energy derivative

$$\frac{\partial f(\mathbf{k})}{\partial \mathbf{k}} = \frac{\partial E_n(\mathbf{k})}{\partial \mathbf{k}} \frac{\partial f}{\partial E} = \hbar \mathbf{v} \frac{\partial f}{\partial E}.$$

In linear response theory, the derivative of the equilibrium distribution function  $f^0$  is

---

used instead of the actual equilibrium distribution function. This simplifies the current density to

$$\mathbf{j} = \frac{1}{(2\pi)^2} \sum_n \int_{\text{BZ}} \left( \mathbf{v} - \frac{q}{\hbar} \mathbf{E} \times \boldsymbol{\Omega}_n(\mathbf{k}) \right) \left( f^0 - q\tau \mathbf{E} \cdot \mathbf{v} \frac{\partial f(\mathbf{k})}{\partial E} \right) d^2k.$$

For small fields the term proportional  $E^2$  can be dropped; the integral over  $v f^0$  gives zero, leading to

$$\mathbf{j} = -\frac{1}{(2\pi)^2} \sum_n \int_{\text{BZ}} \left[ \mathbf{v} \left( q\tau \mathbf{E} \cdot \mathbf{v} \frac{\partial f(\mathbf{k})}{\partial E} \right) + \frac{q}{\hbar} \mathbf{E} \times \boldsymbol{\Omega}_n(\mathbf{k}) f^0 \right] d^2k.$$

Considering the currents applied along  $x$  with  $\boldsymbol{\Omega}_n(\mathbf{k}) = \Omega_n^z(\mathbf{k}) \mathbf{e}_z$  gives

$$j_x = -\frac{1}{(2\pi)^2} \sum_n \int_{\text{BZ}} \left[ v_x \left( q\tau E \cdot \mathbf{v} \frac{\partial f(\mathbf{k})}{\partial E} \right) + \frac{q}{\hbar} E_y \Omega_n^z(\mathbf{k}) f^0 \right] d^2k.$$

Note, that due to periodicity of the Brillouin zone  $\int_{\text{BZ}} v_x v_y d k_x d k_y = 0$ . Therefore, the longitudinal and transverse conductivity can be identified as

$$\begin{aligned} \sigma_{xx} &= -e^2 \frac{1}{2\pi} \sum_n \int_{\text{BZ}} v_{n,x}(\mathbf{k})^2 \tau_n(\mathbf{k}) \frac{\partial f^0}{\partial E} \Big|_{E=E_n(\mathbf{k})} d^2k, \\ \sigma_{xy} &= -\frac{e^2}{\hbar} \frac{1}{2\pi} \sum_n \int_{\text{BZ}} \Omega_n^z(\mathbf{k}) f^0 (E_n(\mathbf{k}) - E_F) d^2k. \end{aligned}$$

---

## B Appendix: Landauer-Büttiker formalism

The Landauer-Büttiker formalism is an alternative method for calculating the electronic transport properties. Instead of considering a perfectly periodic bulk system for which statements about the edges of the sample can only be made indirectly via the topological invariants, the Landauer-Büttiker approach considers a finite sample directly. For this reason, it allows to determine local properties, e. g., a charge or spin accumulation or the propagation of edge states in real space. It can therefore be used to simulate the local detection of non-collinear spin textures at a certain position in a racetrack as has been shown in publication [BG6]. Furthermore, it allows to calculate also longitudinal transport properties.

In the following, the approach is introduced on a level that allows to use and understand the software package Kwant [145], which has been used in publication [BG6]. This python-based package undertakes the calculation of the transition matrix, which is the numerically most demanding part. The derivation follows Refs. [126, 169, 170].

The general idea of the Landauer-Büttiker approach is to consider a finite sample and to attach semi-infinite terminals (index  $i$ ) to model flowing currents  $I_i$  and accumulated charges or voltages  $U_i$ . For a system with multiple terminals, a set of linear equations has to be solved

$$I_m = \frac{e^2}{h} \sum_n T_{mn} U_n.$$

The calculation of the transition matrix  $T$  is the most demanding part as it depends on the tight-binding Hamiltonian  $H$ , the energy  $E$  and the self energies of the leads  $\Sigma_i$ . It is calculated from the retarded Green's function  $G$ ; a short excursion is appropriate.

In a single-particle picture, the Green's function  $\hat{G}$  is defined as the solution of

$$[E - \hat{H}(\mathbf{r})]\hat{G}(\mathbf{r}, \mathbf{r}', E) = \delta(\mathbf{r} - \mathbf{r}'),$$

written here in position space;  $\hat{H}$  is the Hamiltonian of the full system. Simply inverting  $(E - \hat{H})$  is not well defined when the energy is equal to an eigenenergy of the system. For this reason, a small imaginary energy is added, giving the retarded Green's function

$$G(\mathbf{r}, \mathbf{r}', E) = \lim_{\delta \rightarrow 0^+} \hat{G}(\mathbf{r}, \mathbf{r}', E + i\delta),$$

satisfying

$$[E + i\delta - \hat{H}(\mathbf{r})]G(\mathbf{r}, \mathbf{r}', E) = \delta(\mathbf{r} - \mathbf{r}').$$

The general solution for the retarded Green's is therefore

$$G = \lim_{\delta \rightarrow 0^+} (E + i\delta - \hat{H})^{-1}.$$

This expression is still inconvenient for a calculation in the present system: one contribution to the full Hamiltonian  $\hat{H}$  of the system is the Hamiltonian of the semi-infinite leads. Since it has an infinite rank, it cannot be inverted straightforwardly. The trick is



---

to condense the properties of the leads in self energies. Then, the full Hamiltonian

$$\hat{H} = H + \sum_i (H_{\text{lead}}^i + V_i + V_i^\dagger),$$

given by the Hamiltonian of the finite sample  $H$ , the Hamiltonian of the lead  $H_{\text{lead}}^i$  and their interaction potential  $V_i$ , becomes

$$\hat{H} = H + \sum_i \Sigma_i.$$

The self energy of lead  $i$  is given by

$$\Sigma_i = V_i(E + i\delta - H_{\text{lead}}^i)^{-1}V_i^\dagger.$$

This quantity can be calculated for nearest-neighbor hoppings since now only the interface elements of  $V_i$  are non-zero.

Following from this consideration, the retarded Green's function of the considered system reads

$$G = \left( E - H - \sum_i \Sigma_i \right)^{-1}$$

and the transition matrix is calculated as

$$T_{mn} = \text{Tr}(\Gamma_m G_{mn} \Gamma_n G_{mn}^\dagger),$$

with  $\Gamma_i = i(\Sigma_i - \Sigma_i^\dagger)$ . Another self energy  $\Gamma_{\text{inelast}} = -i\eta$  can be considered to model inelastic scattering (electrons interacting with other electrons or phonons).

Depending on the considered measurement setup, some of the voltages  $U_n$  and currents  $I_n$  are fixed. In order to quantify a Hall effect, one can consider a crossbar geometry with the terminals attached at the up (u), down (d), left (l), and right (r) directions. One considers a current which flows from left to right ( $I_l = -I_r \equiv I$  and  $I_u = I_d = 0$ ) and is interested in the charge accumulation in the transverse directions (up and down). A small potential gradient is simulated  $U_l - U_r = \Delta U$ .

The resistivity is given as

$$R_{xy} = (U_u - U_d)/I, \quad R_{xx} = (U_l - U_r)/I,$$

from where the conductance  $\underline{G} = \underline{R}^{-1}$  can be calculated

$$G_{xy} = -R_{xy}/(R_{xx}^2 + R_{xy}^2), \quad G_{xx} = R_{xx}/(R_{xx}^2 + R_{xy}^2).$$

Since the Landauer-Büttiker formalism does also account for extrinsic contributions, the longitudinal conductance is well defined. This allows to calculate a Hall angle

$$\theta_H = \frac{U_u - U_d}{U_l - U_r}.$$

---

## Local detection of skyrmions

Since the topological Hall effect of electrons is the hallmark of the skyrmion crystal phase, the idea arose to utilize this effect for a local detection of individual skyrmions, for example in a racetrack device [170]. For this example, I generalize the results of that paper to detect a sequence of skyrmionic bits.

By analogy with Ref. [170] I considered  $s$  electrons on a lattice (here a square lattice) without taking spin-orbit coupling into account. Especially for Fermi energies near the band bottom of the zero-field band structure (here the carriers behave similar to free electrons) an unambiguous detection is possible, as shown in Fig. 30. A significant peak arises whenever a skyrmion traverses the area between the two leads. This peak is in good approximation proportional to the topological charge density integrated over this area. When no skyrmion is present, only oscillations around zero occur. The experimental realization of such a measurement has recently been reported in Ref. [14], as presented in the experimental overview (Fig. 13 in Sec. 2.4).

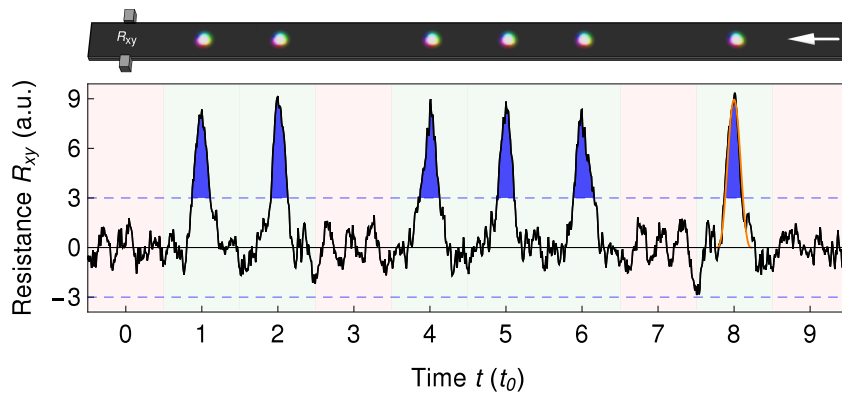


Figure 30: **Simulated detection of a sequence of skyrmions in a racetrack geometry.** A peak appears in the transverse resistance (proportional to the detected voltage) whenever a skyrmion is located between the two thin contacts.  $t_0$  is the time constant of the racetrack. The parameters are like in publication [BG6].

---

**References**

- [1] Moore, G. E. *et al.* Cramming more components onto integrated circuits. *Electronics* **38**, 8 (1965).
- [2] Waldrop, M. M. The chips are down for Moore's law. *Nat. News* **530**, 144 (2016).
- [3] Parkin, S. S. Shiftable magnetic shift register and method of using the same (2004). US Patent 6,834,005.
- [4] Parkin, S. S., Hayashi, M. & Thomas, L. Magnetic domain-wall racetrack memory. *Science* **320**, 190–194 (2008).
- [5] Sampaio, J., Cros, V., Rohart, S., Thiaville, A. & Fert, A. Nucleation, stability and current-induced motion of isolated magnetic skyrmions in nanostructures. *Nat. Nanotechnol.* **8**, 839 (2013).
- [6] Nagaosa, N. & Tokura, Y. Topological properties and dynamics of magnetic skyrmions. *Nat. Nanotechnol.* **8**, 899 (2013).
- [7] Jonietz, F. *et al.* Spin transfer torques in MnSi at ultralow current densities. *Science* **330**, 1648 (2010).
- [8] Mühlbauer, S. *et al.* Skyrmion lattice in a chiral magnet. *Science* **323**, 915 (2009).
- [9] Yu, X. *et al.* Real-space observation of a two-dimensional skyrmion crystal. *Nature* **465**, 901 (2010).
- [10] Heinze, S. *et al.* Spontaneous atomic-scale magnetic skyrmion lattice in two dimensions. *Nat. Phys.* **7**, 713 (2011).
- [11] Dzyaloshinsky, I. A thermodynamic theory of "weak" ferromagnetism of antiferromagnetics. *J. Phys. Chem. Solids* **4**, 241 (1958).
- [12] Moriya, T. Anisotropic superexchange interaction and weak ferromagnetism. *Phys. Rev.* **120**, 91 (1960).
- [13] Romming, N. *et al.* Writing and deleting single magnetic skyrmions. *Science* **341**, 636 (2013).
- [14] Maccariello, D. *et al.* Electrical detection of single magnetic skyrmions in metallic multilayers at room temperature. *Nat. Nanotechnol.* **13**, 233 (2018).
- [15] Jiang, W. *et al.* Direct observation of the skyrmion Hall effect. *Nat. Phys.* **13**, 162 (2017).
- [16] Litzius, K. *et al.* Skyrmion Hall effect revealed by direct time-resolved X-ray microscopy. *Nat. Phys.* **13**, 170 (2017).
- [17] Skyrme, T. H. R. A non-linear field theory. *Proc. Royal Soc. Lond. A: Math. Phys. Eng. Sci.* **260**, 127 (1961).
- [18] Skyrme, T. H. R. A unified field theory of mesons and baryons. *Nucl. Phys.* **31**, 556 (1962).

- 
- [19] Bessarab, P. F. *et al.* Lifetime of racetrack skyrmions. *Sci. Reports* **8**, 3433 (2018).
- [20] Malozemoff, A. & Slonczewski, J. *Magnetic Domain Walls in Bubble Materials* (Academic press, 1979).
- [21] Eschenfelder, A. H. *Magnetic bubble technology* (Springer-Verlag Berlin Heidelberg New York, 1980).
- [22] Bobeck, A. H., Gianola, U. F., Sherwood, R. C. & Shockley, W. Magnetic domain propagation circuit (1969). US Patent 3,460,116.
- [23] Michaelis, P. & Richards, W. Magnetic bubble mass memory. *IEEE Transactions on Magn.* **11**, 21 (1975).
- [24] Fert, A., Cros, V. & Sampaio, J. Skyrmions on the track. *Nat. Nanotechnol.* **8**, 152 (2013).
- [25] Bogdanov, A. & Yablonskii, D. Thermodynamically stable vortices in magnetically ordered crystals. The mixed state of magnets. *Zh. Eksp. Teor. Fiz* **95**, 182 (1989).
- [26] Bogdanov, A. & Hubert, A. Thermodynamically stable magnetic vortex states in magnetic crystals. *J. Magn. Magn. Mater.* **138**, 255 (1994).
- [27] Bogdanov, A. & Rößler, U. Chiral symmetry breaking in magnetic thin films and multilayers. *Phys. Rev. Lett.* **87**, 037203 (2001).
- [28] Sondhi, S., Karlhede, A., Kivelson, S. & Rezayi, E. Skyrmions and the crossover from the integer to fractional quantum Hall effect at small Zeeman energies. *Phys. Rev. B* **47**, 16419 (1993).
- [29] Al Khawaja, U. & Stoof, H. Skyrmions in a ferromagnetic Bose–Einstein condensate. *Nature* **411**, 918 (2001).
- [30] Fukuda, J. & Žumer, S. Quasi-two-dimensional Skyrmion lattices in a chiral nematic liquid crystal. *Nat. Commun.* **2**, 246 (2011).
- [31] Adkins, G. S., Nappi, C. R. & Witten, E. Static properties of nucleons in the Skyrme model. *Nucl. Phys. B* **228**, 552 (1983).
- [32] Rózsa, L. *et al.* Formation and stability of metastable skyrmionic spin structures with various topologies in an ultrathin film. *Phys. Rev. B* **95**, 094423 (2017).
- [33] Spaldin, N. A., Fiebig, M. & Mostovoy, M. The toroidal moment in condensed-matter physics and its relation to the magnetoelectric effect. *J. Physics: Condens. Matter* **20**, 434203 (2008).
- [34] Mook, A. *Der Magnon-Hall-Effekt*. Thesis, Martin-Luther-Universität Halle-Wittenberg (2013).
- [35] Nolting, W. & Ramakanth, A. *Quantum theory of magnetism* (Springer Science & Business Media, 2009).

- 
- [36] Okubo, T., Chung, S. & Kawamura, H. Multiple-q states and the skyrmion lattice of the triangular-lattice Heisenberg antiferromagnet under magnetic fields. *Phys. Rev. Lett.* **108**, 017206 (2012).
- [37] Leonov, A. & Mostovoy, M. Multiply periodic states and isolated skyrmions in an anisotropic frustrated magnet. *Nat. Commun.* **6**, 8275 (2015).
- [38] Yosida, K. *Theory of magnetism: Edition en anglais*, vol. 122 (Springer Science & Business Media, 1996).
- [39] Fert, A. & Levy, P. M. Role of anisotropic exchange interactions in determining the properties of spin-glasses. *Phys. Rev. Lett.* **44**, 1538 (1980).
- [40] Thiaville, A., Rohart, S., Jué, É., Cros, V. & Fert, A. Dynamics of Dzyaloshinskii domain walls in ultrathin magnetic films. *EPL (Europhysics Lett.)* **100**, 57002 (2012).
- [41] Nayak, A. K. *et al.* Magnetic antiskyrmions above room temperature in tetragonal Heusler materials. *Nature* **548**, 561 (2017).
- [42] Hoffmann, M. *et al.* Antiskyrmions stabilized at interfaces by anisotropic Dzyaloshinskii-Moriya interactions. *Nat. Commun.* **8**, 308 (2017).
- [43] Vansteenkiste, A. & Van de Wiele, B. Mumax: a new high-performance micro-magnetic simulation tool. *J. Magn. Magn. Mater.* **323**, 2585 (2011).
- [44] Vansteenkiste, A. *et al.* The design and verification of MuMax3. *AIP Adv.* **4**, 107133 (2014).
- [45] Derrick, G. Comments on nonlinear wave equations as models for elementary particles. *J. Math. Phys.* **5**, 1252 (1964).
- [46] Aharoni, A. *et al.* *Introduction to the Theory of Ferromagnetism*, vol. 109 (Clarendon Press, 2000).
- [47] Moreau-Luchaire, C. *et al.* Additive interfacial chiral interaction in multilayers for stabilization of small individual skyrmions at room temperature. *Nat. Nanotechnol.* **11**, 444 (2016).
- [48] Woo, S. *et al.* Observation of room-temperature magnetic skyrmions and their current-driven dynamics in ultrathin metallic ferromagnets. *Nat. Mater.* **15**, 501 (2016).
- [49] Boulle, O. *et al.* Room-temperature chiral magnetic skyrmions in ultrathin magnetic nanostructures. *Nat. Nanotechnol.* **11**, 449 (2016).
- [50] Soumyanarayanan, A. *et al.* Tunable room-temperature magnetic skyrmions in Ir/Fe/Co/Pt multilayers. *Nat. Mater.* **16**, 898 (2017).
- [51] Woo, S. *et al.* Current-driven dynamics and inhibition of the skyrmion Hall effect of ferrimagnetic skyrmions in GdFeCo films. *Nat. Commun.* **9**, 959 (2018).
- [52] Seki, S., Yu, X., Ishiwata, S. & Tokura, Y. Observation of skyrmions in a multiferroic material. *Science* **336**, 198 (2012).
-

- 
- [53] Nahas, Y. *et al.* Discovery of stable skyrmionic state in ferroelectric nanocomposites. *Nat. Commun.* **6**, 8542 (2015).
- [54] Legrand, W. *et al.* Hybrid chiral domain walls and skyrmions in magnetic multilayers. *Sci. Adv.* **4**, eaat0415 (2018).
- [55] Zhang, X., Ezawa, M. & Zhou, Y. Magnetic skyrmion logic gates: conversion, duplication and merging of skyrmions. *Sci. Reports* **5**, 9400 (2015).
- [56] Zhang, X., Zhou, Y., Ezawa, M., Zhao, G. & Zhao, W. Magnetic skyrmion transistor: skyrmion motion in a voltage-gated nanotrack. *Sci. Reports* **5**, 11369 (2015).
- [57] Wang, W., Beg, M., Zhang, B., Kuch, W. & Fangohr, H. Driving magnetic skyrmions with microwave fields. *Phys. Rev. B* **92**, 020403 (2015).
- [58] Zhang, X. *et al.* All-magnetic control of skyrmions in nanowires by a spin wave. *Nanotechnology* **26**, 225701 (2015).
- [59] Dürrenfeld, P., Xu, Y., Åkerman, J. & Zhou, Y. Controlled skyrmion nucleation in extended magnetic layers using a nanocontact geometry. *Phys. Rev. B* **96**, 054430 (2017).
- [60] Flovik, V., Qaiumzadeh, A., Nandy, A. K., Heo, C. & Rasing, T. Generation of single skyrmions by picosecond magnetic field pulses. *Phys. Rev. B* **96**, 140411 (2017).
- [61] Zhang, S. *et al.* Direct writing of room temperature and zero field skyrmion lattices by a scanning local magnetic field. *Appl. Phys. Lett.* **112**, 132405 (2018).
- [62] Hsu, P.-J. *et al.* Electric-field-driven switching of individual magnetic skyrmions. *Nat. Nanotechnol.* **12**, 123 (2017).
- [63] Finazzi, M. *et al.* Laser-induced magnetic nanostructures with tunable topological properties. *Phys. Rev. Lett.* **110**, 177205 (2013).
- [64] Schäffer, A. F., Dürr, H. A. & Berakdar, J. Ultrafast imprinting of topologically protected magnetic textures via pulsed electrons. *Appl. Phys. Lett.* **111**, 032403 (2017).
- [65] Jiang, W. *et al.* Blowing magnetic skyrmion bubbles. *Science* **349**, 283 (2015).
- [66] Lin, S.-Z. Edge instability in a chiral stripe domain under an electric current and skyrmion generation. *Phys. Rev. B* **94**, 020402 (2016).
- [67] Iwasaki, J., Mochizuki, M. & Nagaosa, N. Current-induced skyrmion dynamics in constricted geometries. *Nat. Nanotechnol.* **8**, 742 (2013).
- [68] Jiang, W. *et al.* Skyrmions in magnetic multilayers. *Phys. Reports* **704**, 1 (2017).
- [69] Everschor-Sitte, K., Masell, J., Reeve, R. & Kläui, M. Perspective: Magnetic skyrmions – Overview of recent progress in an active research field. *J. Appl. Phys.* **124**, 240901 (2018).
-

- 
- [70] Schulz, T. *et al.* Emergent electrodynamics of skyrmions in a chiral magnet. *Nat. Phys.* **8**, 301 (2012).
- [71] Li, Y. *et al.* Robust formation of skyrmions and topological Hall effect anomaly in epitaxial thin films of MnSi. *Phys. Rev. Lett.* **110**, 117202 (2013).
- [72] Landau, D. P. & Binder, K. *A guide to Monte Carlo simulations in statistical physics* (Cambridge university press, 2014).
- [73] Metropolis, N., Rosenbluth, A. W., Rosenbluth, M. N., Teller, A. H. & Teller, E. Equation of state calculations by fast computing machines. *The J. Chem. Phys.* **21**, 1087 (1953).
- [74] Mook, A. *Topological magnon materials and transverse magnon transport*. Thesis, Martin-Luther-Universität Halle-Wittenberg (2017).
- [75] Göbel, B. *Topologische Eigenschaften von Skyrmionen*. Thesis, Martin-Luther-Universität Halle-Wittenberg (2016).
- [76] Landau, L. D. & Lifshitz, E. On the theory of the dispersion of magnetic permeability in ferromagnetic bodies. *Phys. Z. Sowjetunion* **8**, 101 (1935).
- [77] Gilbert, T. A Lagrangian formulation of the gyromagnetic equation of the magnetization field. *Phys. Rev.* **100**, 1243 (1955).
- [78] Slonczewski, J. C. Current-driven excitation of magnetic multilayers. *J. Magn. Magn. Mater.* **159**, L1 (1996).
- [79] Gerhardt, T. *Micromagnetic simulations of ferromagnetic domain walls in nanowires*. Thesis, Universität Hamburg (2015).
- [80] Zhang, S., Levy, P. & Fert, A. Mechanisms of spin-polarized current-driven magnetization switching. *Phys. Rev. Lett.* **88**, 236601 (2002).
- [81] Khvalkovskiy, A. *et al.* Matching domain-wall configuration and spin-orbit torques for efficient domain-wall motion. *Phys. Rev. B* **87**, 020402 (2013).
- [82] Dyakonov, M. & Perel, V. Possibility of orienting electron spins with current. *Sov. J. Exp. Theor. Phys. Lett.* **13**, 467 (1971).
- [83] Dyakonov, M. & Perel, V. Current-induced spin orientation of electrons in semiconductors. *Phys. Lett. A* **35**, 459 (1971).
- [84] Kato, Y. K., Myers, R. C., Gossard, A. C. & Awschalom, D. D. Observation of the spin Hall effect in semiconductors. *Science* **306**, 1910–1913 (2004).
- [85] Zhang, S. & Li, Z. Roles of nonequilibrium conduction electrons on the magnetization dynamics of ferromagnets. *Phys. Rev. Lett.* **93**, 127204 (2004).
- [86] Thiele, A. Steady-state motion of magnetic domains. *Phys. Rev. Lett.* **30**, 230 (1973).
- [87] Simon, E., Rózsa, L., Palotás, K. & Szunyogh, L. Magnetism of a Co monolayer on Pt (111) capped by overlayers of 5 d elements: A spin-model study. *Phys. Rev. B* **97**, 134405 (2018).
-

- 
- [88] Tao, X. *et al.* Self-consistent determination of spin Hall angle and spin diffusion length in Pt and Pd: The role of the interface spin loss. *Sci. Adv.* **4**, eaat1670 (2018).
- [89] Berry, M. V. Quantal phase factors accompanying adiabatic changes. *Proc. Royal Soc. Lond. A: Math. Phys. Eng. Sci.* **392**, 45 (1984).
- [90] von Bergmann, J. & von Bergmann, H. Foucault pendulum through basic geometry. *Am. J. Phys.* **75**, 888 (2007).
- [91] Bloch, F. Über die Quantenmechanik der Elektronen in Kristallgittern. *Zeitschrift für Physik* **52**, 555 (1929).
- [92] Zak, J. Berry's phase for energy bands in solids. *Phys. Rev. Lett.* **62**, 2747 (1989).
- [93] Rauch, T. *Topologische Isolatoren im Tight-Binding-Modell*. Thesis, Martin-Luther-Universität Halle-Wittenberg (2012).
- [94] Thouless, D., Kohmoto, M., Nightingale, M. & Den Nijs, M. Quantized Hall conductance in a two-dimensional periodic potential. *Phys. Rev. Lett.* **49**, 405 (1982).
- [95] Hasan, M. Z. & Kane, C. L. Colloquium: topological insulators. *Rev. Mod. Phys.* **82**, 3045 (2010).
- [96] Peierls, R. Zur Theorie der galvanomagnetischen Effekte. *Zeitschrift für Physik* **53**, 255 (1929).
- [97] Jones, H. & Zener, C. The general proof of certain fundamental equations in the theory of metallic conduction. *Proc. R. Soc. Lond. A* **144**, 101 (1934).
- [98] Sundaram, G. & Niu, Q. Wave-packet dynamics in slowly perturbed crystals: Gradient corrections and Berry-phase effects. *Phys. Rev. B* **59**, 14915 (1999).
- [99] Hatsugai, Y. Edge states in the integer quantum Hall effect and the Riemann surface of the Bloch function. *Phys. Rev. B* **48**, 11851 (1993).
- [100] Hatsugai, Y. Chern number and edge states in the integer quantum Hall effect. *Phys. Rev. Lett.* **71**, 3697–3700 (1993).
- [101] Zhang, Y., Železný, J., Sun, Y., van den Brink, J. & Yan, B. Spin Hall effect emerging from a noncollinear magnetic lattice without spin-orbit coupling. *New J. Phys.* **20**, 073028 (2018).
- [102] Sinova, J., Valenzuela, S. O., Wunderlich, J., Back, C. & Jungwirth, T. Spin Hall effects. *Rev. Mod. Phys.* **87**, 1213 (2015).
- [103] Röntgen, W. C. Über die durch Bewegung eines im homogenen elektrischen Felde befindlichen Dielectricums hervorgerufene electrodynamische Kraft. *Annalen der Physik* **271**, 264 (1888).
- [104] King-Smith, R. & Vanderbilt, D. Theory of polarization of crystalline solids. *Phys. Rev. B* **47**, 1651 (1993).
- [105] Resta, R. Macroscopic polarization in crystalline dielectrics: the geometric phase approach. *Rev. Mod. Phys.* **66**, 899 (1994).
-



- 
- [106] Gao, Y., Vanderbilt, D. & Xiao, D. Microscopic theory of spin toroidization in periodic crystals. *Phys. Rev. B* **97**, 134423 (2018).
- [107] Fiebig, M. Revival of the magnetoelectric effect. *J. Phys. D: Appl. Phys.* **38**, R123 (2005).
- [108] Hayami, S., Kusunose, H. & Motome, Y. Toroidal order in metals without local inversion symmetry. *Phys. Rev. B* **90**, 024432 (2014).
- [109] Xiao, D., Shi, J. & Niu, Q. Berry phase correction to electron density of states in solids. *Phys. Rev. Lett.* **95**, 137204 (2005).
- [110] Chang, M.-C. & Niu, Q. Berry phase, hyperorbits, and the Hofstadter spectrum: Semiclassical dynamics in magnetic Bloch bands. *Phys. Rev. B* **53**, 7010 (1996).
- [111] Raoux, A., Piéchon, F., Fuchs, J.-N. & Montambaux, G. Orbital magnetism in coupled-bands models. *Phys. Rev. B* **91**, 085120 (2015).
- [112] Dias, M. d. S., Bouaziz, J., Bouhassoune, M., Blügel, S. & Lounis, S. Chirality-driven orbital magnetic moments as a new probe for topological magnetic structures. *Nat. Commun.* **7**, 13613 (2016).
- [113] Lux, F. R., Freimuth, F., Blügel, S. & Mokrousov, Y. Engineering chiral and topological orbital magnetism of domain walls and skyrmions. *Commun. Phys.* **1**, 60 (2018).
- [114] Slater, J. C. & Koster, G. F. Simplified LCAO method for the periodic potential problem. *Phys. Rev.* **94**, 1498 (1954).
- [115] Ashcroft, N. W. & Mermin, N. D. *Solid State Physics* (Holt, Rinehart and Winston, New York, 1976).
- [116] Rauch, T. *Topological Insulators and Semimetals: Theory for Bulk and Surface Electronic Properties*. Thesis, Martin-Luther-Universität Halle-Wittenberg (2016).
- [117] Löwdin, P.-O. On the non-orthogonality problem connected with the use of atomic wave functions in the theory of molecules and crystals. *The J. Chem. Phys.* **18**, 365 (1950).
- [118] Yusufaly, T., Vanderbilt, D. & Coh, S. Tight-Binding Formalism in the Context of the PythTB Package (Program documentation) (2018), accessed August 2019: [http://www.physics.rutgers.edu/pythtb/\\_downloads/915304f3240dca549efa8f491463a797/pythtb-formalism.pdf](http://www.physics.rutgers.edu/pythtb/_downloads/915304f3240dca549efa8f491463a797/pythtb-formalism.pdf).
- [119] Dobardžić, E., Dimitrijević, M. & Milovanović, M. Generalized Bloch theorem and topological characterization. *Phys. Rev. B* **91**, 125424 (2015).
- [120] Hall, E. H. On a new action of the magnet on electric currents. *Am. J. Math.* **2**, 287 (1879).
- [121] Zhang, Y., Tan, Y.-W., Stormer, H. L. & Kim, P. Experimental observation of the quantum Hall effect and Berry's phase in graphene. *Nature* **438**, 201 (2005).

- 
- [122] Landau, L. & Lifshitz, E. *Quantum Mechanics: Non-relativistic theory, Course of Theoretical Physics. Vol. 3* (Pergamon Press, London, 1977).
- [123] Klitzing, K. v., Dorda, G. & Pepper, M. New method for high-accuracy determination of the fine-structure constant based on quantized Hall resistance. *Phys. Rev. Lett.* **45**, 494 (1980).
- [124] Novoselov, K. S. *et al.* Electric field effect in atomically thin carbon films. *Science* **306**, 666 (2004).
- [125] Peierls, R. Zur Theorie des Diamagnetismus von Leitungselektronen. *Zeitschrift der Physik* **80**, 763 (1933).
- [126] Metalidis, G. *Electronic Transport in Mesoscopic Systems*. Thesis, Martin-Luther-Universität Halle-Wittenberg (2007).
- [127] Onsager, L. Crystal statistics. I. A two-dimensional model with an order-disorder transition. *Phys. Rev.* **65**, 117 (1944).
- [128] Onsager, L. Interpretation of the de Haas-van Alphen effect. *The London, Edinburgh, Dublin Philos. Mag. J. Sci.* **43**, 1006 (1952).
- [129] Zhang, X. *et al.* Skyrmion-skyrmion and skyrmion-edge repulsions in skyrmion-based racetrack memory. *Sci. Reports* **5**, 7643 (2015).
- [130] Pfeleiderer, C. *et al.* Skyrmion lattices in metallic and semiconducting B20 transition metal compounds. *J. Physics: Condens. Matter* **22**, 164207 (2010).
- [131] Hamamoto, K., Ezawa, M. & Nagaosa, N. Quantized topological Hall effect in skyrmion crystal. *Phys. Rev. B* **92**, 115417 (2015).
- [132] Seki, S., Ishiwata, S. & Tokura, Y. Magnetoelectric nature of skyrmions in a chiral magnetic insulator  $\text{Cu}_2\text{OSeO}_3$ . *Phys. Rev. B* **86**, 060403 (2012).
- [133] Kézsmárki, I. *et al.* Néel-type skyrmion lattice with confined orientation in the polar magnetic semiconductor  $\text{GaV}_4\text{S}_8$ . *Nat. Mater.* **14**, 1116 (2015).
- [134] Ruff, E. *et al.* Multiferroicity and skyrmions carrying electric polarization in  $\text{GaV}_4\text{S}_8$ . *Sci. Adv.* **1**, e1500916 (2015).
- [135] Saito, H. *et al.* Evidence for a New Magnetoelectric Effect of Current-Induced Magnetization in a Toroidal Magnetic Ordered State of  $\text{UNi}_4\text{B}$ . *J. Phys. Soc. Jpn.* **87**, 033702 (2018).
- [136] Yu, X. *et al.* Biskyrmion states and their current-driven motion in a layered manganese. *Nat. Commun.* **5**, 3198 (2014).
- [137] Zhang, X. *et al.* Skyrmion dynamics in a frustrated ferromagnetic film and current-induced helicity locking-unlocking transition. *Nat. Commun.* **8**, 1717 (2017).
- [138] Loudon, J. C. *et al.* Do Images of Biskyrmions Show Type-II Bubbles? *Adv. Mater.* **31**, 1806598 (2019).

- 
- [139] Yao, Y. *et al.* Magnetic hard nanobubble: A possible magnetization structure behind the bi-skyrmion. *Appl. Phys. Lett.* **114**, 102404 (2019).
- [140] Kharkov, Y., Sushkov, O. & Mostovoy, M. Bound states of skyrmions and merons near the Lifshitz point. *Phys. Rev. Lett.* **119**, 207201 (2017).
- [141] Meynell, S. *et al.* Neutron study of in-plane skyrmions in MnSi thin films. *Phys. Rev. B* **96**, 054402 (2017).
- [142] Bogdanov, A. & Hubert, A. The stability of vortex-like structures in uniaxial ferromagnets. *J. Magn. Magn. Mater.* **195**, 182–192 (1999).
- [143] Zheng, F. *et al.* Direct imaging of a zero-field target skyrmion and its polarity switch in a chiral magnetic nanodisk. *Phys. Rev. Lett.* **119**, 197205 (2017).
- [144] Zhang, S., Kronast, F., van der Laan, G. & Hesjedal, T. Real-space observation of skyrmionium in a ferromagnet-magnetic topological insulator heterostructure. *Nano Lett.* **18**, 1057 (2018).
- [145] Groth, C. W., Wimmer, M., Akhmerov, A. R. & Waintal, X. Kwant: a software package for quantum transport. *New J. Phys.* **16**, 063065 (2014).
- [146] Zhang, X., Zhou, Y. & Ezawa, M. Magnetic bilayer-skyrmions without skyrmion Hall effect. *Nat. Commun.* **7**, 10293 (2016).
- [147] Barker, J. & Tretiakov, O. A. Static and Dynamical Properties of Antiferromagnetic Skyrmions in the Presence of Applied Current and Temperature. *Phys. Rev. Lett.* **116**, 147203 (2016).
- [148] Zhang, X., Zhou, Y. & Ezawa, M. Antiferromagnetic skyrmion: stability, creation and manipulation. *Sci. Reports* **6**, 24795 (2016).
- [149] Jin, C., Song, C., Wang, J. & Liu, Q. Dynamics of antiferromagnetic skyrmion driven by the spin Hall effect. *Appl. Phys. Lett.* **109**, 182404 (2016).
- [150] Buhl, P. M., Freimuth, F., Blügel, S. & Mokrousov, Y. Topological spin Hall effect in antiferromagnetic skyrmions. *physica status solidi (RRL)-Rapid Res. Lett.* **11**, 1700007 (2017).
- [151] Legrand, W. *et al.* Room-temperature stabilization of antiferromagnetic skyrmions in synthetic antiferromagnets. *Nat. Mater.* (2019).
- [152] Ozawa, R., Hayami, S. & Motome, Y. Zero-field skyrmions with a high topological number in itinerant magnets. *Phys. Rev. Lett.* **118**, 147205 (2017).
- [153] Kim, S. K., Lee, K.-J. & Tserkovnyak, Y. Self-focusing skyrmion racetracks in ferrimagnets. *Phys. Rev. B* **95**, 140404 (2017).
- [154] Bhukta, M. M. M. *et al.* A novel chiral spin texture: Antiferromagnetic Skyrmionium. *arXiv preprint: 1810.08262* (2018).
- [155] Obadero, S., Yamane, Y., Akosa, C. & Tatara, G. Current-driven nucleation and propagation of antiferromagnetic skyrmionium. *arXiv preprint: 1904.06870* (2019).
-

- [156] Shen, L. *et al.* Current-Induced Dynamics and Chaos of an Antiferromagnetic Bimeron. *arXiv preprint: 1905.09007* (2019).
- [157] Rybakov, F. N., Borisov, A. B., Blügel, S. & Kiselev, N. S. New type of stable particlelike states in chiral magnets. *Phys. Rev. Lett.* **115**, 117201 (2015).
- [158] Zheng, F. *et al.* Experimental observation of chiral magnetic bobbbers in B20-type FeGe. *Nat. Nanotechnol.* **13**, 451 (2018).
- [159] Hopf, H. Über die Abbildungen der dreidimensionalen Sphäre auf die Kugelfläche. *Math. Ann.* **104**, 637 (1931).
- [160] Sutcliffe, P. Vortex rings in ferromagnets: Numerical simulations of the time-dependent three-dimensional Landau-Lifshitz equation. *Phys. Rev. B* **76**, 184439 (2007).
- [161] Tanigaki, T. *et al.* Real-space observation of short-period cubic lattice of skyrmions in MnGe. *Nano Lett.* **15**, 5438 (2015).
- [162] Zhang, X.-X., Mishchenko, A. S., De Filippis, G. & Nagaosa, N. Electric transport in three-dimensional skyrmion/monopole crystal. *Phys. Rev. B* **94**, 174428 (2016).
- [163] Lai, P. *et al.* An improved racetrack structure for transporting a skyrmion. *Sci. Reports* **7**, 45330 (2017).
- [164] Fernandes, I. L., Bouaziz, J., Blügel, S. & Lounis, S. Universality of defect-skyrmion interaction profiles. *Nat. Commun.* **9**, 4395 (2018).
- [165] Kong, L. & Zang, J. Dynamics of an insulating skyrmion under a temperature gradient. *Phys. Rev. Lett.* **111**, 067203 (2013).
- [166] Wang, X. *et al.* Efficient skyrmion transport mediated by a voltage controlled magnetic anisotropy gradient. *Nanoscale* **10**, 733 (2018).
- [167] Cercignani, C. *The Boltzmann equation and its applications* (Springer, 1988).
- [168] Callaway, J. *Quantum theory of the solid state* (Academic Press, 2013).
- [169] Yin, G., Liu, Y., Barlas, Y., Zang, J. & Lake, R. K. Topological spin Hall effect resulting from magnetic skyrmions. *Phys. Rev. B* **92**, 024411 (2015).
- [170] Hamamoto, K., Ezawa, M. & Nagaosa, N. Purely electrical detection of a skyrmion in constricted geometry. *Appl. Phys. Lett.* **108**, 112401 (2016).





## Acknowledgements

I thank everyone who has accompanied and supported me scientifically during the last three years: my colleagues, the discussion partners and proofreaders, the inspiring collaborators in the works published and those who are yet to come. These were exciting years and I am grateful for the many experiences.

In this regard, a special word of thanks is attributed to my supervisor Ingrid Mertig. She found the perfect topic for me so that science became a joyful part of my life. I am in debt to thank her for always giving me the freedom to pursue whichever path I found promising. She has proven great trust in me by allowing me to work in this ambitious field of research and was always keen on hearing new ideas. I found great support on a scientific, creative, financial and personal level. Furthermore, I was blessed with many possibilities to present our results at conferences and to have discussions with internationally renowned scientists.

Zu guter Letzt möchte ich meinen tiefsten Dank denen entgegenbringen, die mein persönliches Leben bereichern: meinen Freunden und meiner Familie. Insbesondere denen, auf die ich immer zählen kann und die schon immer für mich da waren, gebührt eine Dankbarkeit, der keine Danksagung gerecht werden kann.





# Curriculum vitae

## Personal Data

*Name*           Börge Göbel  
*Birth*           December 03, 1992 in Freiberg, Germany  
*Nationality*   German  
*Gender*        Male  
*Address*       Weidenplan 2, 06108 Halle (Saale), Germany

## Education

*since July 2018*   Member and student speaker of the International Max Planck Research School for Science and Technology of Nano-Systems

*since Oct 2016*   PhD studies at the Max Planck Institute of Microstructure Physics, Halle (Saale), Germany and the Martin Luther University Halle-Wittenberg, Halle (Saale), Germany  
Supervisor: Prof. Dr. Ingrid Mertig

*Sep 2016*         Master of Science in Physics at the Martin Luther University  
Master thesis: Topologische Eigenschaften von Skyrmionen  
Final grade: 1.1

*Sep 2014*         Bachelor of Science in Physics at the Martin Luther University  
Bachelor thesis: Translationsdynamik von Molekülen auf Oberflächen  
Final grade: 1.2

*2003 – 2011*       Gymnasium (grammar school) Friedrich-Schiller-Schule,  
Leipzig, Germany  
Final grade: Abitur 1.0

*1999 – 2003*       Grundschule (elementary school) Grundschule Wiederitzsch,  
Leipzig, Germany

## Academic work experience

*since Oct 2016*   Research assistant, Max Planck Institute of Microstructure Physics,  
Fellow Group Ingrid Mertig

*2014 – 2016*       Student assistant, Institute of Physics, Martin Luther University

*2012*             Student assistant, Institute of Mathematics, Martin Luther University

Halle (Saale), 11.09.2019    Börge Göbel



## Eidesstattliche Erklärung

Hiermit erkläre ich, Börge Göbel, die vorliegende Arbeit *Emergent electrodynamics of non-collinear spin textures* selbständig und ohne fremde Hilfe verfasst zu haben. Es wurden keine anderen als die von mir angegebenen Quellen und Hilfsmittel benutzt. Die den benutzten Werken wörtlich oder inhaltlich entnommenen Stellen sind als solche kenntlich gemacht worden. Ich erkläre, die Angaben wahrheitsgemäß gemacht, keine vergeblichen Promotionsversuche unternommen und keine Dissertation an einer anderen wissenschaftlichen Einrichtung zur Erlangung eines akademischen Grades eingereicht zu haben. Ich bin weder vorbestraft noch sind gegen mich Ermittlungsverfahren anhängig.

Halle (Saale), 11.09.2019      Börge Göbel